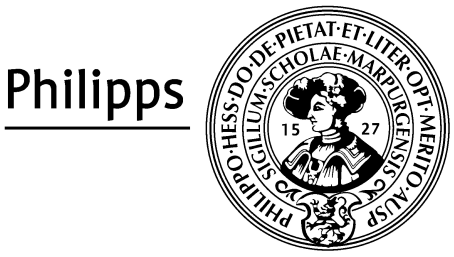

Microstructural Characterization of Dilute N-Containing Semiconductor Alloys and Heterostructures by Scanning Transmission Electron Microscopy

Dissertation

zur
Erlangung des Doktorgrades
der Naturwissenschaften
(Dr. rer. nat.)

dem

Fachbereich Physik
der Philipps-Universität Marburg

vorgelegt von

Tatjana Wegele

aus

Presnowka, Kasachstan

Marburg/Lahn, 2016

Vom Fachbereich Physik der Philipps-Universität Marburg
als Dissertation angenommen am: 22.06.2016
Erstgutachter: Prof. Dr. Kerstin Volz
Zweitgutachter: Prof. Dr. Wolfgang Heimbrodt
Tag der mündlichen Prüfung: 24.06.2016
Hochschulkennziffer: 1180

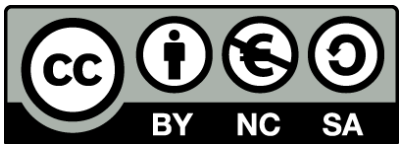

Contents

CHAPTER 1

Introduction

It is impossible to imagine today's world without an Internet connection for private use, e-business, or transfer of research data. In 2015, according to statistical data, $3.2 \cdot 10^9$ people were using the Internet.[59] In 2014, $2 \cdot 10^8$ emails were sent every minute and $2 \cdot 10^{16}$ bytes of information were daily processed by Google.[22] Fibre optics is the most suitable for fast transmission of such huge data volume. Semiconductor lasers have already established themselves as perfect transmitters for fibre-optic communication for 40 years. They have small spot sizes, high output power, and narrow linewidth.[46] In order to minimize the loss of a fibre-optic system, the wavelengths of 1.55 μm for long distances and 1.3 μm for short distances have to be used.[33]

The optimal wavelength for chip-to-chip and on-chip optical data communication can be enabled by Ga(NAsP)-multi quantum well heterostructures (MQWHs) lattice-matched grown on Si(001).[42] A tunable direct band gap and the absence of threading or misfit dislocations make it to the very promising material system for the realization of a stable high-efficiency laser on Si.[37,40,55]

The requirement for a high crystalline quality of MQWH is the optimized growth conditions. The changes in MQWH for varied growth parameters can be detected using many different methods, e.g. high-resolution X-ray diffraction (HR-XRD) and Raman and photoluminescence (PL) spectroscopies. However, these methods do not reveal any change in the structure or only indirectly point it out. The annular dark-field (ADF) scanning transmission electron microscopy (STEM) and a cross-sectional specimen preparation provide a unique opportunity to see the differences between the samples grown at different conditions. The intensity contrast, depending on the atomic number Z, allows to interpret a STEM micrograph more intuitively than the phase-contrast of a TEM micrograph.[50] A qualitative comparison can be directly made during measurement. It helps to find a starting point for further research, thereby explaining the structural changes that have taken place in the QWs. The quantitative analysis of the micrograph structures implies, however, deep knowledge of the image formation in a STEM and the interaction processes of the electrons with the investigated material. The aim of this work is to find an appro-

priate method for quantification of the QW quality at low as well as at high magnification. This research was financially supported by the German Science Foundation (DFG) in the framework of the GRK 1782 Functionalization of Semiconductors.
This doctoral thesis is written cumulatively and has the following structure: Chapter 2.2 describes the main properties of Si, GaP, and GaAs as well as the direct band formation of Ga(NAsP). The image formation in the STEM-mode is explained in Chapter 3, while Chapter 4 contains those results that were not published. All results are summed up in Chapter 5. The detailed discussion of the published results is presented in Chapter 6.
List of Publications:

1. N. Knaub, A. Beyer, T. Wegele, P. Ludewig, and K. Volz, *Quantification of Bi distribution in MOVPE-grown Ga(AsBi) via HAADF STEM*, Journal of Crystal Growth **433**, 89-96 (2016). DOI: 10.1016/j.jcrysgro.2015.10.007.

2. K. Jandiery, P. Ludewig, T. Wegele, A. Beyer, B. Kunert, P. Springer, S. D. Baranovskii, S. W. Koch, K.Volz, and W. Stolz, *Compositional dependence of the band gap in Ga(NAsP) quantum well heterostructures*, Journal of Applied Physics **118**, 065701 (2015). DOI: 10.1063/1.4928331.

3. P. Ludewig, S. Reinhard, K. Jandieri, T. Wegele, A. Beyer, L. Tapfer, K. Volz, and W. Stolz, *MOVPE growth studies of Ga(NAsP)/(BGa)(AsP) multi quantum well heterostructures (MQWH) for the monolithic integration of laser structures on (001) Si-substrate*, Journal of Crystal Growth **438** (2016) 63-69.
DOI: 10.1016/j.jcrysgro.2015.12.024.

4. T. Wegele, A. Beyer, P. Ludewig, P. Rosenow, L. Duschek, K. Jandieri, R. Tonner, W. Stolz, and K. Volz, *Interface morphology and composition of Ga(NAsP) quantum well structures for monolithically integrated LASERs on silicon substrates*, Journal of Physics D: Applied Physics **49** (2016) 075108. DOI: 10.1088/0022-3727/49/7/075108.

5. S. Gies, M. Zimprich, T. Wegele, C. Kruska, A. Beyer, W. Stolz, K. Volz, and W. Heimbrodt, *Annealing effects on the composition and disorder of Ga(N,As,P) quantum wells on silicon substrates for laser application*, Journal of Crystal Growth **402** (2014) 169-174. DOI: 10.1016/j.jcrysgro.2014.05.012.

6. T. Wegele, A. Beyer, S. Gies, M. Zimprich, W. Heimbrodt, W. Stolz, and K. Volz, *Correlation of the nanostructure with optoelectronic properties during rapid thermal annealing of Ga(NAsP) quantum wells grown on Si(001) substrates*, Journal of Applied Physics **119**, 025705 (2016). DOI: 10.1063/1.4939889.

7. M.K. Shakfa, R. Woscholski, S. Gies, T. Wegele, M. Wiemer, P. Ludewig, K. Jandieri, S. D. Baranovskii, W. Stolz, K. Volz, W. Heimbrodt, and M. Koch, *Carrier dynamics in Ga(NAsP)/Si multi-quantum well heterostructures with varying well thickness*, Superlattices and Microstructures **93** (2016) 67-72. DOI: 10.1016/j.spmi.2016.03.002.

CHAPTER 2

The Investigated Material

In this chapter, the basics of the crystal structures of the investigated materials are explained. There is also a brief description of the formation of the band structures and especially of the direct band formation in the Ga(NAsP) material. Finally, there is some information about the growth conditions.

2.1 Basic Components: Si, GaAs, GaP

Only crystalline semiconductor structures were investigated in this work. The previous sentence contains two terms that should be explained. The term 'semiconductor' is applied to the material for which the electrical conductivity is between that of an insulator and conductor at $T > 0$ K. The optical and electrical properties of such materials can be tuned to the desirable application by doping, varying the temperature, and, in the case of the multiple compound semiconductor alloys (binary, ternary, quaternary, and so on), by the composition.

In order to produce a single crystalline material of high quality, which is crucial for a long lifetime performance of semiconductor devices,the thin semiconductor alloys were epitaxially grown on a large single crystal substrate.[54] The elementary semiconductor Si was used as a substrate. The formation of the investigated Ga(NAsP) quaternary alloys can be described as a partial substitution of P atoms in the GaP material by N and As atoms[1]. The compound alloys crystallize in the same structure as the host material, namely in the zinc blende structure. As the electrical and optical properties of the alloy as well as its lattice parameter can be considered as a result of the combination of its binary compounds, the properties of the latter will be described in more detail in the following. Like any other crystalline solid, Si, GaP, and GaAs crystals can be described as a three-dimensional periodical arrangement of the identical units. Such units are known as unit

1 As the As content in the investigated Ga(NAsP) alloys is about 80%, one can consider GaAs as the host crystal.

cells. All information about the symmetry and structure of a crystal is contained in its unit cell. Thus, the crystal can be reproduced by the translation of the unit cell using the translation vector $\vec{R}$

$$\vec{R} = n_1\vec{a}_1 + n_2\vec{a}_2 + n_3\vec{a}_3, \tag{2.1}$$

whereas n_i and a_i with i=1, 2, 3 are integers and basis vectors that build a unit cell, respectively. The lengths of a_i are described as lattice constants. Si, GaP, and GaAs crystallize in a cubic crystal structure, which can be described as two face-centred cubic (fcc) lattices (Figure 2.1 a)) shifted to each other by a quarter of the space diagonal. In a Si crystal, both fcc lattices are occupied by the same sort of atoms and its structure is known as a diamond cubic structure (Figure 2.1 b)). In GaP and GaAs crystals, the one fcc lattice is built by Ga atoms, while the second one consists of P or As atoms, respectively. Such crystal structure is known as the zinc blende (Figure 2.1 c)).

In momentum ($\vec{k}$) space or reciprocal space, which is important for the description of the properties of semiconductor materials, a primitive – with only one lattice point – unit cell of a reciprocal lattice is known as the first Brillouin zone. Figure 2.2 depicts the Brillouin zone of an fcc lattice, where Γ is the centre of the first Brillouin zone, and X and L are the cross-over points of the [010]-axis and of the space diagonal with the edge of the first Brillouin zone, respectively. The first Brillouin zone contains information about all electron states due to the periodicity of a crystal structure. The electron states can be calculated by solving the Schrödinger equation with the Born-Oppenheimer or adiabatic approximation and the mean-field approximation[73]:

$$H_{1el}\Psi(\vec{r}) = \left(\frac{p^2}{2m} + V_{eff}\right)\Psi(\vec{r}) = E\Psi(\vec{r}), \tag{2.2}$$

with a translation invariant one-electron Hamiltonian H_{1el}, kinetic energy $\frac{p^2}{2m}$, effective potential V_{eff} , a wave function $\Psi(\vec{r})$, and the eigenstate energy of the electron E. The solutions of Equation 2.2 are the Bloch wave functions:

$$\Psi(\vec{r}) = e^{i\vec{r}\vec{k}} \cdot u_k(\vec{r}), \tag{2.3}$$

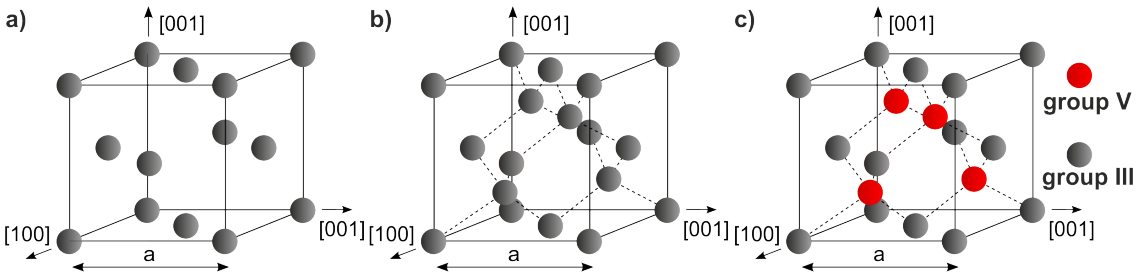

Figure 2.1: Unit cells of the face-centred cubic a), diamond b) and zinc blende c) crystalline structures.

where $u_k(\vec{R}+\vec{r}) = u_k(\vec{r})$. All electron states, together, form energy bands. For free electrons, they have a parabolic shape and the periodicity of the reciprocal lattice. To solve Equation 2.2 for small lattice potential, the perturbation theory is applied. In this case, the states become non-degenerate at the edges of the Brillouin zone and therefore gaps are formed between the energy bands. The band completely filled with electrons at $T = 0$ K is known as a valence band (VB) and the empty one as a conduction band (CB).

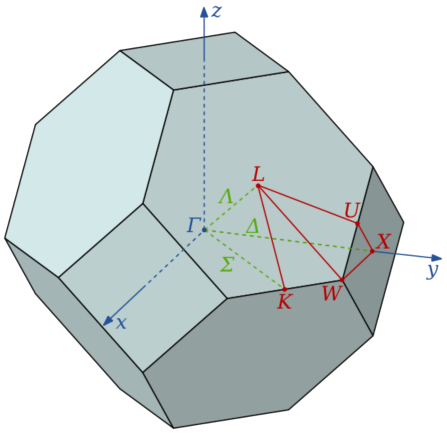

Figure 2.2: The first Brillouin zone of an fcc crystal.[1]

The band structures of GaAs and GaP in Figure 2.3 a) and b), respectively, reveal the different optical properties of these two materials. In GaAs, the VB maximum and CB minimum are at the same position (Γ-point). Thus, a direct optical transition is possible. In GaP, the VB maximum is at Γ, but the CB minimum is at X, and hence a phonon contribution is needed for an optical transition. Si is an indirect semiconductor as well. The direct band gap is not the only advantage of GaAs in comparison with Si. Moreover, its electron mobility and saturation velocity are higher than ones of Silicon. Owing to the wide band gap, it has low thermal conductivity; therefore, GaAs devices produce low noise. Si, however, is much cheaper and has significantly higher purity. Because of its stable crystal, the Si structures of a huge size can be grown. Therefore, the

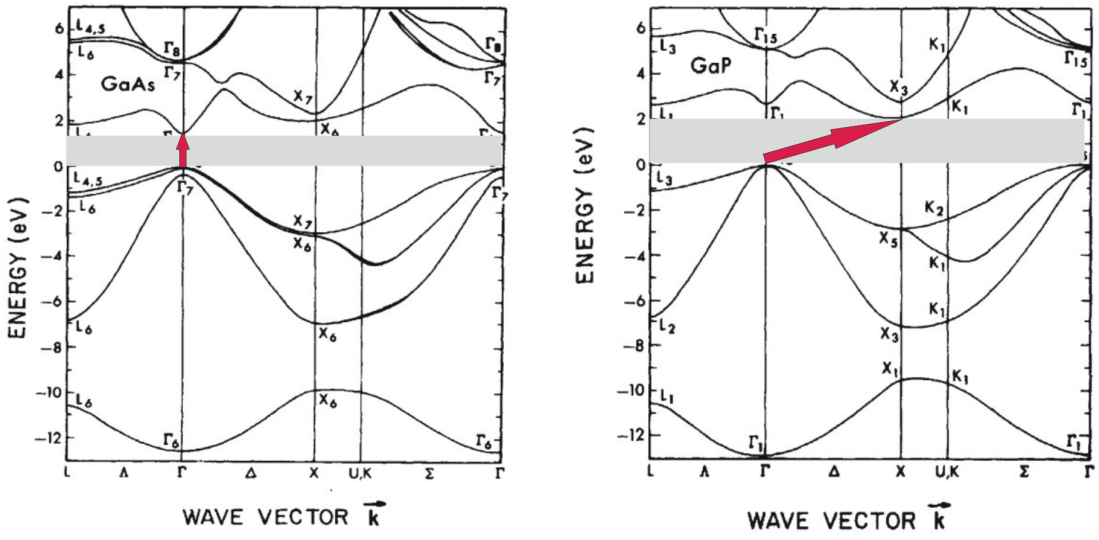

Figure 2.3: Energy band structures of GaAs, with a direct band gap at Γ a), and of GaP, with an indirect band gap at X b). The red arrows show the optical transitions.[28]

use of Si as a substrate is more preferable than GaAs. GaP serves as a link between Si and the quaternary III-V layers. As the lattice constants of Si and GaP match very well, it is possible to grow structures without misfit and threading dislocations.[40,65] Moreover, a GaP layer between an N-containing QW and a B-containing layer prevents formation of B-N bonds that can act as non-radiative centres.[39] Incorporation of N and As atoms in GaP allows to improve its optical properties and produce a material with a tunable direct band gap.

2.2 Direct Band Gap Formation of Ga(NAsP)

The incorporation of As into GaP leads to the decrease of the band gap at Γ point. If the As concentration is 73%, Ga(AsP) turns into a direct band material, as shown by the blue line in Figure 2.4.[37,77] However, owing to the larger covalent radius of As in comparison to one of P, an increase in As content results in an increasing compressive strain, which again shifts the CB up. The incorporation of N atoms, on the contrary, reduces the strain. Moreover, the anti-crossing interaction of the highly localized N level (red straight line) lying in the CB splits of the N-relating band into the E^--band (red line), and E^+-band, the latter is not shown here.[60] The energies of the new bands can be calculated as the following:

$$E^{\pm} = \mp\frac{1}{2}\left(E_N + E_M \pm \sqrt{(E_M - E_N)^2 + 4C^2 x_N}\right), \tag{2.4}$$

where E_M is the edge of the conduction band of Ga(AsP) at the Γ-point, E_N is the energy of the strongly localized N level, x_N is N content and C the coupling constant. Not only the modification of the conduction band but also the change of the valence band has to be taken into account as described in more detail later.[29]

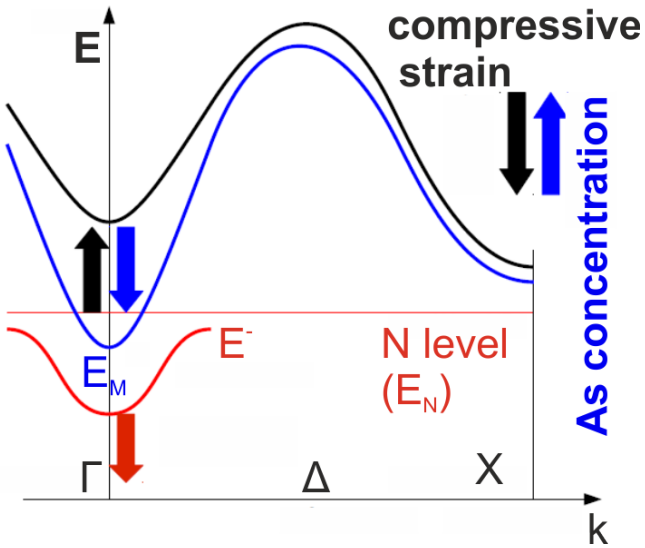

Figure 2.4: Formation of a direct band gap in Ga(NAsP).[77]

2.2.1 Growth Parameters and Structure of the Investigated Layers

The Ga(NAsP)-quantum wells investigated here are part of the multi-QW (MQW) structures grown by metal organic vapour phase epitaxy (MOVPE) in a horizontal reactor system (AIX 200-GFR) at 525 °C on GaP/Si templates. The templates with approximately 32 nm GaP were nucleated on exactly oriented Si(001) substrates in a commercial Aixtron Crius R 300mm III/V-Si-cluster tool.[48,65] Figure 2.5 a) shows schematically the investigated layer stack of the #26461 sample. Starting from bottom to top: the GaP nucleation on the Si was carried at 675 °C. For the growth of following 80 nm thick (BGa)(AsP) and 5 nm thick GaP, a 100 °C lower temperature was used. Then the temperature was decreased to 525 °C under tertiarybutylphosphine (TBP) stabilisation. For the better interface quality, the growth was interrupted and exposed to TBP and tertiarybutylarsine (TBAs) for 10 s. A GaP barrier of 1 nm (nominally) was grown on the approximately 5 nm thick QW. The growth optimization of such thin barriers is carried out to optimize the possible Type-II QW-lasers. For a thinner layer, the overlap of the electron and hole wave functions is bigger.[72] The next (BGa)(AsP)-layer was grown at 575 °C, with the previous heating TBP stabilised. The stack contains 7 Ga(NAsP)-QWs. The concentration of the QW can be found in Figure 2.5 b). The concentration was not determined in the stack that was grown extra to be investigated with an electron microscope, but in the samples whose numbers are listed in the table. The recipes of these samples were used for the growth of the QWs in the #26461 sample. Hence, it should be taken into account that the concentration can deviate from the XRD-measurements.
The epitaxial growth of the #26461 sample as well as the after growth thermal treatment, and the XRD-measurements were carried out by Dr Peter Ludewig.

a)

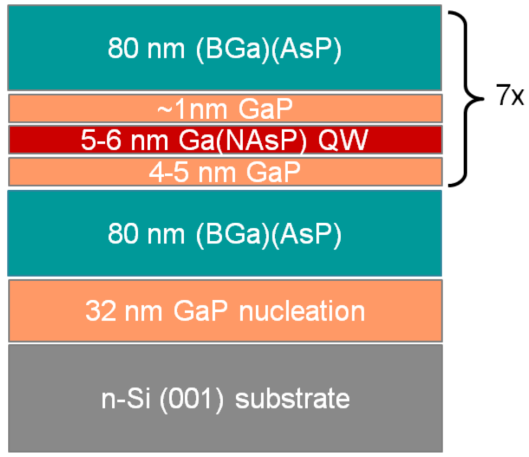

b)

QW	P [%]	N [%]	MQW
7	0	8.6	#26261
6	13.2/14.6	7.2/7.3	#26280/ #26403
5	15.5	5.8	#26459
4	19.7	6.5	26282
3	8.8	7.9	26267
2	24.8	6.1	26309
1	13.2/14.6	7.2/7.3	#26280/ #26403

Figure 2.5: a) Schematic structure of the layers in the #26461 sample. b) Numbers of samples whose growth conditions were chosen for the growth of the QWs in the #26461 sample.

CHAPTER 3

Scanning Transmission Electron Microscopy

The investigations, whose results are presented in Chapter 4, are carried out using the annular dark field (ADF) scanning transmission electron microscopy (STEM[1]) method. Therefore, the basics of image formation and acquisition will be presented in the following.

3.1 Lens Aberrations

The prototype of the first scanning electron microscope was built by Knoll in 1935. However, it had very poor resolution of 100 μm, as the focused electron beam was not yet demagnified.[9] The first TEM with scanning coils was developed and constructed by Ardenne in 1937.[53] It was a good stimulation for the development of a surface-sensitive scanning electron microscopy (SEM). However, the resolution of a conventional TEM was much better in comparison with a STEM and thus the latter was forgotten for over 20 years. The limitation factors were the not-required quality of the electronic equipment, too low brightness of the source, specimen preparation and lens aberrations, all of which nowadays are under better control but still very well-known to each microscopist. The typical lens aberrations are depicted in Figure 3.1. Analogous to the lenses of the light optics, the lines of the magnetic flux become more curved with an increasing radial distance from the optic axis. Consequently, the electrons taking different paths in the magnetic field are differently focused. It results in blurring of the image and degradation of the resolution of smaller details. It is the influence of the **spherical aberration** (C_s).

Chromatic aberration (C_c) also leads to image blurring because the electrons with different kinetic energies experience the Lorentz force more or less strongly. It results in different focal lengths as well. The influence of this aberration is reduced for the field-emission gun, with the energy spread of the beam remaining below 1 eV. This electron source was invented by Crewe in 1960 and ushered in a new STEM era.[51]

The correction of the two following aberrations is the most frequent part of the daily

1 The abbreviation (S)TEM will be used in the following for a method as well as for a microscope.

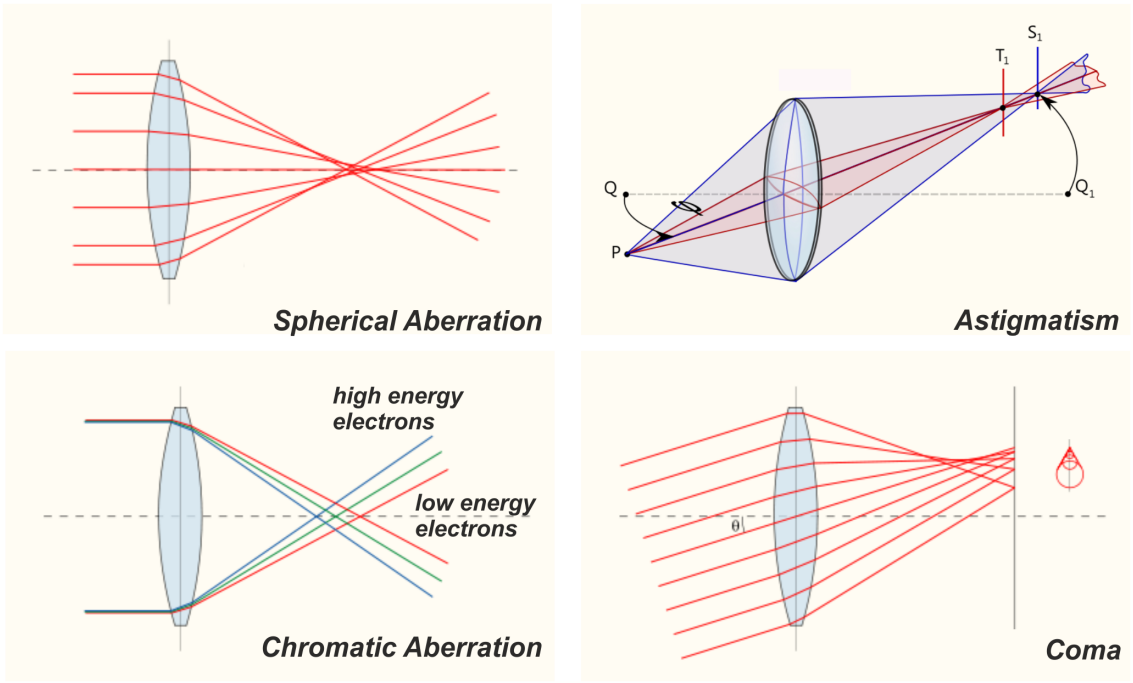

Figure 3.1: The main lens aberrations: spherical aberration, chromatic aberration (left), and astigmatism and coma (right). The dashed lines stand for the optic axes.[2–4,36]

alignment procedure for a microscope operator:

Astigmatism is caused by the asymmetry of the round magnetic lenses. If the e^--beam impinges the magnetic field at a certain angle ϕ (Figure 3.1), the focal length (focal point T_1) in the tangential plane (red) is shorter than the one (focal point S_1) in the saggital plane (blue). It produces an elongated image of the object in each of the mentioned planes. If an off-axis e^--beam impinges a lens suffering from **coma** (B), the electrons propagating through the different zones of the lens are focused at the positions shifted to each other in the image plane. The size of the spots is different and therefore their overlap appears like a spot with a tail.

Hence, the acquisition of a (S)TEM image having an atomic resolution always implies thoroughly corrected aberrations. For this purpose, the alignment of a ronchigram, a 'shadow image', in the STEM mode is very helpful. The formation of a ronchigram is visualized in Figure 3.2 a), where the position of the specimen is labelled by S. The Gaussian, paraxial focus G has a distance R_0 from the specimen and a distance R_1 from the imaging plane.[13] Owing to the spherical aberration, the rays have different angles to the optic axis after passing the lens. The rays with the highest angles cross each other before the specimen. It leads to an unreversed, strongly magnified image of the specimen. As the ray angles decrease, the magnification decreases as well – e.g., the rays with a cross-over at G produce a reversed demagnified image. The special case is if the rays have a focus at S, it results in an infinitely magnified image of the specimen. As the magnification changes strongly from the centre to the edge in the image plane, the

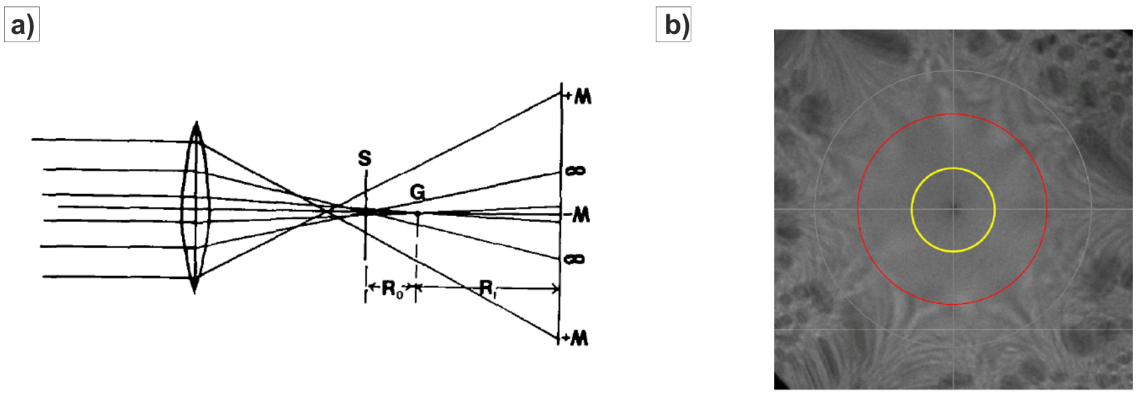

Figure 3.2: a) Formation of a ronchigram by a lens with spherical aberration.[13] b) Ronchigram obtained on a thin amorphous carbon foil. The red circle marks the region with a coherent flat phase, whereas the yellow circle shows the size of the condenser lens aperture.[30]

symmetry in the ronchigram is very sensitive to the aberrations. The use of the ronchigram is very convenient and intuitive for a manual alignment of the two-fold astigmatism (A_1) and second-order axial coma (B_2). It is an important as well as the starting point for a daily alignment of the STEM mode. Figure 3.2 shows the ronchigram obtained on a thin amorphous carbon foil in a JEOL JEM 2200FS microscope.[30] In the region with the homogeneous intensity (red circle) – the region with a coherent flat phase – the incident probe is not affected by lens aberrations. The yellow circle of 24 mrad marks the size of the condenser lens aperture.

A fine correction of the aberrations, and especially of the resolution limiting spherical aberration, is carried out automatically by the correctors nowadays. The revolution in the high-resolution electron microscopy took place for the TEM mode in 1997. It was a result of the cooperation between the theoretical group of Rose, the experimental group of Haider, and the material science group of Urban.[23] The key to the role for the correction of the spherical aberration is the combination of two hexapole elements that compensate the three-fold astigmatism of each other, while their spherical aberrations having negative sign are summed up. Therefore, the spherical aberration of the whole system is minimized. A hexapole corrector can be used for the STEM mode as well. For an automatic correction, we use software based on the Zemlin tableau method in the TEM and STEM modes.[75] In the first case, the shape of the diffractograms, and, in the second case, the shape of the probe, are analysed depending on the tilt angle.[68]

3.2 Image Formation in the STEM Mode

The acquisition of the STEM images, presented in Chapter 4, was performed using a JEOL JEM 2200FS. The microscope is equipped with C_s-correctors for the TEM and STEM modes, as depicted in Figure 3.3 a). The main components of the STEM mode, relevant here, are schematically shown in Figure 3.3 b). A Schottky field emission gun serves as

an electron source. It is a combination of a thermionic and a field emission source: the electrons are extracted from a tip of tungsten wire by heating at 1700 K and application of an intense electric field [71]. It provides a narrow bright e^--beam with a stable beam current. The first condenser lens (CL1) allows changing the intensity of electron beam. The third condenser lens (CL3)[1] is just weakly excited in the STEM mode. Its current value is fixed, and it just transfers the beam through a condenser lens aperture (CLA) to the C_s-corrector. The size of the chosen CLA determines the value of the convergence angle of the e^--beam. For the investigations presented in this work, the semi-convergence angle of 24 mrad was used because it results in a minimum size of the probe. [68] The corrected e^--beam rasterizes by scan coils and gets demagnified at the specimen by the combination of the condenser mini-lens (CM) and the objective pre-field. The post-specimen optics contains the imaging and the projector lens systems. The latter enables a variation of the detected angular range. The microscope has an in-column Ω-filter, which is built in between the imaging and projector lens systems. It allows performing the electron energy loss spectroscopy (EELS). Below the projector lens system there is a ring-shaped DF-detector with a YAP (yttrium aluminium perovskite) scintillator (inside the vacuum) and a light pipe made of solid quartz. The light guide joins the scintillator with a photomultiplier (outside the vacuum). [34] The photocathode has its maximum sensitivity at the same wavelength as the peak of the emission spectrum of the scintillator. In combination with the short decay time of 40 ns, it is a great advantage of the YAP detector. [5] The image acquisition system consists of DigiScan and Digital Micrograph software.

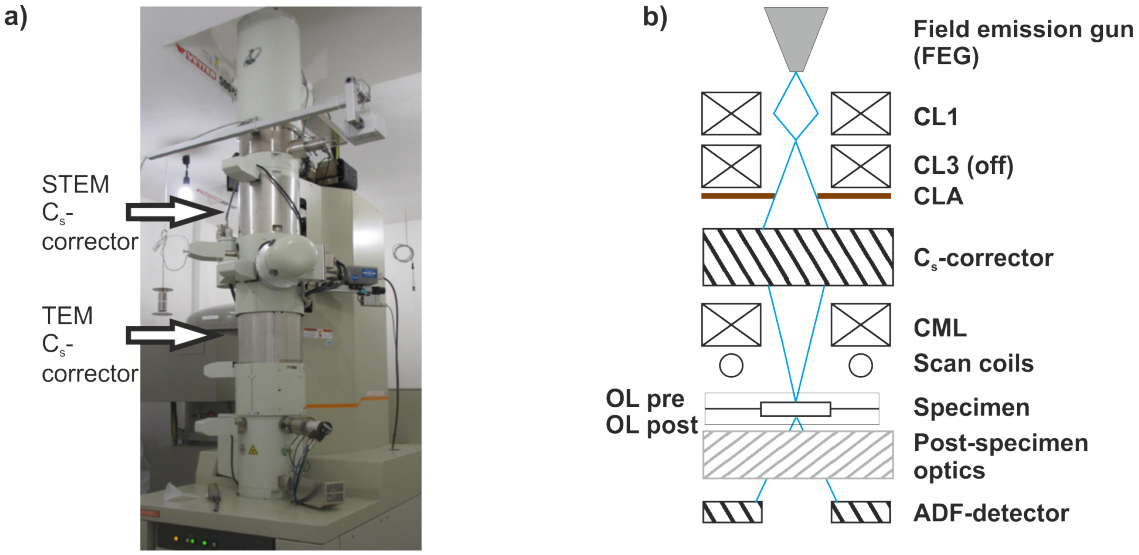

Figure 3.3: a) JEOL JEM 2200FS equipped with C_s-corrector for the TEM and STEM modes. b) Schematic ray path with the main components of the STEM mode.

1 This microscope model does not have a second condenser lens.

3.2.1 Rutherford Scattering

The intensity contrast in HAADF STEM-micrographs is usually described as Z-contrast. The origin of this name becomes clear if one considers the mechanism of the high-angle scattering of electrons on nuclei, which is analogous to the backscattering of the α-particles on the gold foil in the famous Rutherford's experiment[57]. The intensity I is proportional to the total elastic cross section σ[50].
The differential elastic cross section was derived by Rutherford as follows

$$\frac{d\sigma_R(\theta)}{d\Omega} = \frac{Z^2 e^4}{16(4\pi\varepsilon_0 E_0)^2} \frac{1}{sin^4\frac{\theta}{2}}, \tag{3.1}$$

with the atomic number Z of the target material, the elementary charge e, the kinetic energy of the particles E_0, the dielectric constant ε_0 and the scattering angle θ. It was already taken into account that the scattered particle is an electron. The scattering process is thereby incoherent.
Equation 3.1 considers electrons only as particles. However, for the calculation of a σ the wave nature of the electron has to be considered. It can be done using the following approach

$$\frac{d\sigma_R(\theta)}{d\Omega} = |f(\theta)|^2, \tag{3.2}$$

where $f(\theta)$ is related to the amplitude of the scattered electron wave and is also known as the atomic scattering factor.
If the electron propagates far from the nucleus, the scattering effect is weaker. The nucleus of the target atom is screened by its own electrons from the incident electron. For taking screening into account, the sine term in Equation 3.1 is extended by the screening parameter:

$$\theta_0 = \frac{0.117\, Z^{1/3}}{E_0^{1/2}} \tag{3.3}$$

During the measurements, the Jeol JEM 2200 FS was operated at 200 kV. Therefore, the relativistic effects cannot be neglected anymore. Therefore, Equation 3.1 is modified once more:

$$\frac{d\sigma_R(\theta)}{d\Omega} = \frac{Z^2 \lambda^4}{64\,\pi^4 a_0^2} \frac{1}{\left(sin^2\frac{\theta}{2} + \frac{\theta_0^2}{4}\right)^2}, \tag{3.4}$$

where a_0 is the Bohr radius of the scattering atom and λ is the relativistically corrected wavelength of the electron.

Equation 3.2 needs a correction as well. This is, because of by $T > 0$ K, there is a thermal vibration in a crystal. It is the reason for the diffuse background in the diffraction pattern.[74]. The thermal diffused scattering (TDS) can be described by the Einstein model. Hence, the atoms will be considered as independent oscillators with the vibration

amplitude $\bar{u^2}$, a mean-square displacement of an atom from its equilibrium position[52]:

$$\sigma \propto \int_{\theta_{min}}^{\theta_{max}} f^2(\theta) \left[1 - e^{-2M_{TDS}(\theta^2/\lambda^2)}\right] \mathrm{d}^2\theta, \tag{3.5}$$

where $M_{TDS} = 8\pi^2\bar{u^2}$, and θ_{min} and θ_{max} are inner and outer detector angles, respectively.

3.2.2 Static Atomic Displacements

A substitution of one sort of atom in a host crystal by another one leads to a change in the STEM-intensity, not only because of the changed mean value of Z. If after incorporation of N atoms into GaAs crystal, the surrounding atoms stayed on their ideal positions, it would be described as virtual crystal approximation (VCA) (Figure 3.4 a)). However, N atom has a much smaller covalent radius than As atom, leading to a displacements of its neighbours, so-called static atomic displacements (SADs), as shown in Figure 3.4 b), and therefore, to a locally induced strain. Figure 3.4 c) depicts the simulated intensities of Ga(NAs), Ga(NAsP), and Ga(AsP) with dependence on the inner detector angle. The simulations were carried out using the STEMsim software for a specimen thickness of 28 nm each.[56] The concentrations of the material systems were chosen in such a manner that they have an equal lattice constant. It can be clearly seen that at low angles, the ADF intensity becomes sensitive to the content of light atoms due to SADs.[21] M_{TDS} in Equation 3.5 should be replaced by $M = M_{TDS} + M_{SADs}$. The simulated intensities

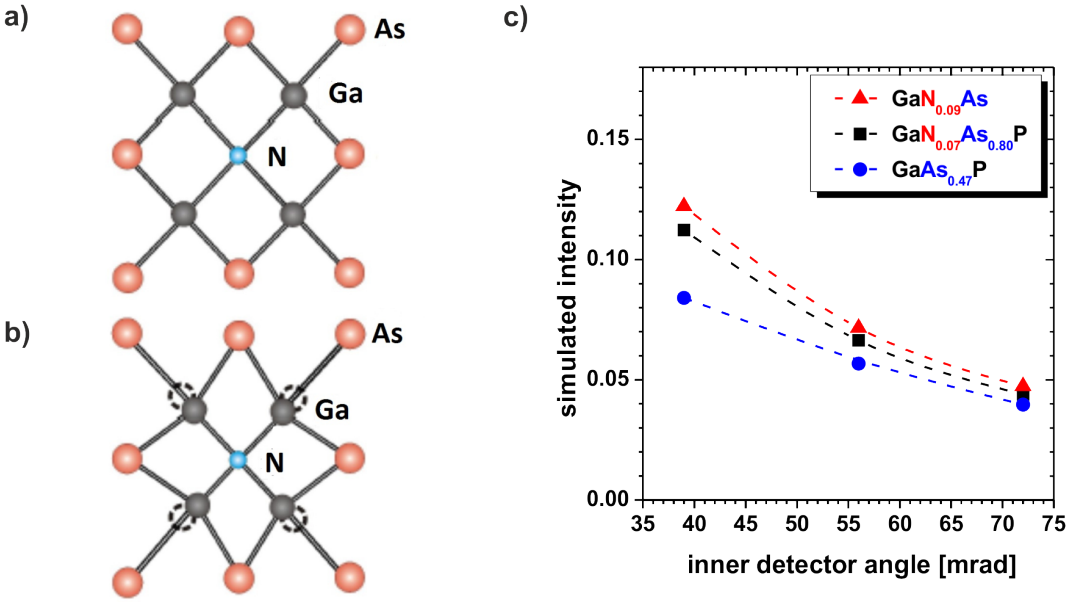

Figure 3.4: a) Virtual crystal approximation (VCA), b) static atomic displacements (SADs) (left top),[17] c) intensity simulated using the STEMsim software[56] for Ga(NAs), Ga(NAsP) and Ga(AsP) materials, 28 nm thick each, parallel to the beam direction ([010]-crystal orientation). The simulated intensity was averaged over the region of ca. 2.5 nm x 2.5 nm in the plane perpendicular to the beam direction.

of N-containing materials Ga(NAs) and Ga(NAsP) show a stronger dependence on an inner detector angle than Ga(AsP) and can be well separated, especially for low detector angles from the latter one. Thus, if a QW had some lattice-matched regions but different concentrations, it would be possible to assign them.

3.2.3 Channelling

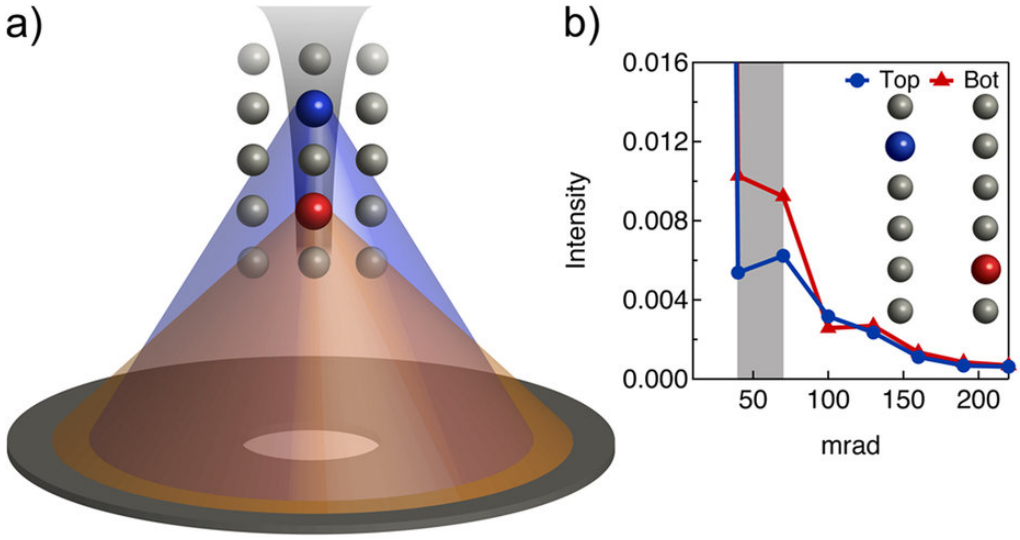

Figure 3.5: a) Schematic description of changing the scattering angles during the channeling of the electron beam along an atomic column. b) The simulated intensities of the top (blue circle) and bottom (red triangle) atoms with dependence on the inner detector angle. The intensities of the both atoms significantly differ in the grey region.[76]

If the electron probe propagates along the high symmetry zone axis in a crystal, the column-wise ordered atoms act as focusing lenses.[16,41] Such propagation is schematically shown in Figure 3.5 a). The top (blue) and the bottom (red) atoms scatter differently focused beams. The broader the beam, the fewer electrons propagate close to the nuclei and the fewer electrons will be scattered to high angles. Therefore, the intensity of the bottom atom has higher intensity than that of the top atom, as the simulated intensities in Figure 3.5 b) affirm, especially in the grey highlighted region. Thus, channelling is another important effect that has to be taken into account.

CHAPTER 4

Results

This chapter focuses on the most recent results originating from the investigation performed on the Ga(NAsP)-QWs grown at 525 °C. At first the evaluations of the STEM micrographs determined at low magnification are presented. In particular, the influence of the variation of the N/P content on the interface roughness and on the homogeneity of the intensity was quantitatively investigated. Moreover, the comparison of the structural properties before and after a thermal treatment to the as grown samples was performed. The last part of this chapter contains the quantitative analysis at the atomic scale. The change of the appearance of the intensity pattern for different detector angles will be discussed along with the comparison with the simulated results.

4.1 Influence of the N/P content on the Quality of Ga(NAsP)-QWs

The primary aim of the STEM investigations is the optimization of the growth conditions. It implies that the quality of the layers has to be defined as a quantitatively comparable characteristic. It is known that the interface roughness strongly correlates with the mobility of carriers in materials such as (AlGa)As/GaAs, Si/SiGe, AlAs/GaAs.[15,49,58] The optical properties of the semiconductor materials are impacted by the interface roughness as well. The reason for this – as reported for Ga(NAs)/GaAs and GaAs/(AlGa)As – is the broadening of electronic density of states.[6,14] In a similar way, optical and electronic properties are influenced by compositional fluctuations because the local change of the composition leads to locally different band gaps.[47,62] Therefore, interface roughness and compositional fluctuation were chosen as the indicators of the quality of the layers investigated within the framework of this thesis.

4.1.1 Interface Roughness With Dependence on the Variation of the N/P Contents

Figure 4.1 a) depicts STEM micrographs (2.5 M magnification) acquired on the #26461 as grown sample that was prepared as a [010] cross-section. The measurement was performed for the inner detector angle of 36 mrad in order to increase the strain sensitivity and to

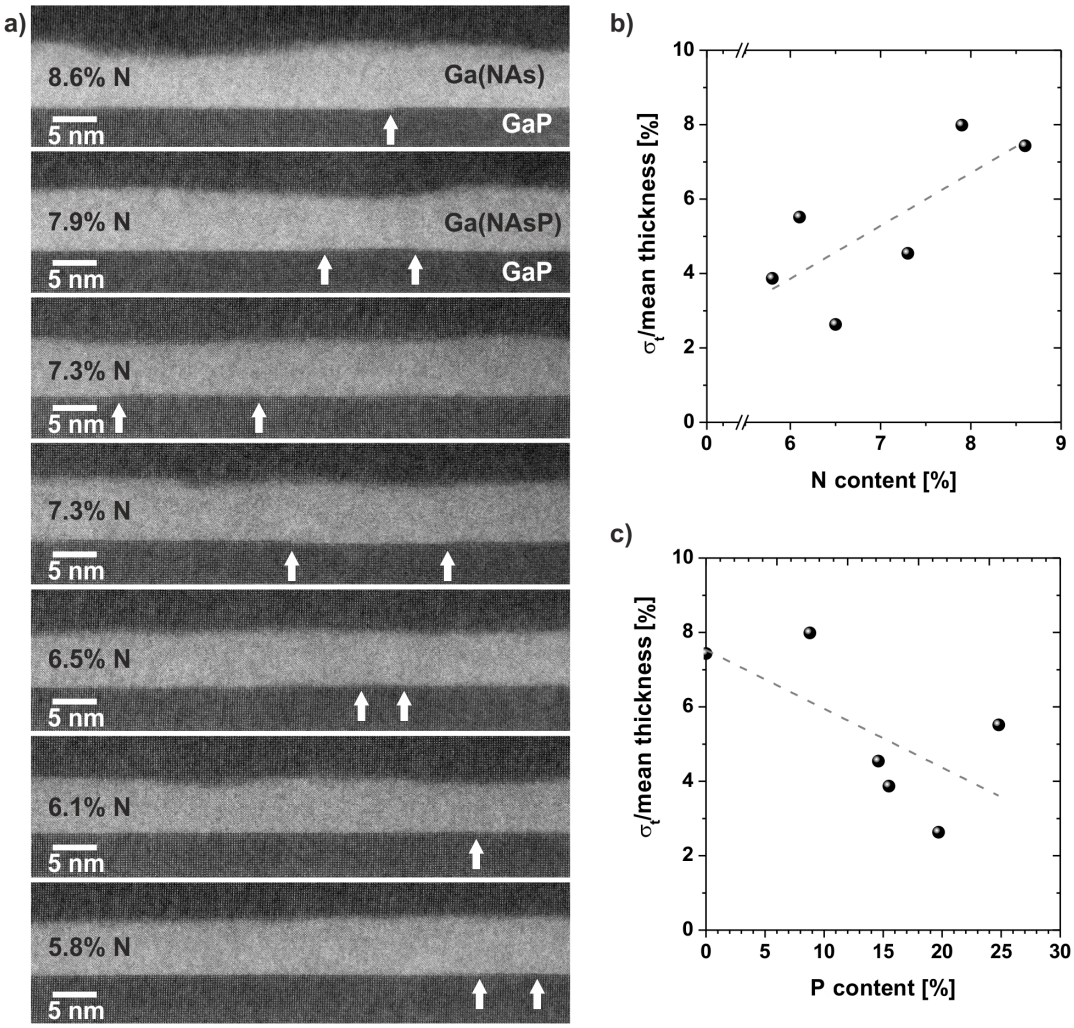

Figure 4.1: [010] STEM micrographs of the Ga(NAsP)-QWs a), bright layers, in the #26461 as grown sample, were acquired for the inner detector angle of 36 mrad and 20 μs dwell time per pixel. The white arrows exemplarily indicate the steps on the lower GaP/Ga(NAsP)-interface. The relative roughness of the Ga(NAsP)-QWs shows the increasing trend if N content increases b). The plot of relative roughness versus the P content reveals the falling character c).(The dashed lines are linear fits.)

get a higher signal-to-noise-ratio.[21,67] The dwell time was set to 20 μs per pixel in order to reduce distortions caused by the specimen drift[31] but still to have a good signal-to-noise ratio. The STEM micrographs of the Ga(NAsP)-QWs, bright layers between the darker GaP barriers, with different N concentrations, are collated in such a manner that N concentration increases from bottom to top. The bright layer in the uppermost STEM micrograph does not contain P atoms. The lower interfaces of the Ga(NAsP)/Ga(NAs)-QWs are very smooth, with exception of the one- and two-monolayer steps marked by the white arrows. The upper interfaces have modulations of the size of a unit cell and higher. A qualitative comparison of the QW with the lowest N content to the one with the highest N content provides hint that the upper interface would become rougher if the

N concentration increases. As the Ga(NAs)-QW is not only the QW with the highest N content but also the uppermost QW in the stack of the layers presented in Figure 2.5, one has to exclude that the increasing roughness is a cumulative effect of the thickness modulations of the layers grown below. Therefore, sample #26461 contains two QWs with the same composition (7.3% N and 14.6% P), which were grown at different positions in the stack: the lower QW with 7.3% N (Figure 4.1) corresponds to the first QW in the stack, while the upper one was grown as the 6th QW. However, there is no striking difference between these two QWs. If there is a real correlation or even a dependence of the interface roughness on N or P content has to be quantitatively investigated.
In order to find a mathematical description of the roughness, a short MATLAB script was written (read for details[70]), which enables the determination of the QW-thickness at each position along the QW. The fineness of the step from one to the next position depends on the resolution as well as on the sampling of a STEM image; it is also responsible for the accuracy of the results. The average of QW-thicknesses at each position along the interface provides a mean QW-thickness – the standard deviation of what we define as an absolute roughness σ_t. For a fair comparison of the layers with different mean thickness, the relative roughness – i. e., the absolute roughness normalized to the mean QW thickness – was used.
If we consider the dependence of the relative roughness of the Ga(NAsP)-QWs on the N/P content, we do not observe a linear correlation between them (compare data points and the linear fits in Figure 4.1 b) and c)). However, there is a clear increasing trend of relative roughness for the higher N content. The dependence of the relative roughness on the P content is the opposite way around. Therefore, the Ga(NAsP)/GaP interfaces become smoother if N content decreases and P content rises with a concurrent decrement of As concentration. One possible explanation is that, in this case, the lattice constant of the QW becomes more similar to the lattice constant of the barrier material. The non-linear behaviour of the roughness can be reasoned by the interplay of many factors. Not only a macroscopic composition is decisive for the quality of a layer, but also a local composition, or in other words, a compositional fluctuation, and consequently a local strain. The composition of the layer – macroscopic as well microscopic – itself is a result of the chosen epitaxial growth conditions such as growth temperature, growth rate, decomposition of the precursors, partial pressure, incorporation of the atomic species, and diffusion processes during the growth and during the after-growth treatment.

4.1.2 Compositional Fluctuation in Ga(NAsP)-QWs with Dependence on the N/P Content Before and After Rapid Thermal Annealing (RTA)

Like the relative roughness term in the last chapter, compositional fluctuation needs to be mathematically defined as well. For this purpose, the standard deviation σ_i of the averaged intensity in the QW-region will be normalized to the value of the latter.

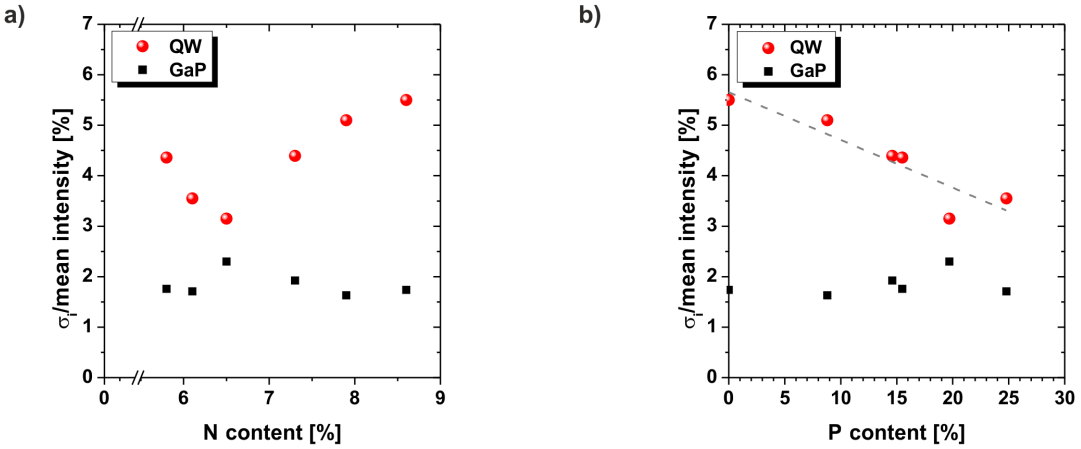

Figure 4.2: Compositional fluctuation in Ga(NAsP)-QWs (red spheres) is investigated in the #26461 as grown sample. With increasing N content, the QWs at first become more homogeneous, but for the N concentrations above, approximately 6.5% of the compositional fluctuation begins to increase a). Between P content and compositional fluctuation there is an unambiguous negative linear correlation b).(Black squared points represent the intensity fluctuation in the GaP barriers and the dashed line is a linear fit.)

As shown in Figure 4.2 a) the compositional fluctuation (red spheres) decreases at first, but at the N content of approximately 6.5%, it starts increasing again. To explain this dependence, we have to observe the situation from a statistical point of view. N atoms lead locally to an increase in the intensity in the STEM images of Ga(NAsP)-QWs at this low-scattering angle. However, if the N content is very low, such regions with increased intensity are very small and are so far apart that they have just a weak impact on the mean intensity in the QW, whereas the standard deviation from the mean intensity becomes higher and hence the ratio σ_i/mean intensity, the compositional fluctuation according to the definition described above, increases on the whole. A further increase of the N content results in a higher density of such areas with increased intensity. Consequently, the mean intensity increases; the value of the standard deviation, on the contrary, becomes lower. Hence, the compositional fluctuation decreases. A further increase of the N content favours the formation of N-chains. Such chains are infrequently distributed, and have most possibly different lengths and therefore different intensities in the STEM images. They do not strongly influence the mean intensity, but the standard deviation increases again and therefore also the value of compositional fluctuation. The pronounced maximum or kink of the intensity fluctuation in the GaP (black squared points) most likely originates from the contamination because the fine adjustment of the astigmatism and focus was performed close to a QW but not on a QW itself. It prevents any damage or modification to the structure due to the much longer exposure time of the strongly focused stationary beam in comparison with the dwell time (20 μs for low resolution STEM images) of the scanning beam. Apart from that, the intensity fluctuation in the GaP barrier stays constant at

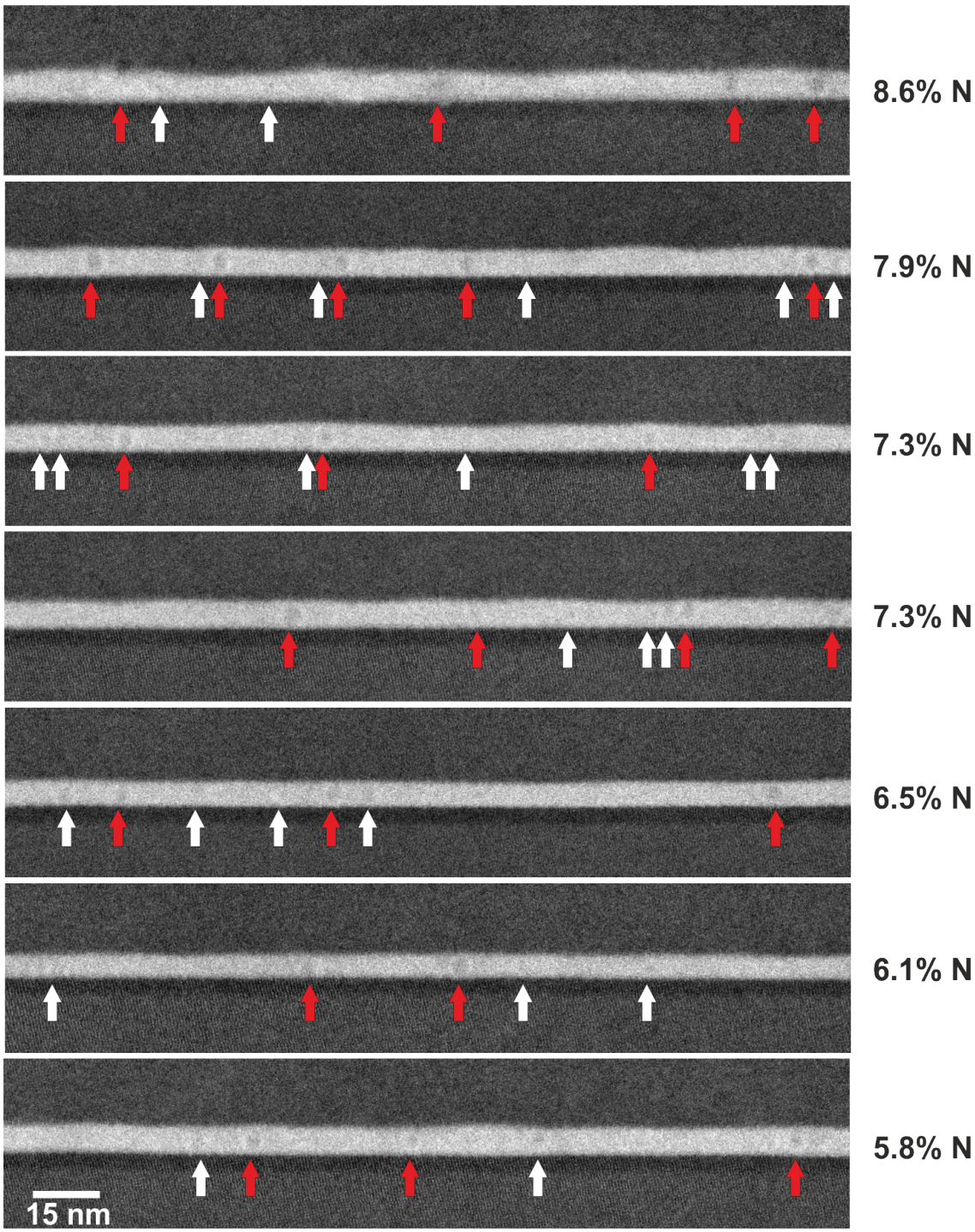

Figure 4.3: STEM micrographs of Ga(NAsP)- and Ga(NAs)-QWs, layers with higher intensity between the darker GaP barriers, the latter are surrounded by (BGa)(AsP) layers, in the #26461 sample reveal voids after annealing after RTA annealing. The big and small voids are exemplarily marked by red and white arrows, respectively. (The growth direction in each STEM micrograph is from bottom to top. The measurement was carried out for an inner detector angle of 36 mrad.)

approximately 2% and is primarily caused by the preamplifier noise. The plot of the compositional fluctuation versus the P content in Figure 4.2 b) reveals a linear correlation with a negative slope and hence, a higher P concentration accompanied by decreasing N content results in more homogeneous Ga(NAsP)-QWs. Further increase of the P content is, however, undesirable. If its value exceeds 25%, Ga(NAsP) loses its direct band gap character and turns into an indirect semiconductor. For Ga(NAsP) with 4 N% it happens already for the P content above 23%.[37]

Usually, laser structures undergo an after-growth thermal treatment to improve the optical properties.[37,40,64] On the one hand, the RTA leads to the reduction of the defects in the crystal lattice. Therefore, the number of the non-radiative recombination centres decreases and consequently, the photoluminescence (PL) intensity becomes higher. On the other hand, it causes a blue shift of the PL-peak and a formation of voids, as was already reported for the laser structures with Ga(NAsP)-QWs grown at 575 °C.[19,38,69] Therefore, it is necessarily to prove the changes in the quality of the Ga(NAsP)-QWs after an annealing process.

Figure 4.3 depicts that the voids appear after RTA treatment even in the Ga(NAsP)-QWs, bright layers, with lowest N content. The big voids of the size about 3.2–4.9 nm are indicated by the red arrows, while the smaller ones are exemplarily marked by the white arrows. The distribution of the voids is very inhomogeneous and their size varies within the QWs and in comparison between the QWs. The QW with the highest N content has the biggest voids. The distances between the big voids, which correspond to the big N-rich regions with the highest intensity in the as grown sample, are about 16 nm and above. The density of the voids increases with ascending N content, and just the QW with 8.6% N does not follow this trend. However, if one reverts toFigure 4.2, this QW has the highest compositional fluctuation with dependence on the N content as well as on the P content. The absence of P atoms leads to a more inhomogeneous N-incorporation because the N-incorporation in GaAs is very low, even lower than in GaP. Moreover, it tends to interstitial incorporations, formation of N-N pairs and clusters of a higher order[26,38,61] The latter turn into big voids after annealing. All of the aforementioned factors are in accordance with the conclusions drawn from the evaluation of the compositional fluctuation (Figure 4.2). Interestingly, for N concentrations of 7.3% and 7.9%, one or more smaller pores are formed in the immediate vicinity of the big voids. It is another confirmation for a clustering of the N atoms and their short-range diffusion during the thermal treatment. The diffusion can occur via vacancies or interstitials. The latter is more probable (for atoms with a small covalent radius) because the bond energy of the interstitial atom is weaker and there are much more sites to move to.[27,61]

As the PL signal of the annealed samples increases in comparison with the as grown ones despite the voids, local improvement of the structure in the QWs is the most probable. In order to check whether these changes become quantitatively noticeable in STEM micrographs, the compositional fluctuation in the Ga(NAsP)-QW of the as grown sample

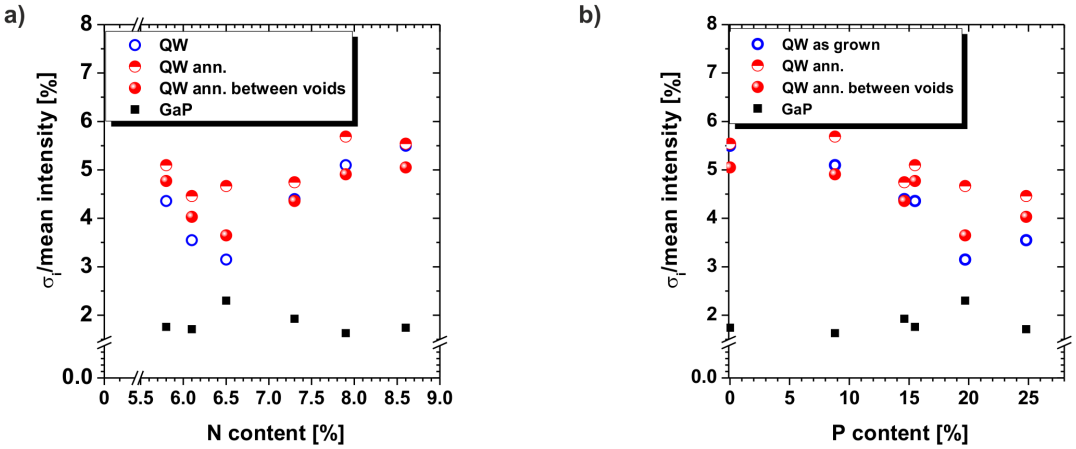

Figure 4.4: Compositional fluctuation of the Ga(NAsP)-QWs investigated in the #26461 as grown (blue empty circles), annealed (red half-filled circles) sample and in regions between the voids in the QWs of the annealed sample ((red-filled spheres) is plotted versus the N content a) and versus the P content b). Black squared points visualize the intensity fluctuation in the GaP barrier.

(blue hollow circles) is depicted together with one of the annealed sample (red half-filled circles), including the voids, along with the regions between the voids (red-filled spheres) in Figure 4.4 a) versus the N content and b) versus the P content. If the voids are included in the evaluated regions, the compositional fluctuation of the annealed sample is, as expected, higher than in the as grown sample for all N/P contents. However, the comparison of the red half-filled circles and red filled spheres shows that the compositional fluctuation between the voids is significantly lower than in the complete regions. In addition, on closer inspection, one notices that the values of compositional fluctuation in the QWs between the voids of the annealed sample for the N content above 7% (or the P content below 15%) are below those of the as grown sample. One possible explanation is that most of the biggest clusters were destroyed during the annealing and the smaller ones are laying closer to each other for higher N concentration, and therefore, there is enough diffusion of N atoms over short distances to achieve their more homogeneous distribution. Owing to the size and the density of the undestroyed N clusters, the compositional fluctuation still shows an upward trend even for the regions between the voids.

4.2 High-resolution Quantitative Analysis of Ga(NAsP)

It is more challenging and more interesting to find a method to determine the local composition at the atomic scale. The first prerequisite is an acquisition of STEM images of very high quality, which would imply the proper alignment of the microscope and of the corrector to keep the values of the spherical aberration, astigmatism, coma, and higher order aberrations as low as possible. Moreover, in order to decrease the influence

of the environmental instabilities, which would lead to distortions within the image and consequently degrade the high resolution, the dwell time was reduced to 3 μs per pixel.[44] However, such short acquisition time results in a STEM image with a very poor signal-to-noise ratio. Therefore, the series of seven STEM micrographs with 3 μs dwell time each were acquired and saved as a stack. Owing to the specimen drift, a small shift between the single images in a stack is unavoidable. Moreover, the scan generator still causes distortions in STEM micrographs, which vary from one image to another. To overcome these problems, the Smart Align MATLAB tool was used, which performs rigid as well as non-rigid alignments of the images and leaves only the area they have in common.[11,32] The aligned images were added together, and the mean intensities of the according columns of the stack were determined. Another requirement is to compare the experimental images with the simulated ones, where the intensity of the impinging beam is set to 1. For this purpose, at first, a background noise depending on the brightness value of the preamplifier was subtracted from a STEM micrograph. A background intensity was determined by acquiring an STEM image in the middle of the hole of the TEM specimen, where the e^--beam does not go through the material, at the same magnification as the HR-STEM micrographs investigated here, namely at 20 M. The normalization to the current of the incident e^--beam was done, as described in elsewhere,[25] by taking into account the contrast value of the preamplifier and the acquisition time.

In a normalized STEM micrograph the positions of the intensity peaks were found using a MATLAB script based on the Peak Pairs algorithm[18]. The assignment of the peak intensities to group III and group V sub-lattices was again achieved by means of a MATLAB script as well as determination of the positions between the atomic columns for determining the background intensity. The latter were defined as the corners of the Voronoi cells constructed around the positions of the atomic columns. Hence, group V, group III, and background intensities can be separately compared to the simulated values. However, there is one further important aspect to be taken into account: the atomic columns are not point objects and have a spatial extent depending on the electron source size, residual aberrations, and specimen thickness. Moreover, the rest of the uncorrected drift and astigmatism deform the intensity distribution of each atomic column in a slightly different way in such a manner that the intensity within the area of the atomic column is distributed asymmetrically. Consequently, the intensity maximum is not necessarily located in the middle of this area and can differ from the maximum of other column despite the same sort of atoms. Therefore, the intensities of the atomic columns have to be integrated within a certain diameter around the peak positions. In order to find a reasonable integration diameter, the evaluation procedure, as described before, was carried out in the lower GaP barrier of the 1st QW in the STEM image of the #26449 as grown sample (Figure 4.5). This STEM micrograph acquired at 36 mrad inner detector angle was chosen only because of its good quality. The pixel size for this magnification (20 M) is approximately 8.3 pm. The GaP barrier is more suitable for this evaluation

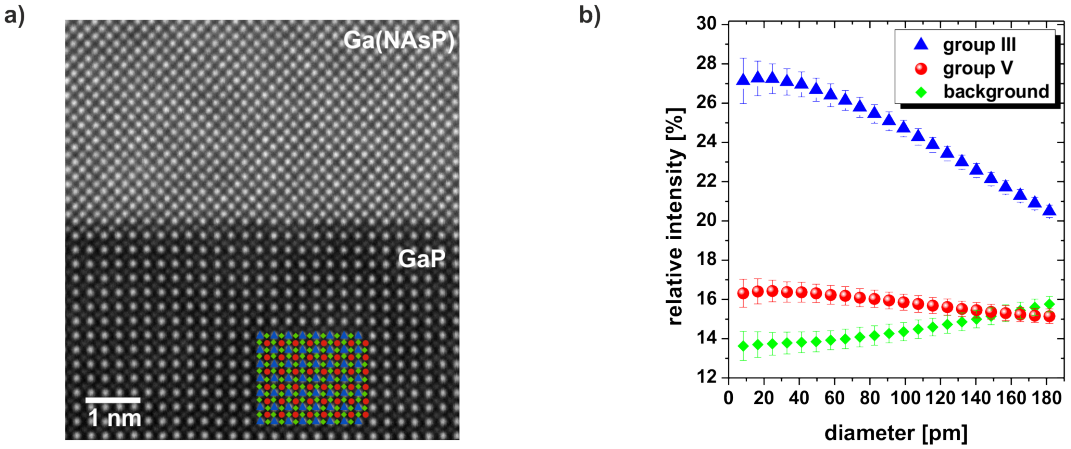

Figure 4.5: Determination of the optimum integration diameter: in the STEM micrograph (growth direction is from bottom to top), acquired at 36 mrad inner detector angle on the 1st QW of the #26449 as grown sample, the positions of atoms in the GaP are determined, the sub-lattices are separated: exemplarily Ga and P atomic columns are marked by blue triangles and red spheres, respectively. The positions between the atomic columns are highlighted as green diamonds. The pixel size in the STEM micrograph (20 M) is approximately 8.3 pm a). The according intensities as fractions of the impinging e^--beam for different integration diameters are shown in b).

because it is nearly completely free of the compressive strain and there are no distortions caused by the occupation of group V sub-lattice by three different sorts of atoms. The positions of group III and group V sub-lattices in the GaP barrier are highlighted by blue triangles and red spheres, respectively, whereas the green diamonds emphasise the background positions in Figure 4.5 a). The actually evaluated area is bigger than the one shown here: 276 atomic columns of each of sub-lattices were considered. Figure 4.5 b) depicts the corresponding intensities normalized to the incident e^--beam with dependence on the integration diameter. The intensity of the Ga columns (blue triangles) is much higher than that of the P columns (red spheres) and than the background intensity (green diamonds). In the absence of the local strain the heaviest atom is still the brightest one, according to the dependence $I \sim Z^{1.6-1.7}$. The letter was shown for an inner detector angle of 36 mrad and outer detector angle of approximately 200 mrad in elsewhere.[24] The intensities of both sub-lattices and the background intensity stay nearly constant for the integration diameter of (16–24) pm. Starting from the approximately 30 pm integration diameter, the intensity of the Ga columns begins rapidly to decrease because of its big difference from the background intensity. The bigger the integration diameter, the bigger part of the background will be included in the integration area – especially if the initial peak position was not at the centre of the atomic column. The intensity of the P columns does not differ very much from the background intensity and therefore proceeds much slowly. For this reason, the intensity does not significantly change for a bigger range of the integration diameters, approximately between 16 pm and 50 pm. On the contrary, the

background intensity is very sensitive to the change of the integration diameter because the space between the atomic columns in the STEM micrographs investigated here is smaller than the width of the atomic columns. For the integration radius of the 157 pm, the background intensity already intersects with the group V intensity, and it does not make sense to choose an integration diameter above this value. As the most reasonable integration diameter was chosen one of 24 pm. It is in the range where both sub-lattices have their highest and nearly constant intensity values. It was consciously decided in favour of the biggest diameter from this range. The reason is the asymmetric distribution of the intensity within an area of the atomic column mentioned above, which also explains the bigger standard deviations for smaller integration diameters visualized as error bars in Figure 4.5 b). The bigger the integration area, the more similar the distributions of the different columns, and consequently, the smaller the standard deviations.

As mentioned before, the group V sub-lattice in Ga(NAsP)-QW contains three different sorts of atoms: N, P, and As. In order to distinguish the contribution of each sort of atoms to the acquired STEM intensity, the measurements were carried out for different ranges of the detector angles: 34–136 mrad, 48–174 mrad, and 71–174 mrad. The acquisitions at low inner detector angles are very sensitive to the presence of the light atoms because of the local strain induced by SADs.[21] On the contrary, high detector angles are more suitable for detection of the heavy atoms because of the strong Z-dependence of the HAADF intensity.[52]. The results of one such investigations are presented in following. Figure 4.6 depicts the HR STEM images (left) of the 3rd Ga(NAsP)-QW of the #26461 and a part of the lower GaP barrier acquired at detector angles of 34, 48 and 71 mrad (considered from bottom to top). The nominal composition of the QW according to the XRD-measurement is 7.9% N, 8.8% P, and 83.3% As. In the middle, the false-colour intensity maps of the group III atomic columns are shown. The Ga columns of the GaP are separated from the Ga columns of the Ga(NAsP) by the white dashed lines until the position of a monoatomic step. In the Ga(NAsP)-QW, at the interface to the GaP barrier, there are some very strained regions that are coloured in intensive red and especially well visible at the inner detector angle of 34 mrad. One would expect the same intensity for all of the atomic columns in this map, because there are only Ga columns. Owing to the conventional TEM specimen preparation, there is a thickness gradient. The thickness increases from upper right to bottom left in the STEM micrographs. However, the maximum thickness difference determined in the GaP barrier for the STEM image acquired at 71 mrad was approximately 0.5 nm. If it would be extended to the whole measured region, it would be slightly higher because of the very small field of view. The thickness difference was determined by comparing the mean intensity in GaP barrier with the mean simulated GaP intensity, which was calculated using STEMSIM software.[56] For the inner detector angle of 71 mrad, the experimental intensities of the Ga columns vary between (2.4–3.8)% of the intensity of the incident beam. This intensity variation cannot be explained by the very low thickness gradient, as mentioned before. Some regions in the QW, in the

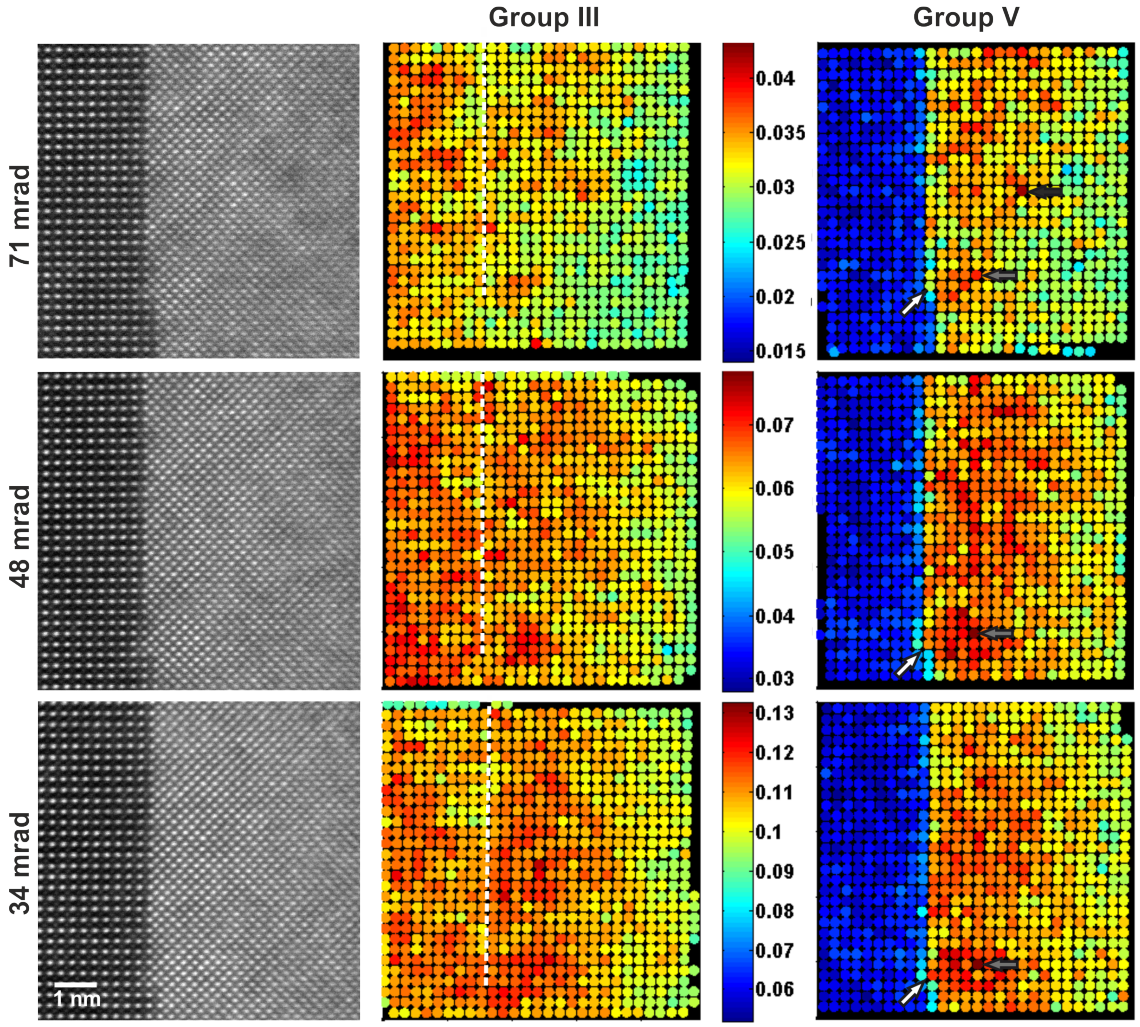

Figure 4.6: HR STEM images of the 3rd QW of the #26461 as grown sample (left) and the false-colour intensity maps of the group III (middle) and group V sub-lattices (right) for inner detector angles of 34, 48, and 71 mrad (from bottom to top). The white arrows mark a monoatomic step at the bottom Ga(NAsP)/GaP interface. The growth direction is from left to right. The grey arrows in the group V intensity map point to the atomic columns that appear to be the brightest at the inner detector angle of 34 and 48 mrad. The brightest atomic column for the inner detector angle of 71 mrad is indicated by black arrow.

group III map, attract attention, especially at the 71 inner detector angle, because their intensities are significantly lower than those in the GaP barrier. At this inner detector angle, the strain no longer contributes to the STEM intensity, or at least its influence is very low. But the SADs reveal themselves in another way. If many Ga atoms are displaced from their ideal positions in the crystal, the alignment of atoms along the optical axis decreases: therefore, the channelling effect decreases as well, and Ga columns appear darker.[74] Channelling of the electrons can be also reduced by local bending of specimen. The specimen on the measured position is very thin: mean thickness is approximately 15 nm. In the bulk material, the Ga(NAsP)-QW is compressively strained on the GaP barrier.

During the preparation the thinning leads to formation of free surfaces, and therefore the compressive strain starts to relax.[7]

In Figure 4.6 (right), the intensity map of group V columns is depicted. The monoatomic step (marked by white arrows) at the Ga(NAsP)/GaP interface is immediately noticeable. At the inner detector angle of 71 mrad the step is very sharp, whereas it is surrounded in the GaP barrier at the lower angles presented here by the atomic columns with higher intensities than other P columns, most likely due to the local strain in this region. The region close to the monoatomic step in the Ga(NAsP)-QW has a very high intensity and contains the brightest atomic column (marked by grey arrows) of the whole map for inner detector angles of 34 and 48 mrad. Interestingly, that for the inner detector angle of 71 mrad, this atomic column is still very bright, but it is not the brightest one anymore. The column with the highest intensity is now at another position (marked by the black arrow). Both atomic columns are mostly comprised of As atoms – the amount of As in the column indicated by the black arrow is even higher than in the marked one by the grey arrow. The latter just appears brighter at lower inner detector angles because its intensity is superimposed with the strain caused by a large amount of the N atoms in its environment. At the inner detector angle of 71 mrad, the influence of the strain almost completely disappears and therefore the intensity of this column decreases. The column indicated by the black arrow becomes, on the contrary, brighter because of the stronger Z-contrast. Most likely, the occurrence of the monoatomic step is caused by the high concentrations of the As and N near the this step.

All in all, the pattern in the intensity maps changes with dependence on the inner detector angle. Interestingly, that the group V map of the QW acquired at the inner detector angle of 48 mrad has a more structured pattern than the two others. It is a hint, that it is possible to determine which column contains more amount of certain sort of atoms. However, to do a fair comparison the intensity scale of the maps has be the same. Therefore, the intensities of group V columns in the Ga(NAsP)-region were normalized to the mean of the group V intensities in this region. The similar procedure was carried out for the group V intensities in the GaP barrier. Thus, the compositional fluctuation maps were produced for inner detector angles of 34 mrad, 48 mrad, and 71 mrad (Figure 4.7). Close to the Ga(NAsP)/GaP interface (the monoatomic step at the interface is marked by the white arrow), the atomic columns in the GaP barrier have significantly higher intensity than the mean intensity of group V columns in the GaP region. There is a clearly pronounced intermixing layer. At 34 mrad and 48 mrad, the atomic columns in the GaP barrier, surrounding the monoatomic step, appear especially bright. However, it changes at 71 mrad. Hence, the high intensity on this position – with the exception of one atomic column directly below the monoatomic step – is due to the strain and not because of the high portion of As atoms in these columns. However, there are still some bright atomic columns at the Ga(NAsP)/GaP interface in the GaP region, even at high inner detector angle. Thus, the intermixing layer is truly present. The brightest atomic column in the

Ga(NAsP)-region (marked by grey arrows) at inner detector angles of 34 mrad and 48 mrad is on the other position – like in Figure 4.6 – in comparison with the brightest one (marked by black arrow) at 71 mrad. Therefore, only the latter actually has the highest portion of As atoms.

For statistical analysis, areas of the same size – i. e., 338 atomic columns of each sub-lattice – were chosen on exactly the same position in STEM images, as shown in Figure 4.6. In such cases, a monoatomic step is very helpful as a point of reference. The intensity between the atomic columns is depicted in Figure 4.8 a) as green histograms so that relative frequency is plotted versus the intensity normalized to the incident beam. The histograms appear very symmetric, even for the inner detector angle of 34 mrad. According to the mean intensity values shown in the boxes and marked by the dashed lines, the background intensity increases for a decreasing inner detector angle. The values of the standard deviations describe the spread of the intensity distribution. For a low inner detector angle, these values are impacted by a local strain induced by the SADs. At a high inner detector angle, broadening of the intensity distribution of the structures with relaxed compressive strain can be caused again by SADs. The Ga atoms displaced from their ideal places in the crystal lattice can contribute to the background intensity. Considering the absolute values of the standard deviations, the intensity distributions become broader with decreasing detector angles. However, considering the fact that the signal-to-noise ratio at a low inner detector angle is better than at a high one, it is useful to consider the relative standard deviations $\sigma_i/mean\,intensity$ (4.1). Thus, the intensity distribution becomes broader with increasing detector angles. Similar changes are observed for the intensity distributions of group V (red histogram) and group III (blue histogram) in Figure 4.8 b) as well. At the inner detector of 34 mrad, the mean

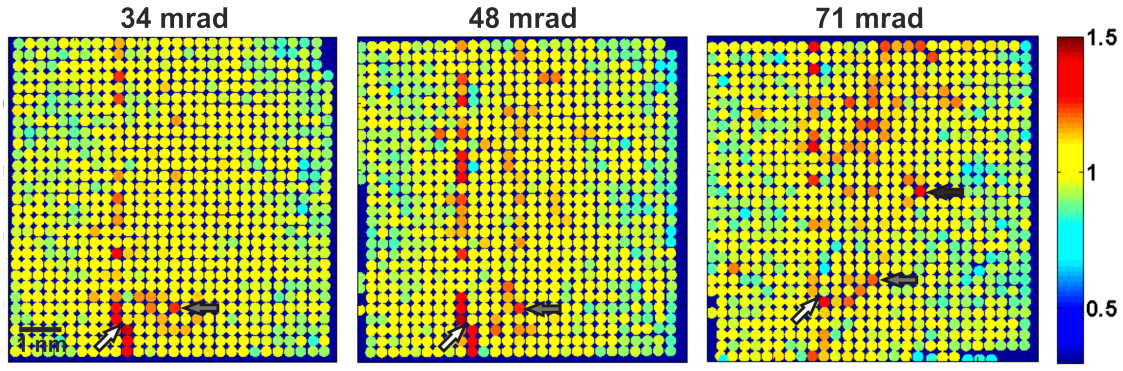

Figure 4.7: The false-colour compositional fluctuation maps of the 3rd QW of the #26461 as grown sample of group V sublattices for inner detector angles of 34, 48, and 71 mrad (from left to right). The white arrows mark a monoatomic step at the bottom Ga(NAsP)/GaP interface. The growth direction is from left to right. The grey arrows in the group V intensity map point to the atomic columns that appear to be the brightest at the inner detector angles of 34 and 48 mrad. The brightest atomic column for the inner detector angle of 71 mrad is indicated by black arrow.

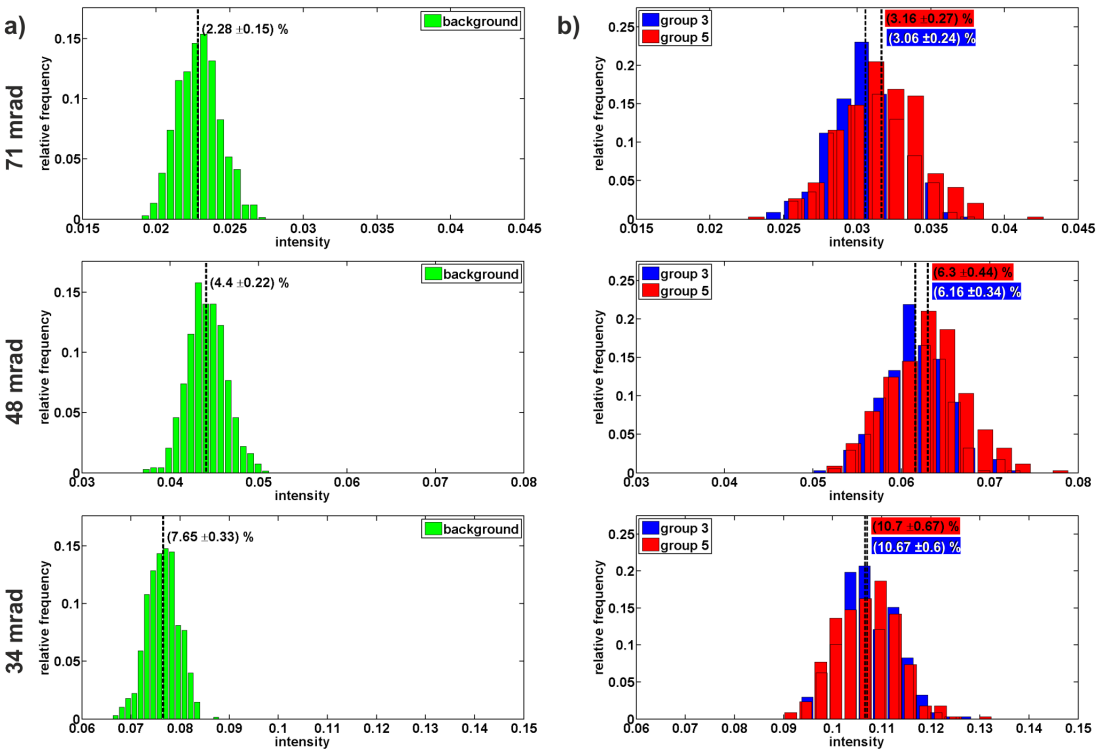

Figure 4.8: Intensity distribution of the background intensities a) and of the group III and group V sub-lattices b) for different inner detector angles. The dashed lines indicate the positions of the means of the intensity distributions. The values of the mean intensities as well as their standard deviations are shown in the boxes. The dashed lines indicate the positions of the mean intensities.

values of the both sub-lattices are almost equal, whereas they are separated for the higher inner detector angles because the strain influence decreases, which is in agreement with the effects observed in the intensity maps in Figure 4.6. However, the distribution of group V atomic columns does not shift to the lower value, as one expect due to the lower mean Z value, but the mean intensity of group III becomes lower because of SADs, as mentioned before.[66] Moreover, this Ga(NAsP)-QW contains large amount of As, almost 8% N and has a rather low P content. According to the results shown in Figure 4.2, the components of the QW are distributed heterogeneously so that the As concentration in investigated region can be higher than the mean concentration determined by XRD for a much bigger area. Interestingly, the separation of the mean values of the group III and group V intensities is the biggest for the inner detector angle of 48 mrad, and their standard deviations differs mostly from each other in this case. However, it is in agreement with the most structured pattern observed in the group V intensity map for this inner detector angle. If the standard deviations are relatively considered, the relevant values for the group V are bigger than ones of the group III for all inner detector angles, how one would intuitively expect (Table(4.1). The distributions become broader with an increasing inner detector angle in this case as well.

It is in agreement with the change of the patterns in 4.7. It was also verified, whether

Inner detector angle [mrad]	**Background [%]**	**Group III [%]**	**Group V [%]**
34	4.31	5.62	6.26
48	5.00	5.52	6.98
71	6.58	7.84	8.54

Table 4.1: Relative standard deviations of the background, group III and group V intensity distributions.

the experimental results could be reproduced for the nominal composition by a multi-slice frozen lattice simulation method.[63] To take into account the influence of the chromatic aberration, seven simulations with different defoci were carried out – for 15 different phonon configurations each.[8] The defocus values were varied between -14 nm and 10 nm in 4 nm steps. The thickness of the Ga(NAsP) relaxed cell parallel to the incident beam direction was approximately 15 nm[1]. The sampling was set to 20 px per unit cell. The simulated data shown in Figure 4.9 a) was resampled afterwards.

At first the experimentally determined thickness was taken as reference. Then, after comparing the experimental mean intensity of the whole Ga(NAsP)-QW (3rd QW of the #26461 sample) with the simulated one, the thickness parallel to the incident beam direction was adapted – i. e., from 14.7 nm to 14.2 nm. The simulated atomic columns appear smaller than the experimental ones because the real source size was not taken into account. We tried to reproduce the blurring effect by folding the simulated peak with a Lorentzian. The σ of the Lorentzian was adjusted in such a way, that the simulated intensities of the simulated group V and group III atomic columns as well as background intensities match the corresponding experimental values. Figure 4.9 b) depicts the evaluation of the experimental and simulated intensities of Ga(NAsP) with dependence on the inner detector angle. Group V (red spheres), group III (blue triangles) as well as the background experimental intensities are in very good agreement with the corresponding simulated intensities (hollow spots with the corresponding shape) for the inner detector angles of 71 mrad and 48 mrad. For the low inner detector angles, the experimental and simulated values have huge deviations. The same was observed (not shown here) for the Ga(NAsP)-QWs, with 7.3% , 6.1%, and 5.8% N (1st, 2nd and 5th QW of the # 26461) as well. The specimen thickness on the investigated positions was approximately the same. One reason for the much lower intensity in the simulated results could be a neglected inelastic fraction of the incident intensity that increases with the thickness of a specimen. However, the inelastic mean-free-path of GaAs is 67$\pm$4 nm.[12] In complex material such as Ga(NAsP), it is most likely lower because of the local strain. The specimen thicknesses on the evaluated positions were approximately 15 nm and hence the inelastic fraction of the incident intensity should not be high. The influence of the plasmon

1 These simulations were carried out by Lennart Duschek

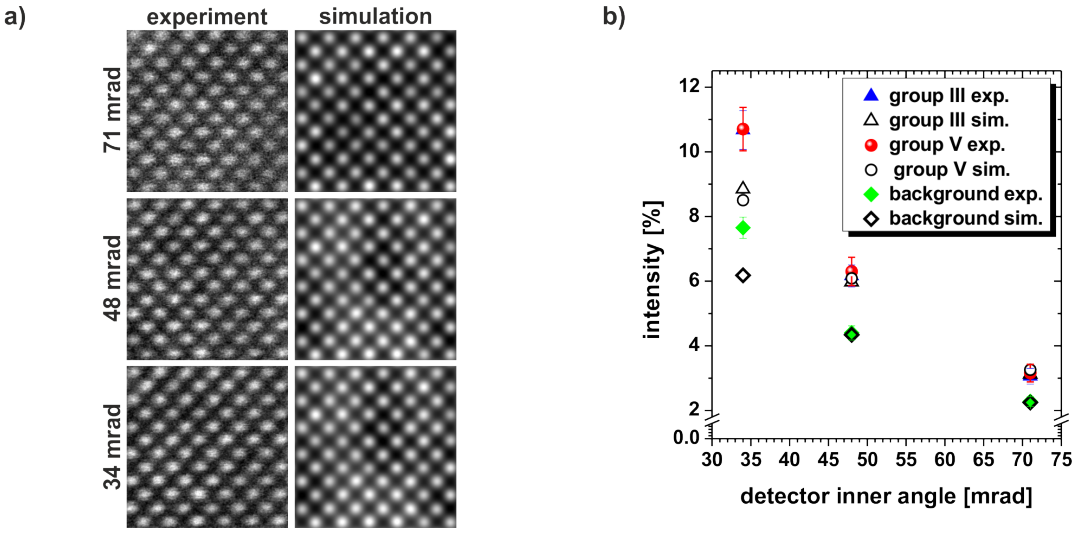

Figure 4.9: The STEM micrographs of the 3rd QW of the #26461 sample are cropped to the size of the simulated cell for a direct comparison a). The experimental mean intensities of the group V (red spheres), group III atomic columns (blue triangles) and of the background (green diamonds), and the according simulated intensities (hollow circles, triangles and diamonds) are plotted with dependence on the inner detector angle.

scattering on the STEM intensity will be found out in the future investigations. Another reason for the discrepancy of simulation intensity from the experimental one could be a strong underestimation of the specimen thickness. On the one hand, the ion sputtering of GaP and Ga(NAsP) most likely proceeds in a different way and thus they have different thicknesses. On the other hand, the surface strain field could cause a significant intensity drop of the intensity in the GaP barrier.[20] Thus, the thickness of the Ga(NAsP) should be verified by an independent measurement technique. Moreover, the influence of the amorphous layer on the specimen surface due to the preparation, which becomes significant for very thin positions of the specimen, was not taken into account.[43]

CHAPTER 5

Summary and Outlook

This final chapter sums up the results of the quantitative investigations on the Ga(NAsP)-material system and contains some suggestions for further research. As the method of choice, the annular dark field (ADF) scanning transmission electron microscopy (STEM) was applied. This experimental method provides a direct insight into the material, in contrast to the high resolution X-ray diffraction, Raman or photoluminescence spectroscopy that are also used for the investigation of the Ga(NAsP)-quantum wells (QWs). Owing to the intensity contrast, depending on the atomic number Z and the cross-sectional preparation of the TEM specimens, the quality of the interfaces of the samples grown at different conditions can be immediately compared in a qualitative manner. However, for a correct interpretation of the quantitative results, an additional information provided by the above-mentioned experimental methods is essential.

5.1 Summary

5.1.1 Low-resolution Investigation of the Ga(NAsP)-QWs

In order to optimize the growth conditions, a method for a quantitative comparison of the quality of the layers in the STEM images acquired at low magnifications was developed. The interface roughness and compositional fluctuation were chosen as indicators of the QW quality and mathematically defined. The evaluation method is not restricted to the Ga(NAsP)-material system, it was successfully applied to the Ga(BiAs).[35]
The investigations of the Ga(NAsP)-QWs grown at 575 °C and having different nominal thicknesses revealed very interesting results. While the absolute roughness of the QWs increases with QW thickness, the relative roughness of the layers as well as their compositional fluctuation is independent of the thickness of the QW layer. However, if the nominal thickness is nearly the same, and the growth temperature is different, it has a significant impact on the relative interface roughness as well as on the compositional fluctuation. Surprisingly, the relative and absolute roughness increases with increasing

growth temperature, whereas the compositional fluctuation decreases, whereby the lowest interface roughness had a sample grown at 525 °C. A phase separation was not observed at all. It is unexpected for a metastable material. However, *ab initio* calculations verified the experimental results and showed that Ga(NAsP) does not get separated into binary components up to the N content of 20%. Such stability can be explained by a good lattice match on the Si substrate.

The investigation of the annealed samples – with 7% N and 11% P grown at 575 °C – has shown that not only the growth temperature but also a temperature of the after-growth treatment has a strong impact on the quality of the layers. The intensity in the neighbouring GaP layers of the Ga(NAsP)-QWs increases after a rapid thermal annealing (RTA). It could be caused by diffusion of the N or As atoms out of the Ga(NAsP)-QW, which could also explain a blue shift of the PL peak and a decrease of the longitudinal optical phonon peak in a Raman spectrum.[19] Moreover, the QWs of the samples, annealed at the temperature of 925 °C and above, contain pore-like dark spots. They are clearly visible in the STEM micrographs. The origin of these spots, due to their spherical form, cannot be explained by the compositional gradient. The density and size of these dark spots increase with increasing annealing temperature. According to a quantitative analysis of the compositional fluctuation with dependence on the inner detector angle, the layer becomes more heterogeneous on average if the annealing temperature increases. Hence, the long-scale structural disorder increases due to the formation of the dark spots in the QWs, which correlates with the long-range electronic disorder described by the slope values of the low-energy tail in the PL spectra acquired at 10 K.[19] The compositional fluctuation in the regions between the dark spots, which can be described as a short-range structural disorder, achieves its minimum at the annealing temperature of 925 °C and increases again for higher annealing temperatures. It correlates with the short-range electronic disorder determined by analysing the S-shape of the PL maximum in temperature dependent measurements.[19]

The best interface quality was achieved for the growth temperature of 525 °C and the best optoelectronic properties were detected for the annealing temperature of 925 °C. Taking it into account, a further optimization of the QWs-quality was tried by the variation of N/P content. The investigation of the as grown samples reveals that the QWs become more homogeneous with increasing P content. The compositional fluctuation decreases up to N concentration of 6.5% and increases again with increasing N content. After annealing at 925 °C the dark spots occur in the QWs for all N/P concentrations investigated in this work. Their density and size increases with increasing N-content in the annealed specimens. The long-range structural disorder is higher than in the as grown samples, whereby it decreases with increasing P content. The dependence on the N concentration is the other way around. The short-range structural disorder has a minimum again at 6.5% N. For N-concentrations above this value (or for P content below 15%) the regions

between the dark spots in the annealed samples are more homogeneous than the QWs in according as grown samples.

5.1.2 High-resolution Investigations of the Ga(NAsP)-QWs

The nature of the dark spots in the QWs was clarified by high-resolution (HR) STEM investigations. Utilizing the reduced depth of focus in an aberration-corrected instrument,[10] the HR STEM images on the positions with the dark spots were acquired at different defocus values. An inquisition of a STEM micrograph, with a simultaneously focused atomic columns in the dark spot regions and the surrounding bright region, was impossible. The significant defocus difference of 30 nm means that the bright and dark QW regions have a different thickness or different amount of material, which confirms the assumption that pores or voids are formed in the Ga(NAsP)-QWs after annealing. The reason for the formation of voids is most probably the high pressure in the QWs caused by the N_2, which can be formed by N-diffusion in the N-rich regions.
The intensity distributions of the group V and group III atomic columns as well as of the background were quantitatively investigated for different detector angles. An excellent agreement between the simulated and experimental results was observed for high and middle detector angles. However, there is huge discrepancy of up 30% between the experimental and simulated results for low inner detector angles. It means that there is a physical process that is still not included into the simulation and has a significant effect at low inner detector angles.

5.2 Outlook

The quantification method presented in this work needs a further optimization. First of all, it is important to apply this evaluation method to Ga(NP) and Ga(NAs) in order to verify some assumptions discussed here. A comparison of the compositional fluctuations in these two material systems for the as grown samples would reveal whether there is a direct relationship between the distribution of the components in the QW and the incorporation efficiency of the N atoms.
A quantitative analysis of the annealed samples of the above-mentioned ternary material systems is important as well. The size and density of voids should be compared for the same N concentration in Ga(NP) and Ga(NAs). It would be also interesting to observe how the size and density of voids in these materials will change, if N content increases. It would provide additional information to the evaluation of the as grown samples concerning the most likely different clustering of N atoms in different material systems. Moreover, the amount of changes in the compositional fluctuation before and after annealing (between the voids) in different ternary dilute nitrides could indicate different concentrations of the point defects and even different kinds of the point defects,

and consequently, different diffusion mechanisms in these material structures. In this regard, the electric field modulation spectroscopy or determination of an absorption of the QWs by measurement of the photocurrent could be very helpful[1].

The quantitative analysis presented here was carried out just on the conventionally prepared TEM specimens. A comparison with the same, but prepared by, e.g., focused ion beam (FIB[2]) technique could be useful. In this case the underestimation of specimen thickness because of the surface strain fields can be excluded because the specimen has a known thickness due to the preparation method. Alternatively, the thickness of a specimen can be determined by the angle-resolved STEM. [45]

In order to explain the big relative deviation of the experimental intensities from the simulated one for the low inner detector angle of 34 mrad, the influence of the plasmon scattering on the STEM intensity has to be investigated. According to the most recent results, it varies depending on the inner detector angle.

The observed change of the pattern in the intensity or compositional fluctuation maps with dependence on the inner detector angle means that the composition of a single atomic column could be determined by comparing it with the single simulated columns with known concentrations.

1 due to the suggestion of Prof. Dr. G. Weiser
2 Focused ion beam)

CHAPTER 6

Publications

6.1 Quantification of Bi distribution in MOVPE-grown Ga(AsBi) via HAADF STEM[1]

N. Knaub, A. Beyer, T. Wegele, P. Ludewig, K. Volz, Journal of Crystal Growth **433**, 89–96 (2016). DOI: 10.1016/j.jcrysgro.2015.10.007.

Abstract

The importance of dilute bismide III/V semiconductors increases and their physical properties open up a wide range for applications. Therefore, high quality layers are required, what is difficult to achieve, as these alloys are highly metastable and phase separation can occur. We use HAADF (high angle annular dark field) imaging in aberration-corrected STEM (scanning transmission electron microscopy) to quantify the Bi distribution in MOVPE (metal organic vapor phase epitaxy) grown material at large length scales as well as down to the nanoscale. This is done for different Bi fractions in the solid, which are achieved by changing the MOVPE growth conditions. The composition of the Ga(AsBi) was determined by comparing frozen lattice annular dark field simulations of different Ga(AsBi) supercells with the experimental HAADF STEM images. The derived compositions are in quantitative agreement with results of HR-XRD (high resolution X-ray diffraction) and SIMS (secondary ion mass spectroscopy) of the same samples. We furthermore show a homogeneous Bi distribution for the investigated samples, which contain up to 5% Bi. By separating the group III intensities from the group V intensities in high resolution HAADF STEMimages, we can investigate the group V intensity distribution only. Moreover from the statistical evaluation, we conclude that the Bi is distributed homogeneously across the group V lattice positions, confirming the excellent structural quality of the layers. This

1 Reprinted from *Journal of Crystal Growth **433** (2016) 89–96*, Copyright 2015, with permission from Elsevier.

result is also important for device applications of dilute bismide alloys, as homogeneous layers are a prerequisite for optimizing optoelectronic applications.

My Contribution

For this publication I determined the intensity fluctuations in the Ga(AsBi) layers using the MATLAB script, which I wrote for investigation of the Ga(NAsP)-layers and whose improved version is now part of the evaluation software STEMulator.

Journal of Crystal Growth 433 (2016) 89–96

Contents lists available at ScienceDirect

Journal of Crystal Growth

journal homepage: www.elsevier.com/locate/jcrysgro

Quantification of Bi distribution in MOVPE-grown Ga(AsBi) via HAADF STEM

Nikolai Knaub*, Andreas Beyer, Tatjana Wegele, Peter Ludewig, Kerstin Volz

Materials Science Center and Faculty of Physics, Philipps-Universität Marburg, 35032 Marburg, Germany

ARTICLE INFO

Article history:
Received 30 July 2015
Received in revised form
25 September 2015
Accepted 10 October 2015
Communicated by T.F. Kuech
Available online 23 October 2015

Keywords:
A1. Characterization
A1. Scanning transmission electron microscopy
A3. Metalorganic vapor phase epitaxy
B1. Bismuth compounds
B2. Semiconducting III–V materials

ABSTRACT

The importance of dilute bismide III/V semiconductors increases and their physical properties open up a wide range for applications. Therefore, high quality layers are required, what is difficult to achieve, as these alloys are highly metastable and phase separation can occur. We use HAADF (high angle annular dark field) imaging in aberration-corrected STEM (scanning transmission electron microscopy) to quantify the Bi distribution in MOVPE (metal organic vapor phase epitaxy) grown material at large length scales as well as down to the nanoscale. This is done for different Bi fractions in the solid, which are achieved by changing the MOVPE growth conditions. The composition of the Ga(AsBi) was determined by comparing frozen lattice annular dark field simulations of different Ga(AsBi) supercells with the experimental HAADF STEM images. The derived compositions are in quantitative agreement with results of HR-XRD (high resolution X-ray diffraction) and SIMS (secondary ion mass spectroscopy) of the same samples. We furthermore show a homogeneous Bi distribution for the investigated samples, which contain up to 5% Bi. By separating the group III intensities from the group V intensities in high resolution HAADF STEM images, we can investigate the group V intensity distribution only. Moreover from the statistical evaluation, we conclude that the Bi is distributed homogeneously across the group V lattice positions, confirming the excellent structural quality of the layers. This result is also important for device applications of dilute bismide alloys, as homogeneous layers are a prerequisite for optimizing optoelectronic applications.

1. Introduction

The ternary bismuth (Bi) containing alloy $Ga(As_{1-x}Bi_x)$ gained significant interest in the semiconductor technology in the past years. Due to the strong influence of Bi on the gallium arsenide (GaAs) band structure [1–3], Ga(AsBi) becomes interesting for photonic devices emitting in the infrared region [4–7]. Alloys with Bi fractions above 10% have been grown mainly by molecular beam epitaxy (MBE) [8,9]. High Bi concentrations are more challenging to be achieved by metal organic vapor phase epitaxy (MOVPE). The reason for this is the metastability of the alloy, which can lead to phase separation at higher growth temperatures [10], which however have to be applied during MOVPE growth due to the requirement of sufficient decomposition of the precursor chemicals [11–14]. The metastability of Ga(AsBi) originates from the highly different covalent radius of the arsenic (As) and Bi atoms, resulting in local strain when incorporating Bi in GaAs and hence a large miscibility gap. In addition, biaxial strain might influence the (meta)stability of the alloy [15].

From the technological point of view, a homogeneous, i.e. statistical, distribution of the Bi atoms is preferred but not automatically given, first of all, as phase separation due to metastability has to be considered; secondly as due to low-temperature growth other structure formation processes could occur due to the limited diffusivity of the deposited atoms on the growth surface. Investigations of the structural quality of Ga(AsBi), also in dependence on the growth conditions, are hence mandatory.

Early electron-spin resonance (ESR) studies of Bi doped GaAs (grown by the liquid encapsulation Czochralski technique from a Bi-doped melt) showed that a fraction, about 10%, of the total Bi content ($2.6 \times 10^{16}\,cm^{-3}$) occupies the gallium (Ga) site [16]. These findings underline the difficulty to grow dilute bismide alloys under thermodynamic equilibrium conditions. Later, extended X-ray absorption fine structure spectroscopy (EXAFS) studies of MBE grown Ga(AsBi) samples with Bi concentrations of 1.9% and 2.4% could verify Bi clustering in form of Bi pairs and Bi tetramers [17,18]. Investigations of MBE grown Ga(AsBi) samples, containing 2.65% Bi, by scanning transmission electron microscopy (STEM) high angle annular dark field (HAADF) in [110] direction

* Corresponding author.
E-mail address: nikolai.knaub@physik.uni-marburg.de (N. Knaub).

http://dx.doi.org/10.1016/j.jcrysgro.2015.10.007
0022-0248/

could also show hints for nanoclustering in form of Bi pairs [19]. Furthermore, STEM HAADF evaluation with additional X-ray diffraction (XRD) of MBE grown Ga(AsBi) films allowed to analyze Bi concentration profiles quantitatively [20] and derive a model for the Bi incorporation in MBE grown material. It was shown that the incorporated Bi fraction fluctuates between 1.5% and 5% over a nominal film thickness of 250 nm. These results underline the importance of in-depth structural characterization, which should go in-line with epitaxial growth. Only when the structure and the Bi depth profile of Ga(AsBi) is known, meaningful conclusions on the optoelectronic properties can be drawn and correlations between both of them as well as the growth conditions can be established. Also Bi concentration profiles of MOVPE grown GaAs/$Ga(As_{1-x}Bi_x)$ superlattices with Bi fractions of 1.4% and 2.7% were investigated via STEM quantitatively [21] in combination with high resolution X-ray diffraction (HR-XRD) rocking curves, where both methods show a highly non-uniform Bi concentration profile in growth direction.

In this report, we examine MOVPE grown samples also systematically in dependence on the Bi composition of the alloy. This can be performed down to the atomic scale by using aberration (C_S) corrected STEM [22]. The HAADF STEM signal of incoherent electron scattering in high angles (Rutherford-like scattering) is well known as the so-called Z-contrast [23,24] and can be applied rather straightforwardly to dilute bismides due to the large difference in the atomic number of Bi with respect to As and Ga. In this paper we present our results obtained using HAADF STEM measurements, performing low resolution as well as high resolution.

2. Materials and methods

The investigated sphalerite type Ga(AsBi) sample consists of five Ga(AsBi) layers with different Bi fractions and one Ga(NAsBi) layer (which will not be discussed here) grown by metal organic vapor phase epitaxy (MOVPE) on GaAs (001) substrate in a commercially available AIX 200-GFR reactor. The Ga(AsBi) quantum wells (QWs) are separated by GaAs barriers with a thickness of 100 nm. This sample was specifically grown for STEM investigation, and is schematically depicted in Fig. 1. The growth conditions of each single layer were calibrated with separately grown Ga(AsBi) multi-quantum well (MQW) structures. Intentionally no specific (composition) stacking sequence was chosen for this sample to not erroneously misinterpret any structural characteristics, which might escalate with increasing number of quantum wells, as Bi is known for segregate to the surface. Triethylgallium (TEGa) was used as Ga precursor, tertiarybutylarsine (TBAs) and trimethylbismuth (TMBi) were applied as group V precursors. The growth temperature of the Ga(AsBi) was chosen between 375 °C (topmost QW) and 400 °C (all other QWs), while the GaAs barrier growth temperature was set to 625 °C to desorb surface-segregated Bi from the growth surface prior to GaAs barrier growth. The Bi incorporation into the Ga(AsBi) alloys was adjusted by variation of TMBi/TBAs. Details of the MOVPE growth procedure of Ga(AsBi) are summarized in [13,14]. The width and nominal Bi composition of each Ga(AsBi) layer were determined (for the calibration samples) by fitting the experimental results from (004) HR-XRD $\omega/2\theta$-scans with a dynamic model. The composition was calculated assuming 0.633 nm [25] as lattice constant for GaBi. For electron microscopy investigation, a wedge-shaped TEM sample in [010] cross-section was prepared conventionally by mechanical grinding, followed by Ar-ion milling with a Gatan PIPS. STEM was performed in a double-C_S corrected JEOL JEM 2200 FS field emission transmission electron microscope operating at 200 kV. For the STEM measurements we used the HAADF method with an inner detector angle of 75 mrad and a semi angle of beam convergence of 24 mrad. To evaluate our results quantitatively, we performed HAADF-simulations of Ga(AsBi) in the frozen lattice multislice approach [26] in virtual crystal approximation (VCA) by using the STEMSIM software-package [27]. Since normalizing of the intensities is necessary for a quantitative interpretation of the measurements, we normalized our background-corrected HAADF images to the incident beam by using a similar method as it is described in [28], where the beam's current is measured with the CCD camera. Additional secondary ion mass spectroscopy (SIMS) measurements were carried out on the multi-layer sample, first of all to control the XRD data, secondly to also confirm that the transfer from the calibration sample to the multi-layer sample resulted in the intended Bi fraction in the individual layers.

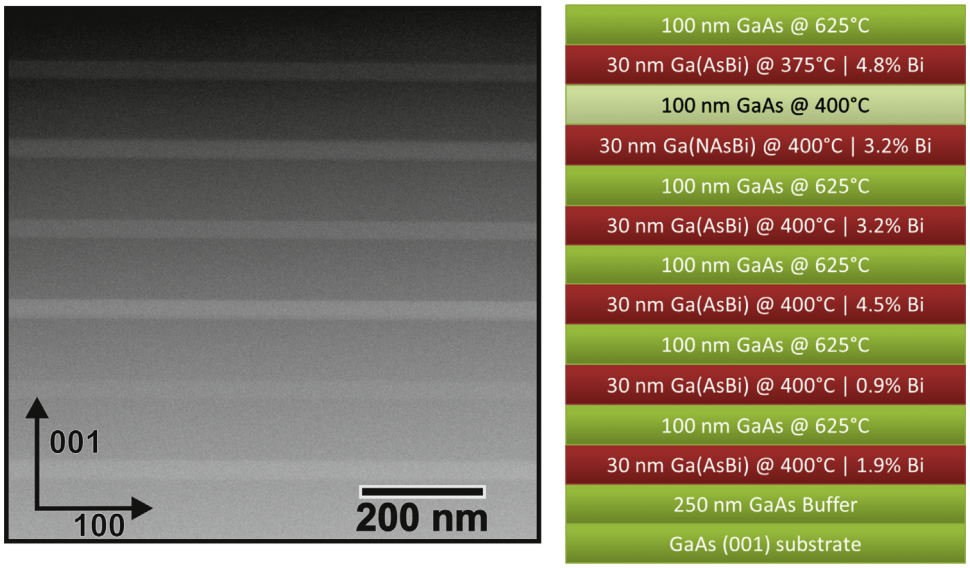

Fig. 1. STEM HAADF micrograph overview of the investigated sample, prepared in [010] zone axis. One can see clearly the intense Ga(AsBi) QW with different Bi fractions. The schematic on the right displays the investigated sample with growth temperature, nominal layer width and Bi fraction obtained from HR-XRD measurements.

3. Results and discussion

The paper is organized as follows: first we show that we can quantitatively determine the Bi fraction in the Ga(AsBi) QWs from STEM HAADF measurements in combination with electron scattering simulations. These results are in agreement with HR-XRD and SIMS results, also giving confidence to the unknown parameters (especially for dilute bismide materials) that go into the evaluation of these two techniques, which are frequently used in the growth community. Second, the intensity fluctuation in low resolution measurements will be evaluated to address any Bi composition fluctuations in the alloy, also in dependence on composition and growth temperature. Finally these results will be compared to a statistical evaluation of atomic resolution STEM HAADF measurements.

3.1. Ga(AsBi) composition quantification

A HAADF overview of the Ga(AsBi) sample containing QWs grown at different temperatures as well as containing different Bi fractions and a schematic of the intended sample structure are depicted in Fig. 1. The Bi containing layers can be clearly seen from their bright contrast with respect to the GaAs barriers. The given values for bulk thickness and Bi fraction, shown in schematic, are obtained from HR-XRD measurements of the reference MQW structures. There are several uncertainties in Bi fractions from HR-XRD measurements as well as SIMS measurements. First of all, in HR-XRD one measures a tetragonally distorted lattice constant. The input parameters which influence the evaluation in XRD are the material constants of the binary GaBi, i.e. the lattice constant and the elastic constants, of which theoretical values exist only [25], as this alloy does not exist in nature. Small deviations of these values could result in large errors of the calculated Bi fraction. Moreover the validity of the simple linear interpolation of lattice constants of mixed alloys between the lattice constant of the two binary endpoints (Vegard's law) has not been proven yet for dilute bismide III/V semiconductors. Furthermore, it is assumed that Bi incorporates on the group V lattice positions only. If this is not true, again a shift in lattice constant and hence an error in the evaluated Bi fraction follows. Quantitative SIMS measurements of the composition might also be error-prone, as Ga(AsBi) standards do not exist and have to be produced by ion implanting Bi in GaAs. Also the presence of antisites would cause some error to the composition. Therefore we quantified the Bi composition of the different alloys by means of STEM HAADF.

In the following part, we will explain the evaluation steps which were performed to determine the mean Bi fraction from the measured HAADF intensity for each Ga(AsBi) layer.

Since every layer was evaluated in the same manner, we will explain the procedure by taking the example of one Ga(AsBi) layer only. Fig. 2a depicts a low resolution HAADF measurement of the topmost Ga(AsBi) layer with a nominal Bi fraction of 4.8%. Here one can see the intense Bi containing layer embedded in GaAs barriers, which serve as reference regions for our TEM sample

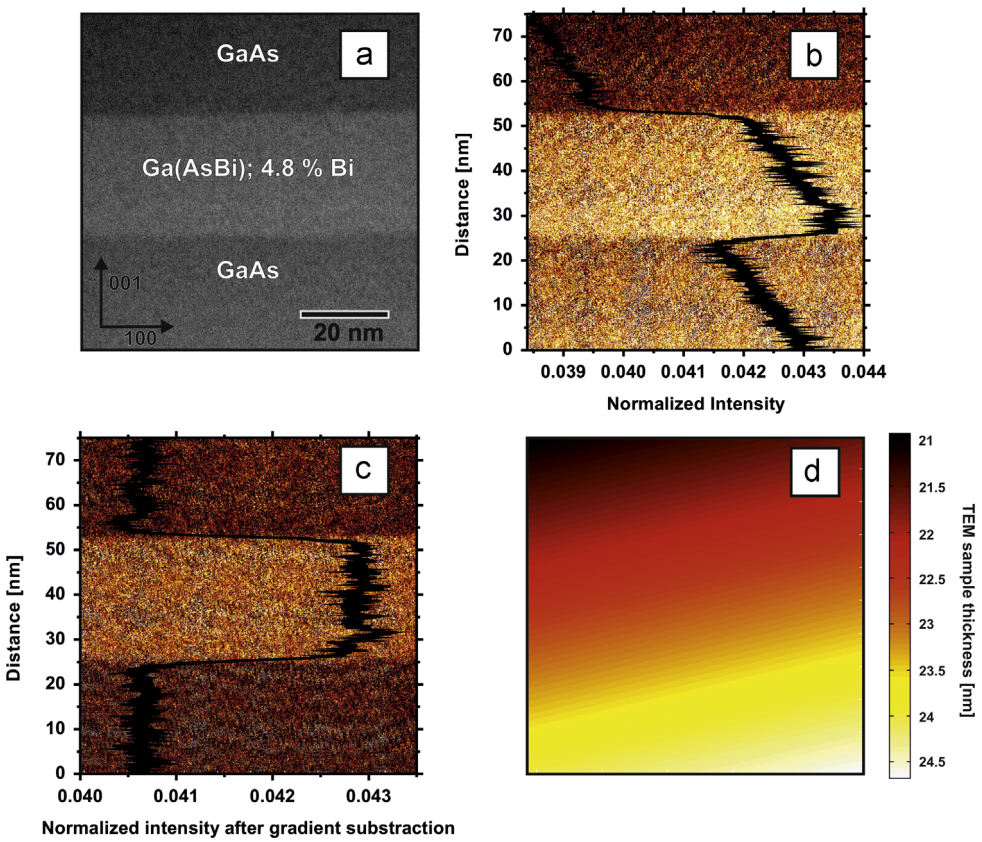

Fig. 2. (a) STEM HAADF low resolution measurement of the topmost Ga(AsBi) QW with a nominal Bi fraction of 4.8%. The measured layer width of the layer is about 28 nm. (b) False color image of the low resolution measurement depicted in (a), normalized to the impinging electron probe (after background subtraction). The inset diagram is an integrated intensity plot over the measurement distance. It reflects the thickness originating from sample preparation. (c) Same false color image as in(b) but after thickness gradient correction. The inset diagram depicts a mean normalized intensity value of 4.3% of the electron probe's intensity for the Ga(AsBi) layer. (d) Interpolated GaAs thickness gradient (false color plot) of the measurement displayed in (a). The scale bar displays the corresponding TEM sample thickness in nm. Here, the determination yields a mean thickness value of 22.7 nm for the Ga(AsBi) QW. (For interpretation of the references to color in this figure legend, the reader is referred to the web version of this article.)

thickness estimation. In the next step, we normalized our images-after correcting them for the background intensity-to the impinging beam's current by using a similar procedure as described in [28]. Thus we obtain a normalized image with absolute intensity values, as depicted in Fig. 2b. The inset graph is an integrated line profile over the whole image and it describes clearly a thickness gradient, which is a side effect of the conventional sample preparation. We performed a gradient correction, where the GaAs intensity from the barriers only was taken into account and a two dimensional surface interpolation as well as a thickness gradient subtraction of the original image was carried out. Both, the result of the gradient corrected image and the integrated line profile (inset) are shown in Fig. 2c. The line profile now clearly displays a constant GaAs intensity level and a higher Ga(AsBi) layer intensity. It is remarkable that the interfaces of the Ga(AsBi) layer with the GaAs barriers are abrupt, which is a consequence of the high growth temperature of the GaAs barrier [14]. If the barriers are grown at the same temperatures as the QWs, there is a significant Bi-segregation into the GaAs barriers observable [13] and the interfaces are not nearly as sharp. From the line profile, which is shown in the inset, we determine the QW layer thickness to 28 nm, what is in a good agreement with the layer thickness of the calibration samples deduced from HR-XRD. The thickness gradient correction provides additionally an interpolated GaAs signal, from which we can calculate the TEM sample thickness, which is needed as input for quantification of the Bi content. The STEMSIM package was used in the frozen lattice multislice approach [26] to simulate the GaAs HAADF intensity in dependence on the TEM sample thickness. Comparing the experimental GaAs intensity with the simulated GaAs intensity yields a thickness value for each pixel (as described in [29]) and thus allows us to create a thickness map at low resolution, as depicted in Fig. 2d. Thus we get a mean sample thickness of approximately 22.7 ± 0.6 nm at the position of the Ga(AsBi) QW for this particular sample. The normalized HAADF Ga(AsBi) intensity in this image was 4.3% of the impinging beam. Further frozen lattice multislice simulations of Ga(AsBi) supercells with Bi concentrations of 1%, 2%, 3% and 5% were carried out to determine the Bi fraction from this data. As a result of the simulation we get the HAADF intensity dependence on the Bi concentration for different TEM sample thicknesses, depicted in Fig. 3a there is an estimated thickness of 22.7 nm. The black points are the calculated values, which were interpolated assuming a linear dependence of the scattered intensity of the Bi fraction. At this point it is worth noting that the distribution of doping atoms in the direction of the electron beam can severely influence the measured HAADF intensity [30]. In our case the deviation of some calculated data points (e.g. 2% Bi) from the linear interpolation can be explained by the crystal model used for the simulation: the Bi was distributed statistically on the group V positions. As the TEM sample is very thin, the Bi in the crystal models might be at different positions (depths) in the TEM sample for each calculated data point. This results in different intensities. We estimate the difference of the scattered intensity for a given Bi concentration, where the Bi is placed at different positions in the crystal model to about 1% of the value. This is included as “error bars” in the figure. However, it should be emphasized that this is not the error of the method, but rather a feature which also occurs in experiment [31]. Comparing the simulated data with the experimental intensity yields a mean Bi fraction of 4.6%, what is in good agreement with the reference value of 4.8% from HR-XRD. It also should be noted at this point that there is no “simple”- Z^2-dependence of the scattered intensity, which is often used to calculate compositions in a hand-waiving way. The calculated intensities rather follow a $Z^{1.6}$-dependence, which confirms the $Z^{1.7}$ proportionality suggested in [32]. This is depicted in Fig. 3b, where the mean Ga(AsBi) intensity is normalized to the GaAs intensity

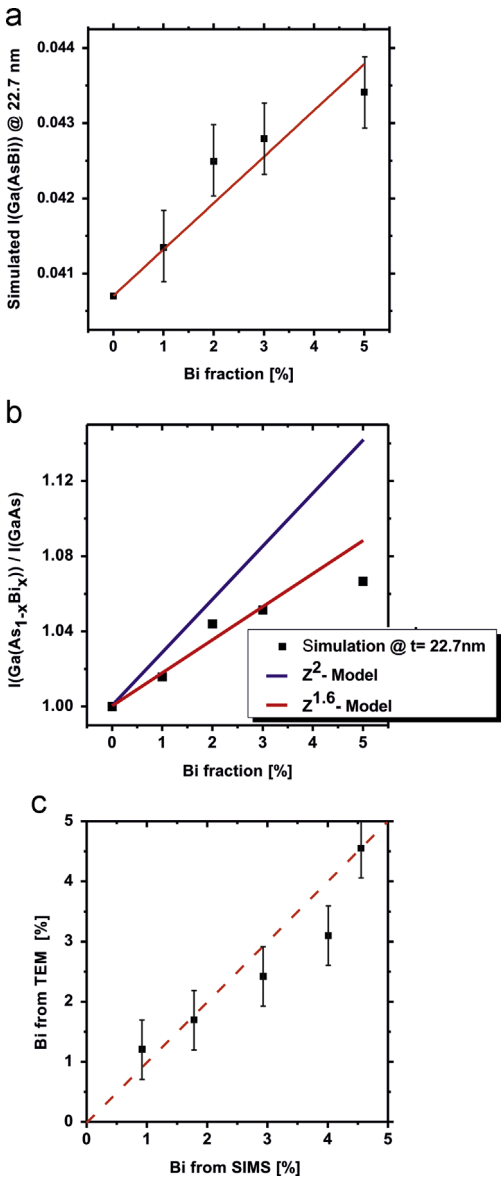

Fig. 3. (a) Dependency of image simulation with frozen lattice approach obtained Ga(AsBi) HAADF intensity on the Bi fraction for a constant TEM sample thickness of 22.7 nm. The red line is a linear fit to the calculated values. Thus it is possible to derive a mean Bi fraction from the measured intensity. (b) Dependency of Ga($As_{1-x}Bi_x$) HAADF STEM intensity normalized on GaAs intensity on the Bi fraction for a Z^2 (red line)- and a $Z^{1.6}$- proportionality (blue line) of the intensity. The black squares are the simulated values from (a). It can be seen that the simulation follows the $Z^{1.6}$- proportionality instead of Z^2. (c) Comparison of the Bi fraction determined by our HAADF measurements and the Bi fraction determined by SIMS in percent. The dashed line is a guide to the eye, which represents an exact agreement of both methods. (For interpretation of the references to color in this figure legend, the reader is referred to the web version of this article.)

and is plotted versus the Bi fraction for the different Z-dependencies mentioned above. Therefore a Bi fraction estimation by assuming a simple Z^2 proportionality of the measured intensity would lead to significantly wrong Bi fractions in experimental investigated Ga(AsBi) layers, for example, the error would be already a factor of two for a Bi concentration of 5%. It should also be noted that comparison to calculations using a VCA crystal model are only justified if the inner angle of the HAADF detector is set to rather large values as in this study. Setting the inner angle to lower values can result in a significant local strain distribution to the material's intensity and would have to be taken into account

by relaxing the atom positions in the crystal model as shown in [29] for Ga(NAs). In a further study we will show, how this can influence image intensity also at an atomic scale.

The procedure just described was applied to the other Ga(AsBi) layers. The results are depicted in Fig. 3c. Here the Bi fraction from quantitative STEM HAADF is plotted versus the estimated Bi fraction obtained by SIMS measurements from the multi-layer sample. The dashed line corresponds to equality between SIMS and quantitative STEM HAADF. The agreement between the quantitative STEM HAADF evaluation and the SIMS data (as well as the HR-XRD data, which is incorporated in the schematic of Fig. 1, but not shown here anymore) shows that there is excellent agreement between the three methods.

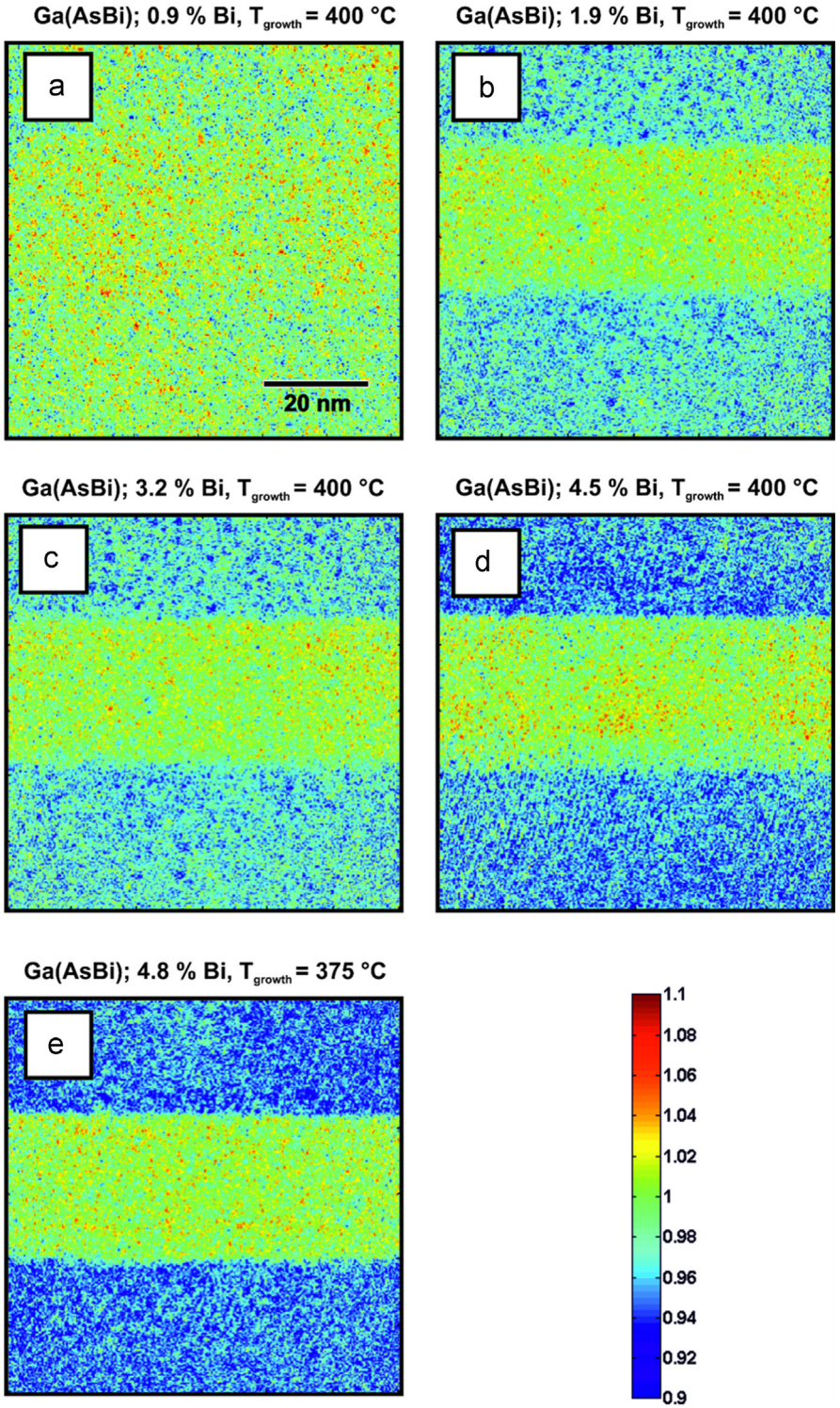

Fig. 4. (a)–(e) Determination of the QWs intensity fluctuation with increasing Bi fraction. The false color plots display the relative standard deviation σ_{rel} of each Ga(AsBi) layer's mean intensity, which serves as a goodness for the layers' homogeneity. One can see almost the same homogeneity for all investigated Ga(AsBi) QWs. (For interpretation of the references to color in this figure legend, the reader is referred to the web version of this article.)

This not only confirms that STEM HAADF is a good method to address the composition quantitatively-what might become important if there are nanoscale fluctuations of the compositions-but also indicates that the potential sources of errors of HR-XRD and SIMS measurements-enumerated above-can be excluded for this material.

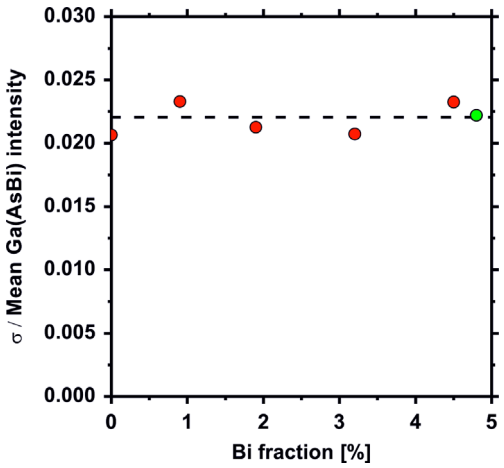

Fig. 5. Comparison of the relative standard deviation σ_{rel} values from Fig. 4 with the Bi fraction in the QWs. The dashed line is a guide to the eye, which shows that all investigated layers are equally homogeneous. The value of the Ga(AsBi) QW grown at 375 °C is green colored. (For interpretation of the references to color in this figure legend, the reader is referred to the web version of this article.)

3.2. Composition homogeneity by low resolution HAADF measurements

Since dilute Bi III/V alloys are metastable and are grown at low temperatures, phase separation into Bi-rich and Bi-poor regions could occur. Therefore, we also analyzed the homogeneity of the investigated Ga(AsBi) layers. Thereto, each pixel intensity in the Ga(AsBi) structure was normalized to the mean intensity of the same QW, which was determined over an area of 2000 nm². As a result we create false color images of each Ga(AsBi) layer (Fig. 4), where the intensity deviation from the mean intensity value is visible, which represents a goodness for the homogeneity. Fig. 4 shows that all Ga(AsBi) layers we investigated exhibit a maximum fluctuation in intensity of only about 2.5% from their mean intensity value. These findings are summarized in Fig. 5, where the standard deviation σ_{rel} of the mean intensity normalized to the mean intensity is plotted in dependence on the Bi fraction in the layers. It is remarkable that all Ga(AsBi) layers have the same low relative standard deviation of intensity irrespective of their composition. Their homogeneity is same as for GaAs, i.e. about 2%, and can be explained by experimental effects due to measuring process in STEM, such as scan noise, specimen drift and TEM sample thickness fluctuation. It should be noted that in order to derive statistical information for the barrier, the GaAs intensity was normalized to the mean GaAs intensity. This means that there are no detectable composition fluctuations in the Ga(AsBi) material in the 10 nm range and above. This is a very important result for the correlation to optical data of the samples, as the length scale, where composition fluctuations would alter for example PL (photoluminescence) characteristics is typically in the range of 10 nm. Smaller scale compositions fluctuations cannot be excluded

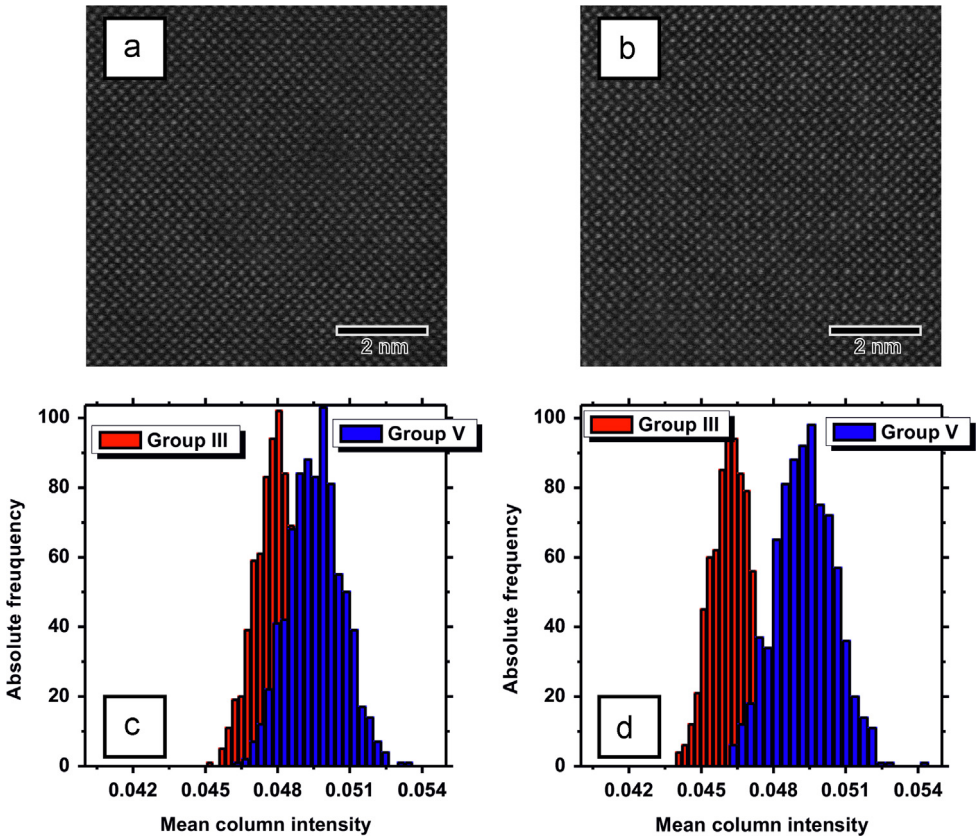

Fig. 6. STEM HAADF high resolution micrographs of the Ga(AsBi) QWs with a nominal Bi fraction of 0.9% (a) and 4.8% (b). The displayed histograms (c) and (d) depict the group III (red) and group V (blue) column intensity distribution corresponding to the high resolution measurements (a) and (b). One can see that the group III and group V intensities separation is more pronounced with increasing Bi fraction. (For interpretation of the references to color in this figure legend, the reader is referred to the web version of this article.)

as the TEM samples shown here had all thicknesses around 25 nm. Hence, extreme short range composition fluctuations could be averaged by projection effects and will be a topic of a separate paper. In the following we will present a method to derive composition fluctuations also from high resolution STEM measurements to address composition fluctuations at an atomic scale.

3.3. Composition homogeneity by high resolution HAADF measurements

Further investigations at an atomic scale are necessary to decide if Bi clustering is present or not in the nanometer range. Therefore we performed additional high resolution HAADF measurements of the Ga(AsBi) layers. Intentionally thick sample regions were chosen to be able to derive statistical data from the high resolution measurements. Even for the sample with the lowest Bi content, each group V column should contain at least one Bi atom, which leads to a required sample thickness of around 25 nm. All high resolution measurements were normalized to the incident beam in the same way as the low resolution measurements in Section 3.1. Fig. 6a and b depicts exemplarily two high resolution HAADF measurements of Ga(AsBi) layers, containing a nominal Bi fraction of 0.9% and 4.8%. The group III and group V sublattices were separated in the images. For the sublattice separation, column peak positions had to be found first. This was carried out with the help of the peak pairs software [33]. Afterwards we separated the group III from the group V sublattice and integrated the pixel intensities of each column within a radius which was defined as one third of the nearest neighbor distance. We have chosen this integration radius because of a reasonable signal to noise ratio without introducing too much crosstalk between the atomic columns. The respective column intensity distribution is plotted in histograms for each sublattice. The intensity distributions depicted in Fig. 6c and d correspond to the high resolution measurements (Fig. 6a and b). The bin size of each histogram was calculated by using the Freedman–Diaconis rule [34]:

$$\text{Bin size} = 2 * \text{IQR}(x) n^{-\frac{1}{3}} \quad (1)$$

where IQR(x) is the interquartile range of the intensity distribution x and n is the number of the intensities within the distribution x.

The histogram depiction of the intensities is helpful for a further analysis. A first comparison of the histograms shows that the intensities of group III and group V sublattices separate the more from each other, the more Bi is incorporated. This seems to be obvious and expectable, since the measured HAADF intensity is proportional to the atomic number $Z^{1.6}$. Furthermore, a more exact analysis of group V column intensities allows to decide whether a specific Bi clustering is present or not. Therefore, the group V histograms were fitted by assuming a Gaussian distribution, which provide us the distributions' mean value μ and their standard deviation σ. The fitted group V column intensities from Fig. 6c and d are depicted in Fig. 7a and b respectively. In addition, also the σ, 2σ and 3σ confidence interval are colored in green, red and yellow. The intensity distribution follows the Gaussian distribution fit (dashed curve) in both cases, which means that no specific Bi clustering could be identified and the Bi is homogenously distributed over the measured region. Otherwise we would expect a significantly larger number of higher group V column intensities in the histogram which would not follow the Gaussian distribution.

Since the standard deviation σ of the Gaussian distribution is a goodness for group V intensity distribution and therefore for the Ga(AsBi) layer quality, we compared each standard deviation of the Ga(AsBi) high resolution measurements containing different Bi fractions. The result is depicted in Fig. 7c, where the standard deviation is plotted versus the Bi fraction. As for the low resolution case (Fig. 5), we see the same standard deviation for each group V

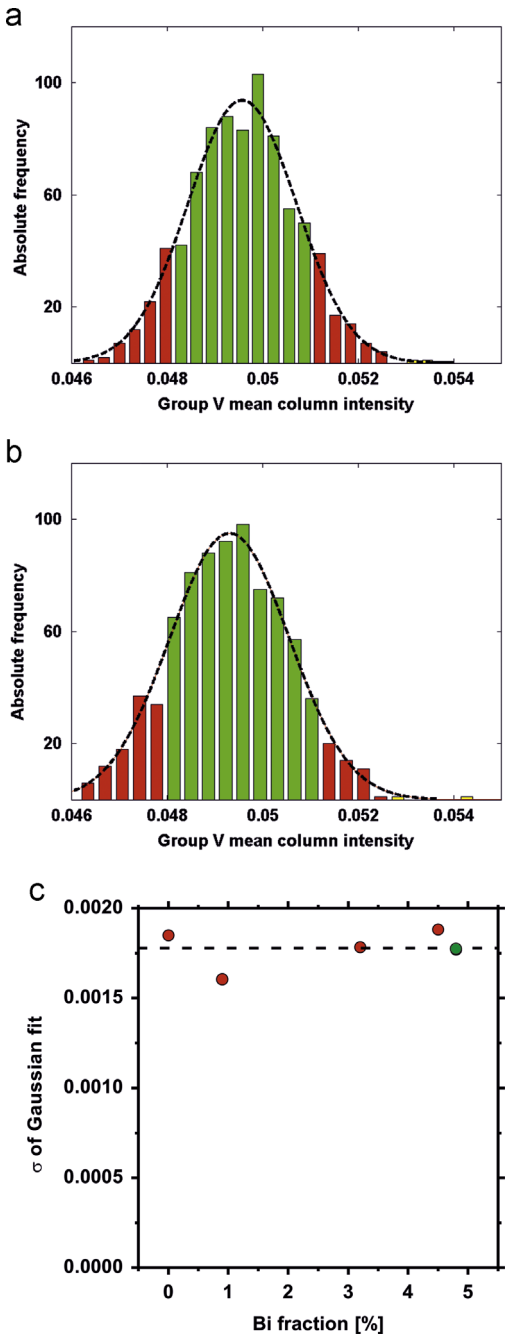

Fig. 7. (a, b) Histogram plot of the group V intensities. The dashed curve corresponds to a Gaussian distribution fit. The colored regions represent the standard deviation σ of the dashed line, where green is the σ, red the 2σ and yellow the 3σ confidence interval. Both histograms show a Gaussian distribution of the group V intensities and therefore Bi clustering cannot be found in the investigated Ga(AsBi) QWs. The diagram in (c) shows the determined standard deviations σ of the group V column intensity distribution measured for each Ga(AsBi) QW. The green colored value is again from the QW grown at 375 °C. The dashed line serves as a guide to the eye and shows an almost equal group V intensity distribution. (For interpretation of the references to color in this figure legend,the reader is referred to the web version of this article.)

intensity distribution (dashed line) in the high resolution measurements. The standard deviation has also the same value for the GaAs. From the structural point of view this means that the Bi atoms are homogeneously (statistically) distributed and all grown Ga(AsBi) layers exhibit a good quality, irrespective of the Bi concentration up to 5% and the growth temperature between 375 °C and 400 °C.

If possible Bi clustering in the nearest neighbor size range should be detected, much thinner TEM samples (5 nm) are required and results will be presented elsewhere.

4. Conclusions

We have shown by means of HAADF measurements how the obtained data can be used, in order to analyze the Bi fraction of dilute Bi material Ga(AsBi) quantitatively. There is excellent agreement of the Bi-composition derived from STEM with the one from HR-XRD and SIMS, making this method very useful to also address composition fluctuations quantitatively. Hence, the Ga(AsBi) layers' homogeneity was analyzed. As a result we find a homogeneous intensity distribution in the Ga(AsBi) layer, meaning that no Bi clustering can be detected for samples containing up to 5% Bi and grown at 375 °C and 400 °C, respectively.

Furthermore, high resolution measurements of the Ga(AsBi) layers were performed for analyzing the occurrence of possible Bi clustering. The group V column intensity histogram could be described well by a Gaussian distribution, proving that the group V intensities of all investigated Ga(AsBi) layers exhibit the same standard deviation σ. Hence, also from high resolution measurements, no Bi clustering becomes evident pointing towards an excellent quality of the metastable Ga(AsBi) material grown by MOVPE. These findings also prove that correlation of optical data to composition from HR-XRD is justified, as no Bi-composition fluctuations at length scales, which would influence optical characteristics, takes place.

Acknowledgments

This work was supported by the German Science Foundation (DFG) in the framework of the Research Training Group "Functionalization of Semiconductors" (GRK 1782) and the European Union Project BIANCHO (FP7-257974).

References

[1] S. Francoeur, M.J. Seong, A. Mascarenhas, S. Tixier, M. Adamcyk, T. Tiedje, Band gap of $GaAs_{1-x}Bi_x$, $0 < x < 3.6\%$, Appl. Phys. Lett. 82 (2003) 3874, http://dx.doi.org/10.1063/1.1581983.

[2] K. Alberi, O.D. Dubon, W. Walukiewicz, K.M. Yu, K. Bertulis, A. Krotkus., Valence band anticrossing in $GaBi_xAs_{1-x}$, Appl. Phys. Lett. 91 (2007) 051909, http://dx.doi.org/10.1063/1.2768312.

[3] S. Imhof, C. Bückers, A. Thränhardt, J. Hader, J.V. Moloney, S.W. Koch, Microscopic theory of the optical properties of Ga(AsBi)/GaAs quantum wells, Semicond. Sci. Technol. 23 (2008) 125009, http://dx.doi.org/10.1088/0268-1242/23/12/125009.

[4] C.A. Broderick, M. Usman, S.J. Sweeney, E.P. O'Reilly, Band engineering in dilute nitride and bismide semiconductor lasers, Semicond. Sci. Technol. 27 (2012) 094011, http://dx.doi.org/10.1088/0268-1242/27/9/094011.

[5] S. Imhof, C. Wagner, A. Thränhardt, A. Chernikov, M. Koch, N.S. Köster, S. Chatterjee, S.W. Koch, O. Rubel, X. Lu, S.R. Johnson, D.A. Beaton, T. Tiedje, Luminescence dynamics in Ga(AsBi), Appl. Phys. Lett. 98 (2011) 161104, http://dx.doi.org/10.1063/1.3580773.

[6] P. Ludewig, N. Knaub, N. Hossein, S. Reinhard, L. Nattermann, I.P. Marko, S.R. Jin, K. Hild, S. Chatterjee, W. Stolz, S.J. Sweeney, K. Volz, Electrical injection Ga(AsBi)/(AlGa)As single quantum well laser, Appl. Phys. Lett. 102 (24) (2013) 242115, http://dx.doi.org/10.1063/1.4811736.

[7] T. Fuyuki, K. Yoshida, R. Yoshioka, M. Yoshimoto, Electrically pumped room-temperature operation of $GaAs_{1-x}Bi_x$ laser diodes with low-temperature dependence of oscillation wavelength, Appl. Phys. Express 7 (2014) 082101, http://dx.doi.org/10.7567/APEX.7.082101.

[8] X. Lu, D.A. Beaton, R.B. Lewis, T. Tiedje, M.B. Whitwick, Effect of molecular beam epitaxy growth conditions on the Bi content of $GaAs_{1-x}Bi_x$, Appl. Phys. Lett. 92 (2008) 192110, http://dx.doi.org/10.1063/1.2918844.

[9] A.J. Ptak, R. France, D. Beaton, K. Alberi, J. Simon, A. Mascarenhas, C.-S. Jiang, Kinetically limited growth of GaAsBi by molecular-beam epitaxy, J. Cryst. Growth 338 (2012) 107–110, http://dx.doi.org/10.1016/j.jcrysgro.2011.10.040.

[10] E. Sterzer, N. Knaub, P. Ludewig, R. Straubinger, A. Beyer, K. Volz, Investigation of the microstructure of metallic droplets on Ga(AsBi)/GaAs, J. Cryst. Growth 408 (2014) 71–77, http://dx.doi.org/10.1016/j.jcrysgro.2014.09.006.

[11] K. Forghani, A. Anand, L.J. Mawst, T.F. Kuech, Low temperature growth of $GaAs_{1-y}Bi_y$ epitaxial layers, J. Cryst. Growth 380 (2013) 23–27, http://dx.doi.org/10.1016/j.jcrysgro.2013.05.033.

[12] K. Forghani, Y. Guan, A.W. Wood, A. Anand, S.E. Babcock, L.J. Mawst, T.F. Kuech, Self-limiting growth when using trimethyl bismuth (TMBi) in the metal-organic vapor phase epitaxy (MOVPE) of $GaAs_{1-y}Bi_y$, J. Cryst. Growth 395 (2014) 38–45, http://dx.doi.org/10.1016/j.jcrysgro.2014.03.014.

[13] P. Ludewig, N. Knaub, W. Stolz, K. Volz, MOVPE growth of Ga(AsBi)/GaAs multi quantum well structures, J. Cryst. Growth 370 (2013) 186–190, http://dx.doi.org/10.1016/j.jcrysgro.2012.07.002.

[14] P. Ludewig, Z. Bushell, L. Nattermann, N. Knaub, W. Stolz, K. Volz, Growth of Ga(AsBi) on GaAs by continuous flow MOVPE, J. Cryst. Growth 396 (2014) 95–99, http://dx.doi.org/10.1016/j.jcrysgro.2014.03.041.

[15] H. Jacobsen, B. Puchala, T.F. Kuech, D. Morgan, Ab initio study of the strain dependent thermodynamics of Bi doping in GaAs, Phys. Rev. B 86 (2012) 085207, http://dx.doi.org/10.1103/PhysRevB.86.085207.

[16] M. Kunzer, W. Jost, U. Kaufmann, H.M. Hobgood, R.N. Thomas, Identification of the Bi_{Ga} heteroantisite defect in GaAs:Bi, Phys. Rev. B 48 (1993) 4437, http://dx.doi.org/10.1103/PhysRevB.48.4437.

[17] G. Ciatto, E.C. Young, F. Glas, J. Chen, R. Alonso Mori, T. Tiedje, Spatial correlation between Bi atoms in dilute $GaAs_{1-x}Bi_x$: from random distribution to Bi pairing and clustering, Phys. Rev. B 78 (2008) 035325, http://dx.doi.org/10.1103/PhysRevB.78.035325.

[18] G. Ciatto, M. Thomasset, F. Glas, X. Lu, T. Tiedje, Formation and vanishing of short range ordering in $GaAs_{1-x}Bi_x$ thin films, Phys. Rev. B 82 (2010) 201304, http://dx.doi.org/10.1103/PhysRevB.82.201304 (R).

[19] D.L. Sales, E. Guerrero, J.F. Rodrigo, P.L. Galindo, A. Yáñez, M. Shafi, A. Khatab, R. H. Mari, M. Henini, S. Novikov, M.F. Chisholm, S.I. Molina, Distribution of bismuth atoms in epitaxial GaAsBi, Appl. Phys. Lett. 98 (2011) 101902, http://dx.doi.org/10.1063/1.3562376.

[20] A.W. Wood, S.E. Babcock, J. Li, A.S. Brown, Increased bismuth concentration in MBE $GaAs_{1-x}Bi_x$ films by oscillating III/V flux ratio during growth, J. Vac. Sci. Technol. A 33 (2015) 031506, http://dx.doi.org/10.1116/1.4916575.

[21] A.W. Wood, Y. Guan, K. Forghani, A. Anand, T.F. Kuech, S.E. Babckock, Unexpected bismuth concentration profiles in metal-organic vapor phase epitaxy-grown $Ga(As_{1-x}Bi_x)$/GaAs superlattices revealed by Z-contrast scanning transmission electron microscopy imaging, Appl. Phys. Lett. Mater. 3 (2015) 036108, http://dx.doi.org/10.1088/1742-6596/522/1/012017.

[22] M. Haider, H. Rose, S. Uhlemann, E. Schwan, B. Kabius, K. Urban, A spherical-aberration-corrected 200 kV transmission electron microscope, Ultramicroscopy 75 (1) (1998) 53–60, http://dx.doi.org/10.1063/1.4915301.

[23] S.J. Pennycook, Z-contrast stem for materials science, Ultramicroscopy 30 (1–2) (1989) 58–69, http://dx.doi.org/10.1016/0304-3991(89)90173-3.

[24] S.J. Pennycook, D.E. Jesson, High-resolution Z-contrast imaging of crystals, Ultramicroscopy 37 (1–4) (1991) 14–38, http://dx.doi.org/10.1016/0304-3991(91)90004-P.

[25] S. Tixier, M. Adamcyk, T. Tiedje, S. Francoeur, A. Mascarenhas, P. Wei, F. Schiettekatte, Molecular beam epitaxy growth of $GaAs_{1-x}Bi_x$, Appl. Phys. Lett. 82 (14) (2003), http://dx.doi.org/10.1063/1.1565499 2245-2247.

[26] E.J. Kirkland, Advanced Computing in Electron Microscopy, Plenum Press, New York (1998) http://dx.doi.org/10.1007/978-1-4419-6533-2.

[27] A. Rosenauer, M. Schowalter, STEMSIM- a new software tool for simulation of STEM HAADF Z-contrast imaging, in: A.G. Cullis, P.A. Midgley (Eds.), Microscopy of Semiconducting Materials (Proceedings in Physics), 120, Springer, Netherlands, 2007, pp. 169–172.

[28] D.S. He, Z.Y. Li, A practical approach to quantify the ADF detector in STEM, J. Phys.: Conf. 522 (2014) 012017, http://dx.doi.org/10.1088/1742-6596/522/1/012017.

[29] T. Grieb, K. Müller, R. Fritz, M. Schowalter, N. Neugebohrn, N. Knaub, K. Volz, A. Rosenauer, Determination of the chemical composition of GaNAs using STEM HAADF imaging and STEM strain state analysis, Ultramicroscopy 117 (2012) 15–23, http://dx.doi.org/10.1016/j.ultramic.2012.03.014.

[30] P.M. Voyles, J.L. Grazul, D.A. Muller, Imaging individual atoms inside crystals with ADF-STEM, Ultramicroscopy 96 (2003) 251–273, http://dx.doi.org/10.1016/S0304-3991(03)00092-5.

[31] P.M. Voyles, D.A. Muller, E.J. Kirkland, Depth-dependent imaging of individual dopant atoms in silicon, Microsc. Microanal. 10 (02) (2004) 291–300, http://dx.doi.org/10.1017/S1431927604040012.

[32] O.L. Krivanek, M.F. Chisholm, V. Nicolosi, T.M. Pennycook, G.J. Corbin, N. Dellby, M.F. Murfitt, C.S. Own, Z.S. Szilagyi, M.P. Oxley, S.T. Pantelides, S.J. Pennycook, Atom-by-atom structural and chemical analysis by annular dark-field electron microscopy, Nature 464 (2010) 571–574, http://dx.doi.org/10.1038/nature08879.

[33] P.L. Galindo, S. Kret, A.M. Sanchez, J.-Y. Laval, A. Yáñez, J. Pizarro, E. Guerrero, T. Ben, S.I. Molina, The Peak pairs algorithm for strain mapping from HRTEM images, Ultramicroscopy 107 (12) (2007) 1186–1193, http://dx.doi.org/10.1016/j.ultramic.2007.01.019.

[34] D. Freedman, P. Diaconis, On the histogram as a density estimator: L_2 theory, Probab. Theory Relat. Fields 57 (4) (1981) 453–476, http://dx.doi.org/10.1007/BF01025868.

6.2 Compositional dependence of the band gap in Ga(NAsP) quantum well heterostructures[1]

K. Jandiery, P. Ludewig, T. Wegele, A. Beyer, B. Kunert, P. Springer, S. D. Baranovskii, S. W. Koch, K.Volz, W. Stolz, Journal of Applied Physics **118**, 065701 (2015). DOI: 10.1063/1.4928331.

Abstract

We present experimental and theoretical studies of the composition dependence of the direct band gap energy in Ga(NAsP)/GaP quantum well heterostructures grown on either (001) GaP- or Si-substrates. The theoretical description takes into account the band anti-crossing model for the conduction band as well as the modification of the valence subband structure due to the strain resulting from the pseudomorphic epitaxial growth on the respective substrate. The composition dependence of the direct band gap of Ga(NAsP) is obtained for a wide range of nitrogen and phosphorus contents relevant for laser applications on Si-substrate.

My Contribution

The preparation of TEM specimens from the samples with the Ga(NAsP)-QWs as well as the acquisition of the STEM micrographs was performed by me in order to prove the quality of the layers and to compare the QW-thickness in the cross-sections with the mean thickness determined by the XRD.

1 Reprinted from *Journal of Applied Physics **118** 065701 (2015)*

JOURNAL OF APPLIED PHYSICS **118**, 065701 (2015)

Compositional dependence of the band gap in Ga(NAsP) quantum well heterostructures

K. Jandieri,[a] P. Ludewig, T. Wegele, A. Beyer, B. Kunert,[b] P. Springer, S. D. Baranovskii, S. W. Koch, K. Volz, and W. Stolz
Materials Science Center and Faculty of Physics, Philipps-University Marburg, Marburg, Germany

(Received 31 March 2015; accepted 25 June 2015; published online 11 August 2015)

We present experimental and theoretical studies of the composition dependence of the direct band gap energy in Ga(NAsP)/GaP quantum well heterostructures grown on either (001) GaP- or Si-substrates. The theoretical description takes into account the band anti-crossing model for the conduction band as well as the modification of the valence subband structure due to the strain resulting from the pseudomorphic epitaxial growth on the respective substrate. The composition dependence of the direct band gap of Ga(NAsP) is obtained for a wide range of nitrogen and phosphorus contents relevant for laser applications on Si-substrate. © *2015 AIP Publishing LLC*.
[http://dx.doi.org/10.1063/1.4928331]

I. INTRODUCTION

Dilute nitride III-V alloys are promising materials for optoelectronic applications with unique physical properties. In particular, the direct band gap Ga(NAsP)-material[1] is gaining particular interest as it can be grown pseudomorphically strained on (001) Si-substrate in a certain composition range, avoiding any misfit dislocation formation processes resulting from the strain-relaxation of standard GaAs- or InP-based III/V-laser materials on (001) Si-substrate. The potential for application is underlined by the recent realization of electrical injection lasers in this material system both on GaP- (Ref. 2) as well as on Si-substrate.[3] In the present communication, we report on an experimental and theoretical study of the dependence of band gap of the Ga(NAsP) on the chemical composition in the range of (3–10)% nitrogen and (0–25)% phosphorus contents. Such a wide compositional variation of Ga(NAsP) samples provides the flexibility in emission wavelength as well as strain in pseudomorphic growth of corresponding laser structures on Si-substrates.

For theoretical interpretation of the composition-dependent band gap in dilute nitride materials, the band anti-crossing (BAC) model[4–6] is widely used. Initially, the BAC model was suggested for dilute nitride compounds as the simplest interpretation of the anti-crossing interaction between the semiconductor host matrix and the states of isolated nitrogen atoms embedded in the matrix. Later, it was found that the BAC model cannot reproduce the experimentally observed band gaps in the samples with comparatively large nitrogen content. For Ga(NAs) compounds on GaAs-substrate, the parametrized modification of the BAC model was suggested[7] assuming that for large nitrogen contents the anti-crossing interaction occurs not between the semiconductor matrix and the states of isolated nitrogen but rather between the matrix and the nitrogen-related impurity band. Later the BAC model was adopted for Ga(NAsP) quaternary compounds,[8] assuming that the band gap in corresponding heterostructures can be calculated as a linear combination of the band gaps in Ga(NAs) and Ga(NP) ternary compounds estimated via the two-level BAC model with taking into account the influence of the inherent strain on both, conduction and valence bands. For small nitrogen concentrations, this approach gives good agreement with experimental data on the direct band gap of Ga(NAsP) with a wide variety of phosphorus contents in the range of $x_P = (6–16)\%$. However, in samples with large nitrogen content, this approach is not able to model the PL peak energies observed in our experimental studies. The main goal of the present paper is, thus, to develop an adequate description of the band gap in Ga(NAsP) compounds with wide variations of both nitrogen and phosphorus contents including the extreme case of Ga(NAs) ternary compound as well as the compositions far apart from the dilute limits. To achieve this goal, we apply the two-level BAC model and take into account the strain-induced shift of the Γ conduction band edge in Ga(AsP) host matrix, assuming a compositional dependent hydrostatic deformation potential, as well as the modifications of the valence subband structure due to the epitaxial strain. In order to verify the validity of the results obtained within the frame of the two-level BAC model, we perform rigorous calculations applying a 8×8 $\mathbf{k} \cdot \mathbf{p}$ theory plus band anticrossing extension. We compare the experimentally observed and the calculated peak energies of the PL signal and show that our approach can be successfully applied to estimate the bandgap in Ga(NAs) and Ga(NAsP) compounds with nitrogen and phosphorus contents as large as $x_N = 10\%$ and $x_P = 25\%$. The paper is organized as follows. Section II presents the details of our experimental studies. The basics of the theoretical approach used to estimate the band gap in Ga(NAs) and Ga(NAsP) and the comparison of the calculation results with experimentally observed PL peak energies are given in Section III. The concluding remarks are summarized in Section IV.

II. EXPERIMENTAL RESULTS

The Ga(NAs) and Ga(NAsP)-quantum well heterostructures (QWH) have been deposited on (001) GaP- and (001) Si-substrates by low-temperature metal organic vapor phase

[a]Electronic mail: kakhaber.jandieri@physik.uni-marburg.de
[b]Present address: IMEC, Kapeldreef 75, Leuven, Belgium.

epitaxy (MOVPE) applying the more efficiently decomposing precursors tertiarybutyl arsine (TBAs), tertiarybutyl phosphine (TBP), and 1,1-dimethylhydrazine (UDMHy) for As, P, and N, respectively. After growth, the samples have been annealed to improve the optoelectronic properties at 800 °C for 30 min under TBP-stabilization.[9] The chemical composition has been determined by high-resolution X-ray diffraction (XRD) analysis together with full dynamical modeling of the XRD pattern assuming Vegard's law for the variation of the lattice constant with composition. The principle experimental procedure for the analysis of the chemical composition of Ga(NAs) and Ga(NAsP)-QWH has been published elsewhere.[10] For the epitaxial growth on Si-substrate, a specific GaP-nucleation template[11] has been applied prior to the deposition of the Ga(NAsP)/GaP/(BGa)(AsP)-QWH. The tensile-strained (BGa)(AsP)-barrier layers have been incorporated in order to strain-balance the compressive-strained Ga(NAsP)-quantum well material as described in Ref. 12. The main structural and compositional characteristics of the studied Ga(NAs)/GaP and Ga(NAsP)/GaP QW structures grown on different substrates are gathered in Table I along with the peak energies of PL spectra observed at room temperature.

One can see from the table that the nitrogen and the phosphorus contents of studied samples vary in essentially wide ranges of $x_N = (3–9)\%$ and $x_P = (0–23)\%$, respectively. Such a large compositional variation creates the useful ground to check the validity and the universality of the approach exploited to estimate the band gap in Ga(NAs)- and Ga(NAsP)-QWH structures, as described in Sec. III. The experimental accuracy of the chemical composition for the ternary Ga(NAs)-QWH is very high around $\pm 0.1\%$ of the N-content. The determination of the chemical composition in the quaternary Ga(NAsP) depends on the assumption that the N-incorporation is directly proportional to the applied partial pressure of the N-precursor as verified for the ternary Ga(NAs),[10] as well as that the As/P-incorporation efficiency is not significantly changed by the incorporation of N. Thus, the accuracy in determining the chemical composition is reduced and is estimated at about $\pm 1\%$ of the N-content (resulting in $\pm 5\%$ of the P-concentration). The quantum well width is determined from the experimental XRD-pattern. For part of the samples, high-resolution transmission electron microscopy (TEM) has been applied to verify the determined well width by XRD. Both methods agree within a range of ± 2 monolayers.

TABLE I. Characteristics of the studied QW structures and PL peak energies observed at RT.

Substrate	Compound	QW width (nm)	x_N (%)	x_P (%)	PL peak energy (eV)
GaP	Ga(NAs)	5.7	3.7	0.0	1.292
		8.3	5.2	0.0	1.169
		7.3	7.6	0.0	1.093
		6.5	9.5	0.0	1.056
GaP	Ga(NAsP)	7.9	3.7	6.0	1.318
		7.9	3.7	16.0	1.404
Si	Ga(NAsP)	4.6	6.9	4.3	1.306
		4.6	6.9	12.9	1.341
		4.5	6.9	22.9	1.377
		4.5	5.1	10.0	1.387
		4.6	6.3	13.1	1.360
		4.9	8.1	12.7	1.311

III. THEORETICAL ANALYSIS AND COMPARISON WITH EXPERIMENT

We estimate the PL peak energy in the studied QW structures as a sum of the band gap E_g in Ga(NAs) and Ga(NAsP) dilute nitride compounds and the ground state quantization energies $E_{0,e}$ and $E_{0,h}$ for confined electrons and holes, respectively

$$E_p = E_g + E_{0,e} + E_{0,h}. \tag{1}$$

The band gap $E_g = E_c - E_v$ is calculated as a difference of the conduction and the valence band edges that are modified by the strain inherent in the QW structures. For the conduction band edge E_c, we apply the two-level BAC model[4–6]

$$E_c = \frac{1}{2}\left[(E_\Gamma + E_N) - \sqrt{(E_\Gamma - E_N)^2 + 4C^2 x_N}\right], \tag{2}$$

where E_Γ is the Γ conduction band edge of the host matrix Ga(AsP), E_N is the energy of the isolated nitrogen atom embedded in the host matrix, x_N is the nitrogen content of the compound, and C is the coupling constant. The modification of the value of the conduction band edge E_c due to strain is taken into account through the energy shift ΔE_Γ of the conduction band edge of the host matrix.

For the valence band edge, we use the standard approach[13,14] giving the possibility to estimate the energy shifts and the splitting of the heavy and the light hole bands under the influence of the hydrostatic and the shear components of the strain. As a result of this splitting, the heavy hole band becomes the uppermost valence band. Accordingly, we assume that the PL output of studied QW structures is determined by the optical transitions between the electron and the heavy hole confined states. Along with modification of the band gap, the strain has an additional influence on the PL peak energy E_p due to the variation of the ground quantum levels $E_{0,e}$ and $E_{0,h}$. These variations are caused by the strain-induced changes of the valence and the conduction band offsets between the QW and the barrier layers, and hence by the changes of the barrier heights in the quantum well. The values of $E_{0,e}$ and $E_{0,h}$ are calculated in frames of the standard theory of quantization in finite barrier quantum wells[15] applying the following expression:

$$E_0 = \frac{\hbar^2 k^2}{2m}, \tag{3}$$

where k is the solution of the transcendent equation

$$kd = \pi - \arcsin\frac{k\hbar}{\sqrt{2mU_1}} - \arcsin\frac{k\hbar}{\sqrt{2mU_2}}, \tag{4}$$

d is the width of the quantum well, $\hbar$ is the Plank constant, U_1 and U_2 are the barrier heights, and m is the carrier effective mass. In our calculations, we use the electron effective mass m_e estimated from BAC theory[6]

$$m_e = 2m_e^{host}\left[1 - \frac{E_\Gamma - E_N}{\sqrt{(E_\Gamma - E_N)^2 + 4C^2x_N}}\right]^{-1}, \quad (5)$$

and the heavy hole effective mass m_{hh} estimated as[24]

$$m_{hh} = \frac{m_0}{\gamma_1 - 2\gamma_2}, \quad (6)$$

where m_e^{host} is the electron effective mass in the host matrix, m_0 is the free electron mass, and γ_1 and γ_2 are the Luttinger parameters of the considered nitride compounds. Some additional calculation details as well as the relevant material parameters are summarized in the Appendix.

The set of Eqs. (1)–(6) along with Eqs. (A1)–(A6) and the values of material parameters summarized in Table II of the Appendix provide the complete theoretical basis to estimate the PL peak energies in the studied QW structures. The only fitting parameter involved in this approach is the BAC-coupling constant C between the host matrix and the embedded isolated nitrogen atoms. It was estimated from the best fitting of the calculated and the experimental results.

The compositional dependencies of the PL peak energy calculated for Ga(NAs)/GaP and Ga(NAsP)/GaP QW structures grown on GaP substrate are shown by the solid circles in Figs. 1(a) and 1(b), respectively. They were obtained assuming $C = 1.9$ eV for the BAC coupling constant. The corresponding compositional dependencies of the strain-induced shift of the valence band edge are shown in the insets of Figs. 1(a) and 1(b) by the dashed lines. In order to verify the validity of the results obtained in frames of the two-level BAC model, we apply a microscopic many-body theory on the basis of the semiconductor luminescence equations.[16] All relevant quantum mechanical scattering processes are explicitly computed at the level of the second Born-Markov approximation.[17] Since the electronic band structure of dilute nitride semiconductors fundamentally differs from conventional semiconductor compounds, the 8×8

TABLE II. Material parameters.

Parameter[a]	Unit	GaAs	GaP	GaN
a_0	(nm)	0.56532	0.54505	0.45000
E_Γ	(eV)	1.42	2.78	…[b]
E_N	(eV)	1.65[c]	2.18[d]	…
α_Γ	(eV)	−7.17	−8.2	…
α_v	(eV)	−1.16	−1.7	…
a_N	(meV/GPa)	40.0[e]	1.0[e]	…
B	(eV)	−2.0	−1.6	…
C_{11}	(GPa)	122.1	140.5	…
C_{12}	(GPa)	56.6	62.0	…
γ_1	arb.u.	6.98	4.05	…
γ_2	arb.u.	2.06	0.98	…

[a]If not indicated explicitly, the values of the parameters are taken from Ref. 24.
[b]Not relevant for our calculations.
[c]Reference 4.
[d]Reference 6.
[e]Reference 28.

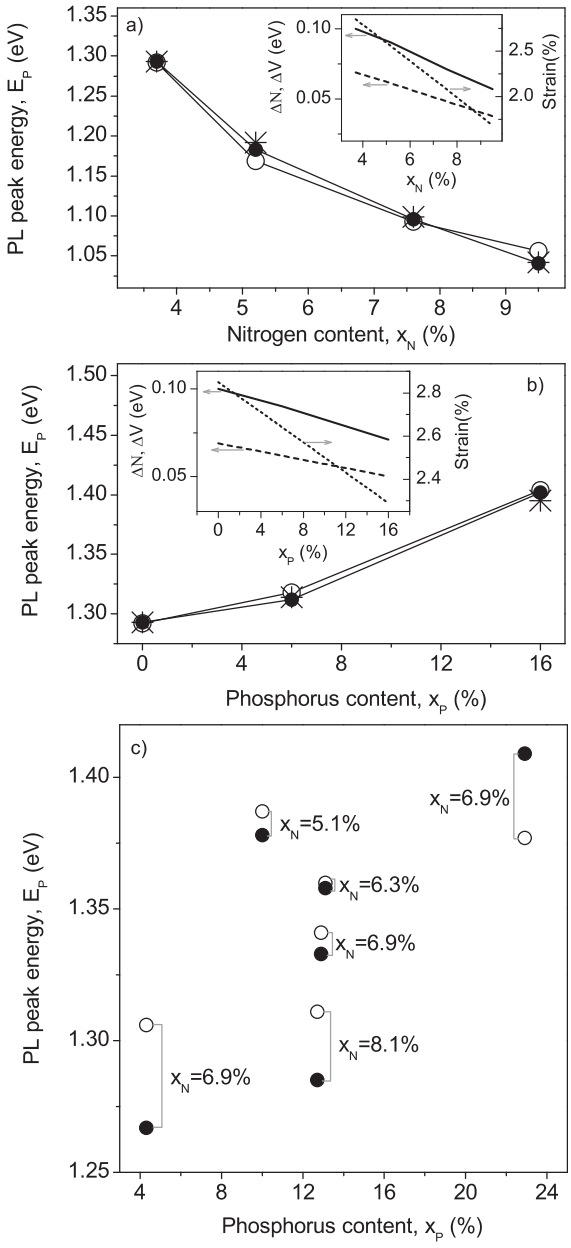

FIG. 1. Compositional dependencies of the PL peak energy observed (open circles) and calculated applying the two-level BAC model (solid circles) in studied Ga(NAs)/GaP QW structures grown on GaP substrate (a) and in Ga(NAsP)/GaP QW structures with $x_N = 3.7\%$ nitrogen content and various phosphorus contents grown on GaP substrate (b). For comparison purpose, the PL peak energies estimated applying the macroscopic many-body theory are also shown by the stars. The lines are the guides to the eye. The corresponding compositional dependencies of the compressive strain and the strain-induced shifts of the valence band edge and of the nitrogen-related level are shown in the insets by the dotted, dashed, and solid lines, respectively. The PL peak energies observed (open circles) and calculated (solid circles) in Ga(NAsP)/GaP QW structures with various nitrogen and phosphorus contents grown on Si substrate are shown in (c). The arrows and the corresponding numbers indicate the nitrogen contents of the considered Ga(NAsP) QW compounds.

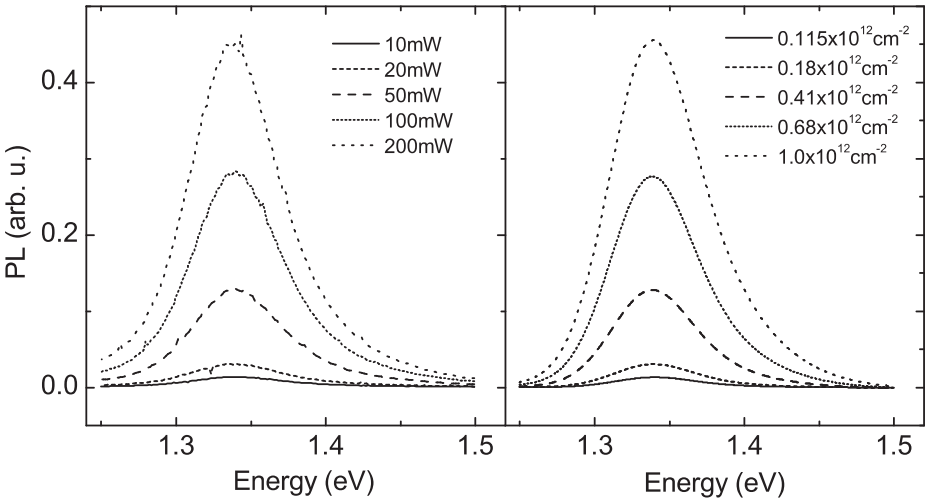

FIG. 2. Comparison of the experimental (left) and theoretical (right) PL spectra for various excitation conditions. Both were obtained by room temperature for the 4.6 nm thick quantum well sample containing 6.9% nitrogen and 12.9% phosphorus.

$\mathbf{k}\cdot\mathbf{p}$ Luttinger Hamiltonian usually utilized to derive single-particle energies is extended to a 10×10 matrix containing a dispersionless nitrogen component. This approach also allows to treat quantum well systems within the envelope function approach, thus including confinement effects.[18–22] We use the BAC model in order to obtain a simple parametrization for the near-bandgap band structure modifications due to the inclusion of a certain nitrogen percentage. The additional set of empirical parameters introduced in this method is the energetic shift α of the conduction band energy due to virtual crystal shifts and the coupling strength C between nitrogen and conduction band.[23] All other $\mathbf{k}\cdot\mathbf{p}$ parameters are taken from Refs. 24 and 25. We also stress that compositional dependent interpolation of any quantity is performed between the host material alone (see the Appendix). The only exception is the lattice constant, for which Vegard's rule can be applied between all binary components of the compound.[25] We further take into account the strain-induced shift of the nitrogen level assuming that the nitrogen level in the host matrix is independent of the nitrogen concentration.[26] The calculated PL peak energies are shown in Figs. 1(a) and 1(b) by stars. They were obtained assuming $\alpha=0\,\text{eV}$ and $C=1.9\,\text{eV}$ for the BAC coupling constant which is in perfect agreement with a previous study[27] and with a two-level BAC model. The corresponding compositional dependencies of the strain-induced shift of the nitrogen level are shown in the insets of Figs. 1(a) and 1(b) by the solid lines.

One can see from the figures that our theoretical approach based on two-level BAC model gives PL peak energies that are very close to the results of microscopic many-body theory and to the experimentally observed values (open circles) in a wide compositional range including the nitrogen and phosphorus contents far apart from their respective dilute limits. For Ga(NAsP)/GaP QW structures grown on Si substrate, the best agreement between the experimental and the calculated results was obtained for the BAC coupling constant $C=1.75\,\text{eV}$. The corresponding compositional dependence of the PL peak energy E_p is shown in Fig. 1(c) by the solid circles. The comparison with experimental data (open circles) shows that in all considered samples the difference between the observed and the estimated PL peak energies is $\Delta E<40\,\text{meV}$. To emphasize the good agreement

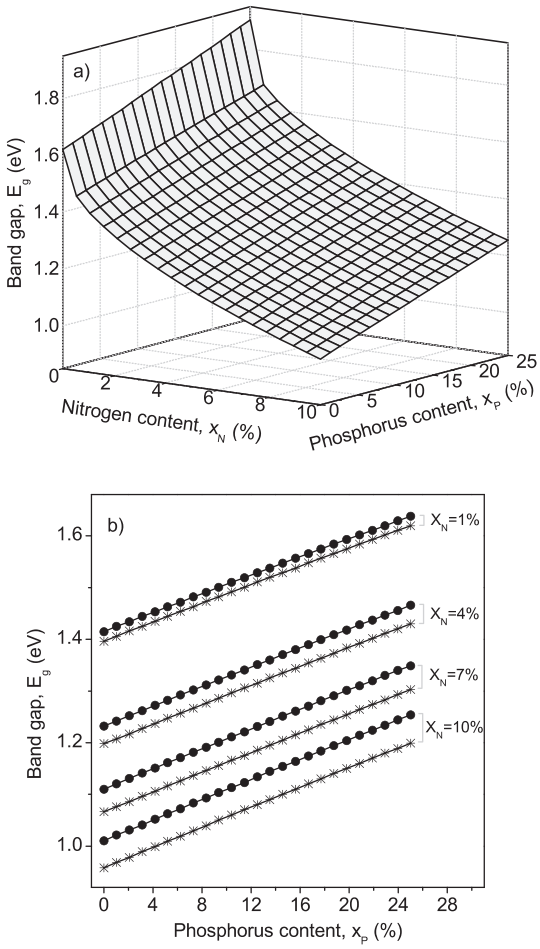

FIG. 3. Band gap in Ga(NAsP) quaternary compound pseudomorphologically grown on Si substrate as a function of the nitrogen and the phosphorus contents (a). The several cross-sections of this dependence calculated at various nitrogen contents x_N are shown in (b) by the solid circles. The band gaps calculated for Ga(NAsP) samples grown on GaP substrate are also shown by the stars. The lines are guides to the eye.

between theoretical estimates and the experimental results obtained in the studied QW structures, we show in Fig. 2(a) side-by-side comparison of the PL spectra for different excitation powers interpreted as carrier densities for the computed spectra. To account for disorder effects, the spectra are convoluted with a Gaussian distribution with a FWHM of 40 meV.

Based on the obtained results, we can assume that our approach can be considered as a general tool for determining the band gap in Ga(NAs) and Ga(NAsP) compounds with a wide variety of nitrogen and phosphorus contents. As an example, the two dimensional compositional dependence on N- and P-content of the band gap in Ga(NAsP) grown on Si substrate is shown in Fig. 3(a). The P-content dependencies for various values of the N-content are shown in Fig. 3(b) by the circles for the deposition on Si-substrates. The compositional dependencies of the band gap calculated for Ga(NAsP) compound grown on GaP substrates are also shown in Fig. 3(b) by the stars.

IV. CONCLUSIONS

The compositional dependence of the photoluminescence peak energy in Ga(NAs)/GaP and Ga(NAsP)/GaP quantum well structures grown on GaP and Si substrates were studied experimentally and theoretically. Using the theoretical approach based on the two-level BAC model, we showed that the observed PL peak energies can be well reproduced in wide ranges of nitrogen and phosphorus contents including the concentrations by far apart from their dilute limits. The key feature of our approach is the modification of both conduction and valence bands as a function of the strain inherent in these QWH. We estimate the values of the BAC coupling constant, necessary to fit the experimental data obtained for Ga(NAs) and Ga(NAsP) nitride compounds yielding values of $C = 1.9\,\text{eV}$ (1.75 eV) for the growth on GaP- (Si-) substrates, respectively.

ACKNOWLEDGMENTS

Various parts of this work have been supported by the Federal Ministry of Research and Education within the MonoLaSi-consortium as well as the German Science Foundation (DFG) within the Research Training Group GRK 1782 "Functionalization of Semiconductors."

APPENDIX: MODIFICATION OF THE BAND GAP DUE TO STRAIN

Strain inherent in QW structures modifies the bandgap and hence the PL emission spectra of QW layers. Modification of the band gap is caused by the variations in both conduction and valence band edge energies.

In case of dilute nitride compounds considered in this paper, the modification of the conduction band can be treated in two different ways: (i) as strain-induced variation of the conduction band edge estimated from Eq. (2) with strain independent Γ conduction band edge E_Γ of the corresponding semiconductor matrix, or (ii) as strain-induced shift of the Γ conduction band edge in a semiconductor matrix resulting in modified conduction band edge of the corresponding nitride compound calculated according to Eq. (2). For theoretical interpretation of our experimental results, we use the last approach.

We begin with the Γ conduction band edge in an unstrained Ga(AsP) matrix calculated as

$$E_\Gamma^0 = \frac{E_\Gamma^{\text{GaAs}} x_{\text{As}} + E_\Gamma^{\text{GaP}} x_{\text{P}}}{x_{\text{As}} + x_{\text{P}}}, \tag{A1}$$

where E_Γ^{GaAs} and E_Γ^{GaP} are the Γ conduction band edges in GaAs and GaP binary compounds, respectively, and $x_{\text{As}} = 1 - x_{\text{p}} - x_{\text{N}}$ is the arsenic concentration in Ga(NAsP) compound.

Knowing the values E_Γ^0 in the unstrained compound, we calculate the values E_Γ in strained QW structure as

$$E_\Gamma = E_\Gamma^0 + \alpha_\Gamma(2\varepsilon_{||} + \varepsilon_\perp), \tag{A2}$$

where

$$\begin{aligned} \varepsilon_{||} &= \frac{a_0^{\text{s}} - a_0^{\text{QW}}}{a_0^{\text{QW}}}, \\ \varepsilon_\perp &= -2\frac{C_{12}}{C_{11}}\varepsilon_{||}, \end{aligned} \tag{A3}$$

are the in-plane and the out-of-plane components of the strain. a_0^{s} is the lattice parameter of the substrate and

$$\begin{aligned} a_0^{\text{QW}} &= a_0^{\text{GaAs}} x_{\text{As}} + a_0^{\text{GaP}} x_{\text{P}} + a_0^{\text{GaN}} x_{\text{N}}, \\ C_{11} &= \frac{C_{11}^{\text{GaAs}} x_{\text{As}} + C_{11}^{\text{GaP}} x_{\text{P}}}{x_{\text{As}} + x_{\text{P}}}, \\ C_{12} &= \frac{C_{12}^{\text{GaAs}} x_{\text{As}} + C_{12}^{\text{GaP}} x_{\text{P}}}{x_{\text{As}} + x_{\text{P}}}, \\ \alpha_\Gamma &= \frac{\alpha_\Gamma^{\text{GaAs}} x_{\text{As}} + \alpha_\Gamma^{\text{GaP}} x_{\text{P}}}{x_{\text{As}} + x_{\text{P}}}, \end{aligned} \tag{A4}$$

are the lattice parameter, elastic constants, and the hydrostatic deformation potential of the Γ conduction band in the Ga(NaAsP) QW layer. (Here, and further all material parameters, except of the lattice constant, are interpolated between their binary endpoints of the Ga(AsP) host matrix). The value of E_Γ determined from Eqs. (A1)–(A4) is used in Eq. (2) to estimate the conduction band edge in all considered Ga(NAs) and Ga(NAsP) nitride compounds.

The strain inherent in QW structures splits the valence band of QW compound in two, heavy and light hole subbands. All QW structures considered in given paper are under compressive strain. Therefore, the uppermost valence band is a heavy hole band. The corresponding band edge measured from the valence band edge of the unstrained structure can be estimated as[13,14]

$$E_{\text{v}} = -[\alpha_{\text{v}}(2\varepsilon_{||} + \varepsilon_\perp) + b(\varepsilon_\perp - \varepsilon_{||})], \tag{A5}$$

where

$$\alpha_v = \frac{\alpha_v^{GaAs} x_{As} + \alpha_v^{GaP} x_{GaP}}{x_{As} + x_P}, \qquad b = \frac{b^{GaAs} x_{As} + b^{GaP} x_P}{x_{As} + x_P}, \tag{A6}$$

are the hydrostatic and the shear deformation potentials for the valence band.

For the estimation of the band gap in frames of the microscopic many-body theory, we additionally take into account the strain-induced energetic shift of the nitrogen level determined as

$$E_N = E_N^0 + \alpha_N(2\varepsilon_{||} + \varepsilon_\perp), \tag{A7}$$

with nitrogen-related energy level in the unstrained structure E_N^0 and the hydrostatic deformation potential α_N estimated as[29]

$$\alpha_N = -\frac{C_{11} + 2C_{12}}{3} a_N, \tag{A8}$$

where

$$a_N = \frac{a_N^{GaAs} x_{As} + a_N^{GaP} x_P}{x_{As} + x_P} \tag{A9}$$

is the pressure coefficient for nitrogen related states in Ga(AsP) host matrix.

The values of material parameters used in Eqs. (A1)–(A9) are gathered in Table II.

[1]B. Kunert, K. Volz, J. Koch, and W. Stolz, Appl. Phys. Lett. **88**, 182108 (2006).
[2]N. Hossain, S. J. Sweeney, S. Rogowsky, R. Ostendorf, J. Wagner, S. Liebich, M. Zimprich, K. Volz, B. Kunert, and W. Stolz, Electron. Lett. **47**, 931 (2011).
[3]S. Liebich, M. Zimprich, A. Beyer, C. Lange, D. J. FranzbachK, S. Chatterjee, N. Hossain, S. J. Sweeney, K. Volz, B. Kunert, and W. Stolz, Appl. Phys. Lett. **99**, 071109 (2011).
[4]W. Shan, W. Walukiewicz, J. W. Ager III, E. E. Haller, J. F. Geisz, D. J. Friedman, J. M. Olson, and S. R. Kurtz, Phys. Rev. Lett. **82**, 1221 (1999).
[5]W. Shan, W. Walukiewicz, K. M. Yu, J. Wu, J. W. Ager III, E. E. Haller, H. P. Xin, and C. W. Tu, Appl. Phys. Lett. **76**, 3251 (2000).
[6]J. Wu, W. Shan, and W. Walukiewicz, Semicond. Sci. Technol. **17**, 860 (2002).
[7]P. J. Klar, H. Grüning, W. Heimbrodt, J. Koch, F. Höhnsdorf, W. Stolz, P. M. A. Vicente, and J. Camassel, Appl. Phys. Lett. **76**, 3439 (2000).
[8]R. Kudrawiec, J. Appl. Phys. **101**, 116101 (2007).
[9]B. Kunert, D. Trusheim, V. Vossebürger, K. Volz, and W. Stolz, Phys. Status Solidi A **205**, 114 (2008).
[10]B. Kunert, K. Volz, J. Koch, and W. Stolz, J. Cryst. Growth **298**, 121 (2007).
[11]K. Volz, A. Beyer, W. Witte, J. Ohlmann, I. Nemeth, B. Kunert, and W. Stolz, J. Cryst. Growth **315**, 37 (2011).
[12]B. Kunert, S. Zinnkann, K. Volz, and W. Stolz, J. Cryst. Growth **310**, 4776 (2008).
[13]C. G. Van de Walle, Phys. Rev. B **39**, 1871 (1989).
[14]Z. Batool, K. Hild, T. J. C. Hosea, X. Lu, T. Tiedje, and S. J. Sweeney, J. Appl. Phys. **111**, 113108 (2012).
[15]L. D. Landau and E. M. Lifshitz, *Quantum Mechanics* (Pergamon Press, 1965), Vol. 3, p. 63.
[16]M. Kira, F. Jahnke, S. W. Koch, J. Berger, D. Wick, T. Nelson, G. Khitrova, and H. M. Gibbs, Phys. Rev. Lett. **79**, 5170 (1997).
[17]M. Lindberg and S. W. Koch, Phys. Rev. B **38**, 3342 (1988).
[18]C. Y.-P. Chao and S. L. Chuang, Phys. Rev. B **46**, 4110 (1992).
[19]S. L. Chuang, Phys. Rev. B **43**, 9649 (1991).
[20]G. Liu and S. L. Chuang, Phys. Rev. B **65**, 165220 (2012).
[21]B. Chen, W. Y. Jiang, and A. L. Holmes, Jr., Opt. Quantum Electron. **44**, 103 (2012).
[22]B. Chen and A. L. Holmes, Jr., Opt. Quantum Electron. **45**, 127 (2013).
[23]A. Lindsay and E. P. O'Reilly, Solid State Commun. **112**, 443 (1999).
[24]I. Vurgaftman, J. R. Meyer, and L. R. Ram-Mohan, J. Appl. Phys. **89**, 5815 (2001).
[25]I. Vurgaftman and J. R. Meyer, J. Appl. Phys. **94**, 3675 (2003).
[26]W. Shan, W. Walukiewicz, K. M. Yu, J. W. Ager III, E. E. Haller, J. F. Geisz, D. J. Friedman, J. M. Olson, S. R. Kurtz, and C. Nauka, Phys. Rev. B **62**, 4211 (2000).
[27]N. Koukourakis, C. Bückers, D. A. Funke, N. C. Gerhardt, S. Liebich, S. Chatterjee, C. Lange, M. Zimprich, K. Volz, W. Stolz, B. Kunert, S. W. Koch, and M. R. Hofmann, Appl. Phys. Lett. **100**, 092107 (2012).
[28]P. R. C. Kent and A. Zunger, Phys. Rev. B **64**, 115208 (2001).
[29]S. Adachi, *Properties of Group-IV, III-V and II-VI Semiconductors* (John Wiley and Sons, Ltd., 2005).

6.3 MOVPE growth studies of Ga(NAsP)/(BGa)(AsP) multi quantum well heterostructures (MQWH) for the monolithic integration of laser structures on (001) Si-substrate [1]

P. Ludewig, S. Reinhard, K. Jandieri, T. Wegele, A. Beyer, L. Tapfer, K. Volz, W. Stolz, Journal of Crystal Growth **438** (2016) 63–69. DOI: 10.1016/j.jcrysgro.2015.12.024.

Abstract

High-quality, pseudomorphically strained Ga(NAsP)/(BGa)(AsP)-multiple quantum well heterostructures (MQWH) have been deposited on exactly oriented(001) Si-substrate by metal organic vapour phase epitaxy (MOVPE) in a wide temperature range between 525 °C and 700 °C. The individual atomic incorporation efficiencies, growth rates as well as nanoscale material properties have been clarified by applying detailed high-resolution X-ray diffraction (HR-XRD), photoluminescence (PL) spectroscopy and high-angle annular dark field (HAADF) scanning transmission electron microscopy (STEM) studies. An almost constant N-incorporation efficiency is obtained for a wide growth temperature range from 550 °C up to 650 °C. The P-incorporation is steadily increasing with increasing growth temperature reaching values at high temperatures in excess of the applied gas phase ratio. While the lower interface from the binary GaP-to the quaternary Ga(NAsP)-material system is very sharp, the upper interface is significantly rougher with a roughness scale of ±0.43 nm in quantum well thickness variation at a growth temperature of 525 °C. This roughness scale increases steadily with increasing growth temperature. No indication of any phase separation effects is detected in the Ga(NAsP)-material system even at the highest growth temperature of 700 °C. The obtained experimental results are briefly discussed with respect to the anticipated metastable character of the novel dilute-nitride Ga(NAsP)-material system grown lattice-matched to (001) Si-substrate.

My Contribution

In order to prove the qualify of the Ga(NAsP)-QWs grown at different temperatures that were presented in this paper. I prepared TEM specimens and performed the ADF-STEM measurements. For quantitative analysis of the experimental results I wrote a MATLAB script, which allows to evaluate a mean thickness and roughness of the QW in the measured region.

1 Reprinted from *Journal of Crystal Growth **438** (2016) 63–69*, Copyright 2016, with permission from Elsevier.

Journal of Crystal Growth 438 (2016) 63–69

Contents lists available at ScienceDirect

Journal of Crystal Growth

journal homepage: www.elsevier.com/locate/jcrysgro

MOVPE growth studies of Ga(NAsP)/(BGa)(AsP) multi quantum well heterostructures (MQWH) for the monolithic integration of laser structures on (001) Si-substrates

P. Ludewig [a,b,*], S. Reinhard [a], K. Jandieri [a], T. Wegele [a], A. Beyer [a], L. Tapfer [c], K. Volz [a], W. Stolz [a,b]

[a] Materials Science Center and Faculty of Physics, Philipps-University Marburg, Germany
[b] NAsP III/V GmbH, Marburg, Germany
[c] ENEA Brindisi Research Center, Brindisi, Italy

ARTICLE INFO

Article history:
Received 10 September 2015
Received in revised form
21 December 2015
Accepted 22 December 2015
Communicated by: C. Caneau
Available online 30 December 2015

Keywords:
A3. Metalorganic vapor phase epitaxy
B1. Dilute nitrides
B2. Semiconducting III–V materials
B3. Laser diodes

ABSTRACT

High-quality, pseudomorphically strained Ga(NAsP)/(BGa)(AsP)-multiple quantum well heterostructures (MQWH) have been deposited on exactly oriented (001) Si-substrate by metal organic vapour phase epitaxy (MOVPE) in a wide temperature range between 525 °C and 700 °C. The individual atomic incorporation efficiencies, growth rates as well as nanoscale material properties have been clarified by applying detailed high-resolution X-ray diffraction (HR-XRD), photoluminescence (PL) spectroscopy and high-angle annular dark field (HAADF) scanning transmission electron microscopy (STEM) studies. An almost constant N-incorporation efficiency is obtained for a wide growth temperature range from 550 °C up to 650 °C. The P-incorporation is steadily increasing with increasing growth temperature reaching values at high temperatures in excess of the applied gas phase ratio. While the lower interface from the binary GaP- to the quaternary Ga(NAsP)-material system is very sharp, the upper interface is significantly rougher with a roughness scale of ± 0.43 nm in quantum well thickness variation at a growth temperature of 525 °C. This roughness scale increases steadily with increasing growth temperature. No indication of any phase separation effects is detected in the Ga(NAsP)-material system even at the highest growth temperature of 700 °C. The obtained experimental results are briefly discussed with respect to the anticipated metastable character of the novel dilute-nitride Ga(NAsP)-material system grown lattice-matched to (001) Si-substrate.

1. Introduction

The realization of efficient and stable laser materials on (001) Si-substrates is of key importance for future application in Si-based optoelectronic (OEIC) and photonic integrated circuits (PIC). Various concepts have been evaluated in the last decades. At present the first device structures based on hybrid integration concepts applying flip-chip die and wafer bonding techniques have been studied in detail [1]. Also a variety of Si-based nanostructure concepts have been suggested [2,3] although no electrical injection laser performance has been reported up to now. The heteroepitaxial integration of standard III/V-materials systems has led to the successful report of both edge- as well as surface emitting GaAs-based laser devices even at a very early stage of these attempts [4,5,6]. Due to the large difference in lattice-constant between Si and the standard III/V-based laser devices composed of GaAs-, InP or GaN-based laser materials, however, no really long-term stable laser operation could be achieved so far [7]. The longest lifetime for a (GaIn)(PAs)/InP-laser on Si-substrate reported to date amounts to 2000 h with a continuous wave (cw) operation of 2 mW at room temperature [8]. However, for laser devices in i.e. telecommunications applications much higher requirements (cw operation up to 10 mW in a temperature range up to 85 °C with lifetimes on the order of 10^4 h) are necessary. These characteristics have not been reported for any hetero-epitaxial laser material system to date.

This behaviour is due to the large number of threading dislocations present in the active laser layers caused by the necessary heteroepitaxial strain-relaxation process. These threading dislocations lead to the formation of dark line defects, which are the

* Corresponding author at: Materials Science Center and Faculty of Physics, Philipps-University Marburg, Germany.
E-mail address: peter.ludewig@physik.uni-marburg.de (P. Ludewig).

http://dx.doi.org/10.1016/j.jcrysgro.2015.12.024
0022-0248/

cause of the limited lifetime of these devices [9]. The GaSb-based lasers [10], strained Ge- [11], GeSn- [12] or III/V-quantum dot concepts [13,14] suggested later are also plagued by the high densities of remaining threading dislocations. In contrast to all of these approaches, we have suggested the Ga(NAsP)-direct band gap material system [15], which for a specific range of compositions can be grown lattice-matched to (001) Si-substrate, completely avoiding the formation of dislocations [16]. Recently, highly efficient Ga(NAsP)-quantum well heterostructures (QWH) [17] as well as the first electrical injection lasers have been reported both on GaP (with operation up to room temperature [18]) as well as on (001) Si-substrate (with operation at low temperatures [19]), clearly pointing to the high potential of the Ga(NAsP)-material system for future applications in Si-OEIC and Si-PIC.

The detailed evaluation and understanding of the epitaxial growth conditions to realize high-quality Ga(NAsP)-MQWH is a key prerequisite for the future application of this novel laser material system. Typically, dilute nitride material systems, i.e. (GaIn)(NAs)/GaAs-MQW on GaAs-substrate are very sensitive to the growth temperature due to their metastable character. First reports in the limited temperature range of 525 °C to 575 °C indicate that the N-incorporation is significantly more efficient in the Ga(NAsP)-material system on GaP-substrate [20] than in dilute nitrides on GaAs substrates. In this study, we have investigated the metal organic vapour phase epitaxy (MOVPE) growth conditions, and in particular the growth temperature dependence, of Ga (NAsP)-MQWH on (001) Si-substrate over the extremely large temperature range of 525–700 °C. The Ga(NAsP)-MQWH have been characterized by a variety of both structural (high-resolution X-ray diffraction (HR-XRD), atomic force microscopy (AFM) and various transmission electron microscopy (TEM) techniques) as well as spectroscopic (photoluminescence (PL)) methods. New insights on the characteristics of Ga(NAsP)-MQWH are obtained with respect to the incorporation efficiencies of the respective group-V-elements as well as the interface properties in this dilute-nitride quaternary MQWH material system as a function of the MOVPE growth conditions, i.e. surprisingly only a minor temperature dependence of the N-incorporation is observed over this large growth temperature range.

This paper is organized as follows: the experimental conditions (MOVPE growth parameters as well as the different investigation techniques) are summarized in Section 2. Section 3 (Results and Discussions) first describes the HR-XRD- and PL-studies to determine the chemical composition of the quaternary Ga(NAsP)-MQWH as well as the characteristic growth rates of all of the constituent materials as a function of MOVPE conditions. Then the first results with respect to the interface formation as studied by real atomic scale resolution TEM-analysis are presented. The obtained experimental results are discussed with respect to the metastable character of the dilute-nitride Ga(NAsP)-material system. Finally, the most important results of this study are summarized in Section 4.

2. Experimental conditions

The Ga(NAsP)/(BGa)(AsP)-MQWH-based epitaxial layer stacks have been deposited by MOVPE in a commercial horizontal reactor system (Aixtron Aix200-gas foil rotation (GFR) reactor system) at a reactor pressure of 50 mbar under H_2-carrier gas for different growth temperatures in the range of 525–700 °C. All other parameters such as the partial pressures of the sources and growth times have been held constant. The actual growth temperature has been obtained by calibrating the thermocouple reading to the surface temperature of the Al/Si-eutectic formation at 577 °C. As source molecules the more efficiently decomposing group-V-

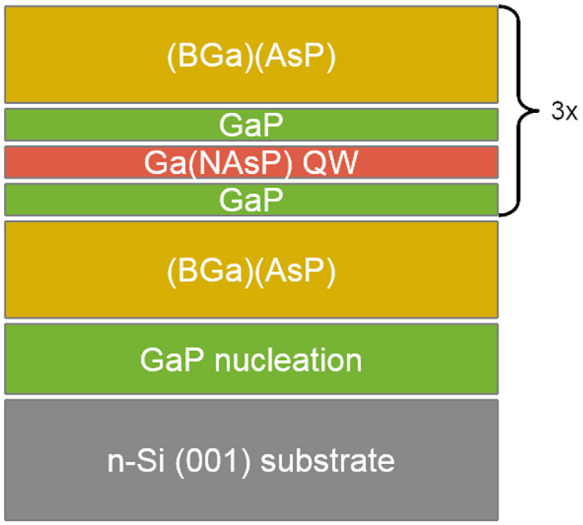

Fig. 1. Schematic layer sequence of the investigated (Ga(NAsP)/(BGa)(AsP)-MQWH grown by MOVPE on a GaP-on-Si-template on exactly oriented (001) Si-substrate ($\pm 0.5°$).

precursors tertiarybutylarsine (TBAs), tertiarybutylphosphine (TBP) and unsymmetrical 1,1-dimethylhydrazine (UDMHy), together with the standard group-III sources triethylgallium (TEGa) and triethylboron (TEB), have been used with a typical As/III-ratio of 15, As/(As+P)-ratio of 0.7 and a N/(As+P)-ratio of 8 for the Ga(NAsP)-growth unless otherwise stated. For the deposition of the Ga(NAsP)-QW-, the GaP-intermediate and the (BGa)(AsP)-barrier layers, an identical TEGa-partial pressure has been used. The MQWH layer stack has been grown lattice-matched on a GaP-on-Si-template structure [21] on exactly oriented Si (001) ($\pm 0.5°$) substrates. All MQWH-samples have been annealed after growth at 925 °C for 10 s in a rapid thermal annealing (RTA) process to improve the optical efficiencies. The schematic layer sequence of the triple QWH stack is indicated in Fig. 1. It is important to note that specific strain-compensation schemes have been applied in this study in order to obtain high-quality Ga(NAsP)/(BGa)(AsP)-MQWH [16]. All of the Ga (NAsP)-quantum well layers are compressively strained with strain values around 1–2%, as evaluated from the HR-XRD-analysis. Based on the strain-relaxation modelling in [22] the obtained epitaxial Ga (NAsP) layer thicknesses of around 5 nm are well below the estimated critical individual Ga(NAsP) layer thickness of around 10 nm for a compressive strain value of 2% [22]. For the chosen 3 period MQWH-layer stack it is, however, crucial to compensate the compressive strain of the Ga(NAsP)-layers by using tensile-strained (BGa)(AsP)-barrier layers, as can be seen by the inspection of the HR-XRD pattern in Fig. 4. In the design of this MQWH-layer stack the difference in the thermal expansion coefficients of the III/V-layers and the Si-substrate also has to be taken into account [16]. The chemical composition of the (BGa)(AsP) is chosen to result in a tensile-strain value of around 0.3% at room temperature, when grown at 575 °C. This tensile strain value as well as the chosen layer thickness of the (BGa)(AsP) of around 80 nm guarantee that the entire MQWH-layer stack is still strain-compensated within the limits of the critical residual integral strain of the MQWH-layer stack at the respective growth temperature [16]. Thin GaP-interlayers in between the Ga(NAsP)-QW and the (BGa)(AsP)-barrier layers have been included to avoid direct bonding configurations of B and N which presumably lead to the formation of non-radiative recombination centers [23].

The Ga(NAsP)/(BGa)(AsP)-MQWHs have been analysed by HR-XRD, using a Panalytical X´Pert materials research diffractometer around the (004)-reflection of Si. The obtained HR-XRD-patterns are modelled using full dynamical XRD theory as detailed in

[24,25]. The PL studies have been performed in a home-built spectroscopy set-up using an Ar-ion laser at an excitation wavelength of 514.5 nm. Typical excitation powers of 100 mW in a spot size of about 200 μm have been used. The PL-signal has been dispersed by a 1 m grating monochromator (Jobin-Yvon) and detected by a Ge-detector, applying standard lock-in techniques. The samples have been mounted in a variable temperature cryostat held at room temperature for the PL-studies reported here. The chemical composition of the grown Ga(NAsP)-QW layer is evaluated by combining HR-XRD- and PL-studies, with absolute error bars of ±1% for the N- and of ±5% for the P-contents, respectively, by applying a procedure described elsewhere [26]. The TEM-analysis has been performed in a double-aberration-corrected microscope (Jeol JEM 2200FS) applying the high-angle annular dark-field (HAADF) scanning TEM technique after specific sample thinning procedures as summarized elsewhere [27].

3. Results and discussions

In different growth runs we have deposited Ga(NAsP)/(BGa)(AsP)-MQWHs according to the schematic layer sequence shown in Fig. 1 for growth temperatures varying in the wide range of 525–700 °C. The other growth parameters (group-III-partial pressures, As/III-, As/(As+P)- as well as N/(As+P)-ratios) have been kept constant as given in Section 2. The HR-XRD patterns of selected samples around the (004) reflection of Si are shown in Fig. 2 for MOVPE growth temperatures of 525 °C, 575 °C, 605 °C, 650 °C and 700 °C, respectively. The XRD-patterns in Fig. 2 are offset in *y*-axis for clarity. The HR-XRD-signatures of the Si-substrate, of the GaP-nucleation layer, of the intentionally tensile-strained (BGa)(AsP)-barriers as well as of the compressively strained Ga(NAsP)-QW layers are clearly visible. In the entire growth temperature range high-quality Ga(NAsP)/(BGa)(AsP)-MQWHs have been realized. While the Ga(NAsP) QW layers are compressively strained for the entire investigated growth temperature range, the strain compensating (BGa)(AsP)-barriers are tensile-strained at room temperature for the growth temperature range of 550–675 °C. For the highest deposition temperature of 700 °C the (BGa)(AsP) is lattice-matched at room temperature,

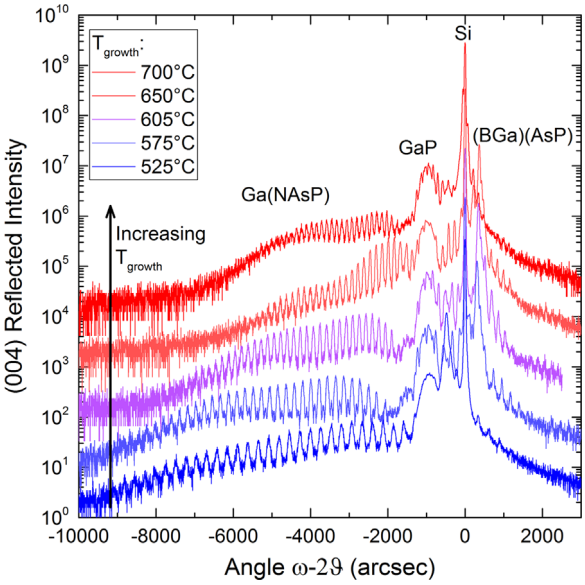

Fig. 2. High-resolution X-ray diffraction (HR-XRD) pattern around the (004) reflection of Si (001) substrate of Ga(NAsP)/(BGa)(AsP)-MQWH for MOVPE growth temperatures of 525 °C, 575 °C, 605 °C, 650 °C and 700 °C, respectively. The individual HR-XRD patterns are shifted on the intensity scale for clarity.

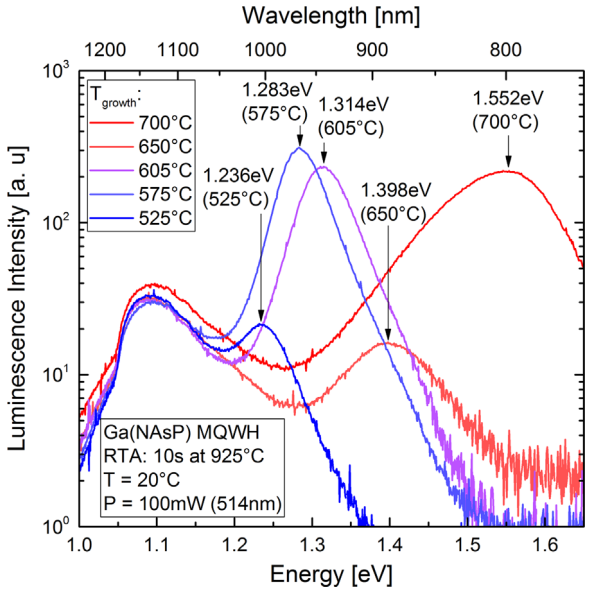

Fig. 3. Photoluminescence spectra of Ga(NAsP)/(BGa)(AsP)-MQWH for MOVPE growth temperatures of 525 °C, 575 °C, 605 °C, 650 °C and 700 °C, measured at room temperature.

which implies that this layer is slightly compressively strained at growth temperature due to the difference in thermal expansion coefficient with respect to the (001) Si-substrate. At the lowest growth temperature of 525 °C the (BGa)(AsP) layer is compressively strained at room temperature as well as at this growth temperature.

For all samples PL studies at room temperature have been performed. The PL spectra of samples grown at 525 °C, 575 °C, 605 °C, 650 °C and 700 °C are summarized in Fig. 3. It is important to note that only the Ga(NAsP)-QW layers are direct semiconductor materials, while all the other constituent layers are indirect semiconductors. This implies that only several percent of the exciting photons are absorbed in the thin QW material, while most of the photons are absorbed in the thick Si-substrate. The relatively weak PL signal from the Si-substrate is observed at an energy of 1.1 eV for all samples, with a comparable intensity. Depending on the chemical composition of the direct band gap Ga(NAsP)-QW, the strong Ga(NAsP)-QW PL-signal is observed at emission energies spanning the range from 1.24 eV to 1.55 eV. Thus, these Ga(NAsP)-QWHs are covering the entire extended data communications wavelength range from 850 nm to 960 nm and beyond.

The obtained crystalline perfection allows for a detailed analysis of the MQWH layer stack by full dynamical XRD-modelling applying the model described in [24,25]. The comparison of an experimental and a theoretical HR-XRD pattern is depicted in Fig. 4 for a growth temperature of 605 °C obtaining a very good overall agreement. From this analysis the precise strain-state of the constituent layers as well as the individual layer thicknesses can be evaluated. In conjunction with room temperature PL-investigations, yielding the emission wavelength and, thus, the direct energy gap of the deposited MQWH when taking quantization effects into account, the individual chemical compositions of the quaternary Ga(NAsP)-QW layers can be determined [26]. From this analysis the Ga(NAsP) QW grown at 605 °C has a width of 5.3 nm with concentrations of [N]=8.3% (±1%) and [P]=18.8% (±5%). The other obtained analysis results are given in the inset of Fig. 4 for this particular MQWH sample. It is important to note that the strain-state of the Ga(NAsP)-QW layer can be determined quite precisely by HR-XRD, while the separation in the constituent N- and P-concentrations is more ambiguous, leading to the given

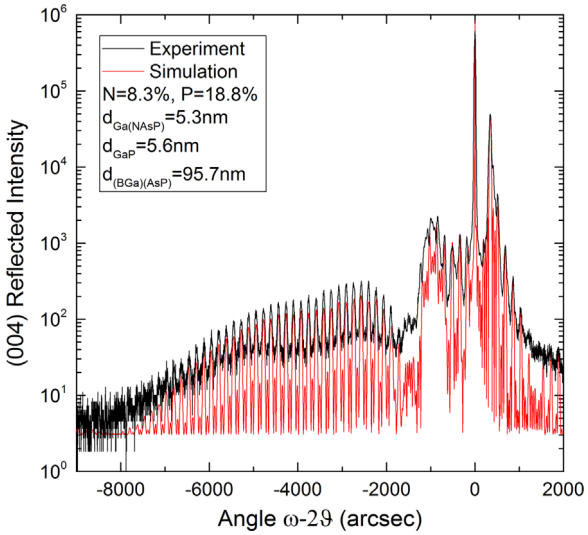

Fig. 4. Comparison of experimental and theoretical HR-XRD patterns around the (004) reflection of the Si (001) substrate of Ga(NAsP)/(BGa)(AsP)-MQWH for an MOVPE growth temperature of 605 °C.

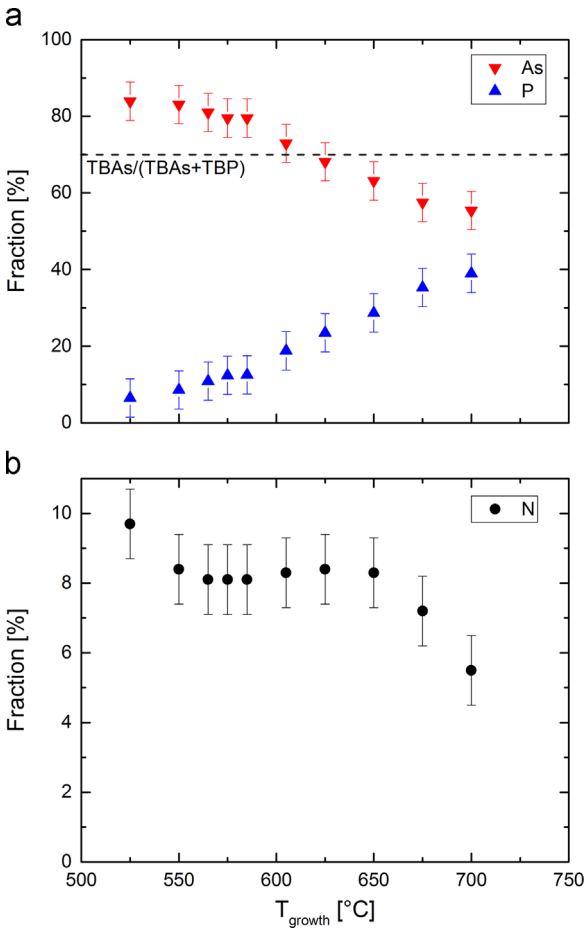

Fig. 5. Evaluated chemical compositions of the Ga(NAsP)-QW material as a function of MOVPE growth temperature.

estimated errors bars for the quaternary Ga(NAsP) material system. Well width fluctuations, as they will be determined later by detailed HAADF-STEM-analysis for the different samples, also contribute to the estimated error bars, even though they are of minor importance compared to the strong impact of N on the Ga (NAsP) band gap. The combination of HR-XRD- and PL-analyses has been performed for all the deposited layer stacks in the entire growth temperature range. The obtained analysis results are summarized in the following diagrams. The chemical composition of the Ga(NAsP)-QW layers as a function of the MOVPE growth temperature is depicted in Fig. 5. At a low deposition temperature of 525 °C the N- and P-contents are 9.7% and 6.5%, respectively, leading to an As-concentration of 83.8% for the chosen growth parameters. With increasing growth temperature, while keeping all other MOVPE parameters constant, surprisingly for a dilute-nitride material system the N-content shows only a minor change with increasing growth temperature, while the P-content increases steadily to a value of 39% and the As-concentration decreases to a value of 55% at the highest chosen deposition temperature of 700 °C. It is important to note that the As-concentration decreases to well below the relative value of the As/(As+P)-ratio of 70% in the solid which would result from an As/(As+P)-gas phase ratio of 0.7 in the case where both precursor molecules TBAs and TBP would be thermally decomposed completely. We will come back to this point later, when we discuss the anticipated metastable character of the Ga(NAsP)-material system.

The N-incorporation efficiency during MOVPE-growth is constant for a very wide range of deposition temperatures in between 550 °C and 650 °C. This surprising effect is of great importance for the reproducible and long scale homogeneous incorporation of N in Ga(NAsP)-layers in particular for the application in large-scale production reactors with deposition on state-of-the-art, large diameter 300 mm Si (001) wafers. The obtained N-concentration in the quaternary Ga(NAsP)-material on Si-substrate, plotted in an Arrhenius-diagram, is summarized in Fig. 6 together with the data obtained for ternary Ga(NAs) on GaAs- as well as Ga(NP) on GaP-substrate in the same reactor using the same precursors [20]. The input V/III- as well as N/V-ratios are given in the description of Fig. 6. Apparently the N-incorporation in the compressively strained Ga(NAsP)-material system is by far more stable as compared to the tensile-strained Ga(NAs)/GaAs- as well as the tensile-strained Ga(NP)/GaP-materials systems. In the present case of Ga (NAsP), only for the very high deposition temperatures in excess of 650 °C is a slight decline in the N-incorporation observed. It is important to note that for the Ga(NAs)/GaAs- and Ga(NP)-materials systems the tensile strain is increased with increasing

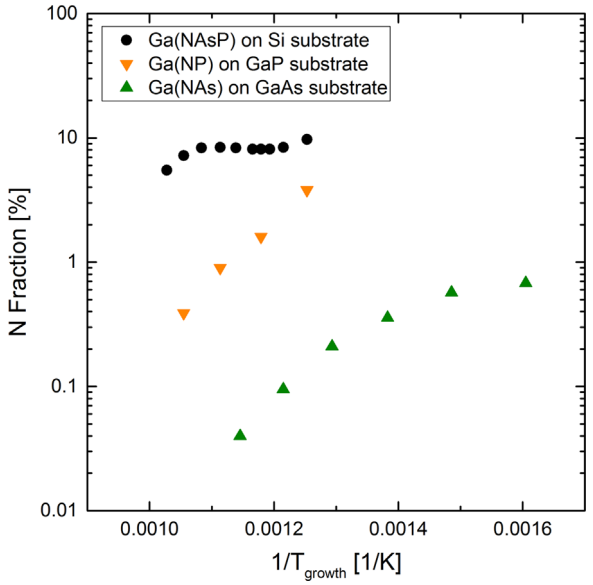

Fig. 6. Arrhenius-diagram of the N-concentration of the Ga(NAsP)-QW material as a function of MOVPE growth temperature including data for Ga(NAs)/GaAs-(UDMHy/TBAs=1, TBAs/TEGa=10) and Ga(NP)/GaP-material (UDMHy/TBP=1, TBP/TEGa=10) obtained in the same reactor system from Ref. [20].

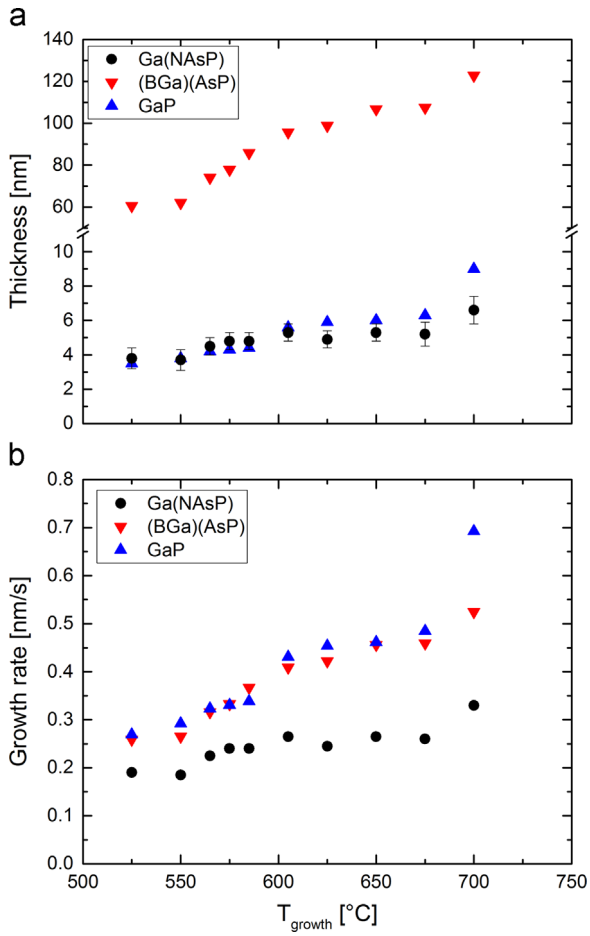

Fig. 7. Layer thicknesses (a) as well as growth rates (b) of the individual constituent Ga(NAsP)-, GaP- and (BGa)(AsP)-layers in Ga(NAsP)/(BGa)(AsP)-MQWH as a function of MOVPE growth temperature.

N-incorporation, while for the Ga(NAsP)-materials system on Si-substrate for the chosen high As-concentrations the compressive strain is reduced with increasing N-content. This observation clearly points to the importance of the actual epitaxial layer strain for the atomic incorporation efficiencies in the Ga(NAsP) mixed crystalline materials system.

In addition to the analysis of the chemical composition, the individual epitaxial layer thicknesses can be obtained from the HR-XRD-modelling. The thicknesses of the Ga(NAsP)-QW-layer, the GaP-interlayer and the (BGa)(AsP)-barrier as a function of the MOVPE growth temperature are summarized in Fig. 7(a). With increasing deposition temperature a slight increase in the epitaxial layer thickness is observed for all constituent materials. This behaviour is shown in Fig. 7(b) for the evaluated growth rates of the constituent materials as a function of the growth temperature. Similar growth rates are obtained for the GaP- as well as the (BGa)(AsP)-layers for identical partial pressures of the growth rate dominating group-III-sources TEGa and TEB. The growth rate of Ga(NAsP) is consistently smaller compared to those of GaP or (BGa)(AsP) for the same input partial pressure of TEGa, presumably due to the changes in the actual carrier gas phase in the vicinity of the epitaxial layer surface due to the decomposition of the N-source UDMHy used in relatively high amounts for the N/(As+P)-ratio of 8 in the present experiments. This reduction in growth rate as a function of the UDMHy-partial pressure has also been reported for the MOVPE growth of other dilute-nitride systems, i.e. (GaIn)(NAs) [28].

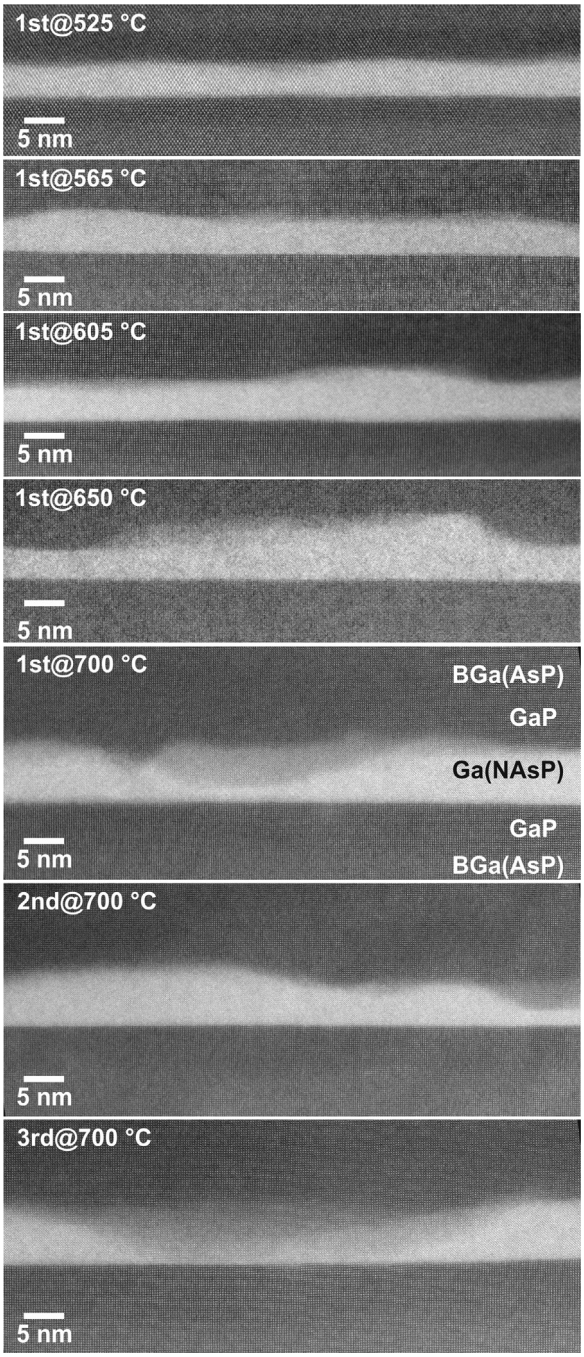

Fig. 8. High-angle annular dark field (HAADF) scanning transmission electron microscopy (STEM) micrographs in [010]-viewing direction of the first Ga(NAsP)-QW layer in Ga(NAsP)/GaP/(BGa)(AsP)-MQWH for MOVPE growth temperatures of 525 °C, 565 °C, 605 °C, and 650 °C, respectively, as well as all three QWs for the growth temperature of 700 °C.

In the following, the first results from a detailed structural analysis of the grown epitaxial layer stacks by different TEM-techniques, in particular applying HAADF-STEM-studies [27], are presented. The HAADF-STEM-micrographs of the first Ga(NAsP)-QW layer of the studied Ga(NAsP)/(BGa)(AsP)-MQWH layer stacks are grouped in Fig. 8 for deposition temperatures of 525 °C, 565 °C, 605 °C, 650 °C and 700 °C. Common to all Ga(NAsP)-QW layers is a high-quality abrupt interface from the GaP-interlayer to the Ga(NAsP)-material, hence, the GaP surface must be flat. This is not only true for the first QW, but also for the following two, even for the roughest QWs deposited at 700 °C (Fig. 8). The GaP and (BGa)

(AsP) layers flatten the surface on top of the QWs so that all three QW have the same scale in roughness.

For low deposition temperatures of 525 °C GaP-biatomic layer steps are detected. With increasing growth temperature the GaP-island size during MOVPE-growth is increasing, thus leading to a larger step separation at the interface from GaP to Ga(NAsP). The second common feature in all analysed samples is the homogeneous contrast of the Ga(NAsP)-QW layers pointing to a relatively homogeneous incorporation of all elements in growth direction as well as in lateral dimensions in these layers. Detailed HAADF-STEM studies in conjunction with sophisticated modelling procedures are underway to quantitatively determine the chemical homogeneity as well as any fluctuations in composition beyond intrinsic statistical alloy fluctuations of the Ga(NAsP)-layers. It is important to note, however, that no phase separation effects of the chemical composition in the Ga(NAsP)-material are detected even at the very high deposition temperature of 700 °C.

With increasing MOVPE growth temperatures, however, a distinct roughening of the Ga(NAsP)-QW material and, thus, an increase in Ga(NAsP)-QW width variation is clearly detected. For the highest deposition temperature of 700 °C the formation of pyramidal structures is even observed. By analysing a large number of HAADF-STEM micrographs of all three QWs of the studied Ga(NAsP)-MQWH-samples an evaluation of the average well width as well as the roughness of the upper interface is obtained. These data are summarized in Fig. 9 for the average well width (Fig. 9(a)) and the roughness evaluation of the upper interface (Fig. 9(b)) as a function of the MOVPE-growth temperature. In

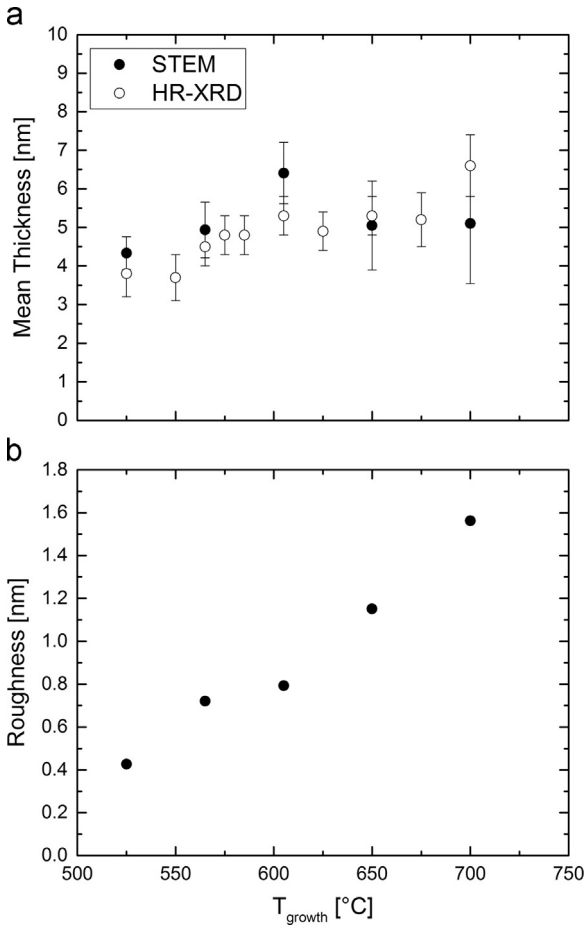

Fig. 9. Evaluated average Ga(NAsP)-QW width (a) for HAADF-STEM- as well as HR-XRD-analysis as well as (b) roughness determination of the upper interface of Ga(NAsP)-QW layers in Ga(NAsP)/(BGa)(AsP)-MQWH as a function of MOVPE growth temperature.

Fig. 9(a) the evaluated well width data from the analysis of the HR-XRD-pattern (as shown and discussed already in conjunction with Fig. 7(a)) are included together with the HAADF-STEM data. Within the uncertainties of the two analysis techniques, the evaluated well width data coincide with one another. It is important to note that HR-XRD, as an integral structural analysis technique, determines the average well width in the respective sample. The roughness of the upper interface amounts to ± 0.43 nm at a growth temperature of 525 °C and increases steadily to a value of ± 1.56 nm for a deposition temperature of 700 °C. For low deposition temperatures the well width fluctuations are in a reasonable range. In future experiments, these well width fluctuations have to be reduced significantly, in particular when applying high deposition temperatures for the Ga(NAsP)-QW layers, as these strong well width fluctuations will lead to non-tetragonal distortions in these strained layers. These non-tetragonal distortions might introduce inhomogeneous, in-plane piezo-electric fields, which would be detrimental in particular for the optoelectronic properties of these MQWHs.

Finally, we would like to briefly discuss the experimental observations with respect to the anticipated metastable character of the Ga(NAsP)-material system grown pseudomorphically strained on Si (001) substrate. The puzzling experimental facts are that i) no phase separation effects in the Ga(NAsP) alloy composition are observed even at the very high growth temperature of 700 °C, ii) the N-incorporation efficiency is almost independent of temperature in an extremely wide temperature range and iii) the As-incorporation efficiency drops significantly below the estimated gas phase ratio, assuming the complete decomposition of the used TBAs and TBP source molecules. All of these observations would be more consistent with the assumption that the Ga(NAsP)-material system would be thermodynamically stable in the investigated composition range also taking the pseudomorphic deposition on the Si-substrate into account.

4. Conclusions

High-quality Ga(NAsP)/(BGa)(AsP)-MQWHs have been deposited pseudomorphically strained on exactly oriented (001) Si-substrate by MOVPE in the wide temperature range of 525–700 °C. Subsequently the MQWHs have been evaluated by HR-XRD, PL-spectroscopy as well as nano-analytical HAADF-STEM. The characteristic incorporation efficiencies of the constituent group-V-elements as well as the different growth rates of the individual layers have been clarified. Surprisingly, an almost constant N-content of 8% in the slightly compressively strained Ga(NAsP) on (001) Si-substrate is observed over a wide temperature range up to 650 °C. In contrast, the P-incorporation efficiency is steadily increasing with increasing deposition temperature reaching values distinctively larger than the input As/(As+P)-ratio. Analysis of the HAADF-STEM photographs yields the same (average) QW width as HR-XRD fitting. The nanoscale material characterization reveals that the lower interface from the binary GaP to the quaternary Ga(NAsP)-QW layer is rather abrupt, while the upper interface is significantly rougher. For the low deposition temperature of 525 °C a roughness scale of the upper Ga(NAsP)-interface of ± 0.43 nm is obtained, which increases steadily for higher temperatures, reaching a value of ± 1.56 nm at 700 °C for the chosen MOVPE-growth conditions. This upper interface roughness has to be improved in the future in particular if high growth temperatures are chosen for the intended laser device applications. It is interesting to note that no indication for any phase separation effects is detected by HAADF-STEM analysis even at the very high temperature of 700 °C for the Ga(NAsP)-material system. These experimental findings may be consistent with the

assumption that the Ga(NAsP)-material system becomes a stable material system in the studied composition and temperature range for the pseudomorphic epitaxial growth on (001) Si-substrate, rather than being of metastable character, which is anticipated for the dilute nitride materials in particular at the high N-concentrations around 8%. This interpretation has to be clarified, however, by detailed total energy calculations of this novel Ga(NAsP)-material system.

Acknowledgments

This work has been supported by the German Science Foundation (DFG) within the Research Training Group GRK 1782 “Functionalization of semiconductors”.

References

[1] A.W. Fang, H. Park, C. Oded, R. Jones, M.J. Paniccia, J.E. Bowers, Opt. Expr. 14 (2006) 9203, http://dx.doi.org/10.1109/LPT.2006.874690.
[2] S.S. Iyer, Y.H. Xie, Science 260 (1993) 40, http://dx.doi.org/10.1126/science.260.5104.40.
[3] D.J. Lockwood, L. Pavesi, Silicon Photonics, Springer, Berlin, Heidelberg (2004) http://dx.doi.org/10.1007/b11504.
[4] H.Z. Chen, A. Ghaffari, H. Wang, H. Morkoc, A. Yariv, Opt. Lett. 12 (1987) 812, http://dx.doi.org/10.1364/OL.12.000812.
[5] T. Egawa, H. Tada, Y. Kobayashi, T. Soga, T. Jimbo, M. Umeno, Appl. Phys. Lett. 57 (1990) 1179, http://dx.doi.org/10.1063/1.103519.
[6] D.G. Deppe, N. Chand, J.P. van der Ziel, G.J. Zydzik, Appl. Phys. Lett. 56 (1990) 740, http://dx.doi.org/10.1063/1.102698.
[7] H.K. Choi, C.A. Wang, N.H. Karam, Appl. Phys. Lett. 59 (1991) 2634, http://dx.doi.org/10.1063/1.105921.
[8] M. Sugo, H. Mori, Y. Sakai, Y. Itoh, Appl. Phys. Lett. 60 (1992) 472, http://dx.doi.org/10.1063/1.106638.
[9] T. Egawa, T. Jimbo, Y. Hasegawa, M. Umeno, Appl. Phys. Lett. 64 (1994) 1401, http://dx.doi.org/10.1063/1.111896.
[10] R. Reboul, L. Cerutti, J.B. Rodriguez, P. Grech, E. Tournie, Appl. Phys. Lett. 99 (2011) 121113, http://dx.doi.org/10.1063/1.3644983.
[11] R.E. Camacho-Aguilera, Y. Cai, N. Patel, J.T. Bessette, M. Romagnoli, L. C. Kimerling, J. Michel, Opt. Expr. 20 (2012) 11316, http://dx.doi.org/10.1364/OE.20.011316.
[12] S. Wirths, R. Geiger, N. von den Driesch, G. Mussler, T. Stoica, S. Mantl, Z. Ikonic, M. Luysberg, S. Chiussi, J.M. Hartmann, H. Sigg, J. Faist, D. Buca, D. Grützmacher, Nat. Photon. 9 (2015) 88–92, http://dx.doi.org/10.1038/NPHOTON.2014.321.
[13] J. Yang, P. Bhattacharya, Z. Mi, IEEE Trans. Electron Devices 54 (2007) 2849, http://dx.doi.org/10.1109/TED.2007.906928.
[14] A. Lee, Q. Jiang, M. Tang, A. Seeds, H. Liu, Opt. Expr. 20 (2012) 22181, http://dx.doi.org/10.1364/OE.20.022181.
[15] B. Kunert, K. Volz, J. Koch, W. Stolz, Appl. Phys. Lett. 88 (2006) 182108, http://dx.doi.org/10.1063/1.2200758.
[16] B. Kunert, S. Zinnkann, K. Volz, W. Stolz, J. Cryst. Growth 310 (2008) 4776, http://dx.doi.org/10.1016/j.jcrysgro.2008.07.097.
[17] N. Rosemann, B. Metzger, B. Kunert, K. Volz, W. Stolz, S. Chatterjee, Appl. Phys. Lett. 103 (2013) 252105, http://dx.doi.org/10.1063/1.4852575.
[18] N. Hossain, S.J. Sweeney, S. Rogowski, R. Ostendorf, J. Wagner, S. Liebich, M. Zimprich, K. Volz, B. Kunert, W. Stolz, Electron. Lett. 47 (2011) 931, http://dx.doi.org/10.1049/el.2011.1927.
[19] S. Liebich, M. Zimprich, A. Beyer, K. Volz, B. Kunert, W. Stolz, C. Lange, S. Chatterjee., N. Hossain, S.J. Sweeney, Appl. Phys. Lett. 99 (2011) 071109, http://dx.doi.org/10.1063/1.3624927.
[20] B. Kunert, K. Volz, J. Koch, W. Stolz, J. Cryst. Growth 298 (2007) 121, http://dx.doi.org/10.1016/j.jcrysgro.2006.10.013.
[21] K. Volz, A. Beyer, W. Witte, J. Ohlmann, I. Nemeth, B. Kunert, W. Stolz, J. Cryst. Growth 315 (2011) 37, http://dx.doi.org/10.1016/j.jcrysgro.2010.10.036.
[22] P.M.J. Maree, J.C. Barbour, J.F. van der Veen, K.L. Kavanagh, C.W.T. Bulle-Lieuwma, M.P.A. Viegers, J. Appl. Phys. 62 (1987) 4413.
[23] B. Kunert, S. Liebich, A. Beyer, R. Fritz, S. Zinnkann, K. Volz, W. Stolz, J. Cryst. Growth 315 (2011) 28, http://dx.doi.org/10.1016/j.jcrysgro.2010.07.068.
[24] L. Tapfer, K. Ploog, Phys. Rev. B40 (1989) 9802, http://dx.doi.org/10.1103/PhysRevB.40.9802.
[25] L. De Caro, C. Giannini, L. Tapfer, J. Appl. Phys. 79 (1996) 4101, http://dx.doi.org/10.1063/1.361773.
[26] K. Jandieri, P. Ludewig, T. Wegele, A. Beyer, B. Kunert, P. Springer, S. D. Baranovskii, S.W. Koch, K. Volz, W. Stolz, J. Appl. Phys. 118 (2015) 065701, http://dx.doi.org/10.1063/1.4928331.
[27] T. Wegele, A. Beyer, P. Ludewig, P. Rosenow, L. Duschek, K. Jandieri, R. Tonner, W. Stolz, K. Volz, J. Phys. D: Appl. Phys. (Accepted: 22 December 2015).
[28] K. Volz, J. Koch, F. Höhnsdorf, B. Kunert, W. Stolz, J. Cryst. Growth 311 (2009) 2418, http://dx.doi.org/10.1016/j.jcrysgro.2008.09.210.

6.4 Interface morphology and composition of Ga(NAsP) quantum well structures for monolithically integrated LASERs on silicon substrates [1]

T. Wegele, A. Beyer, P. Ludewig, P. Rosenow, L. Duschek, K. Jandieri, R. Tonner, W. Stolz and K. Volz, Journal of Physics D: Applied Physics **49** (2016) 075108. DOI:10.1088/0022-3727/49/7/075108.

Abstract

Highly efficient light sources are the remaining item required for the realization of opto-electronically integrated circuits on exactly oriented Si (0 0 1).
Here, we present – using transmission electron microscopy – an investigation on the structure and stability of Ga(NAsP), which is a direct band gap semiconductor. It is shown that Ga(NAsP) can be grown on Si (0 0 1) substrates at a wide range of growth temperatures. No sign of defect formation and phase separation is observed even for the highest growth temperatures used. The interfaces of the quaternary alloys with the GaP barriers roughen significantly with increasing growth temperature. On the contrary, the material deposited at high temperatures is more homogeneous than the one deposited at low temperatures. This is highly surprising as dilute nitride III/V alloys are commonly thought to be metastable. This is resolved by density functional theory calculations, which show that Ga(NAsP) becomes significantly more stable when grown on substrates which have a smaller lattice constant than the equilibrium lattice constant of the alloy. This stability together with the strong room temperature photoluminescence shown by all samples, make the Ga(NAsP) material system highly promising for laser applications on Si substrates.

My contribution

The TEM specimens of all samples mentioned in this publication were prepared and investigated using STEM by me. Moreover, I performed the quantitative determination of the interface roughness and compositional fluctuation using a self-written MATLAB script. I performed the analysis of most results and wrote the first draft of the manuscript.

1 Reprinted from *Journal of Physics D: Applied Physics **49** (2016) 075108*

IOP Publishing Journal of Physics D: Applied Physics

J. Phys. D: Appl. Phys. **49** (2016) 075108 (9pp) doi:10.1088/0022-3727/49/7/075108

Interface morphology and composition of Ga(NAsP) quantum well structures for monolithically integrated LASERs on silicon substrates

Tatjana Wegele[1], Andreas Beyer[1], Peter Ludewig[1], Phil Rosenow[2], Lennart Duschek[1], Kakhaber Jandieri[1], Ralf Tonner[2], Wolfgang Stolz[1] and Kerstin Volz[1]

[1] Faculty of Physics and Materials Science Center, Philipps-Universität Marburg, 35032 Marburg, Germany

[2] Faculty of Chemistry and Materials Science Center, Philipps-Universität Marburg, 35032 Marburg, Germany

E-mail: kerstin.volz@physik.uni-marburg.de

Received 17 November 2015, revised 15 December 2015
Accepted for publication 22 December 2015
Published 14 January 2016

Abstract

Highly efficient light sources are the remaining item required for the realization of optoelectronically integrated circuits on exactly oriented Si(0 0 1).

Here, we present—using transmission electron microscopy—an investigation on the structure and stability of Ga(NAsP), which is a direct bandgap semiconductor. It is shown that Ga(NAsP) can be grown on Si(0 0 1) substrates at a wide range of growth temperatures. No sign of defect formation and phase separation is observed even for the highest growth temperatures used. The interfaces of the quaternary alloys with the GaP barriers roughen significantly with increasing growth temperature. On the contrary, the material deposited at high temperatures is more homogeneous than the one deposited at low temperatures. This is highly surprising as dilute nitride III/V alloys are commonly thought to be metastable. This is resolved by density functional theory calculations, which show that Ga(NAsP) becomes significantly more stable when grown on substrates which have a smaller lattice constant than the equilibrium lattice constant of the alloy. This stability together with the strong room-temperature photoluminescence shown by all samples, make the Ga(NAsP) material system highly promising for laser applications on Si substrates.

Keywords: Laser on Silicon, Ga(NAsP), transmission electron microscopy, density functional theory

S Online supplementary data available from stacks.iop.org/JPhysD/49/075108/mmedia.

(Some figures may appear in colour only in the online journal)

Introduction

Future applications in Si-based optoelectronic (OEIC) and photonic integrated circuits (PIC) require the realization of efficient and stable laser materials on exact (0 0 1) Si. Various concepts have been evaluated in the last decades. Hybrid integration concepts applying flip-chip die and wafer bonding techniques have been studied in detail [1]. Also a variety of Si-based nanostructure concepts have been suggested [2, 3] although no electrical injection laser performance has been reported up to now. The heteroepitaxial integration of standard III/V-materials systems has led to the successful report

of both edge- as well as surface emitting GaAs-based laser devices even at a very early stage of these attempts [4–6]. Due to the large difference in lattice-constant between Si and the standard III/V-based laser devices composed of GaAs-, InP or GaN-based laser materials, however, no really long-term stable laser operation could be achieved so far [7, 8]. More recently also the integration of GeSn alloys has been proven to be very promising as optically pumped lasing has been observed on Si substrates [9].

An especially promising approach to integrate a direct bandgap material on Si is the use of an active laser material which can be grown lattice-matched to Si substrates, as then dislocations, which destroy the long term stability of the lasing process, can be avoided. Ga(NAsP), which has a direct bandgap for As concentrations above around 80%, can be grown pseudomorphically strained on Si substrates [10, 11]. It has been shown recently, that Ga(NAsP)-quantum well heterostructures (QWH) have an internal quantum efficiency above 90% [12]. First electrical injection lasers have been reported on GaP-substrates up to room temperature [13]. On (0 0 1) Si-substrate lasing was observed at low temperatures [14], clearly pointing to the high potential of the Ga(NAsP)-material system for future applications in Si-OEIC and Si-PIC. Moreover, epitaxial growth of an optically active III/V material on Si-substrate allows to reduce the production costs in comparison to e.g. growth on GaAs-substrates.

From a more fundamental point of view the performance of OEIC devices and the quality of their active layers are very strongly connected. Ga(NAsP) is believed to be a metastable material, meaning that it has to be grown under extreme non-equilibrium conditions to incorporate sufficient amounts of nitrogen [15]. Nevertheless, structure formation processes and phase separation into the more stable alloys can occur when those growth conditions are applied. Here, we want to focus on two possible characteristics that can describe the quality of a layer, namely, its interface roughness and compositional fluctuation examined by scanning transmission electron microscopy (STEM) in annular dark field (ADF) mode. The roughness of optically active layers has an influence on electronic properties of the semiconductor materials, e.g. as there is a strong correlation between the interface roughness and electron mobility as shown in [16–18] for AlAs/GaAs, (AlGa)As/GaAs, Si/SiGe heterostructures. Furthermore, the optical properties of semiconductor materials suffer from the interface roughness due to broadening of electronic density of states as reported for example for Ga(NAs)/GaAs and GaAs/(AlGa)As [19, 20]. Therefore, interface roughness and composition fluctuations were chosen as indicators for optimization of growth conditions. These were varied in a wide range of quantum well thicknesses and growth temperatures. To explain the surprising experimental findings, strain relaxation and phase separation energies are computed by *ab initio* methods to quantify the usually assumed metastability of the Ga(NAsP) material class. This gives important insight in the thermodynamic stability of Ga(NAsP) grown on Si substrates and points towards an optimal amount of nitrogen to be incorporated for maximum stability.

Methods

The investigated Ga(NAsP)/GaP/(BGa)(AsP) multi-QWH were grown by metal organic vapour phase epitaxy (MOVPE) on GaP/Si templates, consisting of about 50 nm GaP-layers nucleated on exactly oriented (0 0 1) Si-substrates [21, 22] in a commercial Crius R 300 mm III/V-Si-cluster tool. The growth conditions are detailed in [15]. The schematic structure of the samples investigated here is depicted in figure S1 (stacks.iop.org/JPhysD/49/075108/mmedia).

A first set of samples was grown at 575 °C. For these samples nominal QW layer thicknesses of 1.5 nm, 3 nm, 5 nm, 8 nm and 10 nm were deposited under otherwise unchanged growth conditions. For a second set of samples the growth temperature was varied at a nominal QW thickness of 5 nm (calibrated at a growth temperature of 575 °C). The samples were grown—under otherwise unchanged conditions—at 525 °C, 565 °C, 605 °C, 650 °C and 700 °C, respectively. This resulted in N-contents in the QW of 10%, 7.5%, 8.2%, 8% and 5.1%, respectively. High resolution x-ray diffraction (HRXRD) measurements and dynamical simulation of the HRXRD profiles were performed to determine the strain and layer thickness [23]. From the strain, the composition was calculated using Vegard's law.

TEM specimens were prepared in [0 1 0] and [1 1 0/− 1 1 0] crystallographic directions conventionally: mechanical grinding until a thickness of 100 μm, polishing using diamond paste with a gain size of 3 and 1 μm respectively, using a dimpling grinder model 200 (Fischione Instruments) up to a final thickness of approximately 60 μm. The last preparation step was argon ion milling in a precision polishing system model 691 (Gatan).

Before inserting the specimen into the microscope it was cleaned by plasma cleaning (Plasma Cleaner Model 1020 Fischione Instruments) for 2 min to remove parasitic hydrocarbons.

The STEM investigation of the specimens was performed in a JEOL JEM 2200 FS with Schottky field emission gun, equipped with two Cs-correctors manufactured by CEOS GmbH. The microscope was operated at 200 kV. For data acquisition a EM-24590YPDFI YAP [24] ADF detector (JEOL) was used. The inner radius of the detector in pixels was measured as described in [25] and calibrated for different camera lengths of the microscope using the proportion to the shadow of the condenser lens aperture 3, which radius is known to be 24 mrad. The outer angle of the annular detector is 4 times larger than the inner one. However, it has to be taken into account that the microscope geometry restricts this outer acceptance angle to 170 mrad.

The imaging conditions, namely brightness and contrast values of the detector, were chosen so that, on the one hand, the entire dynamic range of the detector could be used as far as possible and, on the other hand, the saturation of the detector could be avoided for investigations of regions with somewhat varied specimen thicknesses and by changing of range of the detector angles. The beam dwell time was 20 μs or 40 μs per pixel, respectively, the image size was 1024 × 1024 pixels.

The variation of the inner angles (33, 59, 75 mrad) of the detector was undertaken in order to separate the measured signals of the individual components in Ga(NAsP). While for high detector angles the measured ADF-intensity is dominated by the contribution of the heavy atoms ($Z_{Ga} = 31$, $Z_{As} = 33$) and depends on the atomic number Z as well on the thickness of the specimen [26], at low angles the ADF-intensity becomes sensitive to the content of light atoms ($Z_N = 7$) if local strain induced by static atomic displacements is introduced [27, 28] what can be clearly seen in figure S2 (stacks.iop.org/JPhysD/49/075108/mmedia). The simulated intensities of N-containing materials show a stronger increase of the brightness at low inner detector angles than Ga(AsP) and hence dilute nitrides can be well distinguished from N-free material especially for low detector angles. The quantitative evaluation of the STEM images is explained in detail in the *Supporting Information*. In short, a routine has been developed and applied to detect the QW. Subsequently the mean QW-thickness as well as the standard deviation of the thickness are calculated. To compare the quality of different layers the definitions of roughness and compositional fluctuation have to be specified first. We differentiate between absolute roughness σ_t, which stands for the standard deviation from the mean thickness, and relative roughness determined as the ratio of the absolute roughness and the mean thickness of the layer. To describe the compositional fluctuation of the QW material quantitatively, the mean (HA)ADF ((high angle) annular dark field) intensity is determined in the QW region. The ratio σ_i/mean intensity, where σ_i is the standard deviation of the mean intensity is defined as compositional fluctuation. Special care was taken to compare only images acquired at comparable TEM sample thicknesses in beam direction. This ensures that the numbers derived from statistical analysis can be contrasted quantitatively and correlated to sample quality. It is worth noting that there is an 'error' associated with this kind of evaluation, which results on the one hand from the roughness of the TEM specimen due to sample preparation, on the other hand from the (HA)ADF detector characteristics, like detector noise. This has been addressed by always also evaluating the GaP layers adjacent to the Ga(NAsP) QWs. The normalized standard deviation in the GaP reflects this 'error' as there is no compositional fluctuation there. The values measured in the GaP are always in the range of 2% and hence well below the values we measure for the Ga(NAsP).

PL (photoluminescence) studies have been performed using an Ar-ion laser operating at a wavelength of 514.5 nm for excitation. The PL-signal has been dispersed by a 1 m grating monochromator (Jobin-Yvon) and detected by Ge-detector applying standard Lock-in techniques. All PL spectra shown here were recorded at room temperature.

Computational details

Computations have been performed with the Vienna *ab initio* simulation package (VASP 5.3.5) [29–32], employing density functional theory (DFT) in the generalized gradient approximation in the formulation by Perdew, Burke and Ernzerhof (PBE) [33, 34] with pairwise dispersion correction using the DFT-D scheme (D3(BJ)) [35, 36]. A plane wave basis set in conjunction with the projector augmented wave method [37, 38] and an energy cut-off of 500 eV has been used. Sampling of k-space was performed using a Γ-centered Monkhorst-Pack grid [39] with $6 \times 6 \times 6$ intersections for primitive cells and $4 \times 3 \times 2$ intersections for $(2 \times 4 \times 5)$-supercells. Energies for electronic relaxations were converged to 10^{-5} eV, forces for structural relaxations to 10^{-2} eV Å^{-1}. Relaxation in z-direction was performed by stepwise elongating the cell and fitting a second order polynomial to the resulting energy curve.

Results and discussion

This section is organized as follows: first, the influence of nominal QW thickness on its interface morphology and its composition homogeneity is examined. Then, the impact of the growth temperature on the same parameters is determined; the results are put in perspective and correlated to the OEIC properties of the multi-QWH grown on Si substrates. Finally, the experimental results are discussed in the light of the thermodynamic stability of the material system computed by DFT methods.

Figures 1(a) and (c) exemplarily show STEM-images of samples grown at 575 °C with 1.4 nm and 11.8 nm QW mean thicknesses, respectively. In figures 1(b) and (d) the Ga(NAsP)-regions are detected in red and the GaP barriers in blue. It is clearly seen that the Ga(NAsP)-QWs have smooth lower interfaces with the GaP barriers whereas the roughness of the upper interfaces drastically increases for the higher nominal thicknesses. This qualitative impression is supported by the results of the quantitative analysis diagrammed in figure 1(e), where the dependence of absolute roughness σ_i on the QW-thickness is shown. The standard deviation of the mean values (from the evaluation of several images from different positions of the specimen) is plotted as x-axis error bars. The values of σ_t are the mean values of absolute roughness with their standard deviations as y-error bars. According to this diagram a thickness increase of 1 nm results in approximately 0.23 nm roughness increase. If we consider the roughness change relative to the QW-mean thickness (figure 1(f)) the relative roughness for all samples stays the same within the error bars and amounts to approximately 20% of the mean layer thickness. Hence, the interface quality of a layer is independent from its thickness, naturally if the latter one remains below a critical thickness given by plastic relaxation [40].

One possible reason for the roughening of the QWs could be the formation of compositional inhomogeneities, which would lead to a different lattice constant and in turn could lead to faceting and a different growth rate of the material. Therefore it is necessary to verify whether the chemical components are distributed homogeneously.

Figures 2(a) and (b) depict composition fluctuation maps of the STEM-images shown before (see figures 1(a) and (c)). The scattered intensity of the Ga(NAsP)-QWs can fluctuate by about 20% from the average. The regions, where these large deviations from the mean compositions occur are have a

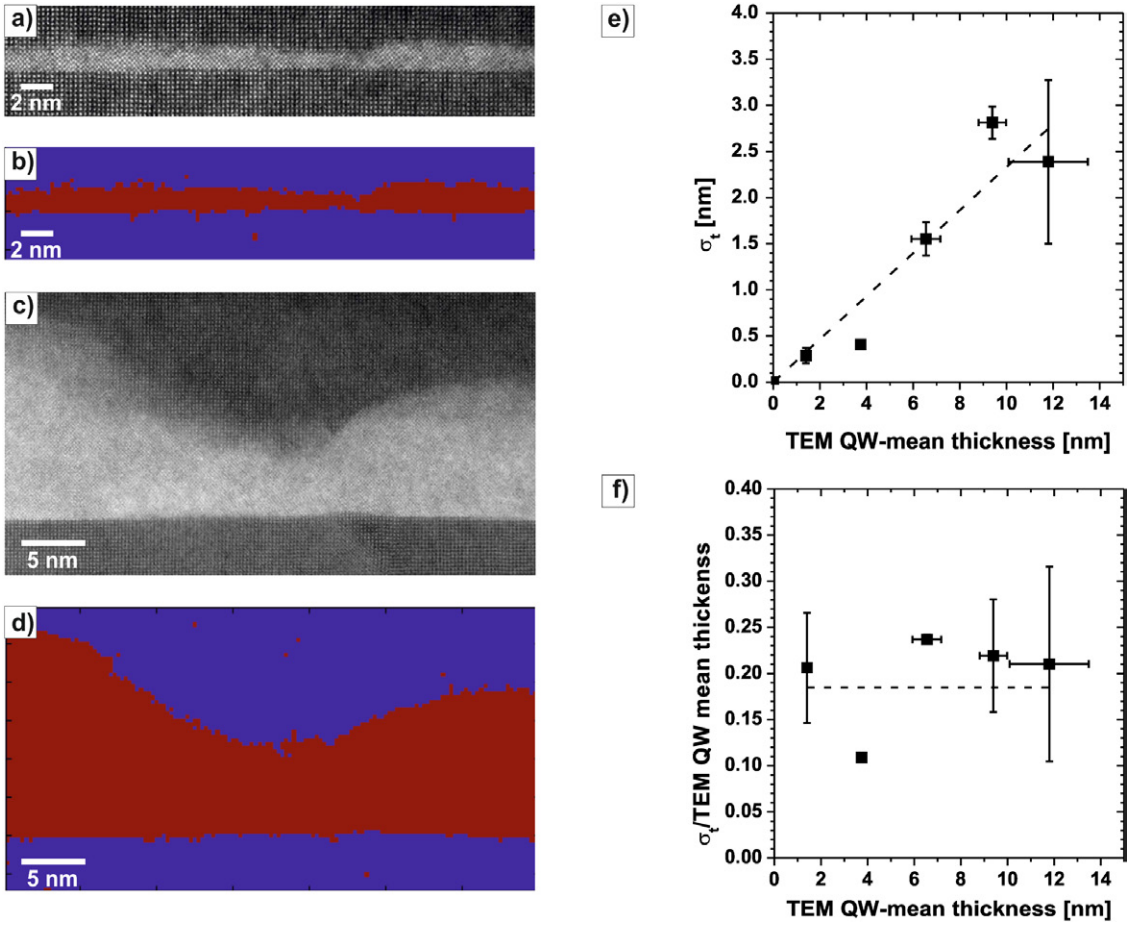

Figure 1. Roughness in dependence on QW-mean thickness. ADF-STEM images (a) and (c) of QWs having TEM mean–thicknesses of 1.4 nm and 11.8 nm, respectively, measured at 50 mrad inner detector angle. The growth direction is from bottom to top. In (b) and (d) the Ga(NAsP)-QW is visualized in red. (e) Shows that the absolute roughness of the Ga(NAsP)-QWs increases for larger QW-mean thickness (The dashed line is a linear fit). (f) The relative roughness does not show a dependence on the QW-mean thickness. (The dashed line is a guide to the eye.)

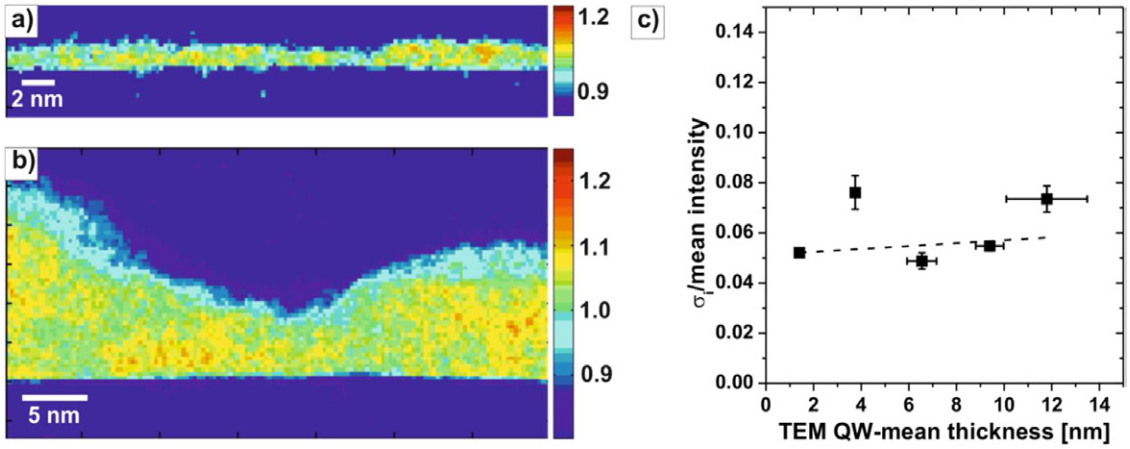

Figure 2. Compositional fluctuations maps of the samples with (a) 1.4 nm and (b) 11.8 nm QW-mean thicknesses. (c) The compositional fluctuation shows negligible dependence on the QW-mean thickness. (The dashed line is a linear fit to the data weighted with the standard deviations.)

size in the nanometer range. On average, the scattered intensity deviates by about ±10% from its mean value, what is also a quantitative measure for the material composition fluctuation. This holds for both structures. Taking into account that the value of the inner detector angle was 50 mrad, at which the ADF-signal becomes already more sensitive to N-content (figure S2) (stacks.iop.org/JPhysD/49/075108/mmedia), the regions with higher scattered intensity should contain more N-atoms. Comparing figures 2(a) and (b) there is, however, no clear difference between these two samples, hence the

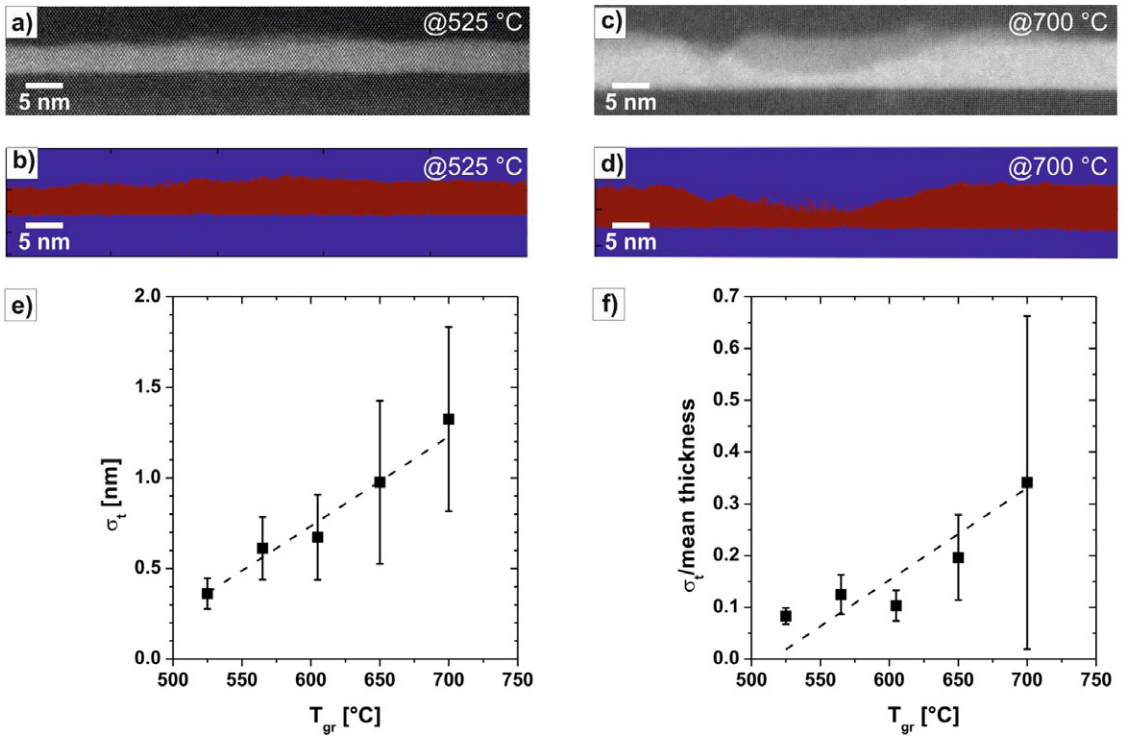

Figure 3. Roughness dependence on the growth temperature. ADF-STEM images of Ga(NAsP)-QWs grown at (a) 525 °C and (b) 700 °C with according visualization of the Ga(NAsP)-QWs in red (c) and (d), respectively, measured at 50 mrad inner detector angle. (e) The absolute roughness shows an increase with increasing growth temperature. (The dashed line is a linear fit). (f) The relative roughness increases as well for higher growth temperatures. (The dashed line is a linear fit.)

composition fluctuation does not increase with increasing QW thickness. Figure 2(c) describes the quantitative dependence of the compositional fluctuation σ_i/mean intensity on the mean QW-thickness. The change of the compositional fluctuation with increase of the QW-thickness is below 0.1% per nm QW thickness, what is negligible for the accuracy of the applied evaluation method. Therefore, we can conclude that there is no influence of the variation of the layer thickness on the compositional fluctuation in the quaternary material. Consequently, the variation of thickness of the Ga(NAsP) layer does not impact its quality: neither its relative interface roughness nor its compositional fluctuation show significant changes. At least the latter should also be true for samples grown at different temperatures. Hence, in the following, QWs with slightly different thickness can be compared.

One would conjecture a severe impact on the QW layer quality by variation of the growth temperature. This especially holds for a metastable material system like Ga(NAsP). Here, one would expect phase separation when tuning the growth conditions towards thermodynamic equilibrium, meaning to higher temperatures.

Figures 3(a) and (c) depict two representative STEM-images of samples grown at 525 °C and 700 °C. In figures 3(b) and (d) the Ga(NAsP)-QWs are visualized as described before. Like in these two exemplary images the lower interfaces of the Ga(NAsP)-QWs of all samples investigated in the frame of this work remain abrupt. However, the upper interface roughens significantly with increasing growth temperatures. The absolute roughness σ_t increases in dependence on growth temperature with 0.3 nm per 100 °C as shown in figure 3(e). The relative roughness σ_t/mean thickness depicted in figure 3(f) has an increasing trend of around 4.5% of QW-mean thickness per 100 °C as well. The regression line in figure 3(e) has its zero value for a growth temperature around 450 °C, so at this growth temperature theoretically we could obtain ideally smooth interfaces if the underlying mechanism leading to the roughening stays the same over this temperature range. The decomposition of the metalorganic precursors becomes much lower resulting in an extremely low growth rate and difficult to control growth conditions for a quaternary material [41]. Moreover, previous investigations show that high quality growth is difficult to achieve at such low temperatures as the incorporation of C-atoms increases [42]. Therefore the estimated temperature for the minimum relative roughness is not an optimum for our growth process. Nevertheless our results allow concluding that the growth temperature is a more important parameter for optimization of growth conditions than the nominal thickness of a QW and indeed has a significant effect on the quality of a layer.

It is a big challenge to find an optimum temperature window for homogeneous distribution of the components in the quaternary layers of metastable materials by non-equilibrium processing. The energy provided to the material system by raising of growth temperature could lead to a phase-separation. Therefore, the compositional fluctuation in Ga(NAsP)-QWs for different temperatures has to be compared.

According to the compositional fluctuations maps in figures 4(a) and (b) for STEM-images measured at 59 mrad inner detector angle the Ga(NAsP)-QW grown at 700 °C is more homogeneous than the one grown at 525 °C. The TEM

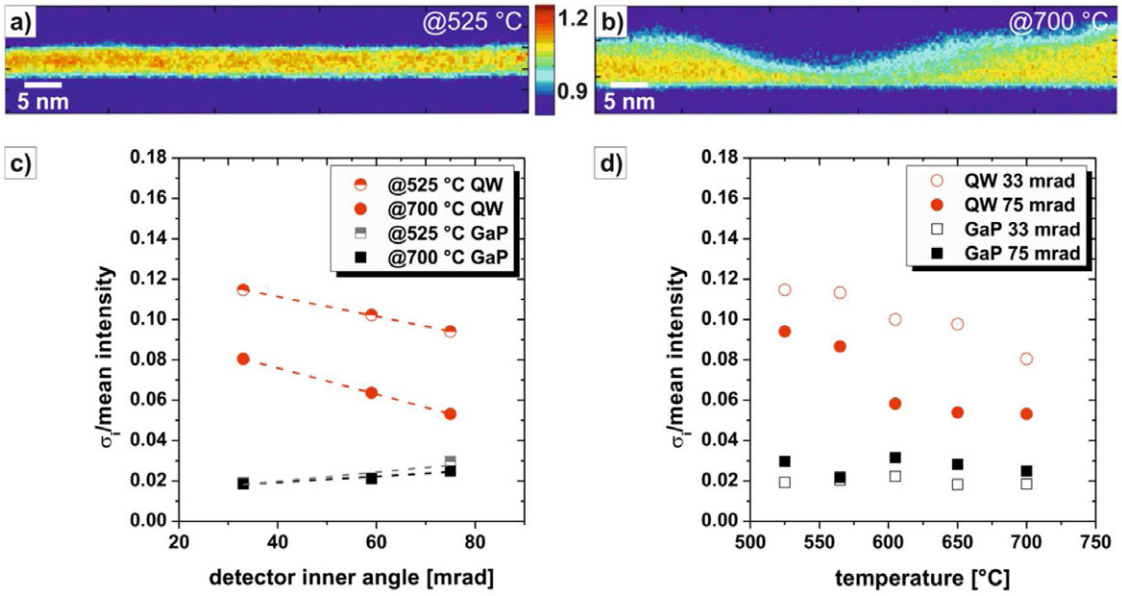

Figure 4. Compositional fluctuation in dependence on growth temperature. Compositional fluctuation maps of samples grown at (a) 525 °C and (b) 700 °C for STEM-images measured at 59 mrad inner detector angle. (c) There is a decreasing trend of the compositional fluctuation for increasing inner detector angle for 525 °C (red half-filled circles) as well as 700 °C (red filled circles) meaning that As-atoms are distributed more homogeneously than N-atoms in Ga(NAsP)-QWs. Squared half-filled and grey data points describe the normalized standard deviation of the intensity in GaP. (d) Compositional fluctuation in Ga(NAsP)-QWs becomes lower with increasing growth temperatures for 33 mrad (red filled circles) as well for 75 mrad (red empty circles) inner detector angles. The squared filled and empty black points are the local composition fluctuation in GaP for 33 mrad and 75 mrad inner detector angles, respectively.

specimen thicknesses at the image positions was 23 nm (525 °C) and 28 nm (700 °C), respectively. It should be mentioned once more that it is important to only compare TEM samples of similar thickness, as, for example, for thicker specimens a QW could just appear to have lower compositional fluctuation because of averaging through the thickness. Therefore, to do a quantitative comparison STEM-images acquired on the positions with a sample thickness with 21–28 nm were chosen for quantitative analysis, as it was also done for the roughness evaluation.

Figure 4(c) depicts the dependence of the compositional fluctuation in the Ga(NAsP)-QW (round red half-filled (525 °C) and filled (700 °C) data points) and in neighboring GaP-layer (squared grey and black data points). The contrast fluctuation was also evaluated in the GaP-layers, which should show no chemical inhomogeneity. The normalized standard deviation of the mean intensity determined in the GaP is 1.8%–3.3% and caused by TEM sample preparation, e.g. thickness variation in the investigated region, by electron beam damage and/or most likely by experimental noise, for example from the HAADF amplifier. Nevertheless, the normalized standard deviation in GaP-layers is significantly lower in comparison to the compositional fluctuation in Ga(NAsP)-QWs for all imaging conditions, as expected. It is also worth mentioning that normalized standard deviations of a mean intensity around 2% have been determined when only vacuum has been measured. This suggests that the standard deviations measured in the GaP are solely due to amplifier noise and not due to sample preparation. The same should consequently be also true for Ga(NAsP). Moreover, the standard deviation in the GaP-layers does not change for different samples and does not show any significant dependence on the variation of the detector angle. On the contrary, intensity fluctuations Ga(NAsP) for a growth temperature of 525 °C (red half-filled circles) and for 700 °C (red filled circles) decrease with increasing inner detector angle. If all species would show the same distribution characteristics, one would expect no dependence (as in GaP) of the intensity fluctuation on the scattering angle. As the scattering at low angles is more influenced by the N-distribution in contrast to the scattering at high angles, which is more influenced by the As-distribution, that means that the As atoms are distributed more homogeneously than the N-atoms.

Furthermore, the compositional fluctuation in Ga(NAsP) becomes lower for a growth temperature of 700 °C for all inner detector angles. This means that the composition homogeneity of samples grown at 700 °C is better than for samples grown at 525 °C. To further underpin our findings we compare the compositional fluctuation in dependence on the growth temperature (figure 4(d)). The standard deviation in GaP shows the same behavior as before, so the following results are reliable. Surprisingly, the compositional fluctuation in Ga(NAsP) for 33 mrad (red filled circles) as well for 75 mrad (red empty circles) inner detector angle becomes lower for higher temperatures. Of course, there could be an impact of a slightly varying N-content in the sample on the compositional homogeneity. However, samples grown between 565 °C and 650 °C have the same N-content, but also show the dependence of the homogeneity on the growth temperature. This trend is followed by the samples grown at 525 °C and 700 °C, which have a slightly higher and lower N-content than the others, respectively. Hence, increasing the growth temperature definitely has a positive impact on the material´s homogeneity.

The experimental findings can be summarized as follows: on one hand, the material grown at higher temperature is more homogeneous. Higher diffusion of the components in comparison to lower temperatures might explain this. On the other hand the absolute and relative roughness of the QWs increase with increasing growth temperature. This means that a complete rearrangement of the QW takes place at the highest growth temperature, which leads to the most homogeneous quaternary material. One would not expect such results, especially for a metastable material system. As there is obviously enough energy to have sufficient surface diffusion to completely rearrange the quantum well into a facetted structure, a metastable material system should phase separate under those growth conditions and not show better compositional homogeneity. It is very interesting to find a model and a quantitative theoretical description for these findings. The model should include the compressive strain state of the Ga(NAsP) layer with respect to the Si-substrate, which of course is reduced when adding N. This might reduce the metastability of Ga(NAsP) on Si substrates, as the biaxial strain is reduced when adding increasing amounts of N. Also, the faceting of the surface with increasing growth temperature might play a role in stabilizing certain metastable compositions, as was also shown theoretically in [43]. The following theoretical considerations are a first step towards addressing the material's stability.

Strain relaxation energies computed by DFT and phase separation energies are presented in figure 5 for $Ga(N_xAs_{0.85-x}P_{0.15})$ on Si and $Ga(As_{0.85}P_{0.15})$ substrates. The quaternary Ga(NAsP) compositions chosen for the theoretical studies are within the range of compositions experimentally accessible on Si substrates. The substrate has been implicitly taken into account by fixing the basis vectors of the simulation cell to the substrate lattice constant in x and y direction while relaxing in z direction (theoretical epitaxy). Strain relaxation energy (SRE) is defined as the energy difference between a fully relaxed Ga(NAsP) bulk cell (which cannot be realized experimentally) and the strained system of the same composition:

$$\mathrm{SRE} = E^{\mathrm{strained}}_{\mathrm{Ga(NAsP)}} - E^{\mathrm{bulk}}_{\mathrm{Ga(NAsP)}}. \quad (1)$$

The phase separation energy (PSE) is defined as the energy difference between strained Ga(NAsP) and the likewise strained components GaAs, GaP and GaN (all in the zinc blende structure) with the respective substrate's lattice parameters:

$$\mathrm{PSE} = E^{\mathrm{strained}}_{\mathrm{Ga(N_xAs_yP_z)}} - N(xE^{\mathrm{strained}}_{\mathrm{GaN}} + yE^{\mathrm{strained}}_{\mathrm{GaAs}} + zE^{\mathrm{strained}}_{\mathrm{GaP}}). \quad (2)$$

The SRE is essentially a measure for the deviation of the quaternary material's optimal lateral lattice constants from the substrate's lateral lattice constants. Thus, the reduction of the lattice constant of Ga(NAsP) by increasing N content leads to a decrease of the SRE on Si substrate up to a concentration of about 20% N (figure 5(a)), filled black symbols). For higher N contents, the SRE increases again while the structure changes from compressively strained to tensilely strained. On a virtual Ga(AsP) substrate, increasing N content leads to an increase of the SRE, since the deviation from the substrate lattice constant increases continuously (figure 5(a)), open red symbols).

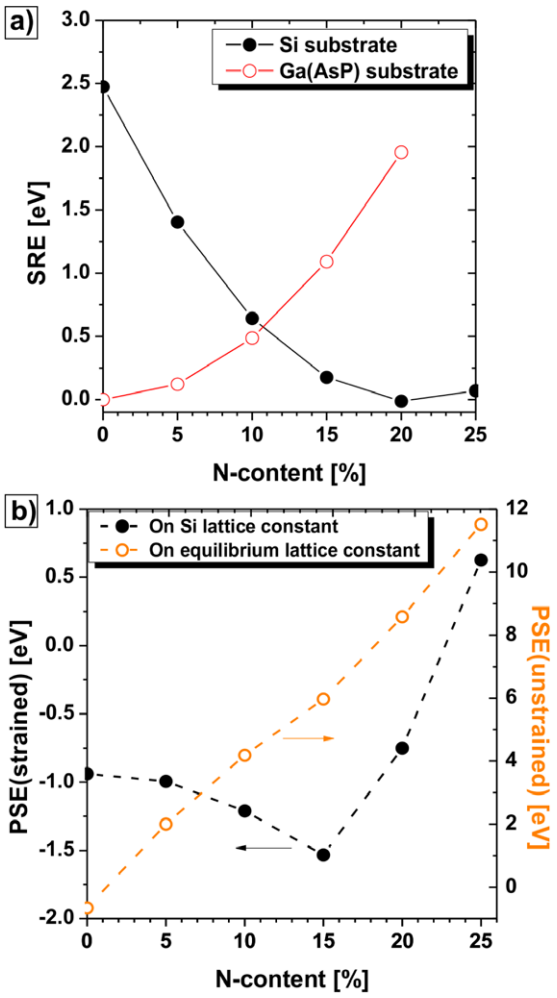

Figure 5. Computational results for (a) strain relaxation energy (SRE) of $Ga(N_xAs_{0.85-x}P_{0.15})$ on Si (filled black symbols) and virtual $Ga(As_{0.85}P_{0.15})$ (open red symbols) substrates. In (b) the values of the phase separation energy (PSE) of $Ga(N_xAs_{0.85-x}P_{0.15})$ strained to Si lattice constant (filled black symbols, left hand side axis) and on its equilibrium lattice constant (open orange symbols, right hand side axis) are plotted. Energy values refer to one $(2 \times 4 \times 5)$ supercell. The lines are guides to the eye.

The phase separation energy into the binary components shows an interesting trend for Si substrate (figure 5(b), filled black symbols). For N contents from 0% up to about 15%, the energy decreases, meaning that the system is increasingly stabilized with respect to phase separation. For higher N concentration, the phase separation energy increases dramatically and becomes even positive (i.e. Ga(NAsP) becomes unstable compared to the components). This can be traced back to the phase separation energy for the respective bulk systems, which is strongly in favor of phase separation and increasingly so for higher N concentration (figure 5(b)), orange open symbols). For smaller N content, this can be mitigated by the SRE, whereas at higher N content the destabilizing phase separation energy is dominating. The largest contribution to the stability of Ga(NAsP) is the phase separation product GaN, which is very instable when highly strained. While these calculations do not allow to draw conclusions on the homogeneity of these

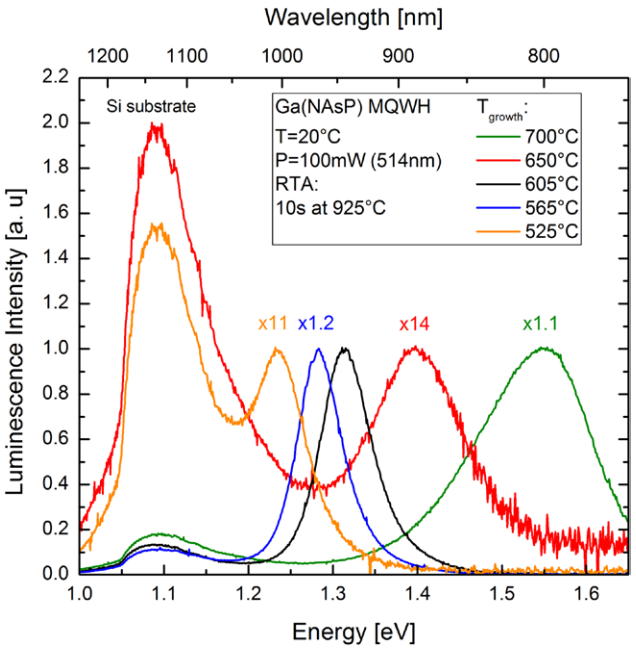

Figure 6. Room temperature photoluminescence spectra of Ga(NAsP) QWs grown at different temperatures on Si substrate. The peak intensity of all spectra have been normalized to the value measured for a growth temperature of 605 °C. All samples have been annealed for 10 s at 925 °C, which has been optimized for samples grown at 575 °C.

systems, the kinetic aspect or the temperature dependence, they give strong hints towards a stabilization of the alloyed systems with respect to strain energy and phase separation for N concentrations up to 20% if the phase separation products keep the substrate's lateral lattice constants. This can help in understanding the temperature dependence of the growth experiments. From a more application point of view, these findings are also extremely valuable to emphasize the future potential of this material system in high efficient active light sources on Si(0 0 1) substrates.

This potential is even more underlined by the optical properties of the investigated Ga(NAsP)/(BGa)(AsP) multi-QWH grown on Si(0 0 1). Figure 6 shows room temperature PL spectra of the structures grown at different temperatures (after 10 s rapid thermal annealing (RTA) at 925 °C). All multi-QWH exhibit room temperature PL, manifesting the excellent properties of the material system. Furthermore, the emission wavelength can be tuned by changing the growth conditions, adopting the material system to different applications.

Conclusion

Ga(NAsP), which can be pseudomorphically grown on Si substrates, is a promising material system for realizing a direct-bandgap laser on Si(0 0 1). The dependence of Ga(NAsP)-QW quality, addressed by the interface roughness and compositional fluctuation, on the variation of growth parameters, like layer thickness and growth temperature reveals very unexpected results. While the absolute roughness of the QWs at a given growth temperature increases with QW thickness, the relative roughness of the layers as well as their compositional fluctuation is independent of the thickness of a QW layer. On the contrary, the growth temperature has an impact on both indicators of layer quality but in a surprisingly contradictory way: relative and absolute roughness increase with increasing growth temperature whereas the compositional fluctuation decreases, so the layers become more homogeneous. This contradicts the assumed metastable character of the Ga(NAsP) material system. In an *ab initio* approach, we could show that the quaternary material is stable against phase separation into binary, epitaxial products up to a N content of 20%, which is mainly due to the good lattice match on silicon substrate. These findings are of extreme importance for the investigated material system, which shows the perspective of being integrated as active light source on Si(0 0 1) substrates. This potential is also underlined by the room temperature PL, which the samples exhibit.

Acknowledgment

This work was supported by the German Science Foundation (DFG) within the GRK 1782 ('Functionalization of Semiconductors').

Supplementary data

Supplementary data on the schematic structure of the samples, the calculation of the HAADF intensity and the evaluation algorithm of the STEM images is available with this article.

References

[1] Fang A W, Hyundai P, Jones R, Cohen O, Paniccia M J and Bowers J E 2006 A continuous-wave hybrid AlGaInAs-silicon evanescent laser *IEEE Photon. Technol. Lett.* **18** 1143–5

[2] Iyer S S and Xie Y-H 1993 Light emission from silicon *Science* **260** 40–6

[3] Pavesi L and Lockwood D J 2004 *Silicon Photonics* vol 94 (Berlin: Springer)

[4] Chen H Z, Ghaffari A, Wang H, Morkoç H and Yariv A 1987 Continuous-wave operation of extremely low-threshold GaAs/AlGaAs broad-area injection lasers on (1 0 0) Si substrates at room temperature *Opt. Lett.* **12** 812

[5] Egawa T, Tada H, Kobayashi Y, Soga T, Jimbo T and Umeno M 1990 Low-threshold continuous-wave room-temperature operation of $Al_xGa_{1-x}As$/GaAs single quantum well lasers grown by metalorganic chemical vapor deposition on Si substrates with SiO_2 back coating *Appl. Phys. Lett.* **57** 1179

[6] Deppe D G, Chand N, Van Der Ziel J P and Zydzik G J 1990 $Al_xGa_{1-x}As$–GaAs vertical-cavity surface-emitting laser grown on Si substrate *Appl. Phys. Lett.* **56** 740–2

[7] Choi H K, Wang C A and Karam N H 1991 GaAs-based diode lasers on Si with increased lifetime obtained

by using strained InGaAs active layer *Appl. Phys. Lett.* **59** 2634
[8] Sugo M, Mori H, Sakai Y and Itoh Y 1992 Stable CW operation at room temperature of a 1.5-μm wavelength multiple quantum well laser on a Si substrate *Appl. Phys. Lett.* **60** 472
[9] Wirths S *et al* 2015 Lasing in direct-bandgap GeSn alloy grown on Si *Nat. Photon.* **9** 88–92
[10] Kunert B, Volz K, Koch J and Stolz W 2006 Direct-band-gap Ga(NAsP)-material system pseudomorphically grown on GaP substrate *Appl. Phys. Lett.* **88** 182108
[11] Kunert B, Zinnkann S, Volz K and Stolz W 2008 Monolithic integration of Ga(NAsP)/(BGa)P multi-quantum well structures on (0 0 1) silicon substrate by MOVPE *J. Cryst. Growth* **310** 4776–9
[12] Rosemann N W, Metzger B, Kunert B, Volz K, Stolz W and Chatterjee S 2013 Temperature-dependent quantum efficiency of Ga(N,As,P) quantum wells *Appl. Phys. Lett.* **103** 252105
[13] Hossain N, Sweeney S J, Rogowsky S, Ostendorf R, Wagner J, Liebich S, Zimprich M, Volz K, Kunert B and Stolz W 2011 Reduced threshold current dilute nitride Ga(NAsP)/GaP quantum well lasers grown by MOVPE *Electron. Lett.* **47** 931–3
[14] Liebich S *et al* 2011 Laser operation of Ga(NAsP) lattice-matched to (0 0 1) silicon substrate *Appl. Phys. Lett.* **99** 071109
[15] Ludewig P, Reinhard S, Jandieri K, Wegele T, Beyer A, Tapfer L, Volz K and Stolz W 2015 MOVPE growth studies of Ga(NAsP)/(BGa)(AsP) multi quantum well heterostructures (MQWH) for the monolithic integration of laser structures on (0 0 1) Si-substrate *J. Cryst. Growth* at press (DOI: 10.1016/j.jcrysgro.2015.12.024)
[16] Sakaki H, Noda T, Hirakawa K, Tanaka M and Matsusue T 1987 Interface roughness scattering in GaAs/AlAs quantum wells *Appl. Phys. Lett.* **51** 1934–6
[17] Dura J A, Pellegrino J G and Richter C A 1996 X-ray reflectivity determination of interface roughness correlated with transport properties of (AlGa)As/GaAs high electron mobility transistor devices *Appl. Phys. Lett.* **69** 1134
[18] Penner U, Rücker H and Yassievich I N 1999 Theory of interface roughness scattering in quantum wells *Semicond. Sci. Technol.* **13** 709–13
[19] Erol A 2008 *Dilute III–V Nitride Semiconductors and Material Systems* (Berlin: Springer)
[20] Dargam T G and Koiller B 1998 Interface roughness and the optical properties of quantum wells *Solid State Commun.* **105** 211–4
[21] Volz K, Beyer A, Witte W, Ohlmann J, Németh I, Kunert B and Stolz W 2011 GaP-nucleation on exact Si (0 0 1) substrates for III/V device integration *J. Cryst. Growth* **315** 37–47
[22] Németh I, Kunert B, Stolz W and Volz K 2008 Heteroepitaxy of GaP on Si: Correlation of morphology, anti-phase-domain structure and MOVPE growth conditions *J. Cryst. Growth* **310** 1595–601
[23] Tapfer L and Ploog K 1989 X-ray interference in ultrathin epitaxial layers: a versatile method for the structural analysis of single quantum wells and heterointerfaces *Phys. Rev.* B **40** 9802–10
[24] Kirkland E J and Thomas M G 1996 A high efficiency annular dark field detector for STEM *Ultramicroscopy* **62** 79–88
[25] Lebeau J M and Stemmer S 2008 Experimental quantification of annular dark-field images in scanning transmission electron microscopy *Ultramicroscopy* **108** 1653–8
[26] Pennycook S J 1989 Z-contrast stem for materials science *Ultramicroscopy* **30** 58–69
[27] Wu X, Robertson M D, Gupta J A and Baribeau J-M 2008 Strain contrast of $GaN_{(y)}As_{(1-y)}$ (1 0 0) GaAs substrates in annular dark ($y = 0.029$ and 0.045) epitaxial layers on field images *J. Phys. Condens. Matter* **20** 075215
[28] Grillo V, Mueller K, Volz K, Glas F, Grieb T and Rosenauer A 2011 Strain, composition and disorder in ADF imaging of semiconductors *J. Phys. Conf. Ser.* **326** 012006
[29] Kresse G and Hafner J 1993 *Ab initio* molecular dynamics for liquid metals *Phys. Rev.* B **47** 558–61
[30] Kresse G and Hafner J 1994 *Ab initio* molecular-dynamics simulation of the liquid-metal-amorphous-semiconductor transition in germanium *Phys. Rev.* B **49** 14251
[31] Kresse G and Furthmüller J 1996 Efficiency of *ab-initio* total energy calculations for metals and semiconductors using a plane-wave basis set *Comp. Mat. Sci.* **6** 15
[32] Kresse G and Furthmüller J 1996 Efficient iterative schemes for *ab initio* total-energy calculations using a plane-wave basis set *Phys. Rev.* B **54** 11169
[33] Perdew J P, Burke K and Ernzerhof M 1996 Generalized gradient approximation made simple *Phys. Rev. Lett.* **77** 3865–8
[34] Perdew J P, Burke K and Ernzerhof M 1997 Erratum: Generalized gradient approxiamtion made simple *Phys. Rev. Lett.* **78** 1396
[35] Grimme S, Antony J, Ehrlich S and Krieg H 2010 A consistent and accurate *ab initio* parametrization of density functional dispersion correction (DFT-D) for the 94 elements H–Pu *J. Chem. Phys.* **132** 154104
[36] Grimme S, Ehrlich S and Goerigk L 2011 Effect of the damping function in dispersion corrected density functional theory *J. Comput. Chem.* **32** 1456–65
[37] Blöchl P E 1994 Projector augmented-wave method *Phys. Rev.* B **50** 17953–79
[38] Kresse G 1999 From ultrasoft pseudopotentials to the projector augmented-wave method *Phys. Rev.* B **59** 1758–75
[39] Monkhorst H J and Pack J D 1976 Special points for Brillouin-zone integrations *Phys. Rev.* B **13** 5188
[40] Marée P M J, Olthof R I J, Frenken J W M, van der Veen J F, Bulle-Lieuwma C W T, Viegers M P A and Zalm P C 1985 Silicon strained layers grown on GaP(0 0 1) by molecular beam epitaxy *J. Appl. Phys.* **58** 3097
[41] Stringfellow G B 1999 *Organometallic Vapor-Phase Epitaxy: Theory and Practice* (San Diego: Academic Press)
[42] Volz K, Torunski T, Kunert B, Rubel O, Nau S, Reinhard S and Stolz W 2004 Specific structural and compositional properties of (GaIn)(NAs) and their influence on optoelectronic device performance *J. Cryst. Growth* **272** 739–47
[43] Teles L K, Furthmüller J, Scolfaro L M R, Tabata A, Leite J R, Bechstedt F, Frey T, As D J and Lischka K 2002 Phase separation and gap bowing in zinc-blende InGaN, InAlN, BGaN, and BAlN alloy layers *Physica* E **13** 1086–9

Supplementary Data

Interface Morphology and Composition of Ga(NAsP) Quantum Well Structures for monolithically integrated LASERs on Silicon Substrates

*Tatjana Wegele[1], Andreas Beyer[1], Peter Ludewig[1], Phil Rosenow[2], Lennart Duschek[1], Kakhaber Jandieri[1], Ralf Tonner[2], Wolfgang Stolz[1], Kerstin Volz[1]**

[1] Faculty of Physics and Material Sciences Centre, Philipps-Universität Marburg, Hans-Meerwein Str. 6, D-35032 Marburg, Germany
[2] Faculty of Chemistry and Material Sciences Centre, Philipps-Universität Marburg, Hans-Meerwein Str., D-35032 Marburg, Germany

Corresponding Author:

*kerstin.volz@physik.uni-marburg.de

Figure S1 shows a schematic sketch of the investigated Ga(NAsP)/(BGa)(AsP) multi-quantum well structure grown on exact Si(001) substrate.

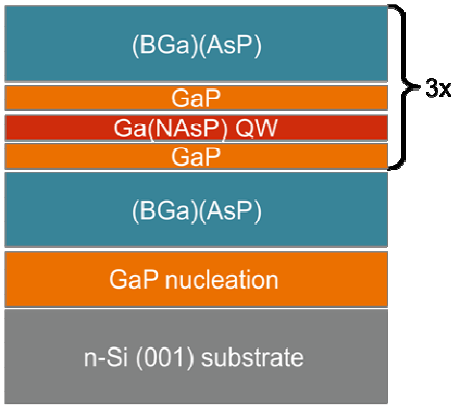

Figure S1. Schematic sketch of the investigated Ga(NAsP)-MQW heterostructures.

In Figure S2 ADF (annular dark field) intensities of the materials Ga(NAs) as well GaAs are calculated using the STEMsim software.[1] The simulated intensities of N-containing materials are higher than GaAs for smaller inner detector angles. Hence, N-containing material can be well distinguished from N-free material especially for low detector angles.

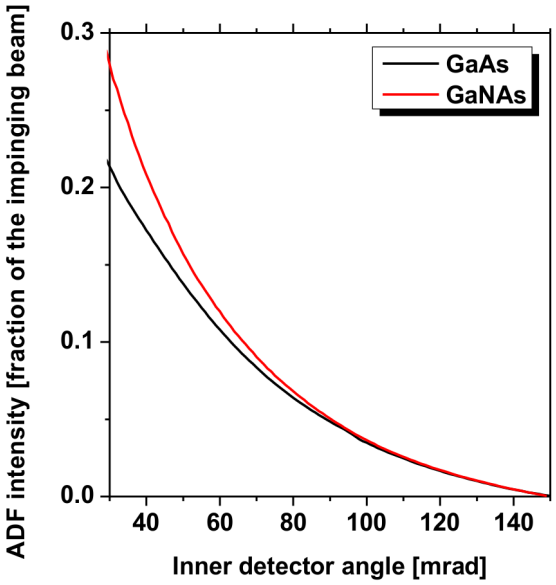

Figure S2. Scattered ADF intensity simulated using the STEMsim software[1] for Ga(NAs) and GaAs. The TEM sample thickness is 28 nm thick each, the electron beam is parallel to the [010]-crystal orientation. The simulated intensity was averaged over a region of 2.5 nm x 2.5 nm in the plane perpendicular to the beam direction.

The STEM images are evaluated quantitatively using the following procedure. Raw STEM-images with brighter Ga(NAsP)-QWs and darker neighboring GaP-barriers (Figure S3a)) acquired at several different positions of the investigated specimens were chosen for the quantitative analyses. No filtering or other modifications except those described below were applied. For data evaluation first the background intensity or a black level I_0 measured in the hole of the investigated specimen was subtracted. Afterwards the STEM-intensity measured in counts was recalculated into current in pA :

$$\frac{I(counts) - I_0}{gain} = I_{\exp}[pA] \qquad \text{(S1).}$$

A gain-factor [counts/pA] for certain brightness and contrast values was determined as reported in.[2] To obtain the relative intensity comparable with a simulated one (Figure S3b)) the current value in experimental image I_{exp} was normalized to the beam current determined as follows:

$$\frac{I_{CCD} * e}{efficiency * t} = beam\,current\ [pA] \qquad \text{(S2).}$$

The beam intensity I_{CCD} was acquired using an UltraScan CCD -Camera Model 994 US 1000XP (Gatan). *e* is the elementary charge, the conversion efficiency of the UltraScan camera is 3.06 ACD counts/primary e^- according to the Certificate of Compliance, *t* is the acquisition time.

Due to the conventional preparation of the specimens these have a wedge shape resulting in an intensity variation in the region of interest, which will have a 2D-thickness gradient. The red intensity profiles in Figure S3a) and S3b) visualize the change of intensity in the STEM-image from bottom to top (growth direction): in the Ga(NAsP)-QW the intensity is higher, in the neighboring GaP-barriers it becomes lower. Moreover, the intensity in the GaP above the QW is lower than the one below the QW because the thickness of the TEM specimen

increases from top to bottom. Figure S3c) depicts the increase of specimen thickness derived across the region of interest. Subsequently, the thickness gradient was fitted in two dimensions in the GaP-barriers and extrapolated over the entire investigated region. Afterwards the image intensity was corrected with respect to this thickness gradient as shown in Figure S3d).

Subsequently, the sampling was intentionally reduced by a factor of 0.3 and 0.25 for the images in [010] and [110] zone axis, respectively, to artificially reduce the resolution in order not to misinterpret the high resolution contrast as fluctuations in the chemical composition. After that a mean value of a relative intensity in GaP-barriers neighboring to the Ga(NAsP)-QWs was used to estimate the TEM specimen thickness in the investigated regions through comparison with the mean intensity in a simulated GaP-image. The mean value $I_{mean}(GaP)$ was also determined for the purpose of defining a threshold b to detect the boundaries of the QW:

$$b = I_{mean}(GaP) + 3\times\sigma, \qquad \text{(S3)}$$

σ is the standard deviation of the GaP intensity. The confidence interval of 3xσ contains 99.7% of GaP-intensity values spread out around $I_{mean}(GaP)$.

Figure S3e) depicts the result of this analysis: the red region is identified as the Ga(NAsP)-QW and the blue regions as the GaP-barriers. In the red region along the Ga(NAsP)-QW the thickness of the QW is determined at each position. From this data the mean QW-thickness as well as the standard deviation of the thickness is calculated.

To describe a compositional fluctuation, a mean ADF-intensity in the Ga(NAsP)-QW, red region in Figure S3e), is calculated and the STEM-image is normalized to this value. This results in a composition fluctuation map shown in Figure S3f), where intensities fluctuate within a standard deviation of the mean intensity σ_i divided by mean intensity around a value

equal to 1. The ratio σ_i/*mean intensity* is defined as compositional fluctuation. This composition fluctuation is quantitative in the QW region.

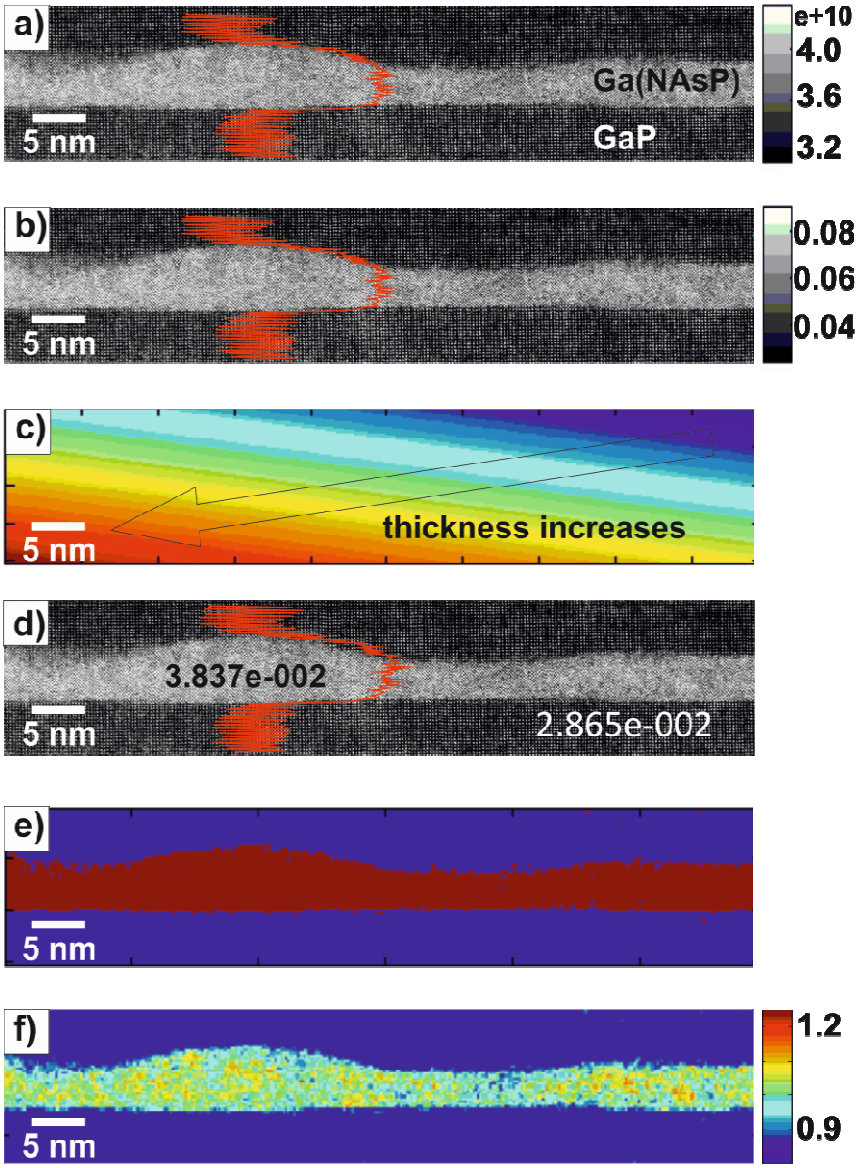

Figure S3. Step-wise evaluation of ADF-STEM images: a) The raw STEM-image (in this case at 50 mrad inner detector angle) is normalized (b) to the electron beam intensity. The grey scale units are then fractions of the impinging beam intensity. c) The 2-D thickness gradient is detected, visualized and corrected. d) The STEM-image without a thickness gradient can be used for quantitative evaluation. e) The Ga(NAsP)-QW region is detected (red) as well as the GaP-barriers are identified (blue). f) Shows the according quantitative map of composition fluctuation. The growth direction is in all images from bottom to top. The red intensity profiles parallel to the growth direction visualize the higher intensity in the Ga(NAsP)-QW and lower intensity in neighboring GaP-barriers as well as thickness increase from top to bottom.

SI REFERENCES

[1] Rosenauer A and Schowalter M 2008 STEMSIM - A New Software Tool for Simulation of STEM *Microsc. Semicond. Mater. 2007* **120** 170–2

[2] He D S and Li Z Y 2014 A practical approach to quantify the ADF detector in STEM *J. Phys. Conf. Ser.* **522** 012017

6.5 Annealing effects on the composition and disorder of Ga(N,As,P) quantum wells on silicon substrates for laser application [1]

S. Gies, M. Zimprich, T. Wegele, C. Kruska, A. Beyer, W. Stolz, K. Volz, W. Heimbrodt, Journal of Crystal Growth **402** (2014) 169–174. DOI: 10.1016/j.jcrysgro.2014.05.012.

Abstract

The influence of a rapid thermal annealing procedure on the properties of Ga(N,As,P) multiple quantum wells grown on silicon substrates has been studied.We reveal the changes in composition and disorder on the basis of photoluminescence, photoluminescence excitation and Raman spectroscopy as well as transmission electron microscopy. The optimal annealing temperature was found to be in the range of 900–925 °C. By increasing the annealing temperature (T_a) from 850°C to 1000 °C, we found a gradual exchange of arsenic and phosphorous atoms between the quantum wells and the barriers. At highest annealing temperatures our results are consistent with a reduction of the As concentration by several percent.

My Contribution

For a comparison of the as grown samples with the annealed samples I prepared the TEM cross-sections of them and investigated using STEM mode of the JEOL JEM 2200FS. I investigated the intensity profiles – perpendicular to the interfaces – that were normalized to the fitted intensity in the (BGa)(AsP) barrier to reduce the influence of a possibly deviating thickness gradient of the TEM specimens and to make a faire comparison. The increase of the intensity in the GaP barrier in the annealed specimens was detected. Thereby, an increasing annealing temperature leads to a higher GaP intensity.

Journal of Crystal Growth 402 (2014) 169–174

Contents lists available at ScienceDirect

Journal of Crystal Growth

journal homepage: www.elsevier.com/locate/jcrysgro

Annealing effects on the composition and disorder of Ga(N,As,P) quantum wells on silicon substrates for laser application

S. Gies, M. Zimprich, T. Wegele, C. Kruska, A. Beyer, W. Stolz, K. Volz, W. Heimbrodt *

Faculty of Physics and Material Sciences Center, Philipps University Marburg, D-35032 Marburg, Germany

ARTICLE INFO

Article history:
Received 24 March 2014
Received in revised form
28 April 2014
Accepted 7 May 2014
Communicated by G.B. Stringfellow
Available online 4 June 2014

Keywords:
A1. Diffusion
A1. Optical spectroscopy
A1. TEM
A1. CMOS compatibility
A3. Quantum wells
B2. Semiconducting quaternary alloys

ABSTRACT

The influence of a rapid thermal annealing procedure on the properties of Ga(N,As,P) multiple quantum wells grown on silicon substrates has been studied. We reveal the changes in composition and disorder on the basis of photoluminescence, photoluminescence excitation and Raman spectroscopy as well as transmission electron microscopy. The optimal annealing temperature was found to be in the range of 900–925 °C. By increasing the annealing temperature (T_a) from 850 °C to 1000 °C, we found a gradual exchange of arsenic and phosphorous atoms between the quantum wells and the barriers. At highest annealing temperatures our results are consistent with a reduction of the As concentration by several percent.

1. Introduction

The realization of suitable light sources for optical data transmission on Si-wafers in combination with Si-based nanoelectronics is one of the predominant goals of optoelectronic integration these days. The quaternary Ga(N,As,P) material system is a promising candidate for the realization of a monolithically integrated laser on Si substrates. A successful operation of laser devices on a GaP [1,2] and a Si [3] substrate have been demonstrated already.

In this paper we present an annealing procedure of Ga(N,As,P) multiple quantum well (MQW) structures grown on Si-substrates with the aim to find optimized annealing conditions of the MQWs for laser application. The optical and structural properties have been studied to reveal the interconnection between structural changes and improvement of the optical performance in dependence on the growth and annealing conditions of the Ga(N,As,P) laser structures.

2. Experimental

The samples under investigation were grown by metal-organic vapor-phase epitaxy (MOVPE) in a commercially available horizontal reactor system (AIX 200-GFR). Growth was performed using a reduced reactor pressure with hydrogen as a carrier gas at a temperature of 575 °C. The substrate for growth was provided by GaP/Si templates, consisting of about 100 nm thick GaP layer nucleated on an exactly oriented Si(001) substrate. A detailed description of the procedure used for defect-free nucleation is given in Reference [4,5]. In order to achieve strong photoluminescence (PL), a multi quantum-well structure was grown with three $Ga(N_{0.07},As_{0.82},P_{0.11})$ layers of 5 nm thickness, separated by barriers consisting of a 5.6 nm GaP layer, a 33 nm (B,Ga)P layer and another 5.6 nm GaP layer prior to the next quantum well. The MQW region is embedded in an optical confinement region consisting of (B,Ga)(As,P) layers. Due to strain compensation by the specific lattice constant of boron containing materials, the formation of misfit dislocations can be avoided what enables the growth of a pseudomorphically strained crystal with arbitrary thickness. The formation of non-radiative B–N containing recombination centers is prevented by introduction of the 5.6 nm thick GaP barrier layer between each nitrogen- and boron-containing layer [6]. Thickness and composition of the layers involved were derived from high resolution X-ray diffractometry (HR-XRD) measurements on these samples and according to test structures which account for a high structural quality and sharp interfaces throughout the entire sample. Due to the metastable growth conditions of Ga(N,As,P), tertiarybutylarsine, tertiarybutylphosphine and 1,1-dimethylhydrazine served as efficiently decomposing group-V sources, whereas triethylgallium and triethylboron served as group-III

* Corresponding author.
E-mail address: wolfram.heimbrodt@physik.uni-marburg.de (W. Heimbrodt).

http://dx.doi.org/10.1016/j.jcrysgro.2014.05.012
0022-0248/

sources. A thermal annealing procedure after growth allows for the healing of certain types of structural defects within the active region. By application of an optimized annealing procedure it is possible to increase the PL emission of Ga(N,As,P) layers significantly. A procedure for optimization on similar structures based on the GaP substrate is described in Reference [7] by applying equilibrium annealing steps in the MOVPE reactor. Here, the annealing was performed in a commercially available rapid thermal annealing (RTA) reactor (Jipelec JetFirst 200C) that allows heating rates up to 50 K/s. The samples discussed underwent a treatment for 10 s at temperatures in the range of 850–1000 °C under a nitrogen atmosphere at ambient pressure.

The photoluminescence (PL) was measured using a Laserglow LLS-532-NM-200-5 diode-pumped solid state laser emitting photons of 2.33 eV. For the photoluminescence excitation (PLE) measurements a Spectra-Physics Model 3900S CW Ti:sapphire laser, which is able to emit light with a photon energy in the range of 1.3–1.7 eV, was used. The beam was splitted by a longpass filter with a cut-off wavelength of 665 nm in its path in order to monitor the power and the wavelength of the exciting light using a Coherent LabMax powermeter and a Ocean Optics HR 4000 spectrometer. In both cases the samples were placed in a microcryostat in which temperatures between 10 K and room temperature can be applied. The PL(E) was detected by means of a standard setup consisting of a 0.5 m grating spectrometer and a liquid-nitrogen cooled germanium detector. Furthermore, the laser light was chopped mechanically in order to amplify the luminescence signal using a lock-in technique.

The Raman measurements were performed using a confocal Raman microscope with a longpass filter to suppress the Rayleigh-scattered light. For excitation an Ar^+ laser emitting photons of 2.41 eV was used. The detection of the Stokes-scattered light was achieved by using a grating spectrometer and a liquid-nitrogen cooled CCD.

The transmission electron microscopy (TEM) was performed using a JEOL JEM 2200 FS double corrected transmission electron microscope. Measurements were performed in high-angle annular dark field (HAADF) scanning mode at 200 kV. The samples used were electron transparent [110] cross-sectional samples prepared by a mechanical thinning followed by argon milling.

3. Experimental results and discussion

In Fig. 1 the PL spectra are depicted for Ga(N,As,P)-MQW samples annealed at various temperatures T_a. The spectra are normalized to the silicon emission at 1.09 eV which is relatively strong at room temperature but disappears almost completely at low temperatures as it is an indirect transition in k-space. The Ga(N,As,P)-QW luminescence shifts in dependence on the annealing temperature from 1.348 eV for T_a=850 °C to 1.428 eV for T_a=975 °C. No QW luminescence at all was detectable for the as-grown sample. For T_a=850 °C a weak luminescence was found. With increasing annealing temperatures the Ga(N,As,P) luminescence intensity rises and reaches a maximum at T_a=925 °C but declines for higher annealing temperatures. The integrated intensity is depicted in the inset of Fig. 1. The luminescence at 10 K (not shown here) exhibits the same dependence but is about one order of magnitude higher in intensity.

A surprising and noteworthy result is the monotonous blueshift of the peak position with increasing annealing temperature. We will come back to this point in what follows.

The PL full width at half maximum (FWHM) is also depicted in the inset of Fig. 1. The minimum is found at T_a=900 °C. The little difference between the maximum in luminescence intensity and the minimum in FWHM is a hint for the complicated interplay

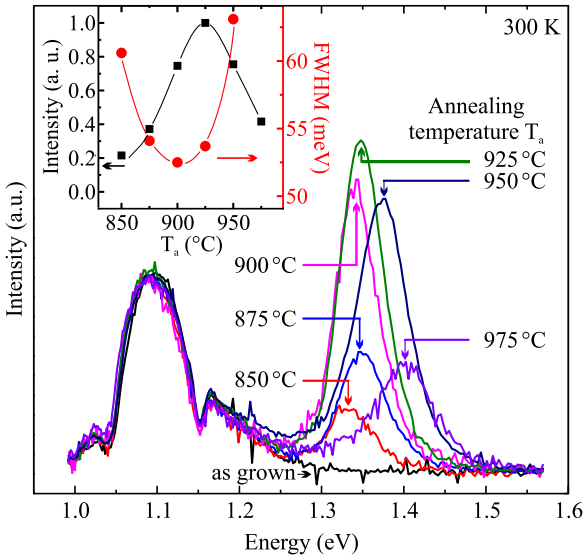

Fig. 1. Photoluminescence spectra of the Ga(N,As,P)-MQW samples measured at room temperature with an excitation energy of 2.33 eV and an excitation power of 7 W/cm^{-2}. The spectra are labeled according to the annealing temperature during RTA processing. The inset shows the integrated intensity of the Ga(N,As,P) luminescence (squares) and the full width at half maximum (circles) as a function of the annealing temperature T_a. The solid lines are guides to the eyes only.

between healing of non-radiative recombination centers on the one hand and creation of interface disorder caused by the enhanced mobility of atoms on the other hand.

Fig. 2 shows the Raman spectra of the Ga(N,As,P)-MQW samples in the range of 220–650 cm^{-1}. For all samples several sharp peaks can be observed. The distinct peak at 522 cm^{-1} can be attributed to the longitudinal and transverse optical phonons (labeled LTO$_\Gamma$) of the silicon substrate [8,9], which are degenerate at the Γ-point in momentum space. Furthermore, two sharp peaks at 404 cm^{-1} and 368 cm^{-1} can be observed corresponding to the LO- and TO-phonons of the GaP [10]. The observation of the TO$_\Gamma$-phonon should be prohibited in backscattering geometry but it can be seen here because (i) the GaP suffers strain due to the lattice mismatch of GaP to Si and (ii) due to the fact that we used a Raman microscope, that also collect light scattered under a small angle to the backscattering direction. The origin of the observed GaP phonons lies in the nucleation layer and in the barriers.

Furthermore, one can see a double structure consisting of a peak and a shoulder at 577 cm^{-1} and 597 cm^{-1}. These lines arise due to local boron modes of the two boron isotopes ^{11}B and ^{10}B on gallium lattice sites in (B,Ga)P [11], which is a substantial part of the MQWs barriers. The slight shift of these lines to higher wavenumbers and the broadening of these lines can be explained by the high concentration of boron (up to 5.5%) in our samples and the known trend of increasing wavenumber and linewidth with increasing boron content [12].

The phonon line at 302 cm^{-1} is caused by the GaAs-like LO-phonon. The GaAs LO-mode at the Γ-point is 292 cm^{-1} [13]. The incorporation of phosphorous [14] as well as of nitrogen [15] shifts the mode to smaller wavenumbers but the strain shifts the modes considerably to higher wavenumbers as has been shown for GaAs on GaP by Castrillo et al. [16].

The origin of the broad peak at 286 cm^{-1}, labeled with a question mark in Fig. 2, remains unclear. One may exclude the GaAs TO$_\Gamma$-phonons as a source for this signal, because one would expect a sharper peak at a lower intensity similar to the situation of the GaP modes. The broad peak may therefore also be a result of the incorporation of boron into the GaP barriers, since Hayes and

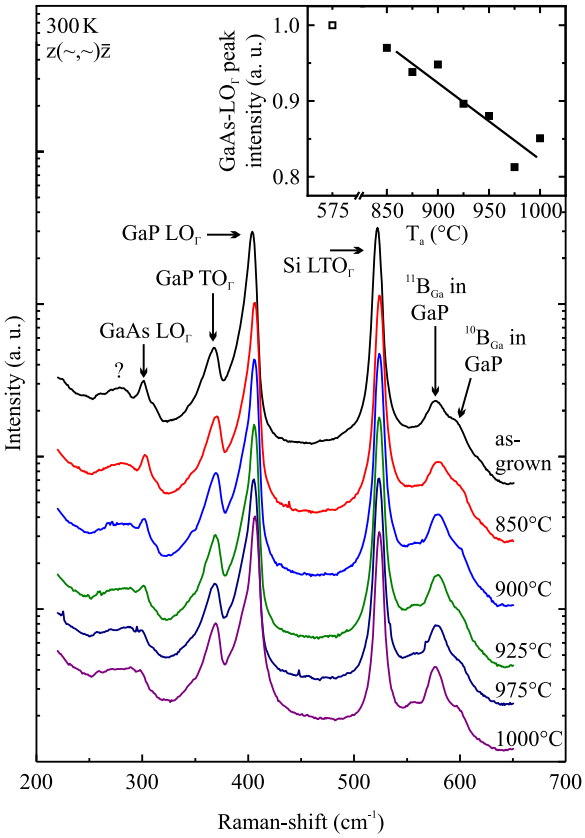

Fig. 2. Raman-spectra of the Ga(N,As,P)-MQW samples. The measurements were performed at room temperature in backscattering geometry using unpolarized light. For clarity the spectra are shifted with respect to each other and labeled according to the thermal annealing they underwent. The inset shows the intensity of the GaAs-LO$_\Gamma$ signal as a function of annealing temperature T_a. The as-grown sample is plotted at the growth temperature of 575 °C as an open symbol and the solid line is a guide to the eyes only.

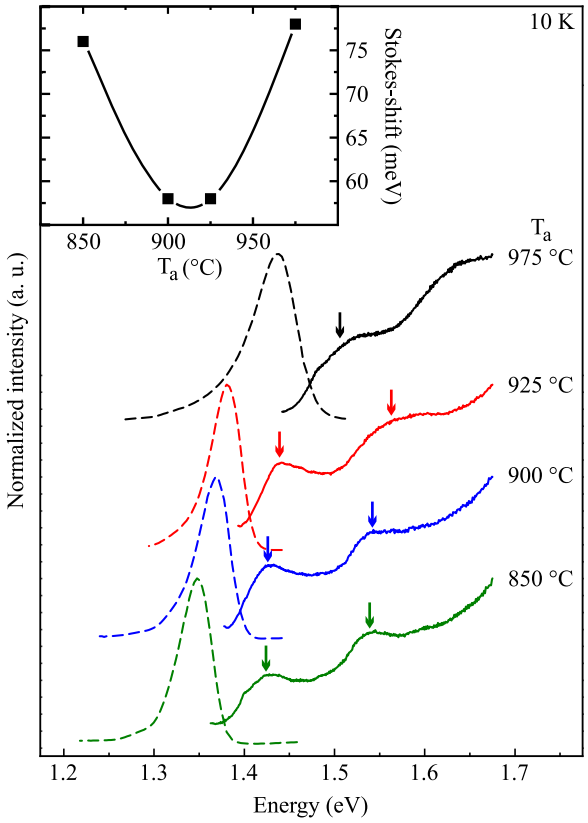

Fig. 3. Excitation spectra of the Ga(N,As,P) luminescence at a sample temperature of 10 K detected at the maximum of the corresponding PL, which is shown as broken lines. The spectra are labeled according to the temperature of each samples thermal annealing and shifted against each other. The arrows mark the positions of the excitation bands. In the inset the Stokes-shift as a function of annealing temperature is shown. The solid line is a guide to the eyes only.

co-workers found two modes at 284.2 cm^{-1} and 293.8 cm^{-1} [11], in boron-doped GaP which may also broaden with increasing boron content.

All these peaks do not shift regardless of the annealing temperature. Furthermore, the intensity of all peaks besides the GaAs LO$_\Gamma$–signal remains unchanged. It is clearly to be seen that the GaAs mode declines with increasing annealing temperature. The intensity of the GaAs LO$_\Gamma$–phonon peak is shown in the inset of Fig. 2. Again, the intensity of the as-grown sample is plotted with an open symbol at the growth temperature. Even for the smallest annealing temperature of 850 °C the intensity is reduced to approximately 97% of its initial value given by the as-grown sample. With increasing annealing temperature the GaAs LO$_\Gamma$–phonon intensity decreases further exhibiting about 85% of its initial value at an annealing temperature of 1000 °C. A diffusion of As atoms into the barriers and a partial exchange of As by P atoms from the barriers might be the reason.

The Raman observation is in accordance with the blueshift of the Ga(N,As,P) emission with increasing annealing temperature as depicted in Fig. 1. An exchange of arsenic and phosphorus between MQWs and barriers leads to lower arsenic and higher phosphorus concentration in the MQWs and therefore the emission undergoes a blueshift, since for Ga(As,P) the bandgap increases with increasing P content. Obviously, this process gets stronger at the higher annealing temperature. Assuming that the decreasing Raman signal is directly connected to a loss of arsenic one can estimate the relative loss between the sample annealed at 850 °C and at 1000 °C to be approx. 10%.

In what follows we want to compare the Raman results with a quantitative estimation of the excitonic blue shift caused by an arsenic–phosphorus-exchange. In order to get accurate access to the electronic changes of the quantum wells during the annealing procedure we performed PL-excitation (PLE) measurements. In Fig. 3 the results of the PLE measurements are depicted together with the corresponding PL peaks (dashed lines). The PLE reveals two excitation bands of the Ga(N,As,P) luminescence for all specimens, which corresponds to the heavy hole transitions e1–hh1 and e2–hh2. The light hole transition e1–lh1 is shifted to much higher energies due to the compressive strain and was beyond the accessible spectral region. It is obvious that the excitation bands follow the same blueshift with increasing annealing temperature as the PL peaks. In the inset of Fig. 3 the Stokes-shift is depicted for the lowest excitation band with respect to the PL peak. The Stokes-shift significantly decreases from approx. 75 meV to 55 meV for the samples annealed at 900 °C and 925 °C and increases again for higher annealing temperatures. This is caused by an initial reduction but an enhancement of disorder effects with rising annealing temperature. We will come back to this point later.

We will compare now the experimentally determined transitions with the results of QW-calculations including the respective band gap change of the QW, the band alignment, the mean strain in the QW and the barrier and the exciton binding energy. The comparison will allow for a quantitative estimation of the arsenic diffusion into the barriers. The bandgap of the quaternary Ga(N,As,P)-QWs is determined following basically the approach of Kudrawiec [17]. This model was slightly adjusted considering that the conduction band in Ga(N,P) undergoes a blueshift with increasing nitrogen content due to the repulsion with the nitrogen states [18].

Therefore, the conduction band is described by the E_+ state of the band anticrossing model (BAC) and not by the E_- solution as done by Kudrawiec. Furthermore, low temperature values for the bandgaps of GaAs and GaP and the positions of the nitrogen levels in these materials were used. To account for the strain we use the formula given by Asai and Oe [19] and calculate the energetic shifts of the bandgap for both the QW and the barriers. It should be noted that the QWs and the barriers are strained compressively with respect to the silicon substrate. The energetic levels of the confined electrons and holes were calculated independently assuming that the three quantum wells do not interact with each other because they are separated by 40 nm-thick barriers. Therefore, the problem is reduced to a single Ga(N,As,P) quantum well calculation with finite barriers of GaP. The parameters needed for the quaternary Ga(N,As,P) material have been determined according to Vegard's law from the respective parent materials. The exciton binding energy was kept constant, e.g. we assumed approximately no change upon the annealing process.

Using the compositions given in Section 2 we could fit the experimental PLE position of the sample annealed at T_a=850 °C. The blueshift for higher annealing temperatures was then translated into a relative change in the QWs composition by changing the bandgap also including the respective changes in strain. The level alignment was adjusted by keeping the offset ratio of conduction band and valence band constant. For the sample annealed at highest temperatures of T_a=975 °C we determined a resulting arsenic and phosphorous exchange in the Ga(N,As,P) layer of about 4% of As atoms. This result does not change significantly by using the smaller interaction matrix element of β=2.5 eV for the BAC in Ga(N,As) as found experimentally in Reference [20] instead of β=2.7 eV used in Reference [17].

It is interesting to note that we calculated a considerably higher change in the arsenic concentrations using the model proposed by Kunert et al. [21]. In the framework of this model we determined a value of approx. 10% As atoms to be exchanged by P at T_a=975 °C. The difference between the two models is caused by the different application of the BAC model. Whereas in the Kudrawiec-model the BAC is calculated only for the parent materials and an interpolation is used for the quaternary semiconductor QWs, in the latter model the BAC calculation was performed using the interpolated bandgap energy of the ternary Ga(As,P) and the nitrogen level. With decreasing As content the resulting anticrossing becomes stronger in the Kunert-model due to the reduced energetic distance between the conduction band and the N level. Therefore, more As atoms need to be exchanged in order to achieve the same blueshift as in the former model, where the transition to Ga(N,As,P) was achieved by using the bowing model and interpolating between Ga(N,As) and Ga(N,P).

As afore mentioned, on the one hand it was found that the highest PL intensity and smallest PL linewidth appears between 900 °C and 925 °C (see the inset of Fig. 1). Usually the maximum in intensity is a measure for highest crystalline perfection. On the other hand the As loss should create new imperfections or vacancies, which used to act as killer centers. To reveal the interplay, we will study in what follows the interplay of annealing temperature and disorder in the Ga(N,As,P) QWs.

In earlier papers [22–24] we could show that in Ga(As,P) containing N two disorder scales appear, a short ranged disorder due to the microscopic fluctuations as well as a long ranged disorder, most likely due to thickness fluctuations of the QWs. The parameters characterizing the respective disorder can be obtained by analyzing the temperature dependent PL of the Ga(N,As,P) MQWs. Fig. 4 depicts the so-called S-Shape, caused by the temperature dependence of the Ga(N,As,P) luminescence peak position. The short ranged disorder can be obtained from the critical temperature of the S-Shape as indicated by the arrows in

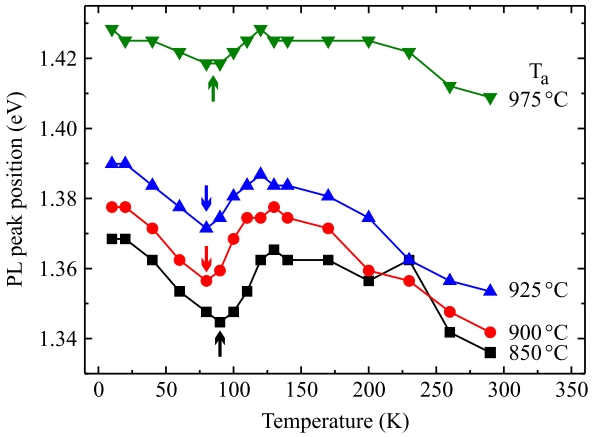

Fig. 4. Peak positions of the Ga(N,As,P) PL as a function of sample temperature. The arrows indicate the critical temperature crucial to calculate the short ranged disorder. For further explanation see text. The curves are not shifted and labeled according to their annealing.

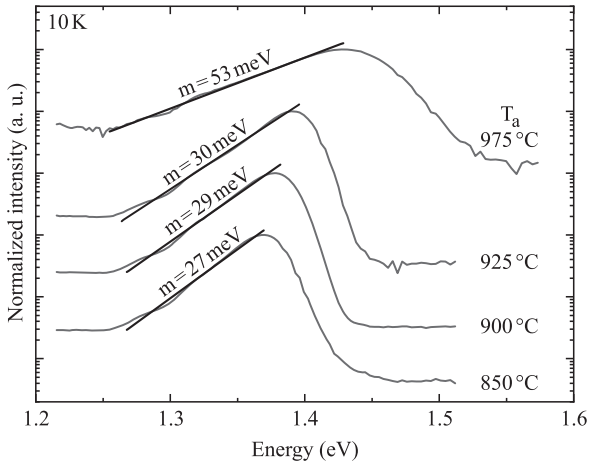

Fig. 5. Low temperature PL spectra of the Ga(N,As,P) luminescence (gray) and the corresponding fit curves of the low energy side (black). Furthermore, the slope for each curve is given. The spectra are labeled according to the annealing conditions.

Fig. 4, while the long ranged disorder scale is connected to the slope of the low energy tail of the low temperature PL [22]. A theoretical description of the correlation between these experimental features and the disorder potentials determined by the energy parameters is given in Reference [23].

The exponential slope of the low energy tail is shown in Fig. 5. As can be seen the long ranged disorder potential, which is determined by this slope, increases monotonously with increasing annealing temperature of the samples. Below T_a=925 °C the disorder parameter characterizing the long range disorder increases only slightly from m=27 meV to m=30 meV. For T_a=975 °C an abrupt increase to m=52 meV occurs, indicating a drastic change in the sample at this high temperature.

The determined energy parameters are depicted in Fig. 6 as a function of the samples annealing temperature. It is obvious that they show a different behavior.

First of all we should note that both disorder scales differ significantly in size. The short ranged scale is in the range of 10 meV, whereas the long range disorder varies between 30 meV and 50 meV. The values are very similar to those found for Ga(N,As,P) on GaP substrates [22]. The short ranged disorder is ascribed to the microscopic disorder mainly caused by the admixture of nitrogen, which strongly disturbs the crystal due to its high electronegativity and its small covalent radius compared to

phosphorous and arsenic. Remarkably, our samples on the Si substrate exhibit a similar value compared to the samples on GaP although the N content is considerably higher. The long ranged disorder is associated with well width fluctuations or strain fields [22]. Considering the trends shown in Fig. 6 we find the short ranged disorder to be minimal in the annealing temperature range between T_a=900 °C and T_a=925 °C, which correlates perfectly with the optimal PL intensity and the minimum of the PL FWHM and the Stokes shift (see the insets of Figs. 1 and 3, respectively). For higher and lower annealing temperatures the short ranged disorder increases. We explain this behavior as follows. Whereas at low T_a the healing of microscopic defects originating from the low temperature growth is not yet perfect an optimum can be achieved at about T_a=900 °C. Increasing the annealing temperature above 950 °C new microscopic defects occur. This new defects might be correlated with the afore mentioned arsenic loss and not perfect As–P exchange. The long ranged disorder shows a distinctly different behavior. For annealing temperatures up to 925 °C the disorder parameter is almost constant within the experimental error bars. For 975 °C, however, a much higher value appears, almost enhanced by a factor of 2. We have to conclude that the high annealing temperature not only enhances microscopic disorder but in parallel results in extra long range disorder. The most likely explanation is the formation of strain fields and/or well width fluctuations due to the As–P exchange.

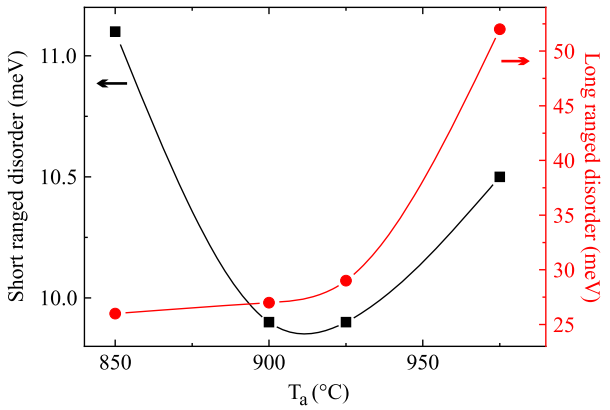

Fig. 6. Comparison of the short ranged disorder (squares) and the long ranged disorder (circles). The short ranged disorder is plotted against the left ordinate and the long ranged disorder against the right ordinate. The lines are guides to the eyes only.

Finally, we want to examine whether these results can be confirmed by TEM measurements. In Fig. 7 TEM images are depicted for the as-grown sample (a) and two specimens annealed at T_a=925 °C (b) and T_a=975 °C (c). The pictures were taken in the HAADF scanning mode. The intensity in these images is proportional to Z^n, where Z is the atomic number and n is a variable close to 2, which is the value for unscreened Rutherford scattering [25]. For materials containing strain at a local scale, there is a further contrast mechanism arising from Huang scattering [26], which can enhance the intensity, however, the contrast depends strongly on the imaging conditions. We have shown this for dilute nitrides on GaAs [27,28]. Therefore, layers containing heavier atoms and higher strain have higher intensities and appear brighter than layers containing lighter atoms or lower strain, as it can be seen in Fig. 7(a)–(c). In these pictures the Ga(N,As,P)-QW appears brighter than the surrounding (B,Ga)P barriers because of the high percentage of As in the QW. Furthermore, in Fig. 7(d)–(f) the corresponding intensity profiles are depicted for the investigated samples. These were obtained from line-scans taken parallel to the growth direction and were integrated over 162.5 nm. The measured intensities were background corrected and normalized to the intensity of the (B,Ga)P barriers. In this way it is accounted for the thickness variation of the TEM samples and its effect on the intensity.

Let us start with the as-grown sample (Fig. 7(a)). The interfaces between QW and barriers are rather sharp. This result is confirmed by the corresponding intensity profile depicted in Fig. 7(d). Taking a closer look, in the interface region a dip in the intensity profile can be seen between the (B,Ga)P barriers and the Ga(N,As,P)-QW. This section is about 5 nm wide and corresponds therefore to the GaP interlayer. From Z-contrast as described above one would expect a higher intensity for the GaP layer than for the (B,Ga)P barrier, because Ga has a higher Z than B. The reason for the opposing behavior is again the reduced strain fluctuations in the binary compound compared to the B containing (B,Ga)P lattice.

At an intermediate annealing temperature of 925 °C the interfaces of the QW, especially the upper one, become rougher and the QW starts to get more disordered, as can be seen in Fig. 7(b). The corresponding intensity profile in Fig. 7(e) also shows a wider QW with a decreased peak intensity compared to the as-grown sample. This effect becomes even stronger with further increasing annealing temperature. In Fig. 7(c) the HAADF-image is given for T_a=975 °C. It is obvious that the disorder is even higher. Correspondingly, the intensity profile of the Ga(N,As,P)-QW exhibits a peak with further reduced height but substantially broadened.

The explanation for this behavior is as follows. With increasing annealing temperature the arsenic and/or nitrogen atoms diffuse

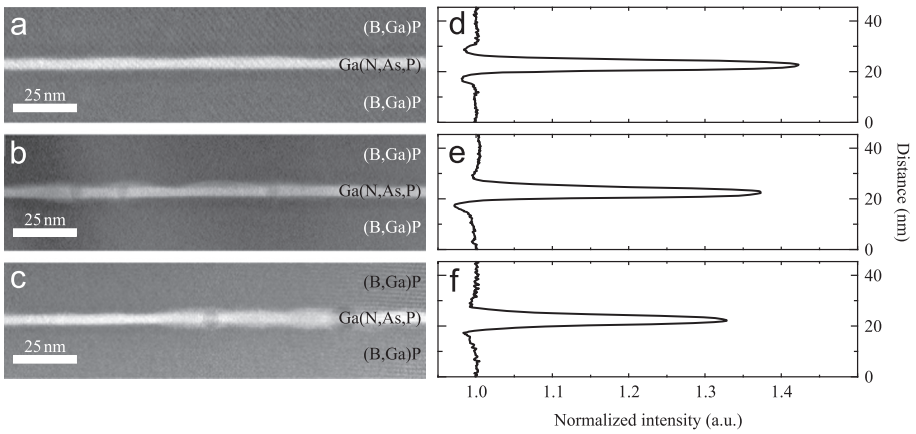

Fig. 7. Low magnification HAADF-images of the as-grown specimen (a) and the samples annealed at T_a=925 °C (b) and T_a=975 °C (c). The corresponding normalized intensity profiles are depicted in (d), (e) and (f). The growth direction is from bottom to top.

out of the QWs. A quantitative discussion how much of the lattice sites are replaced by diffusion of phosphorous atoms from the barrier is not straightforward and therefore beyond this discussion. Anyway, arsenic loss in the QWs is consistent with the overall reduction of the Ga(N,As,P) peak signal with increasing annealing temperature. This result is in perfect agreement with the PL, PLE and Raman measurements, where an exchange of As and P with increasing annealing temperature has been found.

Finally, it should be mentioned that the interdiffusion of QW material with the GaP barrier is obviously not necessarily homogeneous, as it can be seen clearly in Fig. 7(c). Extended areas of the interfaces suffer a strong interdiffusion whereas others seem to be less disturbed. This is most likely the explanation for the strong enhancement of the long ranged disorder parameter at T_a=975 °C afore mentioned and depicted in Fig. 6.

4. Conclusion

The RTA-annealing of Ga(N,As,P)-MQWs has been investigated using PL-, PLE- and Raman-spectroscopy as well as transmission electron microscopy. In terms of disorder the optimal annealing conditions were found to be in the temperature range of 900–925 °C. The short ranged disorder shows the smallest values in this temperature range and the long ranged disorder is just slightly enhanced and rather small compared to higher annealing temperatures. Furthermore, the PL-intensity exhibits a maximum in this temperature interval and the FWHM and the stokes-shift show a minimum. The QW-excitons show a blueshift upon increasing annealing temperature for the emission as well as for the excitation band. This is caused by an exchange of arsenic and phosphorous atoms between the MQWs and barriers. Comparison of the experimental results with QW-calculations reveal an arsenic loss of about 5 to 10% for the sample annealed at T_a=975 °C relative to the sample annealed at T_a=850 °C. The Raman measurements also indicate an As–P exchange in the QWs caused by the annealing. The reduction in the arsenic concentration is estimated from the Raman measurements based on the GaAs LO_I–signal. An As loss of about 10% was found. TEM measurements support this interpretation. The intensity profile is consistent with a diffusion of As out of the QWs. We have to conclude that the annealing procedure which is necessary to improve the PL performance is inevitably accompanied by an As–P exchange in the range of about 5–10%. Finally, we should mention that a nitrogen diffusion may be possible as well. In principle, a diffusion of N out of the QWs would also lead to the observed blueshift of the QWs PL-emission due to the reduced band repulsion of the N states and the conduction band. Even a reduction of the intensity profiles in TEM analysis is expected due to the reduced strain fluctuations. The Raman measurements, however, have shown convincingly an diffusion from As atoms out of the QWs, which alone is sufficient to explain all the results.

Acknowledgments

We gratefully acknowledge support of the German Science Foundation (DFG) in the framework of the GRK 1782.

References

[1] B. Kunert, et al., Phys. Status Solidi C 3 (2006) 614.
[2] B. Kunert, A. Klehr, S. Reinhard, K. Volz, W. Stolz, Electron. Lett. 42 (2006) 601.
[3] S. Liebich, et al., Appl. Phys. Lett. 99 (2011) 071109.
[4] K. Volz, et al., J. Cryst. Growth 315 (2011) 37.
[5] B. Kunert, I. Németh, S. Reinhard, K. Volz, W. Stolz, Thin Solid Films 517 (2008) 140.
[6] B. Kunert, et al., J. Cryst. Growth 315 (2011) 28.
[7] B. Kunert, D. Trusheim, V. Voßbürger, K. Volz, W. Stolz, Phys. Status Solidi A 205 (2008) 114.
[8] J.H. Parker, D.W. Feldman, M. Ashkin, Phys. Rev. 155 (1967) 712.
[9] C. Wang, J. Chen, R. Becker, A. Zdetsis, Phys. Lett. A 44 (1973) 517.
[10] A.S. Barker, Phys. Rev. 165 (1968) 917.
[11] W. Hayes, H.F. Macdonald, C.T. Sennett, J. Phys. C: Solid State Phys. 2 (1969) 2402.
[12] S. Rogowsky, et al., J. Appl. Phys. 109 (2011) 053504.
[13] A. Mooradian, G. Wright, Solid State Commun. 4 (1966) 431.
[14] E. Jahne, B. Ulrici, Phys. Status Solidi B 101 (1980) 169.
[15] M. Güngerich, et al., Phys. Rev. B 71 (2005) 075201.
[16] P. Castrillo, G. Armelles, J.P. Silveira, F. Briones, J. Barbolla, Appl. Phys. Lett. 71 (1997) 1353.
[17] R. Kudrawiec, J. Appl. Phys. 101 (2007) 116101.
[18] M. Güngerich, et al., Phys. Rev. B 74 (2006) 241202.
[19] H. Asai, K. Oe, J. Appl. Phys. 54 (1983) 2052.
[20] P.J. Klar, et al., Appl. Phys. Lett. 76 (2000) 3439.
[21] B. Kunert, K. Volz, J. Koch, W. Stolz, Appl. Phys. Lett. 88 (2006) 182108.
[22] C. Karcher, et al., J. Lumin. 133 (2013) 125.
[23] K. Jandieri, et al., Phys. Rev. B 86 (2012) 125318.
[24] C. Karcher, et al., Phys. Rev. B 82 (2010) 245309.
[25] S. Pennycook, B. Rafferty, P. Nellist, Microsc. Microanal. 6 (2000) 343.
[26] Z.L. Wang, Acta Crystallogr. A 51 (1995) 569.
[27] T. Grieb, et al., Ultramicroscopy 129 (2013) 1.
[28] T. Grieb, et al., Ultramicroscopy 117 (2012) 15.

6.6 Correlation of the nanostructure with optoelectronic properties during rapid thermal annealing of Ga(NAsP) quantum wells grown on Si(001) substrates [1]

T. Wegele, A. Beyer, S. Gies, M. Zimprich, W. Heimbrodt, W. Stolz, and K. Volz, Journal of Applied Physics **119**, 025705 (2016). DOI: 10.1063/1.4939889.

Abstract

Ga(NAsP) quantum wells grown pseudomorphically on Si substrate are promising candidates for optically active light sources in future optoelectronically integrated circuits on Si substrates. As the material is typically grown at low temperatures, it has to be thermally annealed after growth to remove defects and optimize optoelectronic properties. Here we show by quantitative transmission electron microscopy that two different kinds of structural development are associated with the annealing. First of all, the quantum well homogeneity improves with increasing annealing temperature. For annealing temperatures above 925 °C the composition becomes less homogeneous again. Second, voids form in the quantum well for annealing temperatures above 850 °C. Their density and size increase continuously with increasing annealing temperature. These results are correlated to the optical properties of the samples, where we find from temperature-dependent photoluminescence measurements two scales of disorder, which show the same temperature dependence as the structural properties.

My Contribution

The specimen preparation – with the exception of the lamella – and the STEM measurements for different angular ranges of a detector were carried out by me. I quantitatively analysed the STEM micrographs and wrote a first draft of the manuscript.

1 Reprinted from *Journal of Applied Physics* ***119****, 025705 (2016)*

JOURNAL OF APPLIED PHYSICS **119**, 025705 (2016)

Correlation of the nanostructure with optoelectronic properties during rapid thermal annealing of Ga(NAsP) quantum wells grown on Si(001) substrates

Tatjana Wegele, Andreas Beyer, Sebastian Gies, Martin Zimprich, Wolfram Heimbrodt, Wolfgang Stolz, and Kerstin Volz
Faculty of Physics and Material Sciences Center, Philipps-Universität Marburg, 35032 Marburg, Germany

(Received 17 November 2015; accepted 2 January 2016; published online 13 January 2016)

Ga(NAsP) quantum wells grown pseudomorphically on Si substrate are promising candidates for optically active light sources in future optoelectronically integrated circuits on Si substrates. As the material is typically grown at low temperatures, it has to be thermally annealed after growth to remove defects and optimize optoelectronic properties. Here we show by quantitative transmission electron microscopy that two different kinds of structural development are associated with the annealing. First of all, the quantum well homogeneity improves with increasing annealing temperature. For annealing temperatures above 925 °C the composition becomes less homogeneous again. Second, voids form in the quantum well for annealing temperatures above 850 °C. Their density and size increase continuously with increasing annealing temperature. These results are correlated to the optical properties of the samples, where we find from temperature-dependent photoluminescence measurements two scales of disorder, which show the same temperature dependence as the structural properties. © *2016 AIP Publishing LLC*.
[http://dx.doi.org/10.1063/1.4939889]

INTRODUCTION

Efficient and stable laser materials need to be realized for future Si-based optoelectronic and photonic integrated circuits. Thereto, various concepts have been discussed in the past years.[1–7] In this regard it is promising to use an optoelectronically active laser material, which can be pseudomorphically grown on Si(001) substrates, as there are several advantages if dislocations can be avoided from the beginning. Ga(NAsP) was shown to have a direct band gap for compositions of [As] > ∼70% and can be grown pseudomorphically strained on Si.[8–10] Ga(NAsP) quantum wells (QWs) have a high optical quantum efficiency,[11] which is underlined by the observation of room-temperature lasing action on GaP[12] and low temperature lasing action on Si substrates.[13] However, as Ga(NAsP) is conventionally grown at low temperatures to incorporate sufficient amounts of nitrogen, defects, which act as non-radiative recombination centers, are typically incorporated during growth. Thus, thermal annealing procedures have to be applied after growth to recover optimum optoelectronic performance.[14,15] This annealing can go along with rearrangement of the atoms in the QW. From the electronic point of view, two scales of disorder have been shown in dilute nitride samples, and their tentative origin has been attributed to alloy disorder and well width fluctuations. There has, however, been no study yet, where electronic and structural disorders have been correlated. Therefore, the present paper deals with a nanoscale analysis of annealing effects on the structure, morphology, and composition of Ga(NAsP) QWs grown on Si. The findings are correlated to the optoelectronic properties of the samples.

EXPERIMENTAL DETAILS

The Ga(NAsP)-QWs investigated here are part of multi-QW (MQW) laser structures grown by metal organic vapour phase epitaxy (MOVPE) in a horizontal reactor system (AIX 200-GFR) at 575 °C on GaP/Si templates. The GaP/Si templates consist of about 50 nm GaP nucleated on exactly oriented Si(001) substrates in a commercial Aixtron Crius R 300 mm III/V-Si-cluster tool under conditions described in Refs. 9, 16, and 17. Details on the growth and structural characteristics of the Ga(NAsP) material systems directly after growth have been given previously in Refs. 18 and 19. The composition of the Ga(NAsP) QW used for this study was: [N] = 7%, [P] = 11%, and consequently [As] = 82%. Each of the three about five nm thick Ga(NAsP) QWs is sandwiched between two thin GaP-barriers separated from each other by about 30 nm thick (BGa)P-layers. The main function of the GaP-barriers in this case is to prevent the formation of the B-N-bonds that might act as non-radiative recombination centres.[20] The MQW is sandwiched between two 500 nm thick (BGa)(AsP) separate confinement structures. A schematic of the investigated layer structure is shown in Figure 1. In order to improve the optoelectronic properties of the dilute nitride material, rapid thermal annealing (RTA) has been applied[15] (Jipelec JetFirst 200 C). RTA took place at different temperatures starting from 850 °C up to 1000 °C with temperature ramping rates of 50 °C/s. It was conducted for 10 s in N_2 carrier gas at atmospheric pressure. As there is a strong dependence of the optoelectronic properties on the annealing conditions,[14,15] it is the topic of this paper to examine the nanostructure of the annealed samples in detail.

Transmission electron microscopic investigations were hence performed using a JEOL JEM 3010 at 300 kV acceleration voltage and a double-spherical aberration corrected JEM 2200 FS at 200 kV. The JEM 3010 was operated in a dark field (DF)-two beam condition mode whereby the strain

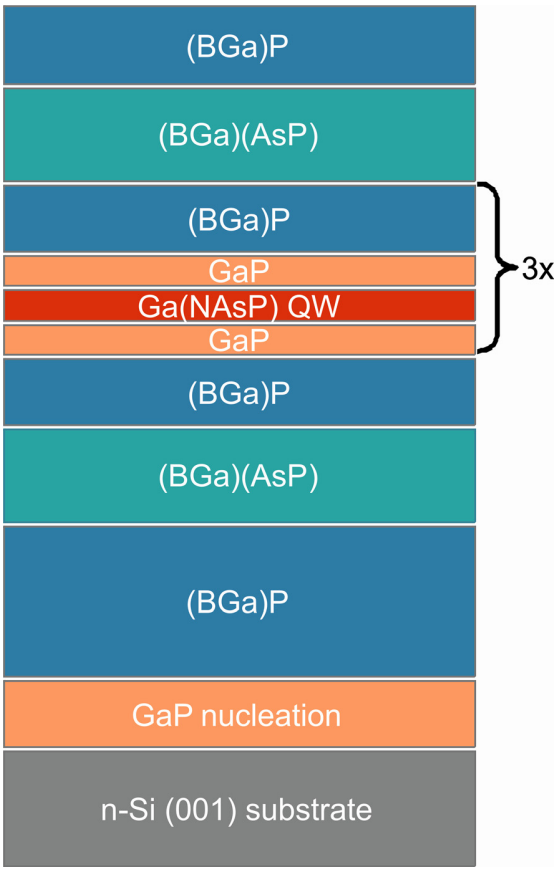

FIG. 1. Schematics of the investigated layer structure.

sensitive (202)-diffraction spot was chosen. The excitation condition with the centre of Laue circle (COLC)[21] at (−10 0 12) was optimized using the JEMS-software[22] so that DF(202)-intensity has its maximum and shows just negligible dependence on the TEM specimen thickness in the thickness range between 20 and 45 nm. The JEM 2200 FS was used in scanning mode (scanning transmission electron microscopy: STEM) to carry out high angle annular DF (HAADF) measurements for different inner angles of the annular detector (33, 57, 75, and 95 mrad) in order to gain information about the distribution of the chemical components in the QWs separately.[19,23–25] For small detector inner angles, the scattered signal is more sensitive to influences of the local strain induced, for example, by the small N atoms in the structure. At higher inner angles, the signal is sensitive to the composition, i.e., to the atomic number of the atoms in the investigated atomic columns as well as to the specimen thickness. The inner radius of the detector was measured as described in Ref. 26 and calibrated for different camera lengths of the microscope using the known diameter of the shadow of a condenser lens aperture for calibration. The outer angle of the annular detector is 4 times larger than the inner one. The microscope geometry, however, restricts this outer acceptance angle to 170 mrad. The brightness and contrast values of the HAADF detector were chosen so that the entire dynamic range of the detector could be used as far as possible and that the saturation of the detector could be avoided for investigations of specimen regions with somewhat varied thicknesses and for changing the range of the detector angles. The beam dwell time was 20 μs, and the image size was 1024 × 1024 pixels. The STEM images were evaluated using a procedure as described in Ref. 19. In short, the evaluation method includes normalization of the scattered HAADF intensity to the intensity of the incident beam,[26] correction of the 2D-thickness gradient in the STEM images, identification the QW position in the image choosing a suitable threshold, and normalization of the QW intensities to the mean intensity in the QW. The standard deviation of the mean intensity in the QW, which is a measure of the compositional fluctuation was corrected for experimental influences as following:

$$\sigma_i/\text{mean intensity} = \sqrt{(\sigma_{\text{QW}}/\text{mean intensity in QW})^2 - (\sigma_{GaP}/\text{mean intensity in GaP})^2}.$$

Here, σ_{QW}/mean intensity in QW is the compositional fluctuation in the QW containing also background fluctuations σ_{GaP}/mean intensity in GaP because of the amplifier noise, beam damage, and sample roughness due to TEM specimen preparation.

The TEM specimens were prepared conventionally by mechanical grinding followed by Ar^+-ion milling in the [010]-direction of the crystal. Parasitic hydrocarbons were removed from the sample surfaces by plasma cleaning prior to inserting the specimen in the TEMs.

Photoluminescence (PL) studies have been performed using an Ar-ion laser operating at a wavelength of 514.5 nm for excitation. The PL-signal has been dispersed by a 1 m grating monochromator (Jobin-Yvon) and detected by a liquid N_2 cooled Ge-detector applying standard lock-in techniques. All PL spectra shown here were recorded at room temperature. Furthermore, PL spectra were measured at temperatures from 4 K to room temperature and the electronic disorder in the samples, which can be determined from the temperature-dependent shift of the maximum PL energy, was calculated according to Refs. 27 and 28.

RESULTS AND DISCUSSION

In the following, the optoelectronic properties for Ga(NAsP) QWs annealed at different temperatures will be correlated to their composition and structure addressed using STEM imaging.

The room temperature PL of the same Ga(NAsP) MQW heterostructures ([N] = 7%, [P] = 11%) annealed at different temperatures is shown in Figure 2. The QW signal is around 1.3–1.5 eV, whereas the PL peak around 1.1 eV results from the doped Si substrate. Whereas the as grown sample does not show any PL from the QW under the excitation conditions used, the PL intensity increases for annealing temperatures up to 925 °C and drops again for higher annealing temperatures. This is also in accordance with the PL linewidth, which reaches its minimum between 875 and 925 °C annealing temperature and increases significantly above 925 °C. By analysing the well-known S-shape of the PL maximum in temperature dependent measurements, two different scales of disorder were previously shown to be present for many dilute nitride materials.[27,28] Also the samples investigated here show these two scales of disorder, which, however, exhibit a highly different behaviour in dependence on the annealing temperature, as depicted in the inset of Figure 2.[15] The short range disorder has its minimum around 925 °C annealing temperature, whereas the long range disorder increases continuously with increasing annealing temperature. Up to now, it is unclear which characteristic structural features of the QWs are the reasons for these two scales of disorder.

For the following structural characterization, the samples annealed at 925 °C (highest PL signal, lowest short range disorder) and 975 °C (low PL signal, strongest long range disorder) have been chosen and are compared with the as grown sample (no PL signal). The TEM micrograph of the as grown Ga(NAsP)-QW (dark middle layer) acquired under DF two beam conditions using the strain-sensitive (202)-diffraction spot is shown in Figure 3. One can clearly see some contrast (i.e., strain) fluctuations caused by an inhomogeneous distribution of the QW components in the Ga(NAsP). The contrast fluctuations reveal some kind of periodicity and one can differentiate between nearly 35 nm large scale strain fields (white arrows) and approximately 5 nm short ranged strain fields (red arrows). The origin of the latter strain fluctuation is most likely the formation of N-chains in the QW because they appear to be very columnar. Hence, there is a significant N-accumulation in these regions. Chain-like arrangement of N in ⟨001⟩ directions has been shown to be stable in several dilute nitride materials.[29,30] The overlap of these short scale strain fields can lead to the observed large scale periodicity like in Ga(NAs) QWs as already described in Ref. 31. The inhomogeneity of the strain in a QW always goes along with a compositional fluctuation. Therefore, we investigated the composition as well as its homogeneity using STEM HAADF at higher magnifications. Figures 4(a)–4(d) show the STEM migrographs of Ga(NAsP) QWs between the two GaP barrier layers grown at the same conditions, but annealed under different conditions. The first one was without thermal treatment after growth, and the three others were annealed for 10 s at 850 °C, 925 °C, and 975 °C, respectively. The as grown Ga(NAsP) QW shows a rough upper interface typical for growth temperatures of 575 °C and above[18] and a very smooth lower interface. The specimen annealed at 850 °C shows no structure development compared with the as grown one. The specimen annealed at 925 °C, however, exhibits spherical features with dark contrast in the QW. Originating from these one also observes brighter contrast spreading out on both sides of the Ga(NAsP) QW into the GaP barrier. The origin of this brighter contrast is outdiffusion of the components of the Ga(NAsP) QW into the GaP or a higher strain in these regions compared with the remaining material. The effect becomes more pronounced at higher annealing temperature: the circular dark features become larger and the width of the QW at some positions becomes twice as large as that in the as grown or 850 °C-annealed QWs. Furthermore, the density of the circular features becomes higher with increasing annealing temperature. It should be noted at this point that "simple" outdiffusion of As and N from the QW into the GaP barrier is unlikely to be the only process observed here. Diffusion is a process following a composition gradient and hence would not result in spherical structures if the underlaying concentration gradient was along a two-dimensional QW. The composition fluctuation map (intensity at each

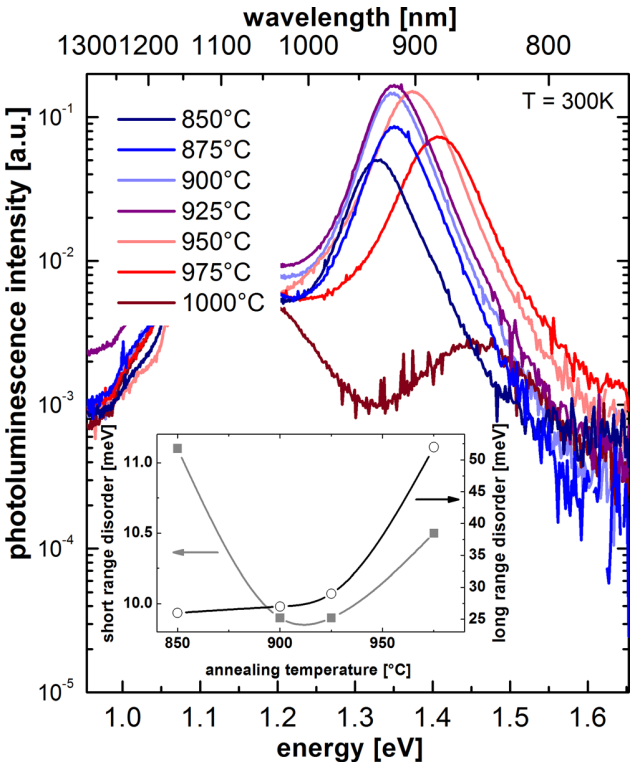

FIG. 2. Room temperature photoluminescence of the same Ga(NAsP) MQW, annealed in an RTA process for 10 s at different temperatures. The inset shows for different annealing temperatures the evaluation of the two different disorder scales present in the samples, as derived from temperature-dependent PL.[15]

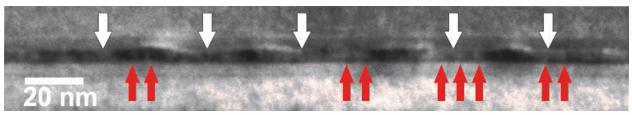

FIG. 3. Strain sensitive DF(202)-TEM micrograph of as grown (BGa)P/GaP/Ga(NAsP)/GaP/(BGa)P-layers in a [010]-cross-section. The white arrows exemplarily mark large scale local strain fields and the red arrows short scale ones. The growth direction is from bottom to top.

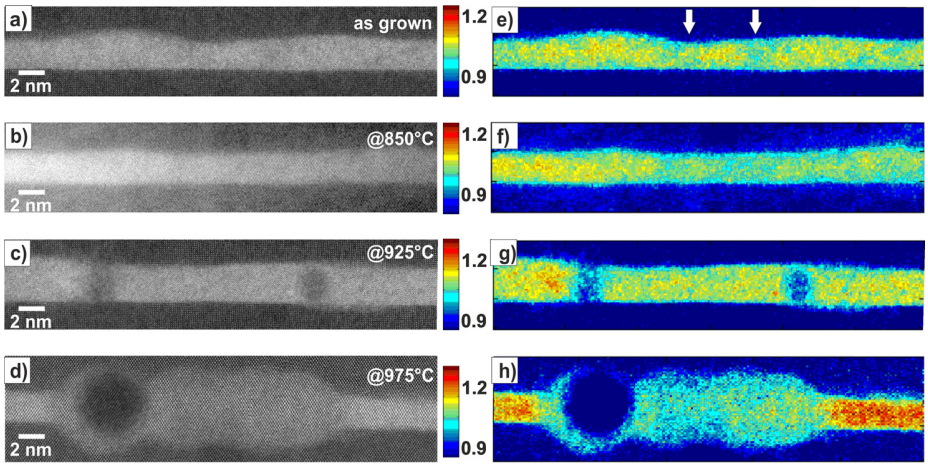

FIG. 4. STEM-micrographs of Ga(NAsP)-layers as grown (a), annealed at 850 °C (b), 925 °C (c), and 975 °C (d) and the corresponding compositional fluctuation maps (e)–(h). The growth direction is from bottom to top. The two white arrows in (e) mark regions with lower dark field intensity. As for this image a large inner detector angle has been used, these regions might contain more nitrogen than the environment. Hence, they would be compatible with the N-chains concluded from Figure 2.

point normalized by the average intensity in the QW)[19] of the as grown (Figure 4(e)) specimen looks rather homogeneous. The same is true for the sample annealed at 850 °C (Figure 4(f)). Figure 4(g) (for the sample annealed at 925 °C) shows the outdiffusion of material into the GaP barrier more clearly than the original STEM-micrograph. The size and distance of the dark contrast regions are in accordance with the short scale strain fields that were observed in the DF(202) image before (Figure 3). The dark contrast features in the Ga(NAsP) annealed at 975 °C (Figure 4(h)) have nearly the same intensity as the GaP-barriers. There is a remarkable overlay of several of these features and again their distance resembles the distance between the N enrichments concluded from Figure 3.

In order to be able to gain more insight into the processes taking place during the rearrangement of the QW material in the annealing process, the compositional fluctuation in the QWs was also evaluated quantitatively. Figure 5 shows the compositional fluctuation in the QW as defined in the experimental section in dependence on the inner detector angles of the HAADF. The samples have been evaluated taking the dark contrast features into account and neglecting them, respectively. Including the dark features in the evaluation shows that the compositional fluctuation increases with increasing annealing temperature for all detector inner angles (compare the grey filled triangle: as grown $\Longleftrightarrow$ green filled sphere: 925 °C $\Longleftrightarrow$ red filled square: 975 °C). Especially for the highest annealing temperature examined, one can clearly conclude that the sample becomes significantly more inhomogeneous on average. It is worth mentioning that the evaluation of the QW material between the dark contrast features results in a different picture: the QW material homogenizes for an annealing temperature of 925 °C compared with the as grown sample before it becomes more inhomogeneous at the annealing temperature of 975 °C again (compare the grey filled triangle: as grown $\Longleftrightarrow$ green half-filled sphere: 925 °C $\Longleftrightarrow$ red half-filled square: 975 °C). This can be seen more clearly in Figure 6, where the data on contrast fluctuation are plotted versus the annealing temperature. As described before, the sample annealed at 925 °C shows minimum inhomogeneity on a short range length scale. This is true for all detector inner angles chosen. This means that the composition is homogenizing/inhomogenizing approximately at the same scale for N (can be seen at low detector inner angles) as for As/P (can be seen at high detector inner angles). The data have been correlated to the short range electronic disorder concluded from PL measurements, which has already been shown in the inset of Figure 2. Clearly, there is the same trend in short range compositional disorder scale as in short range electronic disorder scale. This suggests that the short range electronic disorder is originating from nanoscale compositional fluctuations. The long range electronic disorder scale did, however, increase with increasing annealing temperature. Hence, this cannot be explained with the compositional fluctuations on a short length scale. However, when the compositional fluctuation including the

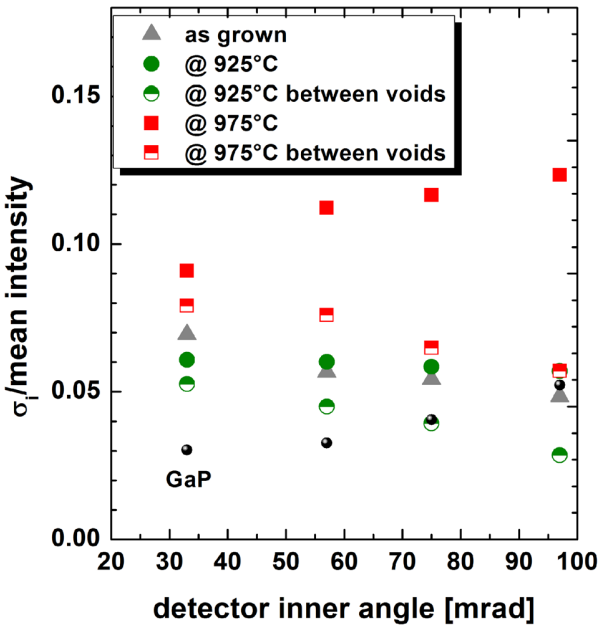

FIG. 5. Compositional fluctuation in the Ga(NAsP) QWs in dependence on the inner detector angle for the as grown specimen (grey triangles), for the specimen annealed at 925 °C (filled green spheres: including dark features; half-filled green spheres: excluding dark features), and for the specimen annealed at 975 °C (filled red squares: including dark features; half-filled red squares: excluding dark features). The data have been corrected by the measured GaP intensity (small black spheres) as described in the experimental section.

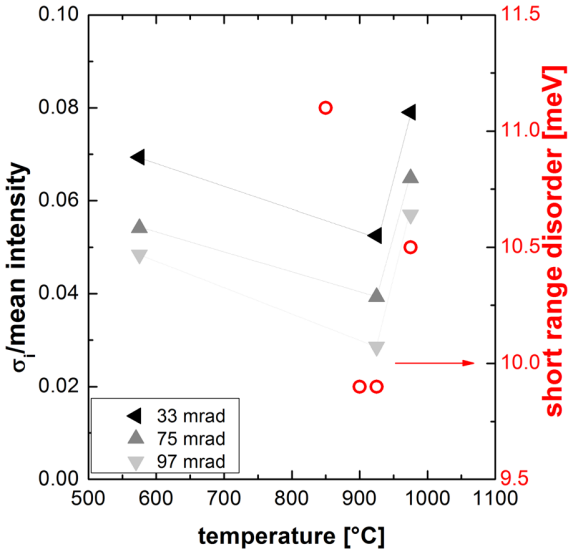

FIG. 6. Compositional fluctuation in the Ga(NAsP) QWs in dependence on the annealing temperature for different detector inner angles (only the homogeneous parts of the QWs have been selected for the analysis). The lines connecting the data points are only guides to the eye. The data have been corrected by the measured GaP intensity shown in Figure 4. To show the correlation, the data on the short range order from the inset of Figure 1 are also shown (red open symbols).

dark contrast features, i.e., on a long length scale, is plotted together with the long range electronic disorder (Figure 7) there is an excellent correlation between those two disorders as well. This suggests that the dark features in the QW, which are responsible for the long range compositional disorder, are also responsible for the long range electronic disorder. Comparing the data on different detector inner angles at the different annealing temperatures with each other, one observes that both the strain-related as well as the As/P-composition-related disorders increase with increasing annealing temperatures.

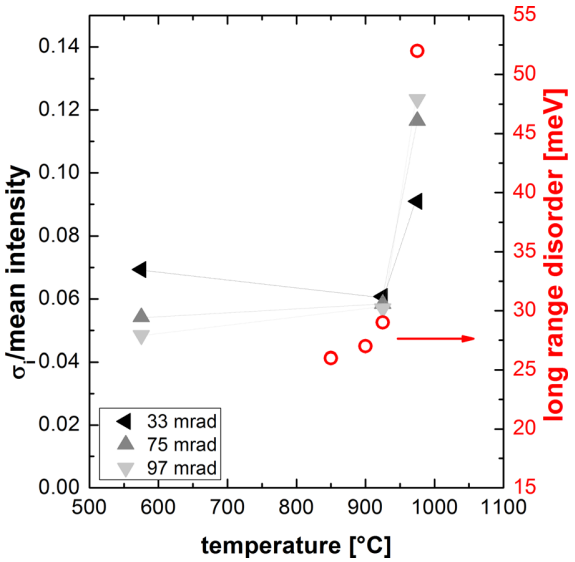

FIG. 7. Compositional fluctuation in the Ga(NAsP) QWs (including the circular contrast features) in dependence on the annealing temperature for different detector inner angles (the data points have been connected with lines to guide the eye). The data have been corrected by the measured GaP intensity shown in Figure 4. To show the correlation, the data on the long range order from the inset of Figure 1 are also shown (red open symbols).

The contrast of the dark regions in Figures 4(c) and 4(d) is compatible with voids in the QW. Those might form during the annealing process. For the clarification, additional high resolution STEM investigations were carried out at different defocus values, utilizing the reduced depth of focus in an aberration corrected instrument.[32] Figure 8(a) shows the region of a Ga(NAsP) QW with a dark contrast feature and the focus of the electron beam adjusted to the dark region. This results in the QW region surrounding the dark feature being out of focus. If the bright QW region is focused, the crystalline planes in the dark feature blur, as shown in Figure 8(b). The defocus difference between these two STEM micrographs was 30 nm. This means that the bright and dark QW regions have a different thickness or different amount of material, what confirms the assumption that voids are formed in the Ga(NAsP) QWs after annealing. As these voids or hollow pores of course have a large surface area, carriers, which are optically excited in the QW, can recombine at the surface

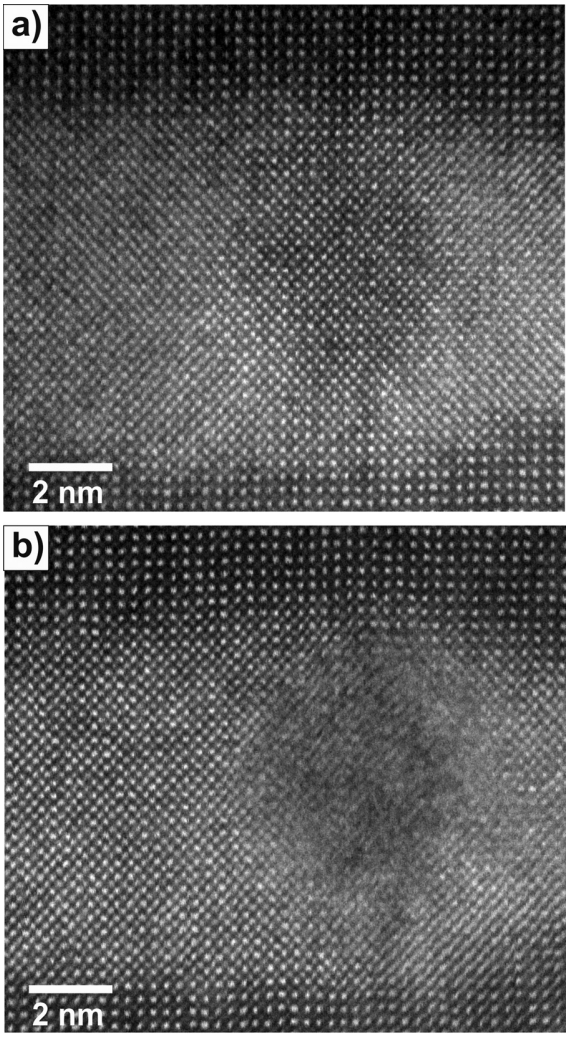

FIG. 8. High resolution STEM micrographs of the dark regions in the Ga(NAsP) QW of the specimen annealed at 925 °C. (a) Focused immediately on the dark region and (b) focused on the QW region surrounding the dark region. The difference in defocus between these two images is 30 nm. The [010]-cross section was measured at 34 mrad inner detector angle.

states associated with the voids. As both, the diameter of the pores as well as their density increases with increasing annealing temperature, this can also explain the increasing long range electronic disorder.

At present, one can only speculate on the processes taking place during RTA leading to the formation of the hollow pores. One explanation is related to the inhomogeneous distribution of N in chain-like arrangements after growth. As has been shown, the strain fields from the N-rich areas have about the same distance than the later voids. It might be that the N diffuses over short distances during the annealing and finds, in regions where its density is already high, another N atom easily. This process might result in the formation of N_2, which in turn could lead to a high gas pressure at these locations and the formation of voids in the structure. The remaining material would, for example, be transported to the edge of the voids, which also is compatible with the observed contrast in STEM imaging.

Future investigations will focus on the understanding of the void formation, especially by investigating the ternary base materials Ga(NP) and Ga(NAs), but also by researching the influence of different group V stabilizations on the void formation. Large group V overpressures could lead to suppressed vacancy-mediated diffusion on the group V sublattice. It is also planned to study these processes *in-situ* in the microscope.

SUMMARY

Ga(NAsP) grown pseudomorphically strained on Si substrates has to be thermally annealed after growth to improve the optoelectronic properties. It is shown that there are two different scales of structural as well as electronic disorder evolving during this annealing process. The short range electronic disorder correlates well with the short range structural disorder, which has a minimum for annealing temperatures of 925 °C and increases again for higher annealing temperatures. The long range electronic disorder can be correlated to void formation in the quantum well material, which sets in at annealing temperatures above 850 °C. This is most probably related to the existence of N-rich regions after growth, in which N_2 is formed by diffusion on the group V sublattice during the annealing, which in turn leads to a high pressure in the quantum well and the void formation. This study not only shows that optoelectronic and structural properties can be correlated well on different length scales, but also that there is the possibility to find low-temperature annealing routines, which optimize the optoelectronic properties and do not lead to void formation.

ACKNOWLEDGMENTS

Financial support by the German Science Foundation (DFG) in the framework of the GRK 1782 "Functionalization of Semiconductors" is gratefully acknowledged.

[1]A. Joullié and P. Christol, C. R. Phys. **4**, 621 (2003).
[2]H. Z. Chen, A. Ghaffari, H. Wang, H. Morkoç, and A. Yariv, Opt. Lett. **12**, 812 (1987).
[3]H. K. Choi, C. A. Wang, and N. H. Karam, Appl. Phys. Lett. **59**, 2634 (1991).
[4]T. Egawa, H. Tada, Y. Kobayashi, T. Soga, T. Jimbo, and M. Umeno, Appl. Phys. Lett. **57**, 1179 (1990).
[5]D. G. Deppe, N. Chand, J. P. Van Der Ziel, and G. J. Zydzik, Appl. Phys. Lett. **56**, 740 (1990).
[6]T. Egawa, T. Jimbo, Y. Hasegawa, and M. Umeno, Appl. Phys. Lett. **64**, 1401 (1994).
[7]S. Wirths, R. Geiger, N. von den Driesch, G. Mussler, T. Stoica, S. Mantl, Z. Ikonic, M. Luysberg, S. Chiussi, J. M. Hartmann, H. Sigg, J. Faist, D. Buca, and D. Grützmacher, Nat. Photonics **9**, 88 (2015).
[8]B. Kunert, K. Volz, J. Koch, and W. Stolz, Appl. Phys. Lett. **88**, 182108 (2006).
[9]B. Kunert, S. Zinnkann, K. Volz, and W. Stolz, J. Cryst. Growth **310**, 4776 (2008).
[10]K. Jandieri, P. Ludewig, T. Wegele, A. Beyer, B. Kunert, P. Springer, S. D. Baranovskii, S. W. Koch, K. Volz, and W. Stolz, J. Appl. Phys. **118**, 065701 (2015).
[11]N. W. Rosemann, B. Metzger, B. Kunert, K. Volz, W. Stolz, and S. Chatterjee, Appl. Phys. Lett. **103**, 252105 (2013).
[12]N. Hossain, S. J. Sweeney, S. Rogowsky, R. Ostendorf, J. Wagner, S. Liebich, M. Zimprich, K. Volz, B. Kunert, and W. Stolz, Electron. Lett. **47**, 931 (2011).
[13]S. Liebich, M. Zimprich, A. Beyer, C. Lange, D. J. Franzbach, S. Chatterjee, N. Hossain, S. J. Sweeney, K. Volz, B. Kunert, and W. Stolz, Appl. Phys. Lett. **99**, 071109 (2011).
[14]B. Kunert, D. Trusheim, V. Voßebürger, K. Volz, and W. Stolz, Phys. Status Solidi **205**, 114 (2008).
[15]S. Gies, M. Zimprich, T. Wegele, C. Kruska, A. Beyer, W. Stolz, K. Volz, and W. Heimbrodt, J. Cryst. Growth **402**, 169 (2014).
[16]K. Volz, A. Beyer, W. Witte, J. Ohlmann, I. Nmeth, B. Kunert, and W. Stolz, J. Cryst. Growth **315**, 37 (2011).
[17]I. Németh, B. Kunert, W. Stolz, and K. Volz, J. Cryst. Growth **310**, 1595 (2008).
[18]P. Ludewig, S. Reinhard, K. Jandieri, T. Wegele, A. Beyer, L. Tapfer, K. Volz, and W. Stolz, "Growth studies of Ga(NAsP)/(BGa)(AsP) multi quantum well heterostructures (MQWH) for the monolithic integration of laser structures on (001) Si-substrates," J. Cryst. Growth (published online).
[19]T. Wegele, A. Beyer, P. Ludewig, P. Rosenow, L. Duschek, K. Jandieri, R. Tonner, W. Stolz, and K. Volz, "Interface morphology and composition of Ga(NAsP) quantum well structures for monolithically integrated LASERs on silicon substrates," J. Phys. D: Appl. Phys. (to be published).
[20]B. Kunert, S. Liebich, A. Beyer, R. Fritz, S. Zinnkann, K. Volz, and W. Stolz, J. Cryst. Growth **315**, 28 (2011).
[21]D. B. Williams and C. B. Carter, *Transmission Electron Microscopy: A Textbook for Materials Science* (Springer, 2009).
[22]P. Stadelmann, Microsc. Microanal. **9**, Suppl. 03, 60 (2003).
[23]V. Grillo, K. Müller, F. Glas, K. Volz, and A. Rosenauer, Microsc. Microanal. **17**, 1862 (2011).
[24]X. Wu, M. D. Robertson, J. A. Gupta, and J.-M. Baribeau, J. Phys. Condens. Matter **20**, 075215 (2008).
[25]V. Grillo, K. Mueller, K. Volz, F. Glas, T. Grieb, and A. Rosenauer, J. Phys. Conf. Ser. **326**, 012006 (2011).
[26]J. M. LeBeau and S. Stemmer, Ultramicroscopy **108**, 1653 (2008).
[27]K. Jandieri, M. K. Shakfa, S. Liebich, M. Zimprich, B. Kunert, C. Karcher, A. Chernikov, K. Volz, W. Stolz, M. Koch, S. Chatterjee, W. Heimbrodt, F. Gebhard, and S. D. Baranovskii, Phys. Rev. B **86**, 125318 (2012).
[28]C. Karcher, K. Jandieri, B. Kunert, R. Fritz, M. Zimprich, K. Volz, W. Stolz, F. Gebhard, S. D. Baranovskii, and W. Heimbrodt, Phys. Rev. B **82**, 245309 (2010).
[29]K. Volz, T. Torunski, and W. Stolz, J. Appl. Phys. **97**, 014306 (2005).
[30]K. Volz, J. Koch, B. Kunert, I. Nemeth, and W. Stolz, J. Cryst. Growth **298**, 126 (2007).
[31]I. Németh, T. Torunski, B. Kunert, W. Stolz, and K. Volz, J. Appl. Phys. **101**, 123524 (2007).
[32]A. Y. Borisevich, J. Electron Microsc. (Tokyo) **55**, 7 (2006).

6.7 Carrier dynamics in Ga(NAsP)/Si multi-quantum well heterostructures with varying well thickness [1]

M.K. Shakfa, R. Woscholski, S. Gies, T. Wegele, M. Wiemer, P. Ludewig, K. Jandieri, S.D. Baranovskii, W. Stolz, K. Volz, W. Heimbrodt, M. Koch, Superlattices and Microstructures **93** (2016) 67–72. DOI:10.1016/j.spmi.2016.03.002.

Abstract

Time-resolved photoluminescence (TR-PL) measurements have been performed in Ga(NAsP)/(BGa)(AsP) multi-quantum well heterostructures (MQWHs) with different well thicknesses. The studied structures have been pseudomorphically grown on Si substrates by metal organic vapor phase epitaxy (MOVPE) with an N content of about 7%. Experimental results reveal a shortening in the PL decay time with increasing QW thickness, meanwhile, accompanied by a decrease in the PL intensity. We attribute this behaviour to an increasing non-radiative recombination rate for broader QWs which arises from an increasing number of defects in the QW material. The emission-energy distribution of the PL decay time is studied at various temperatures. The PL decay time strongly depends on the emission energy at low temperatures and becomes emission-energy-independent close to room temperature. This is discussed in terms of the carrier localization in the studied structures.

My contribution

In order to optimize the growth conditions of the structures with Ga(NAsP)-QWs containing 7% N I performed ADF-STEM investigations for this publication. The preparation of the TEM specimens was aslo done by me.

1 Reprinted from *Superlattices and Microstructures **93** (2016) 67–72 Contents, Copyright 2016, with permission of Elsevier.*

Superlattices and Microstructures 93 (2016) 67–72

Contents lists available at ScienceDirect

Superlattices and Microstructures

journal homepage: www.elsevier.com/locate/superlattices

Carrier dynamics in Ga(NAsP)/Si multi-quantum well heterostructures with varying well thickness

M.K. Shakfa*, R. Woscholski, S. Gies, T. Wegele, M. Wiemer, P. Ludewig, K. Jandieri, S.D. Baranovskii, W. Stolz, K. Volz, W. Heimbrodt, M. Koch

Department of Physics and Material Sciences Center, Philipps-University of Marburg, Renthof 5, 35032 Marburg, Germany

ARTICLE INFO

Article history:
Received 23 February 2016
Received in revised form 29 February 2016
Accepted 2 March 2016
Available online 3 March 2016

Keywords:
Dilute nitride Ga(NAsP)
Heterostructures
Time-resolved photoluminescence
Carrier dynamics
Defects

ABSTRACT

Time-resolved photoluminescence (TR-PL) measurements have been performed in Ga(NAsP)/(BGa)(AsP) multi-quantum well heterostructures (MQWHs) with different well thicknesses. The studied structures have been pseudomorphically grown on Si substrates by metal organic vapor phase epitaxy (MOVPE) with an N content of about 7%. Experimental results reveal a shortening in the PL decay time with increasing QW thickness, meanwhile, accompanied by a decrease in the PL intensity. We attribute this behavior to an increasing non-radiative recombination rate for broader QWs which arises from an increasing number of defects in the QW material. The emission-energy distribution of the PL decay time is studied at various temperatures. The PL decay time strongly depends on the emission energy at low temperatures and becomes emission-energy-independent close to room temperature. This is discussed in terms of the carrier localization in the studied structures.

1. Introduction

Despite previous attempts [1–5], the realization of an efficient and stable light source on Si substrates has been an enormous challenge, primarily due to the large difference in lattice constant between Si and commonly used semiconductors for optoelectronic devices such as GaAs, InP or GaN-based materials. In this context, the dilute nitride Ga(NAsP) alloy material system has been considered as a promising candidate since it has a direct band gap and can be grown lattice-matched to Si [6,7]. Making use of the aforementioned features, laser operation of Ga(NAsP)-based structures grown on Si substrates was demonstrated by Liebich et al. [8] for temperatures up to 150 K. Otherwise, Ga(NAsP) has received much attention in terms of the anticrossing interaction between N-related localized states and the extended states of the host semiconductor matrix, resulting in a multi-band electronic structure [9]. This makes Ga(NAsP), on the other hand, promising for photovoltaic applications, e.g., intermediate band solar cells [10].

The incorporation of N atoms, acting as isovalent impurities, into a III–V semiconductor leads to an increase in the alloy disorder potential because of the differences in size and electronegativity from substituted anions [11]. Besides, possible imperfect interfaces raise the disorder potential in the case of semiconductor heterostructures [12]. The presence of disorder effects within a semiconductor can dramatically affect carrier recombination processes due to increasing density of localized

* Corresponding author.
E-mail address: m.k.shakfa@gmx.de (M.K. Shakfa).

http://dx.doi.org/10.1016/j.spmi.2016.03.002
0749-6036/

states corresponding with an extension in the band-edge toward lower energies, the so-called band-tail states [13]. On the other hand, in order to incorporate a sufficient amount of N atoms in dilute nitrides, such as in the case of Ga(NAsP) [14,15], the growth process is conventionally achieved at low temperatures. Under this condition, one expects a considerable increase in the density of defects which adversely act as non-radiative recombination centers.

Consequently, an enhancement of the quality of Ga(NAsP) structures through the optimization of the growth conditions is absolutely necessary in order to achieve effective optoelectronic devices and improve their performance subsequently. In the present work, we focus on the impact of the well layer thickness on the optical properties and carrier dynamics in Ga(NAsP)/(BGa)(AsP) multi-quantum well heterostructures (MQWHs) grown on Si substrates. Time-resolved photoluminescence (TR-PL) spectroscopy is employed in our study. The paper is organized as follows; initially, the main characteristics of the PL emission from the studied MQWHs are analyzed at a very low temperature of 10 K, then, the thermal evolution of the PL intensity as well as PL decay time is studied, and ultimately, the emission-energy-dependent PL decay time is discussed for different temperatures.

2. Experimental details

The samples under investigation are a set of Ga(NAsP)/(BGa)(AsP) MQWHs grown by metal organic vapor phase epitaxy (MOVPE) on exactly oriented Si (001) substrates. The growth has taken place in a commercially available horizontal reactor system (AIX 200-GFR) using a reduced reactor pressure of 50 mbar with hydrogen as a carrier gas. All samples were deposited under identical growth conditions, where only the growth time of the QW was varied. The growth temperature was set to 525 °C and 575 °C for the Ga(NAsP) QW and (BGa)(AsP) barrier, respectively. As source molecules the more efficiently decomposing group-V-precursors tertiarybutylarsine (TBAs), tertiarybutylphosphine (TBP) and unsymmetrical 1, 1-dimethylhydrazine (UDMHy), together with the standard group-III sources triethylgallium (TEGa) and triethylboron (TEB), have been used. High resolution x-ray diffraction in combination with continuous-wave PL measurements were carried out in order to determine the thickness and composition of the Ga(NAsP) MQWHs [16]. The N content of the studied samples is ~7%, while the P content is ~14%. The QW thickness is varied between 4.0 nm and 9.9 nm.

The samples were mounted at the end of a cold finger fixed inside a liquid-helium-flow microscopy-cryostat. The temperature is controlled between 10 K and room temperature (RT) of 290 K. TR-PL measurements were performed by employing of second-harmonic pulses of a mode-locked Ti:sapphire laser, with a pulse duration of 100 fs at a repetition rate of 80 MHz, as the excitation source. The wavelength of the excitation laser is tuned to 400 nm corresponding to a photon energy of 3.1 eV which exceeds the energy band gap of the barrier. The PL signal is collected normal to the sample surface in reflection geometry. The laser beam was focused on the sample down to a spot size of about 30 μm in diameter. The spectrally as well as temporally resolved detection of the PL signal is obtained by a combination of an imaging spectrometer and a streak camera with an IR-sensitive cathode.

3. Results and discussion

Low-temperature time-integrated PL spectra and the corresponding normalized PL transients of the studied Ga(NAsP) MQWHs, with different QW thicknesses ranging from 4.0 to 9.9 nm, are shown in Fig. 1 (a) and (b), respectively. The PL emission peaks are relatively broad and display an asymmetric shape with a low-energy tail. The latter reflects the recombination of electron-holes pairs trapped in localized band-tail states [13,17] due to alloy disorder potential and QW thickness

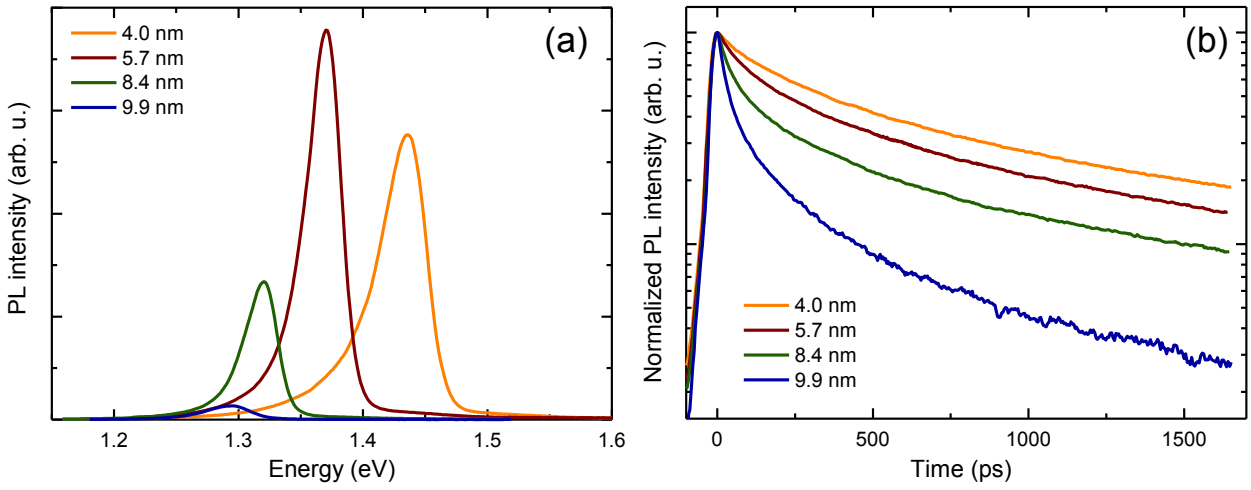

Fig. 1. (a) PL spectra and (b) corresponding normalized PL transients of the Ga(NAsP) MQWs with different well thicknesses measured at an average excitation intensity of 1 mW and a lattice temperature of 10 K.

fluctuations [18,19]. Carrier dynamics in localized band-tail states result in a non-exponential profile of the PL decay [20], as can be seen in Fig. 1(b) for all studied samples. For further analysis of the spectra presented in Fig. 1, the PL peak energy, PL linewidth, integrated PL intensity, and PL decay time are plotted as a function of the well thickness in Fig. 2(a), (b), (c), and (d), respectively. Here, the PL linewidth is given as the value of the full width at half maximum and, since the PL signal non-exponentially decays, the PL decay time is defined as the interval required for the PL intensity to decrease to the fraction of e^{-1} of its initial value. Besides the shift of the PL emission peak toward lower energies by about 140 meV with decreasing well thickness, a fluctuation in the PL linewidth between 32 meV and 45 meV for the samples with a QW thickness of 4.0 nm and 8.5 nm, respectively, is recorded. While the shift of the PL emission peak is attributed to the quantum-confinement effect, the fluctuation of the PL linewidth is due to the different degree of the disorder potential in the studied structures [21], including alloy composition fluctuations and well thickness fluctuations. A similar behavior has been reported for InGaAs QWs [22].

In spite of the slight increase in the PL intensity when the QW thickness is increased from 4.0 to 5.7 nm, a decrease of its value by more than an order of magnitude is observed when the well thickness is further increased. This trend is evidently monitored for all other studied temperatures as illustrated in Fig. 3(a). On the other hand, although the PL decay time is usually expected to increase when the QW width is increased [23], our experimental results show the opposite behavior, as can be seen in Fig. 2(d). The increase of the PL decay time with the QW width has been reported for InGaAs/InP QWs [24] and attributed to the growing dominance of radiative recombination due to the increasing spatial electron-hole separation when the QW width becomes broader. In other words, the electron and hole wave functions will extend further into the barrier regions for the narrower QW. This leads to an increasing carrier recombination outside the QW regions [25,26]. Correspondingly, a decrease of the PL decay time with increasing QW thickness, such as in our case, has been observed in AlGaN QWs [27]. This tendency, in the studied Ga(NAsP) MQWHs, is accompanied by a significant drop in the PL intensity, and hence can be ascribed to an increasing non-radiative recombination rate at the expense of the radiative one. The latter can be understood by considering the following two competing contributions: (I) a *radiative recombination channel* related to localized states due to potential QW thickness fluctuations; the density of such localized states is greater in narrower QWs [27], and (II) a *non-radiative recombination channel* due to defects caused by alloy composition fluctuations essentially associated with the inhomogeneous distribution of N atoms; the amount of defect centers increases when the growth time becomes longer in order to achieve broader QWs. It has been recently reported that although the absolute interface roughness

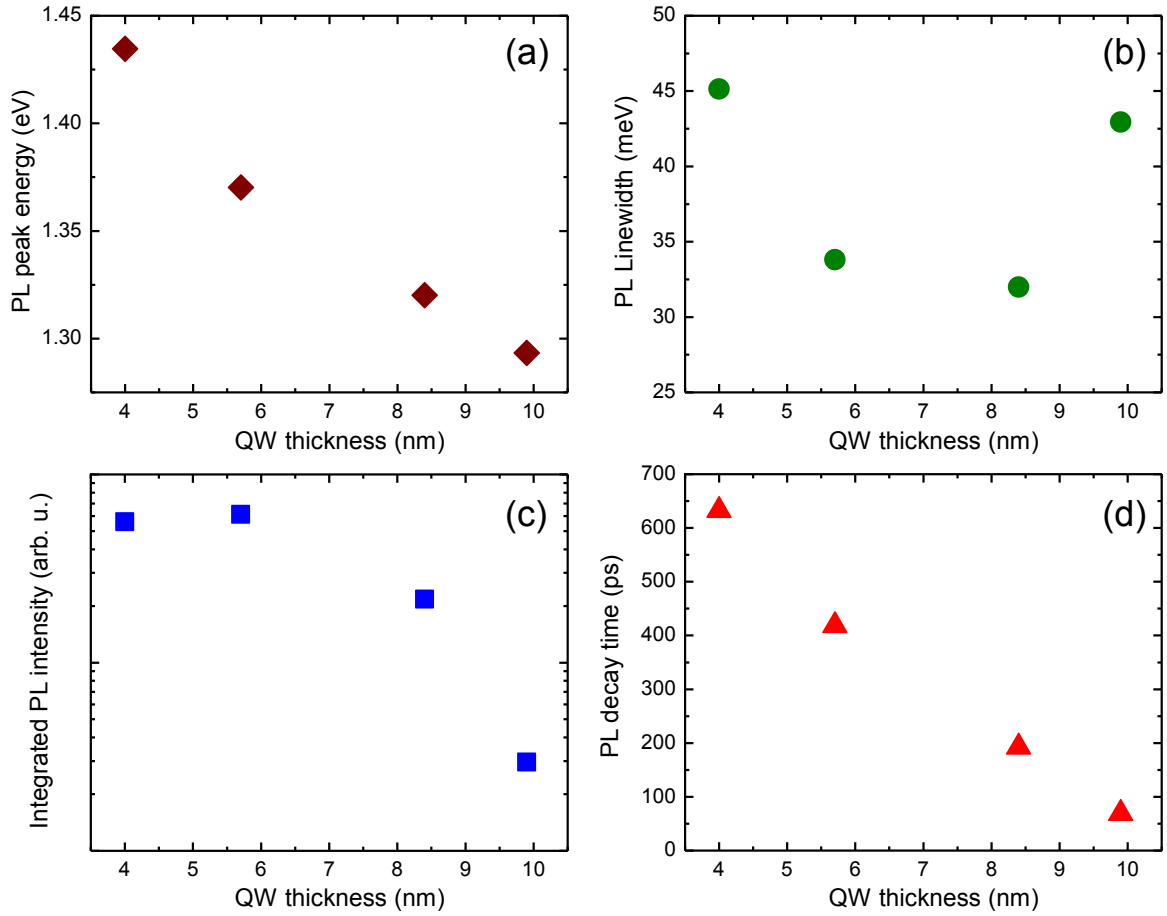

Fig. 2. (a) PL peak energy, (b) integrated PL intensity, (c) PL line width, and (d) PL decay time are plotted as a function of the QW thickness.

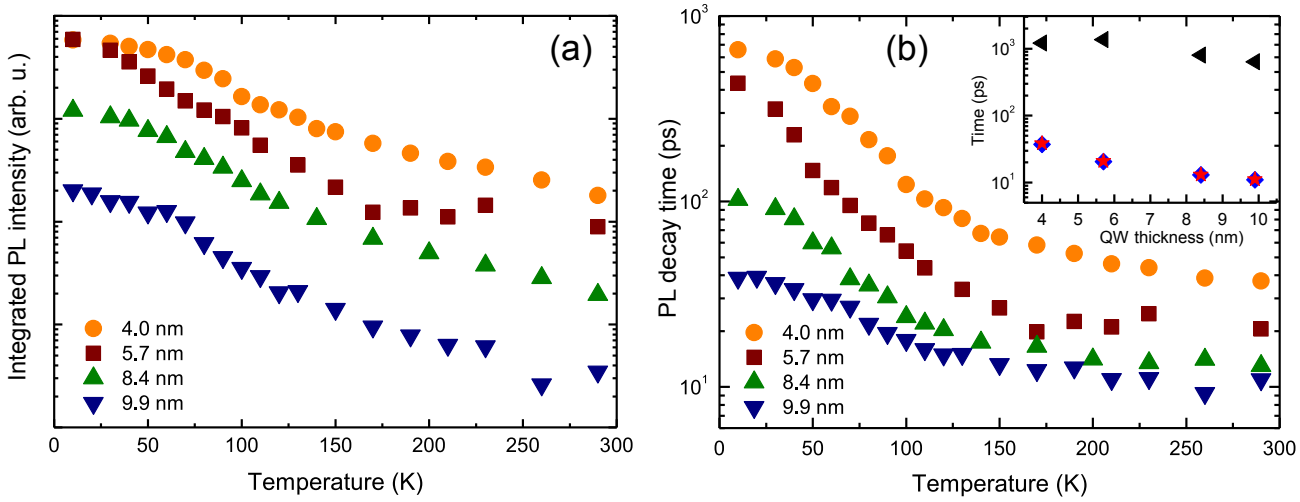

Fig. 3. Temperature-dependent (a) integrated PL intensity and (b) PL decay time of the studied Ga(NAsP) MQWHs obtained for an average excitation intensity of 1 mW. The inset in (b) shows the PL (◆), radiative (◀), and non-radiative (★) decay times as a function of the QW thickness at RT.

of Ga(NAsP) MQWHs—comparable to the structure studied here—increases with increasing well thickness, the relative roughness of the layers together with their compositional fluctuation is independent of the well thickness [28]. This leads us to the conclusion that the observed decrease of the PL decay time is attributed to the increasing density of QW material-related defects.

Fig. 3(a) and (b) show the temperature dependence of the integrated PL intensity and PL decay time, respectively, of the four studied structures obtained at an average excitation intensity of 1 mW. When the well thickness is increased, a pronounced decrease in the PL decay time is observed at all studied temperatures above 10 K. On the other hand, the temperature-dependent PL intensity of the studied samples exhibits a similar characteristic behavior that can be distinguished in three temperature ranges: a relatively weak temperature dependence at low temperatures, followed by a considerable decline in a middle temperature range, and ultimately, a relatively slow quenching with further increase of the temperature up to RT. The temperature evolution of the PL intensity plotted in Fig. 3(a) is typical for disordered semiconductors and can be interpreted in terms of carrier localization in the band-tail states [29]. In particular, as above-mentioned, at very low temperatures the PL emission arises mainly from the radiative recombination of electron-hole pairs trapped in localized states. Furthermore, in the condition of low excitation intensities, these carriers can perform phonon-assisted hopping transitions between localized states [30,32]. Such dynamics result in a slow decay of the PL signal, i.e. relatively long PL decay time, as can be seen in Fig. 3(b). For higher temperatures, the carriers become more and more mobile and an increased number of them can be captured by non-radiative centers. Here, the decay time shortening is associated with the competition between radiative and non-radiative processes. When the temperature is further increased up to RT, the majority of carriers is thermally delocalized and the non-radiative recombination channel dominates. This can explain the dramatic decrease of the PL intensity in comparison with its value at low temperatures. The internal quantum efficiency (IQE) at RT can be approximately estimated from the ratio between the PL intensity at RT to that measured at very low temperature (10 K). While the IQE value is about 3.1% for the sample with a QW thickness of 4.0 nm, it is almost 1.7% for the sample with a 9.9-nm-thickness. Besides, one can obtain the value of radiative as well as non-radiative decay time following the approach given in Ref. [31]. The inset of Fig. 3(b) shows the PL, radiative, and non-radiative decay times as a function of the QW thickness. Obviously, the radiative decay time is relatively long and, on the other hand, the PL decay time is corresponding to the non-radiative decay time. This undoubtedly confirms the dominance of non-radiative recombination at RT.

For further understanding of the carrier dynamics in the studied Ga(NAsP) MQWHs, the emission-energy dependence of the PL decay time is studied at different temperatures under the same excitation condition. Fig. 4(a), (b) and (c) show normalized spectrally-integrated PL transients of the sample with 4-nm-well thickness for some selected emission-energies at lattice temperatures of 10 K, 130 K, and 290 K, respectively. Fig. 4(a) demonstrates a strong emission-energy dependence of the PL decay rate at low temperatures. This dependence weakens when the temperature is increased (cf. Fig. 4(b)). However, the PL decay rate becomes rather independent of the emission-energy close to RT, as can be seen in Fig. 4(c). For further clarification, the PL decay times are determined from the spectrally-integrated PL transients and presented in Fig. 4(d). The low-temperature PL spectrum of the sample under consideration is also presented in Fig. 4(d). At a very low temperature of 10 K, a substantial increase by almost two orders of magnitude is observed in the PL decay time with decreasing emission-energy across the PL spectrum. The shortening of the PL decay time on the high-energy side of the PL spectrum can be attributed to the carrier relaxation among the band-tail states, i.e. carriers transfer from higher energy states to lower empty ones [33]. In addition, under low excitation conditions, these carriers can hop between localized band-tail states through phonon-assisted tunnelling transitions [17,30]. Such an emission-energy distribution of the PL decay time is widely reported

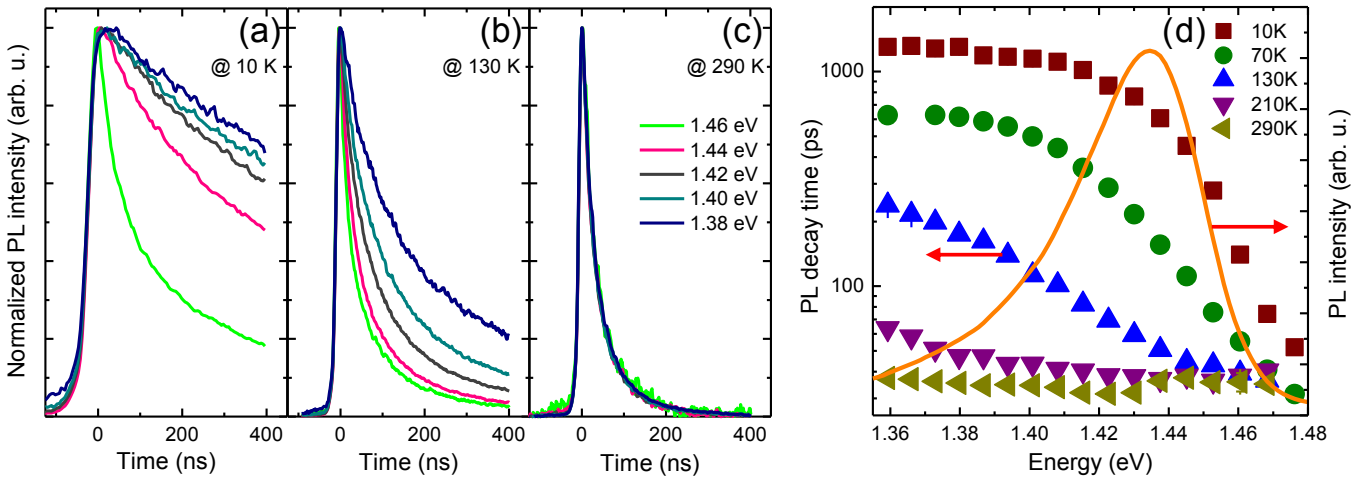

Fig. 4. PL transients of the sample with an QW width of 4.0 nm for some selected emission-energies at lattice temperatures of (a) 10 K, (b) 130 K, and (c) 292 K. (d) the PL spectrum at 10 K and the emission-energy dependence of the PL decay time at different lattice temperatures.

for disordered semiconductors at low temperatures [13,17,33–35]. However, this trend obviously weakens with increasing temperature and disappears at RT. These experimental observations are compatible with the aforementioned qualitative description of the temperature-dependent PL intensity and PL decay time. In particular, downward hopping relaxation transitions of localized carriers are dominant at low temperatures. When the temperature is increased, localized carriers are more mobile and gradually able to hop upward in energy. At high temperatures, most of the carriers are delocalized and, furthermore, dissociated into the band states by thermal activation. In the case that the rates of downward and upward carrier-transfers—between energy levels—are equal, the PL decay time is quite emission-energy independent, as can be seen at RT in Fig. 4(d).

4. Conclusions

We have investigated the optical properties and carrier dynamics in a set of Ga(NAsP)/(BGa)(AsP) multi-quantum well heterostructures (MQWHs) grown on Si substrates with respect to the well thickness using time-resolved photoluminescence (TR-PL) measurements. The N content is set to about 7% and the QW thickness is varied between 4.0 nm and 9.9 nm. An unexpected decrease in the PL decay time corresponding with a decline in the PL intensity is observed over the studied temperature range between 10 K and 290 K. This behavior is attributed to the increasing amount of defects, acting as non-radiative centers, in the QW material when the well thickness is increased. Furthermore, the thermal quenching of the PL intensity accompanied by a shortening in the PL decay time is mainly associated with the competition between radiative and non-radiative recombination processes. The emission-energy dependence of the PL decay time is studied at different temperatures. We observed a considerable increase in the PL decay time with decreasing emission-energy at low temperatures. This is attributed to carrier transfer in the energy band-tail states. The gradual disappearance of this trend with increasing temperature can be understood from the thermal carrier-delocalization.

Acknowledgments

The authors gratefully acknowledge the financial support by the German Science Foundation (DFG) through the Research Training Group (GRK 1782): *Functionalization of Semiconductors*.

References

[1] H.Z. Chen, A. Ghaffari, H. Wang, H. Morkoç, A. Yariv, Opt. Lett. 12 (1987) 812–813.
[2] H.K. Choi, C.A. Wang, N.H. Karam, Appl. Phys. Lett. 59 (1991) 2634–2635.
[3] M. Sugo, H. Mori, Y. Sakai, Y. Itoh, Appl. Phys. Lett. 60 (1992) 472–473.
[4] A.W. Fang, P. Hyundai, R. Jones, O. Cohen, M.J. Paniccia, J.E. Bowers, IEEE Phot. Technol. Lett. 18 (2006) 1143–1145.
[5] S. Wirths, R. Geiger, N. von den Driesch, G. Mussler, T. Stoica, S. Mantl, Z. Ikonic, M. Luysberg, S. Chiussi, J.M. Hartmann, H. Sigg, J. Faist, D. Buca, D. Grützmacher, Nat. Photonics 9 (2015) 88–92.
[6] B. Kunert, K. Volz, W. Stolz, Phys. Status Solidi B 244 (2007) 2730–2739.
[7] O. Durand, S. Almosni, Y. Ping Wang, C. Cornet, A. Létoublon, C. Robert, C. Levallois, L. Pedesseau, A. Rolland, J. Even, J.M. Jancu, N. Bertru, A. Le Corre, F. Mandorlo, M. Lemiti, P. Rale, L. Lombez, J.-F. Guillemoles, S. Laribi, A. Ponchet, J. Stodolna, Energy Harvest. Syst. 1 (2014) 147.
[8] S. Liebich, M. Zimprich, A. Beyer, C. Lange, D.J. Franzbach, S. Chatterjee, N. Hossain, S.J. Sweeney, K. Volz, B. Kunert, W. Stolz, Appl. Phys. Lett. 99 (2011) 071109.
[9] K.M. Yu, W. Walukiewicz, J.W. Ager, D. Bour, R. Farshchi, O.D. Dubon, S.X. Li, I.D. Sharp, E.E. Haller, Appl. Phys. Lett. 88 (2006) 092110.
[10] R. Kudrawiec, A.V. Luce, M. Gladysiewicz, M. Ting, Y.J. Kuang, C.W. Tu, O.D. Dubon, K.M. Yu, W. Walukiewicz, Phys. Rev. Appl. 1 (2014) 034007.
[11] A. Erol, Dilute III-V Nitride Semiconductors and Material Systems, Springer, Berlin- Heidelberg, Germany, 2008.

[12] C. Karcher, K. Jandieri, B. Kunert, R. Fritz, M. Zimprich, K. Volz, W. Stolz, F. Gebhard, S.D. Baranovskii, W. Heimbrodt, Phys. Rev. B 82 (2010) 245309.
[13] I.A. Buyanova, W.M. Chen, C.W. Tu, Solid State Electron 47 (2003) 467–475.
[14] B. Kunert, K. Volz, J. Koch, W. Stolz, J. Cryst. Growth 298 (2007) 121–125.
[15] S. Almosni, C. Robert, T. Nguyen Thanh, C. Cornet, A. Létoublon, T. Quinci, C. Levallois, M. Perrin, J. Kuyyalil, L. Pedesseau, A. Balocchi, P. Barate, J. Even, J. M. Jancu, N. Bertru, X. Marie, O. Durand, A. Le Corre, J. Appl. Phys. 113 (2013) 123509.
[16] P. Ludewig, S. Reinhard, K. Jandieri, T. Wegele, A. Beyer, L. Tapfer, K. Volz, W. Stolz, J. Cryst. Growth 438 (2016) 63.
[17] S. Permogorov, A. Reznitsky, J. Lumin. 52 (1992) 201–223.
[18] C. Karcher, K. Jandieri, B. Kunert, R. Fritz, K. Volz, W. Stolz, F. Gebhard, S.D. Baranovskii, W. Heimbrodt, J. Lumin. 133 (2013) 125–128.
[19] V.V. Tishchenko, N.V. Bondar, A.V. Kovalenko, M.P. Halsall, P. Lilley, Superlattices Microstruct. 24 (1998) 143–147.
[20] K. Jandieri, B. Kunert, S. Liebich, M. Zimprich, K. Volz, W. Stolz, F. Gebhard, S.D. Baranovskii, N. Koukourakis, N.C. Gerhardt, M.R. Hofmann, Phys. Rev. B 87 (2013) 035303.
[21] S.D. Baranovskii, U. Doerr, P. Thomas, A. Naumov, W. Gebhardt, Phys. Rev. B 46 (1993) 17149–17154.
[22] A. Patanè, A. Polimeni, M. Capizzi, F. Martelli, Phys. Rev. B 52 (1995) 2784–2788.
[23] J. Feldmann, G. Peter, E.O. Göbel, P. Dawson, K. Moore, C. Foxon, R.J. Elliott, Phys. Rev. Lett. 59 (1987) 2337–2340.
[24] U. Cebulla, G. Bacher, A. Forchel, G. Mayer, W.T. Tsang, Phys. Rev. B 39 (1989) 6257.
[25] U. Cebulla, G. Bacher, G. Mayer, A. Forchel, W.T. Tsang, M. Razeghi, Superlattices Microstruct. 5 (1989) 227–230.
[26] K.C. Zeng, J. Li, J.Y. Lin, H.X. Jiang, Appl. Phys. Lett. 76 (2000) 3040–3042.
[27] J. Mickevičius, G. Tamulaitis, E. Kuokštis, K. Liu, M.S. Shur, J.P. Zhang, R. Gaska, Appl. Phys. Lett. 90 (2007) 131907.
[28] T. Wegele, A. Beyer, P. Ludewig, P. Rosenow, L. Duschek, K. Jandieri, R. Tonner, W. Stolz, K. Volz, J. Phys. D. Appl. Phys. 49 (2016) 075108.
[29] O. Rubel, S.D. Baraovskii, K. Hantke, W.W. Ruhle, P. Thomas, K. Volz, W. Stolz, Phys. Rev. B 73 (2006) 233201.
[30] S.D. Baranovskii, R. Eichmann, P. Thomas, Phys. Rev. B 58 (1998) 13081–13087.
[31] Y. Kawakami, K. Omae, A. Kaneta, K. Okamoto, T. Izumi, S. Saijou, K. Inoue, Y. Narukawa, T. Mukai, S. Fujita, Phys. Status Solidi A 183 (2001) 41.
[32] T. Makino, K. Saito, M. Kawasaki, Superlattices Microstruct. 42 (2007) 206–211.
[33] C. Gourdon, P. Lavallard, Phys. Status Solidi B 153 (1989) 641–652.
[34] A. Hoffmann, R. Heitz, A. Kaschner, T. Lüttgert, H. Born, A.Y. Egorov, H. Riechert, Mater. Sci. Eng. B 93 (2002) 55–59.
[35] M.K. Shakfa, D. Kalincev, X. Lu, S.R. Johnson, D.A. Beaton, T. Tiedje, A. Chernikov, S. Chatterjee, M. Koch, J. Appl. Phys. 114 (2013) 164306.

CHAPTER 7

Zusammenfassung und Ausblick

In diesem abschließenden Kapitel werden die Ergebnisse der quantitativen Untersuchungen des Ga(NAsP)-Materialsystems zusammengefasst vorgestellt. Es wird außerdem auf einige Verbesserungsvorschläge für die weitere Forschung eingegangen. Als Untersuchungsmethode wurde in dieser Arbeit die Rastertransmissionselektronenmikroskopie (STEM[1]) mittels eines ringförmigen Dunkelfelddetektors (ADF[2]) verwendet. Diese experimentelle Methode ermöglicht einen direkten Einblick in das Material im Gegensatz zu der hochauflösenden Röntgenbeugung, Photolumineszenz- (PL) oder Raman-Spektroskopie, welche auch für die Untersuchung der Ga(NAsP)-Quantum Wells (QWs) verwendet werden.

7.1 Zusammenfassung

7.1.1 Niedrigauflösende Untersuchung der Ga(NAsP)-QWs

Für die Optimierung der Wachstumsbedingungen wurde eine Methode entwickelt, um die Qualität der Schichten in den niedrigaufgelösten STEM-Bildern quantitativ zu vergleichen. Rauigkeit der Grenzflächen und Zusammensetzungsfluktuation wurden als Indikatoren der QW-Qualität gewählt und mathematisch definiert. Diese Auswertungsmethode beschränkt sich nicht nur auf das Ga(NAsP)-Materialsystem, sondern wurde auch erfolgreich auf Ga(BiAs)-Schichten angewendet.[35]
Die Untersuchungen der Ga(NAsP)-QWs, welche bei 575 °C gewachsen wurden und unterschiedliche nominelle Schichtdicke haben, zeigten sehr interessante Ergebnisse. Obwohl die absolute Rauigkeit der QWs mit einer steigender QW-Dicke größer wird, sind die relative Rauigkeit der Schichten und auch ihre Zusammensetzungsfluktuation unabhängig von der QW-Dicke. Hingegen, wenn nominelle Dicke nahezu konstant gehalten wird und nur die Wachstumstemperatur verändert wird, stellt man einen deutlichen Effekt sowohl auf die

1 Scanning transmission electron microscopy
2 Annular Dark Field

relative Rauigkeit der Grenzflächen als auch auf die Zusammensetzungsfluktuation fest. Überraschenderweise, werden die relative und absolute Rauigkeiten größer, während die Zusammensetzungsfluktuation abnimmt. Dabei hat die bei 525 °C gewachsene Probe die niedrigste Grenzflächenrauigkeit. Es wurde überhaupt keine Phasenseparation beobachtet, was man nicht für ein metastabiles Material erwartet. Jedoch, die Ab-initio-Berechnungen haben die experimentellen Ergebnisse bestätigt und gezeigt, dass Ga(NAsP) bis zum N-Gehalt von 20% nicht in binäre Komponente separiert wird. Solche Stabilität kann aus der guten Gitteranpassung an das Si-Substrat resultieren.
Die Untersuchung der thermisch ausgeheizten Proben – mit 7% N und 11% P und der Wachstumstemperatur von 575 °C – haben gezeigt, dass nicht nur die Wachstumstemperatur, sondern auch die Temperatur der thermischen Behandlung nach dem Wachstum einen starken Effekt auf die Schichtqualität hat. Die Intensität in den zu den Ga(NAsP)-QWs benachbarten GaP-Schichten steigt nach einer schnellen thermischen Ausheilung (RTA[1]). Das könnte die Diffusion der N- oder As-Atomen aus den Ga(NAsP)-QWs verursacht haben. Dies würde die Blauverschiebung des PL Peaks und die Abnahme des Peaks des longitudinalen optischen Phonons erklären.[19] Außerdem, enthalten die QWs der Proben, welche bei 925 °C und höheren Temperaturen ausgeheizt wurden, porenartige dunkle Bereiche. Die Letzteren sind deutlich in den STEM-Bildern zu sehen. Die Ursache für diese Spots kann nicht durch einen Kompositionsgradient aufgrund ihrer sphärischen Form erklärt werden. Die Dichte und Größe dieser Spots steigt mit einer steigenden Ausheilungstemperatur. Eine quantitative Analyse der Kompositionsfluktuation in Abhängigkeit vom inneren Detektorwinkel hat gezeigt, dass die Schichten im Durchschnitt mit steigender Ausheilungstemperatur inhomogener werden. Demzufolge steigt aufgrund der Entstehung der dunklen Spots in den QWs die strukturelle Unordnung auf einer langen Skala. Das korreliert mit der elektronischen Unordnung auf einer langen Skala, welche mit der Steigung des niederenergetischen Teils der Tieftemperatur-PL-Messungen zusammenhängt.[19] Die Zusammensetzungsfluktuation in den Bereichen zwischen den dunklen Spots – strukturelle Unordnung auf einer kurzen Skala – erreicht ihr Minimum bei der Ausheilungstemperatur von 925 °C und steigt bei höheren Temperaturen wieder. Das korreliert mit der kurzreichweitigen elektronischen Unordnung, welche bei der Analyse der S-Form des PL-Maximums in den temperaturabhängigen Messungen bestimmt wurde.[19] Unter der Berücksichtigung der Ergebnisse, dass die beste Grenzflächenqualität bei Wachstumstemperatur von 525 °C erreicht wurde und die besten opto-elektronischen Eigenschaften für die Ausheilungstemperatur von 925 °C gemessen wurden, wurde eine weitere Optimierung der QW-Qualität durch Variation des N/P-Gehaltes ausprobiert. Die Untersuchung der Proben ohne einer thermischen Behandlung nach dem Wachstum (as grown) hat gezeigt, dass die Proben mit dem steigenden P-Gehalt homogener werden.

1 Rapid thermal annealing

Die Abhängigkeit an der N-Konzentration weist ein anderes Verhalten auf. Bis zu einem N-Gehalt von 6.5% N nimmt die Zusammensetzungsfluktuation ab und steigt danach mit dem steigenden N-Gehalt wieder. Nach der thermischen Behandlung bei 925 °C entstehen dunkle Spots in den QWs für alle N/P-Konzentrationen, welche im Rahmen dieser Arbeit untersucht wurden. Die Dichte der Spots und ihre Größe steigen mit dem steigenden N-Gehalt in den ausgeheizten Proben. Die langreichweitige strukturelle Unordnung ist größer in diesem Fall im Vergleich zu den 'as grown' Proben. Diese nimmt mit dem steigenden P-Gehalt ab. Die Abhängigkeit vom N-Gehalt ist umgekehrt. Die kurzreichweitige strukturelle Unordnung hat ihr Minimum wieder bei 6.5% N. Bei den höheren N-Konzentrationen (oder P-Gehalt unter 15%) werden die Bereiche zwischen den dunklen Spots nach dem Annealing homogener als in den 'as grown' Proben.

7.1.2 Hochauflösende Untersuchung der Ga(NAsP)-QWs

Die Art der dunklen Spots ging aus den hochauflösenden STEM-Untersuchungen hervor. Durch das Anwenden der reduzierten Fokustiefe in einem aberrations-korrigierten Mikroskop, wurden die hochaufgelöste STEM-Bilder auf den Positionen mit den dunklen Bereichen für verschiedene Defokuswerte aufgenommen.[10] Die Aufnahme eines STEM-Bildes mit gleichzeitig fokussierten Atomsäulen in den dunklen Spots und in den umliegenden hellen Bereichen war nicht möglich. Ein signifikanter Defokusunterschied von 30 nm bedeutet, dass die hellen und dunklen Bereiche im QW eine unterschiedliche Dicke haben. Dies bestätigt die Annahme, dass porenartige Strukturen oder Löcher nach dem Annealing entstehen. Es ist davon auszugehen, dass der Grund für die Entstehung der Poren der hohe Druck in den QWs ist, der durch N_2 entstehen könnte. Zur Bildung der N_2-Moleküle kann es bei der Diffusion der N-Atome in den N-reichen Bereichen kommen.
Die Intensitätsverteilung der Gruppe-III und Gruppe-V Atomsäulen und sowie im Hintergrund wurden für unterschiedliche Detektorwinkeln quantitativ untersucht. Eine ausgezeichnete Übereinstimmung der simulierten und der experimentellen Ergebnisse wurde für die hohen und mittleren Detektorwinkel festgestellt. Dennoch, trat eine enorme Abweichung bis zu 30% zwischen den experimentellen und simulierten Ergebnissen für die niedrigen inneren Detektorwinkel auf. Das bedeutet, dass es einen physikalischen Prozess gibt, welcher noch nicht bei der Simulation berücksichtigt wurde. Er scheint nur einen signifikanten Effekt für die niedrigen inneren Detektorwinkel zu haben.

7.1.3 Ausblick

Die in dieser Arbeit präsentierte Quantifizierungsmethode benötigt eine weitere Optimierung. Erstens, es ist wichtig diese Auswertungsmethode auf Ga(NP)- und Ga(NAs)-Schichten anzuwenden, um die hier diskutierten Annahmen zu überprüfen. Ein Vergleich

der Zusammensetzungsfluktuationen in diesen zwei Materialsystemen für 'as grown' Proben würde zeigen, ob ein direkter Zusammenhang zwischen der Verteilung der Komponenten in den QWs und der Einbaueffizienz der N-Atome besteht.
Eine quantitative Analyse der ausgeizten Proben, der oben erwähnten ternären Materialsysteme ist auch von großer Bedeutung. Die Größe und Dichte der Löcher sollten für die gleiche N-Konzentration in Ga(NP) und Ga(NAs) verglichen werden. Es wäre außerdem sehr interessant zu bestimmen, wie sich Dichte und Größe der Löcher mit dem steigenden N-Gehalt auch in diesen Materialien ändern werden. Das würde die Auswertungserbnisse an den 'as grown' Proben ergänzen und eine zusätzliche Information über unterschiedliches Clustering der N-Atome in den verschiedenen Materialsystemen liefern. Außerdem könnte die Größe einer Änderung der Zusammensetzungsfluktuation vor und nach dem Ausheilen (zwischen den Poren) in unterschiedlichen ternären verdünnten N-haltigen Materialsystemen auf unterschiedliche Konzentrationen der Punktdefekte und sogar auf eine unterschiedliche Art dieser Punktdefekte hinweisen. Das Letztere hätte auch unterschiedliche Diffusionsmechanismen zur Folge. Sehr hilfreich wäre die Anwendung der feldmodulierten Spektroskopie oder die Bestimmung der Absorption des QWs durch eine Messung des Photostromes.[1]
Die in dieser Arbeit präsentierte quantitative Analyse wurde nur an den konventionell präparierten TEM-Proben durchgeführt. Ein Vergleich mit denselben Proben, aber präpariert, z. B. mittels eines fokussierten Ionenstrahles (FIB[2]), könnte auch sinnvoll sein. In diesem Fall könnte eine Unterschätzung der Probendicke aufgrund des Verspannungsfeldes der Oberfläche ausgeschlossen sein. Die Dicke dabei ist schon nach der Präparation bekannt. Alternativ, könnte die Probendicke auch mit Hilfe des Winkel-aufgelösten STEMs bestimmt werden.[45]
Für die Erklärung der großen relativen Abweichung der experimentellen Daten von den Simulationsergebnissen für den niedrigen Detektorwinkel von 34 mrad, muss der Einfluss der Plasmonenstreuung auf STEM-Intensität untersucht werden. Nach den letzten Ergebnissen variieren diese Streuprozesse in Abhängigkeit vom gewählten inneren Detektorwinkel.
Die festgestellte Änderung des Musters in den Mappen der Intensitäts- oder Zusammensetzungsfluktuation in Abhängigkeit vom inneren Detektorwinkel bedeutet, dass die Komposition einer einzelnen Atomsäule durch einen Vergleich mit den einzelnen simulierten Atomsäulen mit bekannten Konzentrationen bestimmt werden könnte.

1 empfohlen von Prof. Dr. Weiser
2 Focused ion beam

Bibliography

[1] Brillouin zone. URL https://upload.wikimedia.org/wikipedia/commons/thumb/c/c1/Brillouin_Zone_(1st,_FCC).svg/600px-Brillouin_Zone_(1st,_FCC).svg.png.

[2] Chromatic Aberration. URL http://dev.laptop.org/pub/content/wp/images/400px-Lens6a.svg.png.

[3] Coma. URL http://dev.laptop.org/pub/content/wp/images/400px-Lens-coma.svg.png.

[4] Sperical Aberration. URL http://dev.laptop.org/pub/content/wp/images/400px-Lens5.svg.png.

[5] YAP. URL https://www.emsdiasum.com/microscopy/products/sem/scintillator.aspx.

[6] Dilute III-V Nitride Semiconductors and Material Systems. pages 183–184. Springer, 2008. ISBN 9783540745280.

[7] L. Alexandre, G Jurczak, C. Alfonso, W Saikly, C. Grosjean, A Charai, and J. Thibault. CBED and FE Study of Thin Foil Relaxation in Cross-Section Samples of Si /Si1-xGex and Si /Si1-xGex /Si Heterostructures. In *Microscopy of Semiconducting Materials 2007*, volume 0, pages 415–418. Springer Netherlands, Dordrecht, 2008. ISBN 978-1-4020-8615-1. doi: 10.1007/978-1-4020-8615-1_90.

[8] A. Beyer, R. Straubinger, J. Belz, and K. Volz. Local sample thickness determination via scanning transmission electron microscopy defocus series. *Journal of Microscopy*, 262(2):171–177, may 2016. ISSN 00222720. doi: 10.1111/jmi.12284.

[9] A. Bogner, P.-H. Jouneau, G. Thollet, D. Basset, and C. Gauthier. A history of scanning electron microscopy developments: Towards 'wet-STEM' imaging. *Micron*, 38(4):390–401, jun 2007. ISSN 09684328. doi: 10.1016/j.micron.2006.06.008.

[10] A. Y. Borisevich, A. R. Lupini, and S. J. Pennycook. Depth sectioning with the aberration-corrected scanning transmission electron microscope. *Proceedings of the*

National Academy of Sciences, 103(9):3044–3048, feb 2006. ISSN 0027-8424. doi: 10.1073/pnas.0507105103.

[11] N. Braidy, Y. Le Bouar, S. Lazar, and C. Ricolleau. Correcting scanning instabilities from images of periodic structures. *Ultramicroscopy*, 118:67–76, 2012. ISSN 03043991. doi: 10.1016/j.ultramic.2012.04.001.

[12] S. Chung, D. J. Smith, and M. R. McCartney. Determination of the Inelastic Mean-Free-Path and Mean Inner Potential for AlAs and GaAs Using Off-Axis Electron Holography and Convergent Beam Electron Diffraction. *Microscopy and Microanalysis*, 13(05):329–335, oct 2007. ISSN 1431-9276. doi: 10.1017/S1431927607070687.

[13] J. M. Cowley. Adjustment of a STEM instrument by use of shadow images. *Ultramicroscopy*, 4(4):413–418, 1979. ISSN 03043991. doi: 10.1016/S0304-3991(79)80018-2.

[14] T. G. Dargam and B. Koiller. Interface Roughness and the Optical Properties of Quantum Wells. *Solid State Communications*, 105(4):211–214, 1998.

[15] J. A. Dura, J. G. Pellegrino, and C. A. Richter. X-ray reflectivity determination of interface roughness correlated with transport properties of (AlGa)As/GaAs high electron mobility transistor devices. *Applied Physics Letters*, 69(8):1134, 1996. ISSN 00036951. doi: 10.1063/1.117082.

[16] J. Fertig and H. Rose. Resolution and contrast of crystalline objects in high-resolution scanning-transmission electron-microscopy. *Optik*, 59:407–429, 1981.

[17] R. Fritz. *Elektronenmikroskopische Untersuchungen zur quantitativen Analyse an verdünnt stickstoffhaltigen III / V- Halbleiter- Heterostrukturen*. PhD thesis, Philipps-Universität Marburg, 2008.

[18] P. L. Galindo, S. Kret, A. M. Sanchez, J. Y. Laval, A. Yáñez, J. Pizarro, E. Guerrero, T. Ben, and S. I. Molina. The Peak Pairs algorithm for strain mapping from HRTEM images. *Ultramicroscopy*, 107(12):1186–1193, 2007. ISSN 03043991. doi: 10.1016/j.ultramic.2007.01.019.

[19] S. Gies, M. Zimprich, T. Wegele, C. Kruska, A. Beyer, W. Stolz, K. Volz, and W. Heimbrodt. Annealing effects on the composition and disorder of Ga(N,As,P) quantum wells on silicon substrates for laser application. *Journal of Crystal Growth*, 402:169–174, 2014. ISSN 00220248. doi: 10.1016/j.jcrysgro.2014.05.012.

[20] T. Grieb, K. Müller, E. Cadel, A. Beyer, M. Schowalter, E. Talbot, K. Volz, and A. Rosenauer. Simultaneous Quantification of Indium and Nitrogen Concentration in InGaNAs Using HAADF-STEM. *Microscopy and Microanalysis*, 20(06):1740–1752, 2014. ISSN 1431-9276. doi: 10.1017/S1431927614013051.

[21] V. Grillo, K. Mueller, K. Volz, F. Glas, T. Grieb, and A. Rosenauer. Strain, composition and disorder in ADF imaging of semiconductors. *Journal of Physics: Conference Series*, 326:012006, 2011. ISSN 1742-6596. doi: 10.1088/1742-6596/326/1/012006.

[22] S. Gunelius. The Data Explosion in 2014 Minute by Minute - Infographic. URL http://aci.info/2014/07/12/the-data-explosion-in-2014-minute-by-minute-infographic/.

[23] M. Haider, P. Hartel, H. Müller, S. Uhlemann, and J. Zach. Current and future aberration correctors for the improvement of resolution in electron microscopy. *Philosophical transactions. Series A, Mathematical, physical, and engineering sciences*, 367 (1903):3665–82, 2009. ISSN 1364-503X. doi: 10.1098/rsta.2009.0121.

[24] P. Hartel, H. Rose, and C. Dinges. Conditions and reasons for incoherent imaging in STEM. *Ultramicroscopy*, 63(2):93–114, 1996. ISSN 03043991. doi: 10.1016/0304-3991(96)00020-4.

[25] D. S. He and Z. Y. Li. A practical approach to quantify the ADF detector in STEM. *Journal of Physics: Conference Series*, 522:012017, jun 2014. ISSN 1742-6588. doi: 10.1088/1742-6596/522/1/012017.

[26] M. Henini, A. Patanè, and L. Eaves. *Dilute Nitride Semiconductors*. 2005. ISBN 9780080445021. doi: 10.1016/B978-008044502-1/50008-1. URL http://www.sciencedirect.com/science/article/pii/B9780080445021500081.

[27] S. Hunklinger. *Festkörperphysik*, volume 1. de Gruyter Oldenbourg, München, 2 edition, 2009. ISBN 978-3-486-59045-6.

[28] H. Ibach and H. Lüth. *Festkörperphysik*. Springer-Lehrbuch. Springer Berlin Heidelberg, Berlin, Heidelberg, 5. edition, 2009. ISBN 978-3-540-85794-5. doi: 10.1007/978-3-540-85795-2.

[29] K. Jandieri, P. Ludewig, T. Wegele, A. Beyer, B. Kunert, P. Springer, S. D. Baranovskii, S. W. Koch, K. Volz, and W. Stolz. Compositional dependence of the band gap in Ga(NAsP) quantum well heterostructures. *Journal of Applied Physics*, 118(6), 2015. ISSN 10897550. doi: 10.1063/1.4928331.

[30] H. Jiang, J. Ruokolainen, N. Young, T. Oikawa, A. G. Nasibulin, A. Kirkland, and E. I. Kauppinen. Performance and early applications of a versatile double aberration-corrected JEOL-2200FS FEG TEM/STEM at Aalto University. *Micron*, 43(4): 545–550, 2012. ISSN 09684328. doi: 10.1016/j.micron.2011.10.004.

[31] L. Jones and P. D. Nellist. STEM Image Post-processing for Instability and Aberration Correction for Transfer Function Extension. *Journal of Physics: Conference Series*, 371:012001, 2012. ISSN 1742-6596. doi: 10.1088/1742-6596/371/1/012001.

[32] L. Jones, H. Yang, T. J. Pennycook, M. S. J. Marshall, S. V. Aert, N. D. Browning, M. R. Castell, and P. D Nellist. Smart Align âĂŤ a new tool for robust non-rigid registration of scanning microscope data. *Advanced Structural and Chemical Imaging*, pages 1–16, 2015. ISSN 2198-0926. doi: 10.1186/s40679-015-0008-4.

[33] T. Katsuyama. Development of Semiconductor Laser for Optical Communication. *SEI TECHNICAL REVIEW*, (69):13–20, 2009.

[34] E. J. Kirkland and M. G. Thomas. A high efficiency annular dark field detector for STEM. *Ultramicroscopy*, 62(1-2):79–88, 1996. ISSN 03043991. doi: 10.1016/0304-3991(95)00092-5.

[35] Nikolai Knaub, Andreas Beyer, Tatjana Wegele, Peter Ludewig, and Kerstin Volz. Quantification of Bi distribution in MOVPE-grown Ga(AsBi) via HAADF STEM. *Journal of Crystal Growth*, 433:89–96, jan 2016. ISSN 00220248. doi: 10.1016/j.jcrysgro.2015.10.007.

[36] Sebastian Kosch. Astigmatism. URL http://media-2.web.britannica.com/eb-media/46/3246-004-AF8D2D7B.jpg.

[37] B. Kunert, K. Volz, J. Koch, and W. Stolz. Direct-band-gap Ga(NAsP)-material system pseudomorphically grown on GaP substrate. *Applied Physics Letters*, 88(18):1–4, 2006. ISSN 00036951. doi: 10.1063/1.2200758.

[38] B. Kunert, K. Volz, J. Koch, and W. Stolz. MOVPE growth conditions of the novel direct band gap, diluted nitride Ga(NAsP) material system pseudomorphically strained on GaP-substrate. *Journal of Crystal Growth*, 298(SPEC. ISS):121–125, 2007. ISSN 00220248. doi: 10.1016/j.jcrysgro.2006.10.013.

[39] B. Kunert, S. Liebich, A. Beyer, R. Fritz, S. Zinnkann, K. Volz, and W. Stolz. Correlation between hetero-interface properties and photoluminescence efficiency of Ga(NAsP)/(BGa)P multi-quantum well structures on (0 0 1) Si substrate. *Journal of Crystal Growth*, 315(1):28–31, 2011. ISSN 00220248. doi: 10.1016/j.jcrysgro.2010.07.068.

[40] S. Liebich, M. Zimprich, A. Beyer, C. Lange, D. J. Franzbach, S. Chatterjee, N. Hossain, S. J. Sweeney, K. Volz, B. Kunert, and W. Stolz. Laser operation of Ga(NAsP) lattice-matched to (001) silicon substrate. *Applied Physics Letters*, 99(7):10–13, 2011. ISSN 00036951. doi: 10.1063/1.3624927.

[41] R. F. Loane, E. J. Kirkland, and J. Silcox. Visibility of single heavy atoms on thin crystalline silicon in simulated annular Dark-Field STEM images. *Acta Crystallographica Section A*, 44(6):912–927, 1988. ISSN 16005724. doi: 10.1107/S0108767388006403.

[42] P. Ludewig, S. Reinhard, K. Jandieri, T. Wegele, A. Beyer, K. Volz, and W. Stolz. MOVPE growth studies of Ga(NAsP)/(BGa)(AsP) multi quantum well heterostructures (MQWH) for the monolithic integration of laser structures on (001) Si-substrate. *Journal of Crystal Growth*, 438:63–69, 2016. ISSN 00220248. doi: 10.1016/j.jcrysgro.2015.12.024.

[43] K. A. Mkhoyan, S. E. Maccagnano-Zacher, E. J. Kirkland, and J. Silcox. Effects of amorphous layers on ADF-STEM imaging. *Ultramicroscopy*, 108(8):791–803, 2008. ISSN 03043991. doi: 10.1016/j.ultramic.2008.01.007.

[44] D. A. Muller and J. Grazul. Optimizing the environment for sub-0.2 nm scanning transmission electron microscopy. *Journal of Electron Microscopy*, 50(3):219–226, 2001. ISSN 00220744. doi: 10.1093/jmicro/50.3.219.

[45] K. Müller-Caspary, O. Oppermann, T. Grieb, M. Schowalter, F. F. Krause, T. Mehrtens, P. Potapov, A. Beyer, and K. Volz. Angle-resolved scanning transmission electron microscopy. 2016.

[46] E. Murphy. The semiconductor laser: Enabling optical communication. *Nature Photonics*, 4(5):287–287, 2010. ISSN 1749-4885. doi: 10.1038/nphoton.2010.107.

[47] S. Nakamura and S. F. Chichibu. *Introduction to nitride semiconductor blue lasers and light emitting diodes*. 2000. ISBN 0748408363.

[48] I. Németh, B. Kunert, W. Stolz, and K. Volz. Heteroepitaxy of GaP on Si: Correlation of morphology, anti-phase-domain structure and MOVPE growth conditions. *Journal of Crystal Growth*, 310(7-9):1595–1601, 2008. ISSN 00220248. doi: 10.1016/j.jcrysgro.2007.11.127.

[49] U. Penner, H. Rücker, and I. N. Yassievich. Theory of interface roughness scattering in quantum wells. *Semiconductor Science and Technology*, 13(7):709–713, 1999. ISSN 0268-1242. doi: 10.1088/0268-1242/13/7/009.

[50] S. J. Pennycook. Z-contrast stem for materials science. *Ultramicroscopy*, 30(1-2): 58–69, 1989. ISSN 03043991. doi: 10.1016/0304-3991(89)90173-3.

[51] S. J. Pennycook. Seeing the atoms more clearly: STEM imaging from the Crewe era to today. *Ultramicroscopy*, 123:28–37, 2012. ISSN 03043991. doi: 10.1016/j.ultramic.2012.05.005.

[52] S. J. Pennycook and D. E. Jesson. High-resolution Z-contrast imaging of crystals. *Ultramicroscopy*, 37(1-4):14–38, 1991. ISSN 03043991. doi: 10.1016/0304-3991(91)90004-P.

[53] S. J. Pennycook and P. D. Nellist, editors. *Scanning Transmission Electron Microscopy*. Springer New York, New York, NY, 2011. ISBN 978-1-4419-7199-9. doi: 10.1007/978-1-4419-7200-2.

[54] A. Rockett. *The Materials Science of Semiconductors*. Springer US, Boston, MA, 2008. ISBN 978-0-387-25653-5. doi: 10.1007/978-0-387-68650-9.

[55] N. W. Rosemann, B. Metzger, B. Kunert, K. Volz, W. Stolz, and S. Chatterjee. Temperature-dependent quantum efficiency of Ga(N,As,P) quantum wells. *Applied Physics Letters*, 103(25), 2013. ISSN 00036951. doi: 10.1063/1.4852575.

[56] A. Rosenauer and M. Schowalter. STEMSIM – a New Software Tool for Simulation of STEM HAADF Z-Contrast Imaging. In *Microscopy of Semiconducting Materials 2007*, volume 120, pages 170–172. Springer Netherlands, Dordrecht, 2008. ISBN 978-1-4020-8615-1.

[57] E. Rutherford. The scattering of α and β particles by matter and the structure of the atom. *Philosophical Magazine*, 21:669–688, 1911.

[58] H. Sakaki, T. Noda, K. Hirakawa, M. Tanaka, and T. Matsusue. Interface roughness scattering in GaAs/AlAs quantum wells. *Applied Physics Letters*, 51(23):1934–1936, 1987. ISSN 00036951. doi: 10.1063/1.98305.

[59] B. Sanou. ICT Facts & Figures. 2015. URL http://www.itu.int/en/ITU-D/Statistics/Documents/facts/ICTFactsFigures2015.pdf.

[60] W. Shan, W. Walukiewicz, J. Ager, E. Haller, J. Geisz, D. Friedman, J. Olson, and S. Kurtz. Band Anticrossing in GaInNAs Alloys. *Physical Review Letters*, 82(6): 1221–1224, 1999. ISSN 0031-9007. doi: 10.1103/PhysRevLett.82.1221.

[61] S. G. Spruytte, M C Larson, W Wampler, C W Coldren, and H E Petersen. Nitrogen incorporation in group III – nitride – arsenide materials grown by elemental source molecular beam epitaxy. 228:506–515, 2001.

[62] G. B. Stringfellow. Thermodynamics. In *Organometallic Vapor-Phase Epitaxy: Theory and Practice*, pages 59–60. Academic Press, New York, 2nd edition, 1999. ISBN 9780126738421.

[63] D. Van Dyck. Is the frozen phonon model adequate to describe inelastic phonon scattering? *Ultramicroscopy*, 109(6):677–682, 2009. ISSN 03043991. doi: 10.1016/j.ultramic.2009.01.001.

[64] K. Volz, J. Koch, B. Kunert, I. Nemeth, and W. Stolz. Influence of annealing on the optical and structural properties of dilute N-containing III/V semiconductor heterostructures. *Journal of Crystal Growth*, 298(SPEC. ISS):126–130, 2007. ISSN 00220248. doi: 10.1016/j.jcrysgro.2006.10.014.

[65] K. Volz, A. Beyer, W. Witte, J. Ohlmann, I. Nmeth, B. Kunert, and W. Stolz. GaP-nucleation on exact Si (0 0 1) substrates for III/V device integration. *Journal of Crystal Growth*, 315(1):37–47, 2011. ISSN 00220248. doi: 10.1016/j.jcrysgro.2010.10.036.

[66] T. Walther. A new experimental procedure to quantify annular dark field images in scanning transmission electron microscopy. *Journal of Microscopy*, 221(2):137–144, 2006. ISSN 00222720. doi: 10.1111/j.1365-2818.2006.01551.x.

[67] T. Walther, Y. Qiu, and A. G. Cullis. Measuring the contrast in annular dark field STEM images as a function of camera length. *Journal of Physics: Conference Series*, 241:012068, 2010. ISSN 1742-6596. doi: 10.1088/1742-6596/241/1/012068.

[68] M. Watanabe. The Aberration Corrected JEOL JEM-2200FS FEG- STEM/TEM Fitted with an Ω Electron Energy-Filter: Performance Characterization and Selected Applications. 41(1), 2006.

[69] T. Wegele, A. Beyer, S. Gies, M. Zimprich, W. Heimbrodt, W. Stolz, and K. Volz. Correlation of the nanostructure with optoelectronic properties during rapid thermal annealing of Ga(NAsP) quantum wells grown on Si(001) substrates. *Journal of Applied Physics*, 119(2):025705, jan 2016. ISSN 0021-8979. doi: 10.1063/1.4939889.

[70] T. Wegele, A. Beyer, P. Ludewig, P. Rosenow, L. Duschek, K. Jandieri, R. Tonner, W. Stolz, and K. Volz. Interface morphology and composition of Ga(NAsP) quantum well structures for monolithically integrated LASERs on silicon substrates. *Journal of Physics D: Applied Physics*, 49(7):075108, feb 2016. ISSN 0022-3727. doi: 10.1088/0022-3727/49/7/075108.

[71] D. B. Williams and C. B. Carter. *Transmission Electron Microscopy: A Textbook for Materials Science*, volume V1-V4. 2009. ISBN 9780387765006. doi: 10.1007/978-1-61779-415-5_23.

[72] J. Y. Yeh, L. J. Mawst, A. A. Khandekar, T. F. Kuech, I. Vurgaftman, J. R. Meyer, and N. Tansu. Characteristics of InGaAsN-GaAsSb type-II "W" quantum wells. *Journal of Crystal Growth*, 287(2):615–619, 2006. ISSN 00220248. doi: 10.1016/j.jcrysgro.2005.10.087.

[73] P. Y. Yu and M. Cardona. *Fundamentals of Semiconductors*, volume 1 of *Graduate Texts in Physics*. Springer Berlin Heidelberg, Berlin, Heidelberg, 2010. ISBN 978-3-642-00709-5. doi: 10.1007/978-3-642-00710-1.

[74] Z. Yu, D. A. Muller, and J. Silcox. Study of strain fields at a-Si/c-Si interface. *Journal of Applied Physics*, 95(7):3362–3371, 2004. ISSN 00218979. doi: 10.1063/1.1649463.

[75] F. Zemlin, K. Weiss, P. Schiske, W. Kunath, and K. Herrmann. COMA-FREE ALIGNMENT OF HlGH RESOLUTlON ELECTRON MlCROSCOPES WITH THE AID OF OPTlCAL DIFFRACTOGRAMS. *Ultramicroscopy*, 3:49–60, 1978.

[76] J. Y. Zhang, J. Hwang, B. J. Isaac, and S. Stemmer. Variable-angle high-angle annular dark-field imaging: application to three-dimensional dopant atom profiling. *Scientific Reports*, 5(February):12419, 2015. ISSN 2045-2322. doi: 10.1038/srep12419.

[77] M. Zimprich. *Optimierung Ga(NAsP)-basierender Heterostrukturen auf Si-Substrat für Laseranwendungen*. PhD thesis, Philipps-Universität Marburg, 2013.

Danksagung

An dieser Stelle möchte ich allen, ohne die diese Arbeit nicht gelungen wäre, ganz herzlich danken.
Frau Prof. Dr. Volz danke ich für die Aufnahme in ihre Arbeitsgruppe, die richtig gute Betreuung, ein tiefes Interesse an meiner Arbeit, Motivation, ständige Unterstüzung, ihr Humor und Hartnäckigkeit. Ganz besonderen Dank für die Möglichkeit mit so einem hervorragenden Gerät, wie das TEM, arbeiten zu können und für das Glauben an mich.
Herrn Dr. habil. Stolz danke ich für die interessanten Denkanstöße, Verbesserungsvorschläge. Ich danke ihn herzlich auch für die guten Worte, die er immer findet, wenn es jemandem nicht gut geht, und natürlich für das Ga(NAsP)-Materialsystem.
Herrn Prof. Dr. Heimbrodt möchte ich für die freundliche Übernahme des Zweitgutachtens danken.
Herrn Prof. Dr. Gebhard und Herrn Dr. Tonner danke ich für die Zusage in meiner Prüfungskommission zu sein.
Herrn Dr. Beyer danke ich für die Betreuung, einfallsreiche Ideen und Hilfe.
Ich möchte auch Frau Vaupel vom ganzen Herzen danken. Liebe Elke, danke, dass es dich gibt.
Herrn Dr. Ludewig danke ich für die Proben, die man gern misst.
Das gesamte STRL Team danke ich für die schöne Zeit, interessante Konferenzen, lustige Mittagszeiten und ständige Unterstützung.
Rocío, Andrea und Katha danke ich für die freundlichen und aufrichtigen Gespräche.
Isabelle und Marina danke ich vor allem für ihre Geduld.
Der größte Dank geht an meine Familie: meine Eltern und meine Geschwister. Danke, dass ihr für mich immer da seid.
Auch einen riesigen Dank geht an meinen lieben Marcus :-)

.